



University of
Massachusetts
Amherst

Engineering Advanced Morphologies for Structurally Reinforced Polyolefins

Item Type	dissertation
Authors	Cromer, Brian M
DOI	10.7275/8414086.0
Download date	2024-12-16 07:58:55
Link to Item	https://hdl.handle.net/20.500.14394/19866

ENGINEERING ADVANCED MORPHOLOGIES FOR STRUCTURALLY
REINFORCED POLYOLEFINS

A Dissertation Presented

by

BRIAN MICHAEL CROMER

Submitted to the Graduate School of the
University of Massachusetts Amherst in partial fulfillment
of the requirements for the degree of

DOCTOR OF PHILOSOPHY

May 2016

Polymer Science and Engineering

© Copyright by Brian Michael Cromer 2016

All Rights Reserved

ENGINEERING ADVANCED MORPHOLOGIES FOR STRUCTURALLY
REINFORCED POLYOLEFINS

A Dissertation Presented

by

BRIAN MICHAEL CROMER

Approved as to style and content by:

Professor E. Bryan Coughlin, Co-Chair

Professor Alan J. Lesser, Co-Chair

Professor Jonathan Rothstein, Member

Professor David A. Hoagland,
Department Head
Polymer Science and Engineering

DEDICATION

To my parents and my beloved wife, Molly

ACKNOWLEDGMENTS

Firstly, I would like to thank my advisors Prof. E. Bryan Coughlin and Prof. Alan Lesser for their invaluable contributions to my growth and maturation as a person and as a scientist. In addition to being a brilliant scientist, Professor Coughlin is also a natural teacher and mentor, which significantly influenced my intellectual development. His patience, enthusiasm, and wisdom continuously inspired and motivated me throughout my studies. Professor Lesser also impacted me greatly through his guidance and support. His enthusiasm and brilliant ideas taught me how to think with an innovative mindset through challenging conventional approaches to research. Under his direction, I've expanded my scientific skillset and accomplished things I never thought I could do. Secondly, I would like to thank my committee member Prof. Jonathan P. Rothstein, whose valuable input improved my thesis work through provoking me to consider my research from other scientific perspectives.

Next I would like to thank the members of Lesser Group and Coughlin Group for teaching me so much and helping me to enjoy my time at UMass Amherst. In Lesser group, Naveen, Sinan, Andrew, Jared, Jan, Connor, Matt, Madhura, Amy, Henry, Angela, Silas, Wei and Polina and in Coughlin Group, Liz, Piril, Xiaohui, Huseyin, Tsung-Han, Sahas, Rohit, Rebecca, Wenxu, Nomsu, Haomiao, Pat, Josh, and Shilpi. It has been my honor to learn from these esteemed scientists, as well as enjoy their friendship. I look forward to sharing their friendship for many years to come.

Additionally, I would like to thank my collaborators: Herr Prof. Dr. Gerrit A Luinstra and Dr. Saskia Scheel of the University of Hamburg for thoughtful conversation and facility use. It was my pleasure to work with Saskia in Germany in 2012 and the United

States in 2013, not only because I learned a tremendous amount of chemistry from her, but also because we became dear friends.

I am also grateful to the PSE staff, especially Lisa, Maria, and Jessica for simplifying the administrative part of graduate school life and allowing me to focus on my research. Also, I would like to thank the Conte night custodial staff, Jim and Tommy, for always taking the time to converse with weary graduate students during late-night laboratory experiments.

My research was made possible through generous financial contributions through various organizations, for which I am tremendously appreciative. The Center for UMass/Industry Research on Polymers Cluster M (Mechanics of Polymers and Composites) and Cluster F (Fire-Safe Polymers and Composites) provided laboratory and overhead funding resources essential to my research. Most notably, I am grateful to the National Defense Science and Engineering Graduate Research Fellowship Program (NDSEG) for funding my research and affording me the freedom to pursue my scientific interests.

I am indebted to my church family at MERCYhouse in Amherst, MA for their critical support role during my time at UMass Amherst. In particular, Robert, Melanie, Lois, Cindy, Erin, Ashley, Mike, Becky, and so many others walked with me through a variety of circumstances and facilitated my growth as a follower of Christ. Also, through MERCYhouse I had the opportunity to use my background in chemistry to help Kevin Moforte start a non-profit organization, Upward Ventures, in order to provide jobs and empowerment to families in an impoverished community in Santo Domingo, DR. Through this opportunity, I was exposed to diverse people, circumstances, and viewpoints that

compelled me to reconsider my outlook on poverty, wealth, justice, community, human nature, the human spirit, the role of science in poverty, and God's sovereignty.

I am also thankful for the unending love and support of my parents, Mark Cromer and Jayne Cromer, as well as my brother Dan Cromer. They were the ones that always believed in me and consistently helped me through every chapter of life. Also, my interest in science was first initiated by my family, through my mother sharing her experiences as a nurse, and my brother teaching me how to build everything from Legos to pneumatic guns. My family owns a big part of this work.

Finally, I would like to thank my wife Molly for being a pillar of my thesis work, and indeed my life. She is my best friend, teammate, cheerleader, boss, helper, counselor and partner. Life is immeasurably fuller and richer with her faith, noble character, humor, and grace by my side.

Ultimately this work was only possible through God's *Chesed*, or steadfast love through Christ, for which I am the most grateful.

ABSTRACT

ENGINEERING ADVANCED MORPHOLOGIES FOR STRUCTURALLY REINFORCED POLYOLEFINS

MAY 2016

BRIAN MICHAEL CROMER, B.S., CASE WESTERN RESERVE UNIVERSITY

Ph.D., UNIVERSITY OF MASSACHUSETTS AMHERST

Directed by: Professors E. Bryan Coughlin and Alan J. Lesser

The primary objective of this research is to develop new methods to enhance the mechanical properties of isotactic polypropylene (iPP). Two complementary methods were developed to produce reinforced iPP-nanographite nanocomposites. In the first method, nanocomposites were prepared through an *in-situ* metallocene-catalyzed polymerization technique. In the second method, a new compounding strategy was used to prepare iPP-nanographite nanocomposites with improved spatial size distribution of nanoparticle agglomerates. Finally, a new process referred to as Melt-Mastication (MM) was developed as a means to improve the mechanical properties of pure iPP through generating unique and beneficial crystal morphologies.

Reinforced iPP-nanographite nanocomposites were prepared through an *in-situ* polymerization technique and compared to analogous composites prepared by conventional melt processing. *In-situ* preparation of iPP-nanographite nanocomposites was accomplished via single site metallocene catalyzed polymerization of propylene within a toluene dispersion of xGnP nanoparticles. For comparison, analogous iPP-nanographite nanocomposites were prepared by melt compounding. Mechanical analysis showed all iPP-nanographite nanocomposites demonstrated improved stiffness and strength relative to neat

iPP, however the non-linear mechanical properties were influenced by both the preparation method and nanoparticle loading. The results are discussed with regard to the thermal and morphological properties, as well as the preparation technique.

A new polymer processing method referred to as “Melt-Mastication” (MM) was developed as a means to augment the crystal morphology of iPP and thereby enhance the thermal and physical properties. Melt-Mastication is a low temperature mixing technique that subjects an iPP melt to flow induced crystallization within a chaotic flow field. Thermal calorimetry and SAXS showed that MM substantially increases the lamellar crystal thickness and crystallinity of iPP, resulting in a 50% improvement to yield strength, 55% improvement to elastic modulus, and improved temperature stability. The property improvements were attributed to a unique hierarchical organization of lamellar crystals produced by MM, distinct from conventionally prepared iPP materials.

Finally, Melt-Mastication was repurposed as a compounding method for preparation of iPP-nanographite nanocomposites with enhanced nanographite dispersion. Due to flow induced crystallization, the process viscosity increases significantly during Melt-Mastication, which produces higher mixing torque and therefore shear resulting in the fragmentation of nanoparticle agglomerates. The spatial size distribution of nanographite agglomerates was evaluated via a quantitative stereological technique, and a model for agglomeration in shear flow is proposed and discussed with respect to the results.

TABLE OF CONTENTS

	Page
ACKNOWLEDGMENTS	v
ABSTRACT	viii
LIST OF TABLES	xiv
LIST OF FIGURES	xv
CHAPTER	
1. INTRODUCTION	1
1.1 Motivation.....	1
1.2 Fundamentals of iPP Crystal Structure	4
1.2.1 Chain Microstructure	5
1.2.2 Crystallinity of iPP.....	7
1.2.3 Lamellar Morphology	8
1.2.3 Organized Lamellar Structures	10
1.2.4 Structure-Process-Property Relationships of iPP.....	12
1.3 Nanoparticle Reinforced Isotactic Polypropylene	14
1.4 Thesis Overview	17
1.5 References.....	18
2. IN-SITU POLYMERIZATION OF ISOTACTIC POLYPROPYLENE- NANOGRAPHITE NANOCOMPOSITES	24
2.1 Introduction.....	25
2.1.1 Chemical Methods for Preparation of PNCs	25
2.1.2 Metallocene Catalyzed Polymerization of Polyolefins.....	29
2.1.3 <i>In-Situ</i> Polymerization of iPP-Nanographite PNCs.....	31
2.2 Materials and Methods.....	33
2.2.1 Materials	33
2.2.2 Sedimentation Studies of xGnP-Toluene Suspensions	33
2.2.3 <i>In-Situ</i> Synthesis of iPP-xGnP Nanocomposites	34
2.2.4 Melt-Compounding of iPP-xGnP Composites	37
2.2.5 Characterization Methods	37
2.3 Results and Discussion	40
2.3.1 Surface Characterization of xGnP	40
2.3.2 ²⁷ Al NMR Investigation of xGnP-MAO Interactions.....	42

2.3.3 Sedimentation Studies of Toluene-xGnP Suspensions	45
2.3.4 <i>In-Situ</i> Synthesis of iPP-xGnP PNCs.....	47
2.3.5 Morphology of iPP-xGnP Nanocomposites.....	51
2.3.6 Mechanical Characterization	57
2.4 Conclusions.....	59
2.5 Notes	60
2.6 References.....	60
3. MELT-MASTICATION PROCESSING OF SEMICRYSTALLINE POLYOLEFINS.....	65
3.1 Introduction.....	66
3.1.1 Processing of Semicrystalline Thermoplastic Polymers.....	66
3.1.2 Flow Induced Crystallization of Semicrystalline Polymer Melts	68
3.1.3 Processing Techniques for “Self-Reinforced” Semicrystalline Polymer Articles	70
3.2 Materials and Methods.....	74
3.2.1 Materials	74
3.2.2 Processing with FIC via Melt-Mastication	74
3.2.3 Compression Molding of iPP.....	76
3.2.4 Forging of Melt-Masticated iPP.....	77
3.2.5 Morphological Characterization	77
3.2.6 Thermal and Mechanical Characterization	80
3.3 Results and Discussion	81
3.3.1 Optimizing Melt-Mastication Conditions for Isotactic Polypropylene	82
3.3.2 Shaping of Melt-Masticated iPP	85
3.3.3 Degradation Analysis.....	87
3.3.4 Thermal Calorimetry.....	88
3.3.5 Morphological Structure	91
3.3.5.1 X-ray Diffraction	91
3.3.5.2 Small Angle X-Ray Scattering.....	92
3.3.5.3 Atomic Force Microscopy	99
3.3.5.4 Scanning Electron Microscopy.....	102
3.3.5.5 Polarized Optical Microscopy.....	105
3.3.6 Mechanical Properties.....	107
3.3.6.1 Dynamic Mechanical Properties	107

3.3.6.2 Tensile Properties.....	108
3.3.6.3 Compressive properties.....	112
3.3.6.4 Impact Properties	114
3.4 Conclusions.....	118
3.5 References.....	118
4. IMPROVED POLYMER NANOCOMPOSITE DISPERSIONS BY A MELT MASTICATION PROCESS.....	124
4.1 Introduction.....	125
4.1.1 Physical Methods for Preparation of PNCs	125
4.1.2 Methods to Evaluate PNC Dispersion State	127
4.1.3 Quantitative Stereology	129
4.2 Materials and Methods.....	131
4.2.1 Materials	131
4.2.2 Processing of Polyolefin Nanocomposites.....	131
4.2.3 Characterization of PNC Dispersion State.....	133
4.3 Results and Discussion	138
4.3.1 Characterization of Dispersion State via Thermal Analysis	138
4.3.2 Rheology	146
4.3.3 Impedance Spectroscopy	147
4.3.3 Microscopy	149
4.3.4 Quantitative Stereology	153
4.3.5 Model for Agglomerate Fragmentation	163
4.3.6 Mechanical properties.....	167
4.3.6.1 Uniaxial compression tests	167
4.3.6.1 Izod Impact Resistance Tests.....	171
4.4 Conclusions.....	174
4.5 Notes	174
4.6 References.....	174
5. FUTURE WORK.....	180
5.1 Proposed Future Directions.....	180
5.1.1 Reactor Design for <i>In-Situ</i> Polymerization of iPP- Nanocomposites.....	180

5.1.2 Alternative Nanoparticle Surface Chemistries for <i>In-Situ</i> Polymerization	182
5.1.3 Advancing Melt-Mastication Toward Commercialization	183
5.1.4 Engineering Optimized Polyolefin Resins for Melt- Mastication.....	185
5.1.5 New Polyolefin “Self-Nucleation” Agents	186
5.2 References.....	186
APPENDIX: DESIGN AND CONSTRUCTION OF AN INSTRUMENTED IZOD IMPACT TESTER	188
BIBLIOGRAPHY.....	204

LIST OF TABLES

Table	Page
2.1 Sedimentation time in minutes of various xGnP grades in Toluene or Toluene and Methylaluminoxane (MAO)	47
2.2 Reaction parameters and properties of iPP-xGnP nanocomposites prepared by <i>in-situ</i> polymerization and melt compounding. T_p = polymerization temperature set point. Propylene pressure = 3 bars. *kg iPP mmol Zr ⁻¹ bar ⁻¹ h ⁻¹ . **M _w /M _n	49
3.1 Parameters of semicrystalline thermoplastic polymers relevant to MM.	82
3.2 Degradation study of Melt-Masticated iPP	88
3.3 Summary of thermal calorimetry results of semicrystalline polymers prepared with MM. Processing parameters of each resin is discussed in section 4.2.2.	89
3.4 Fitted KWW parameters from tensile stress relaxation studies of iPP at 1% and 3% strain.....	112
3.5 Summary of the mechanical test results of compression molded and MM iPP. *Compression molded samples treated with annealing.	117
4.1 Melt-Mastication parameters for semicrystalline polyolefin resins. Values correspond to Figure 3.1. T_m and T_c were determined via differential scanning calorimetry.....	133
4.2 Non-isothermal crystallization temperatures of HDPE-xGnP nanocomposites.....	140
4.3 Non-isothermal crystallization temperatures of iPP nanocomposites	142
4.4 Non-isothermal crystallization temperatures of LLDPE-xGnP nanocomposites.....	143
4.5 Processing parameters of iPP-xGnP PNCs. Samples were prepared by either MM or CMP.....	158
4.6 Tabulated results from uniaxial compression tests of Figure 4.18.	170

LIST OF FIGURES

Figure	Page
1.1 Projected iPP market size in 2020, by application. Semi-structural and non-structural applications are highlighted.	2
1.2 Storage modulus and price of commodity and engineering thermoplastic polymers.	4
1.3 Schematic illustration of stereo-chemical configurations of Polypropylene (PP) A: Isotactic PP, B: Atactic PP, C: Isotactic PP with one stereospecific error, D: Isotactic iPP with one regio-error.	6
1.4 Schematic of iPP crystal lamella. Black curved lines represent iPP chains. Crystallographic axes (a, b, c) and lamellar crystal thickness (d_c) noted.	9
1.5 Schematic representation of “cross-hatched” lamellar morphology within an α -iPP spherulite.	11
1.6 Schematic of the interphase phenomena with permission from Vaia <i>et al.</i> The top “Macro” composite, or fiber reinforced composite, illustrates a filled polymer containing 1 μm x 25 μm fibers in a polymer matrix. The bottom “Nano” composite illustrates a filled polymer containing 1 nm x 25 nm fibers in a polymer matrix at higher magnification. The bottom composite has a percolating interphase.	16
2.1 Steel reactor used for <i>in-situ</i> polymerization trials of iPP-xGnP nanocomposites. Reactor located in Professor G. Luinstra’s lab at the University of Hamburg.	35
2.2 Schematic of the small scale polymerization vessel described in Coughlin <i>et al.</i>	36
2.3 Reactor powder from <i>in-situ</i> synthesis of iPP-xGnP nanocomposites. (A) Pure iPP (IS-0) (B) 2 wt% xGnP in iPP (IS-2) (C) 4 wt% xGnP in iPP (IS-4).	37
2.4 FTIR absorption spectra of xGnP-c-750 in transmission mode.	41
2.5 XPS spectra of xGnP-c-750. (Top Left) Survey spectrum. (Top Right) O1s spectrum. (Bottom) C1s spectrum.	42
2.6 ^{27}Al NMR spectra of MAO/Toluene solutions and MAO/Toluene-xGnP suspensions. A) 0.3 M MAO/Toluene. B) 0.5 M MAO/Toluene-xGnP (0.1% w/v). C) 0.5 M MAO/Toluene-xGnP (1.5% w/v).	45

2.7	Transmission optical microscopy images of 50 μm thick iPP-xGnP films. (A) MC-2 (B) IS-2 (C) MC-4 (D) IS-4.....	52
2.8	Transmission Electron Microscopy images of iPP-xGnP sections. (A,B) IS-0 (C,D) IS-2 (E,F) IS-4 (G,H) MC-2.	54
2.9	Differential Scanning Calorimetry of IS- and MC-samples. (A) cooling and (B) heating curves.	56
2.10	Tensile properties of iPP-xGnP nanocomposites.....	58
3.1	Three step temperature profile for Melt-Mastication. Step 1 (red): Melting and mixing. Step 2 (yellow): Cooling to T_M . Step 3 (blue) isothermal mixing at T_M	76
3.2	Schematic of forging tools for forming Melt-Masticated iPP “pseudo-melts” into testing specimens. A) Compression plates for forging biaxially oriented specimens. B) Channel die for forging uniaxially oriented specimens.....	77
3.3	Temperature and torque vs time recorded by Brabender Plasti-Corder during optimization of Melt-Mastication processing parameters for iPP. A) Four different temperature profiles, each with different T_M . B) Torque vs. time resulting from the temperature profiles in A. C) Torque vs time from varying mixing rate.....	85
3.4	Mold shrinkage of compression molded (left) and MM (right) iPP.	87
3.5	Physical appearance of iPP prepared by compression molding (left) and Melt-Mastication (right).....	87
3.6	Thermal calorimetry of CMP and MM iPP, heating rate 10 K/min. A) Melting endotherms within the first heating curve, up to 200 °C. B) Non-isothermal crystallization exotherms within the first cooling curve.	90
3.7	Powder diffraction profile of iPP prepared by MM or compression molding.	92
3.8	Two-dimensional SAXS scattering profile of iPP prepared by MM or compression molding, at various temperatures. The calculated lamellar crystal thickness (d_c) is listed on each image.....	95
3.9	General schematic of melting, recrystallization, and crystallization processes of Polypropylene, adapted from Strobl.....	96

3.10	Two-dimensional SAXS scattering profile of MM-iPP uniaxially forged at several forging stresses. Top row: Imaged parallel to forging flow direction. Bottom row: Imaged perpendicular to forging flow direction. Compression molded sample was not prepared by MM. All samples at 20 °C	98
3.11	Atomic force microscopy phase mode images of iPP prepared by MM or compression molding. Dark regions = low phase angle, bright regions = high phase angle.....	101
3.12	Scanning electron microscopy images of iPP surfaces treated with chemical etching. A-C: Compression Molded iPP. D-F: MM-iPP.....	104
3.13	Polarized optical microscopy images of iPP prepared by glass knife microtomy. A-C: MM-iPP. D-F: Compression molded iPP. The angle between crossed polarizers is denoted at top of the image.	106
3.14	Dynamic mechanical temperature sweep of compression molded iPP, unoriented MM iPP, and biaxially oriented MM iPP. A) Storage modulus and B) Dimensional change. Modulus values recorded in Table 3.5.	108
3.15	Tensile behavior of iPP prepared by compression molding, annealing, or MM with uniaxial forging. Strength and modulus recorded in Table 3.5.	110
3.16	Uniaxial compressive behavior of iPP prepared by compression molding or Melt-Mastication without forging. Modulus and strength values recorded in Table 3.5.	114
3.17	Izod Impact energy of compression molded iPP and MM-iPP conditioned at several temperatures.....	116
3.18	Impact energy vs displacement during Izod fracture, recorded by instrumented Izod device (Appendix A-1). A) Compression molded iPP. B) Melt-Masticated iPP.....	116
4.1	Illustration of a spherical agglomerate of maximum size intersected by random test plane h	130
4.2	Illustration of the process flow for image analysis and Quantitative Stereology of 2 wt% iPP-xGnP nanocomposites.....	136
4.3	DSC cooling scans of HDPE-xGnP nanocomposites	139
4.4	DSC cooling scans of iPP nanocomposites.	141
4.5	DSC cooling scans of LLDPE-xGnP nanocomposites	143

4.6	Dynamic mechanical analysis of polyolefin-xGnP nanocomposites.....	145
4.7	Rheological storage modulus vs angular frequency of HDPE-xGnP nanocomposites of various loadings (0 to 36 wt%).....	147
4.8	Conductivity of 5.5 wt% iPP-carbon black PNCs measured by impedance spectroscopy. Samples were prepared by conventional melt processing (CMP), Melt-Mastication (MM), or Melt-Mastication and forging (MM-Forged).....	149
4.9	Optical microscopy of iPP-xGnP (2 wt%) PNCs. A: Sample prepared by CMP (200 °C_70 RPM). B: Sample prepared by MM (154°C_70 RPM).	150
4.10	TEM images of iPP-xGnP (2 wt%) PNCs. A: CMP (200°C_70 RPM), 15,000x magnification, B: MM (154°C_70 RPM), 15,000x. C: CMP (200°C_70 RPM), 100,000x. D: MM (154°C_70 RPM), 100,000x.....	152
4.11	SEM image of iPP-xGnP (2 wt%) PNCs treated with chemical etching. Samples prepared by MM (154 °C/70 RPM) and CMP (200 °C/70 RPM) demonstrated similar results.	153
4.12	Two-dimensional section size distribution of xGnP agglomerates.....	155
4.13	Three-dimensional spatial size distribution of xGnP agglomerates. Inset: Differential particle size distribution (200 °C/70 RPM from 154 °C/70 RPM).....	156
4.14	Volume fraction distribution of xGnP agglomerates	157
4.15	Particle size distribution characteristics and observed torque for each iPP-xGnP sample recorded in Table 4.5. A: Standard deviation of fitted Gaussian functions. B: Maximum observed particle size.....	160
4.16	Particle size distribution characteristics and number of mixing cycles for each iPP-xGnP sample recorded in Table 4.5. A: Standard deviation of fitted Gaussian functions. B: Maximum observed particle size.	162
4.17	Schematic for fragmentation of exfoliated graphene nanoplatelet (xGnP) agglomerates	167

4.18	Uniaxial compression tests of iPP-nanocomposites prepared by various techniques. Data from Figure 3.16 is also plotted for comparison. A: 2 wt% xGnP in iPP, conventionally melt processed and compression molded. B: 2 wt% xGnP in iPP, Melt-Masticated and compression molded. C: 2 wt% xGnP in iPP, Melt-Masticated and forged. D: 2 wt% HNT in iPP, Melt-Masticated and forged.....	170
4.19	Notched Izod impact resistance tests of iPP-xGnP nanocomposites prepared by various techniques. Impact was evaluated on the instrumented Izod impact tester (Appendix 1).....	173
5.1	Schematic of proposed reactor design for in-situ polymerization of polyolefin nanocomposites	182
A.1	Schematic representation of a conventional Izod pendulum impact resistance test machine (ASTM D256).....	190
A.2	Instrumented Izod impact test device.	193
A.3	Sample clamp corresponding to Figures A.4, A.5, and A.6.	193
A.4	Technical drawing for sample clamp base of Figure A.3.	194
A.5	Technical drawing for sample clamp floating plate of Figure A.3.	195
A.6	Technical drawing for sample clamp lateral plates of Figure A.3.....	196
A.7	Horizontal position and velocity of a freely swinging Izod pendulum.....	198
A.8	Total energy of the freely swinging Izod pendulum.....	199
A.9	Force vs. time and displacement vs. time of sub-perforating impact at various striker hammer masses.	200
A.10	Force vs. displacement curves of sub-perforating impact at various striker hammer masses	202

CHAPTER 1

INTRODUCTION

The motivation behind this thesis work is the investigation of strategies to improve the mechanical properties of Isotactic Polypropylene (iPP), including mechanical modulus, strength, toughness, and impact resistance. The strategies that will be investigated include both chemical and physical preparation techniques to prepare iPP-nanocomposites, and a processing technique to promote unique and useful iPP crystal structures. The present chapter is divided to the motivation for mechanically reinforced iPP, the fundamentals of semicrystalline polyolefin morphology, and current methods to improve the mechanical properties of iPP through composite materials science.

1.1 Motivation

Isotactic Polypropylene (iPP) is a commercially important material selected for a variety of applications due to its low cost, light weight, ease of handling, and moderate mechanical integrity. Today, several high volume industries rely on iPP, including the packaging, automotive, construction, and appliance industries. By 2020, the global consumption of iPP is estimated to be 62.3 million metric tons, worth an estimated \$93.5 billion USD and will likely continue growing by 4.6% per year.^{1,2} It follows that technologies to improve the properties and performance of iPP are highly desirable, and have the potential to significantly impact a variety of global industries.

**Projected PP Market Size for 2020 by Industry
(millions of metric tons)**

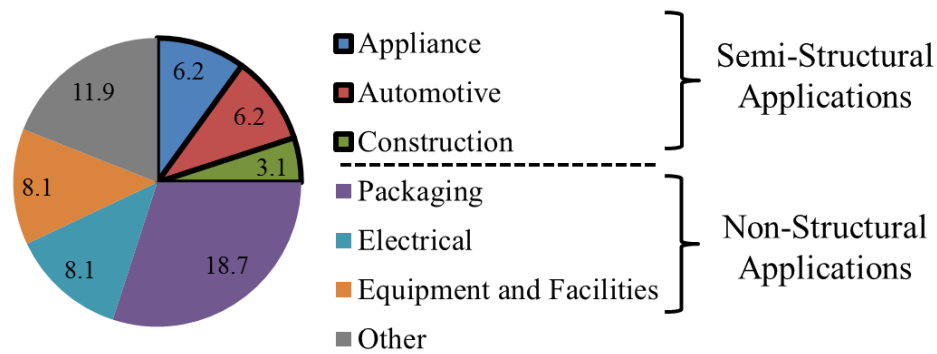


Figure 1.1: Projected iPP market size in 2020, by application. Semi-structural and non-structural applications are highlighted.²

Among thermoplastics, iPP is one of the least expensive (Figure 1.2), and possesses sufficient mechanical integrity for non-structural and many semi-structural applications. Non-structural applications include food packaging, disposable products, and non-woven fabrics. Semi-structural applications include automotive materials, construction materials, and some appliance components. Recently, demands from end users are pushing the iPP industry to innovate formulation and processing methods that improve the mechanical performance of iPP, such that iPP can be expanded to more semi-structural applications in current and emerging markets.³ Additionally, recent government regulations are creating demand for innovations to reduce weight and save material costs in current applications where iPP is already used. Most notably, the United States Environmental Protection Agency issued new fleet-wide emissions compliance targets, which will require that U.S. auto fleets average 54.5 miles per gallon gasoline by 2025. Undoubtedly, vehicle weight reduction innovations will be a vital component to global strategies to reduce U.S. oil consumption and greenhouse gas emissions.

In order to meet consumer demands and comply with government regulations, the automotive industry is progressively moving toward replacing engineering thermoplastics

and performance materials like Nylon, Poly(ethylene terephthalate) (PET), and metal components with lighter and cheaper iPP components to reduce weight and material costs.⁴ This strategy applies to specific application areas including automotive door panels, seat backs, trunk inserts and scratch resistant interior surfaces. In fact, 9.6% of automotive plastics in 2010 were iPP components, up from 7.6% in 2000.⁵ The automotive industry is also moving toward down-gauging polypropylene components to further reduce weight and material costs and increase fuel economy. However, iPP currently lacks the mechanical integrity necessary for down-gauging and many semi-structural applications, requiring manufacturers to use more expensive engineering thermoplastics to achieve performance requirements. Accordingly, there is significant commercial interest in developing a processing method to improve the mechanical integrity of iPP, allowing iPP to penetrate markets and compete for applications traditionally dominated by engineering thermoplastics. Specifically, methods to improve the mechanical storage modulus of PP (~1600 MPa) to meet or exceed the modulus of PET (~2500) would enable iPP to replace PET components and save ~\$0.15-0.20 per pound material, a significant competitive advantage in largely commodity markets.

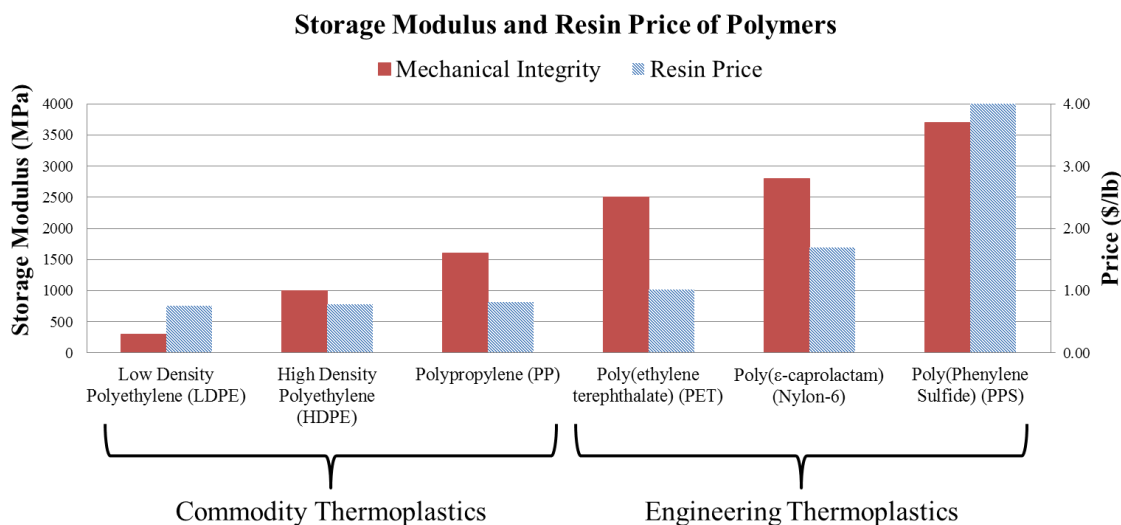


Figure 1.2: Storage modulus and price of commodity and engineering thermoplastic polymers.

1.2 Fundamentals of iPP Crystal Structure

Isotactic Polypropylene is a semicrystalline thermoplastic polymer. Like all thermoplastic polymers, iPP may be melted and readily formed into a variety of useful polymer articles through polymer processing techniques. Additionally, like all semicrystalline polymers, iPP can be considered a multiphase composite solid, comprised of crystalline regions and amorphous regions.⁶ In crystalline regions, iPP chains organize into highly ordered, repeating structures with defined melting points, while the amorphous regions consist of unstructured entangled chains. The crystal morphology of iPP is organized into a hierarchy of characteristic scales, including the chain microstructure (primary level), crystal unit-cell (secondary level), lamellae structure (tertiary level), and organized lamellar structures (quaternary), which will be successively discussed in the proceeding sections. Ultimately, the final properties of an iPP polymer article is strongly related to the chain microstructure, crystal morphology, and processing technique chosen to form the polymer article.

1.2.1 Chain Microstructure

The elementary structure of the iPP crystal morphology is the iPP polymer chain itself, which is a long series of covalently bonded, repeating propylene units as shown in Figure 1.3. The properties of the chain, or the “chain microstructure,” govern the propensity of the chain to undergo crystallization, significantly affecting the morphology and properties of iPP. The first aspect of the chain microstructure is the stereospecificity, which refers to the arrangement of pendant methyl groups with respect to the iPP backbone. Figure 1.3 is a schematic illustrating the distinctions between isotactic, atactic, stereospecific defects, and regio-defects in the iPP chain microstructure. Isotactic iPP (Figure 1.3A) easily crystallizes due to its long, uninterrupted repeating structure along the chain, which is both stereospecific and regiospecific. In contrast, fully atactic iPP will not crystallize, and instead form a fully amorphous polymer. The atactic iPP schematically illustrated in Figure 1.3B is not stereospecific, but is regiospecific. In reality, it is never possible to produce 100% isotactic polypropylene because residual stereospecific and regio-defects always exist. Stereospecific defects occur when the propylene monomer is incorrectly added to a growing chain such that it produces a stereoisomer (Figure 1.3C).⁷ The methyl-group bearing atom in the iPP repeating structure is a chiral center, and the chirality of each methyl-group bearing atom may be characterized as *meso* (*m*) or *racemo* (*r*). True 100% isotactic polypropylene should be entirely the *m* stereoisomer. Another type of defect are regio-errors, which occur when a propylene monomer is “mis” inserted to the growing chain such that it produces an isomer that isn’t a stereoisomer (Figure 1.3D). These types of defects usually occur when a “2-1” insertion occurs to a chain comprised of mostly ‘1-2’ insertions.⁸

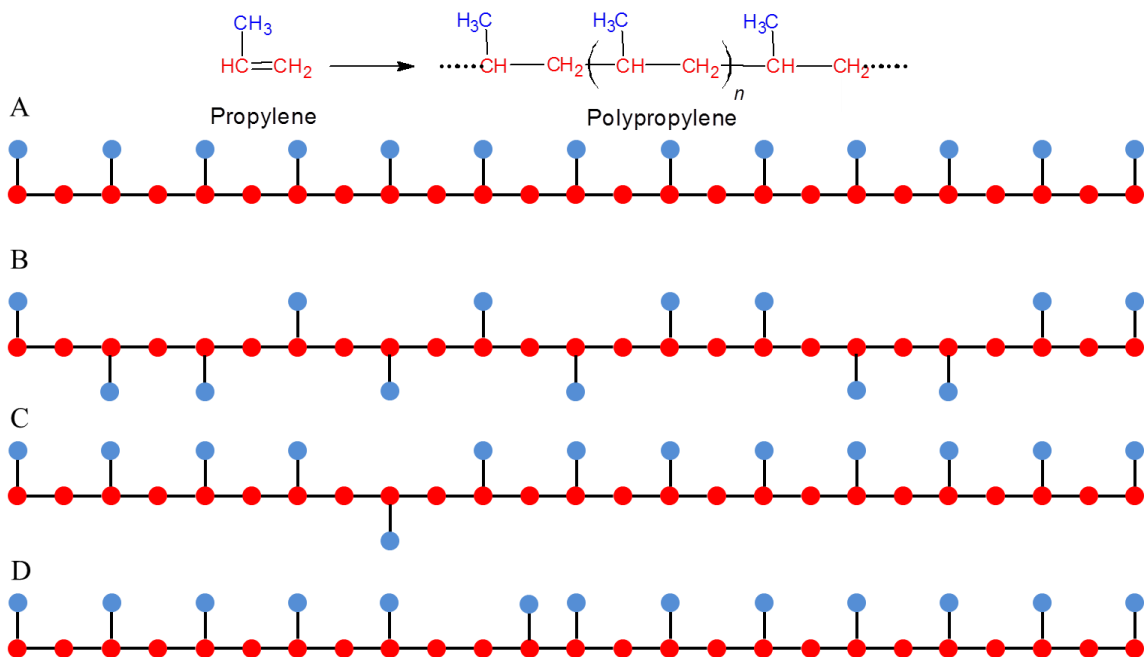


Figure 1.3: Schematic illustration of stereo-chemical configurations of Polypropylene (PP) A: Isotactic PP, B: Atactic PP, C: Isotactic PP with one stereospecific error, D: Isotactic iPP with one regio-error.

Recent advancements in iPP polymerization catalyst technology have enabled fine control over the chain microstructure, including molecular weight distribution and control over the amount and distribution of stereospecific defects and regio-defects.⁹ Currently the two main classes of iPP polymerization catalysts are the established “Ziegler-Natta” supported heterogeneous catalysts and the relatively recent metallocene catalysts. Ziegler-Natta heterogeneous supported catalysts are catalysts based on Titanium or Vanadium compounds used in combination with organoaluminum cocatalysts, and are usually supported on MgCl_2 .¹⁰ It is generally accepted that these catalysts are useful for producing highly isotactic iPP with excellent stereospecificity and regiospecificity, as well as a broad molecular weight distribution. Additionally, Ziegler-Natta heterogeneous supported catalysts are known to produce heterogeneous inter-chain defect distributions, where most chains have excellent stereospecificity and regiospecificity, and a small population fraction of chains have many defects.¹¹ Metallocene catalysts are organometallic, single-site

catalysts consisting of Zn, Hf, Ti or other transition metal coordinated with an organic ligand framework. The advantage of metallocene catalysts is that the chain microstructure of the resulting PP may be varied continuously between highly isotactic PP and completely atactic PP, which enables a range of mechanical properties from relatively stiff thermoplastics to low modulus amorphous materials. Metallocene catalysts cannot produce iPP with the high stereospecificity and regio-specificity of Ziegler-Natta heterogeneous supported catalysts, however metallocenes do produce a homogeneous inter-chain defect distribution, where stereo- and regio-defects are evenly distributed to all chains.¹² Furthermore, metallocene catalysts produce comparatively narrow molecular weight distributions. The control of iPP chain microstructure enabled by metallocene catalysts allows customization of the chain microstructure, morphology, and ultimately the properties of iPP.

1.2.2 Crystallinity of iPP

The secondary level of hierarchical structure in iPP is the crystal unit cell. The dominant and most stable crystal form of iPP produced by the vast majority of commercial process is the α -iPP crystal type. In this crystal type, iPP chains assume a 3_1 -helical conformation where the methyl groups face outward from the helix axis. The crystal unit cell was identified by Natta and Corradini to be a monoclinic crystal unit cell, with parallel iPP helices.¹³ The dimensions of the monoclinic unit cell are $a = 6.65 \text{ \AA}$, $b = 20.96 \text{ \AA}$, $c = 6.5 \text{ \AA}$, and $\beta = 99.62^\circ$. The axis of the 3_1 iPP chain helix is parallel to the c -axis of the unit cell.^{13,14} Within the α -iPP crystal type, there are variations based on the “handedness” of the helix (right or left) as well as the position of the methyl groups (up or down). More detailed information about the α -iPP crystal type may be found elsewhere.¹⁵ Finally, the

density of the crystalline phase (0.941 g/cm^3) is greater than the amorphous phase (0.852 g/cm^3) and the melt.^{16,17} Accordingly, iPP normally undergoes significant dimensional change as the material crystallizes, which ultimately affects the dimensions of the final iPP article.

1.2.3 Lamellar Morphology

The next level of hierarchy in the iPP crystal structure is the lamellar crystal. Lamellae are ordered assemblies comprised of many α -iPP crystal cells arranged into a folded chain structure schematically represented in Figure 1.4. The thin dimension of the lamellar crystal is parallel to the c -axis of the α -iPP crystal type. Therefore iPP chains residing in the lamella exit, fold, and reenter parallel to the smallest dimension of the lamella, as shown in Figure 1.4. The thickness of lamellar crystals along the c -axis is $\sim 50 \text{ \AA}$ to 200 \AA under normal processing conditions.¹⁸⁻²⁰

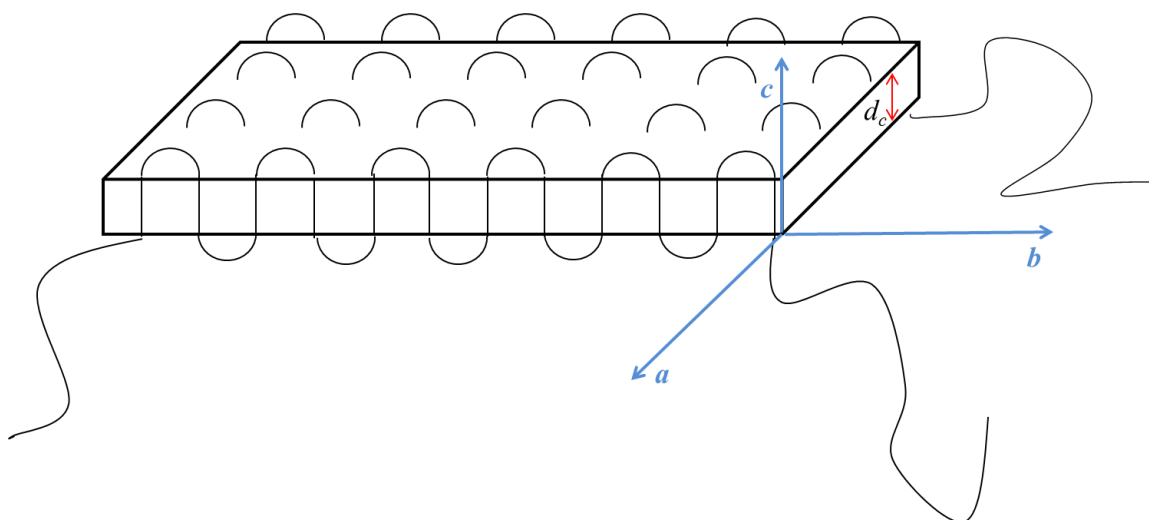


Figure 1.4: Schematic of iPP crystal lamella. Black curved lines represent iPP chains. Crystallographic axes (a, b, c) and lamellar crystal thickness (d_c) noted.

The melting behavior of iPP is strongly related to the thickness of lamellar crystals.²¹ The thermodynamics of melting are well described by the Gibbs Thomson equation:

$$T_m = T_m^0 \left(1 - \frac{2\sigma_e}{\Delta h_f d_c} \right) \quad (1.1)$$

Where T_m is the observed melting point, T_m^0 is the melting point of an infinitely large iPP crystal, $2\sigma_e$ represents the fold surface energy, Δh_f is the heat of fusion per unit volume of crystal, and d_c is the lamellar crystal thickness. Equation 1.1 predicts the melting point as a function of lamellar crystal thickness, where thin lamellae require low T_m , while thick lamellae require higher T_m .

It is generally observed that the T_m of metallocene iPP is less than Ziegler-Natta iPP, and this is observed in the present work (section 2.3.5). The difference is attributed to stereodefects in the chain microstructure that affect the crystallizability of iPP chains produced from each type of catalyst, ultimately affecting d_c . Specifically, metallocene catalysts produce more regio-defects iPP as well as a homogeneous inter-chain distribution

of defects. VanderHart *et al.* proposed that regio-defects impart severe enthalpic penalties to iPP crystallization, and showed empirically that iPP chains with regio-defects are preferentially excluded from the crystal phase during crystallization.²² However because metallocene iPP possesses homogeneously distributed regio-errors, these defects must be included in the lamellar crystals, thus reducing d_c and T_m . In contrast, Ziegler-Natta iPP has more heterogeneous interchain defect distribution. Defects are concentrated within a small fraction of low molecular weight chains which are partitioned and do not participate in crystallization. The remaining highly isotactic and regiospecific chains undergo crystallization.^{23,24} Finally, T_m is strongly dependent on the tacticity of iPP chains, and Ziegler-Natta iPP is usually the most isotactic^{25,26}. The melting points of Ziegler Natta iPP and Metallocene iPP are reflected in the present work.

1.2.3 Organized Lamellar Structures

The final level of hierarchical crystal morphology is organized lamellar structures, such as spherulites and flow oriented structures. Spherulites are spherical structures approximately 1-50 μm in size, comprised of multiple lamellae organized into a radial pattern emanating from a central point.²⁷ In the case of α -iPP, lamellae in spherulites demonstrate a “cross-hatched” morphology where radial lathlike lamellae are intersected with nearly orthogonal oriented lamellae, as illustrated in Figure 1.5.^{28,29} This phenomenon is unique to α -iPP, and is caused by homo-epitaxial nucleation from the a -crystallographic direction of the radial lamellae with the c -axis of the orthogonal lamellae. Accordingly, radial lamellae are termed “parent lamellae,” while the orthogonal lamellae are termed “daughter lamellae.” During quiescent crystallization, the radial lamellae grow first and then nucleate daughter lamellae, which often results in a bimodal distribution of lamellar

crystal thicknesses.^{19,30,28,29,31} Spherulite structures are favored under quiescent crystallization conditions.

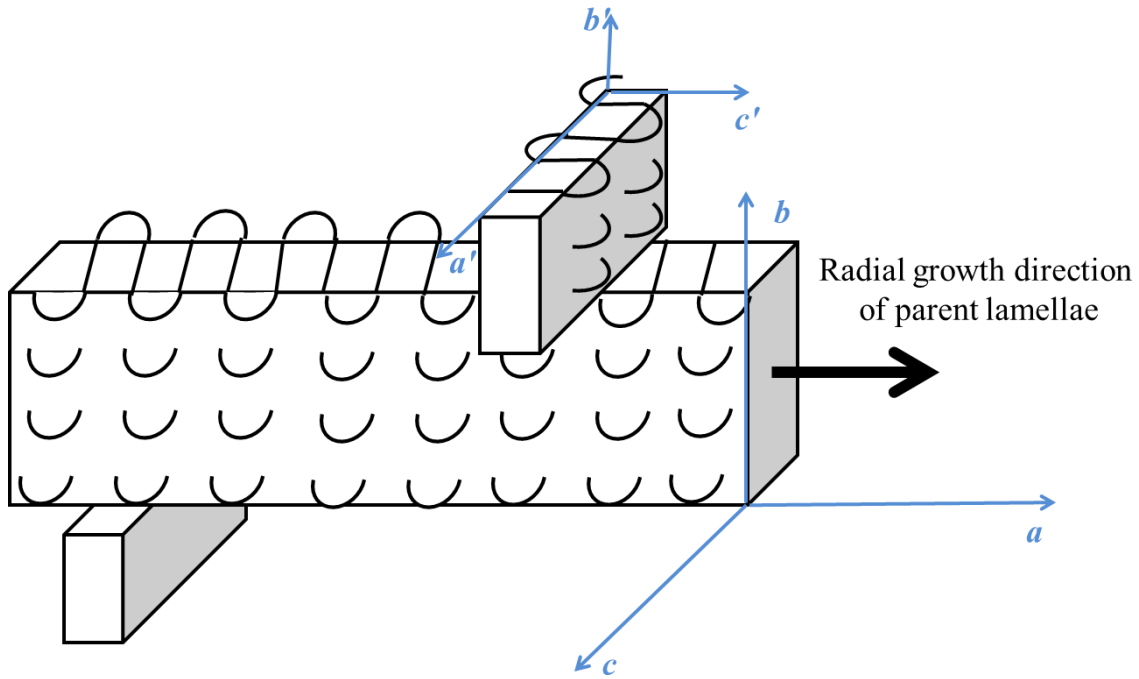


Figure 1.5: Schematic representation of “cross-hatched” lamellar morphology within an α -iPP spherulite.

Many polymer processing methods for iPP such as injection molding involve crystallization under shear, which produces flow oriented structures. In contrast to quiescent melt crystallization, crystallization under simultaneous shear produces non-homogeneous morphologies through the thickness of a molded polymer article.^{32–34} This non-homogeneous morphology is often referred to as “skin-core” morphology, where the portion of the molded part near the surface consists of highly oriented structures, and the portion near the center of the part contains spherulites. This morphology is attributed due to the non-uniform flow field experienced by molten iPP before and during crystallization, as well as the non-uniform temperature gradient during cooling.³⁵ The extent of orientation and the thickness of the skin layer are highly sensitive to molding conditions, such as flow

rate and mold temperature. The morphology of the flow oriented structures produced by injection molding usually consists of highly oriented fibrillar cores with lateral lamellar crystal overgrowths. The fibrillar cores possess lamellae with the *a*-crystallographic axis preferentially oriented parallel to the flow direction, while the lamellar crystal overgrowths possess lamellae with the *c*-crystallographic axis oriented parallel to flow.^{33,34} These structures are attributed to a complex nucleation mechanisms where highly oriented fibrillar cores promote nucleation of secondary crystal overgrowths through a process termed flow induced crystallization.^{36,37}

1.2.4 Structure-Process-Property Relationships of iPP

The properties of iPP polymer articles are strongly influenced by complex interrelationships between the processing conditions and the crystal morphology. In fact, characteristics of the crystal morphology at all levels of hierarchy have profound effects on the mechanical properties. Through control of chain microstructure, and polymer processing conditions such as crystallization temperature, cooling rate, and shear rate, a wide variety of crystal morphologies and mechanical property ranges are possible in iPP.

For example, the relative proportion of crystalline to amorphous regions (crystal volume fraction) is strongly influenced by the stereospecificity and regio-specificity of iPP chains. Furthermore, the crystal volume fraction generally increases at higher crystallization temperatures, or reduced cooling rates from the melt.^{38,39} The mechanical modulus of iPP is strongly influenced by the crystal volume fraction, as more highly crystalline materials have greater modulus.⁶

Also, the lamellar crystal thickness is controlled by both the chain microstructure and processing conditions, and determines the yield strength of iPP. As discussed

previously, stereo- and regio-defects produce lamellar crystals with reduced thickness of the c -crystallographic axis (d_c), and ultimately reduced T_m . Additionally, d_c is also affected by the crystallization temperature during processing. Thicker lamellae are favored at higher crystallization temperatures and slower cooling rates. However d_c is also the critical parameter governing yield of semicrystalline iPP.³⁹ It was shown first by Young *et al.* and studies since that yield is the result of lamellar crystal dislocations propagating through lamellae and fragmenting the crystals.⁴⁰ It follows that processing methods to increase d_c will result in improvements to yield strength.

The size and distribution of spherulites heavily influences the mechanical properties of iPP. Generally, iPP with large spherulites demonstrates reduced ductility and impact resistance. Lustiger *et al.* attributed this trend to the interface between adjacent spherulites, which present mechanically weak zones for strain localization and failure.⁴¹ Conversely, smaller spherulites have been shown to improve the tensile response and impact properties of iPP.⁴² The size of spherulites may be controlled by addition of nucleation agents, selection of crystallization temperature, and/or control of the melt flow field during polymer processing.^{42,43}

Finally, polymer processing methods may be engineered to improve the mechanical properties and produce mechanical anisotropy in iPP articles. Flow oriented structures demonstrate mechanical anisotropy, where mechanical properties in the flow direction differ from transverse directions. For example, the elastic modulus and flexural modulus of injection molded iPP articles increases in the flow direction with increasing orientation.^{34,35,44} Additionally, other properties like heat distortion and mold shrinkage are influenced by mechanical anisotropy.⁴⁵

1.3 Nanoparticle Reinforced Isotactic Polypropylene

Composite materials science is an effective tool to improve the mechanical properties of iPP and enable new application areas. Conventional iPP composite materials are usually involve fiber reinforcement, where 10-50 vol% of a strong and stiff fiber, such as glass fiber or carbon fiber, is incorporated into an iPP matrix, therefore increasing the strength and stiffness of the iPP-fiber composite. However, fiber-reinforced iPP is costly due to the raw materials costs as well as the cost of fabricating the composites. More recently, iPP-nanocomposites have been developed as an economical alternative to traditional fiber reinforced iPP composites. Compared to traditional fiber-reinforced composites, nanocomposites only require small (< 6 vol %) concentrations of reinforcement to create property enhancements.^{46,47} Accordingly, PNCs are ideally situated to penetrate new markets and add value to a variety of applications. Several economical iPP-nanocomposites have been reported using various low-cost discrete phase materials, including fumed silica, titanium dioxide, layered mineral silicates, carbon black, and graphite-derived particles, such as graphite oxide, thermally reduced graphite oxide, and expanded graphite. Polymer nanocomposites with these discrete phase reinforcements demonstrated commercially advantageous property improvements, including increased strength, modulus, thermal/electrical conductivity, crystallization kinetics, and/or barrier properties.⁴⁸⁻⁶¹

Recently, graphene nanoplatelets (GNPs) have been investigated as nanoreinforcements for iPP.^{46,47} The production of GNPs can be achieved by the thermal exfoliation of mineral graphite. Most notably, Drzal *et al.* developed an efficient method to produce Exfoliated Graphene Nanoplatelets (xGNP™) using acid intercalation followed by microwave assisted exfoliation.^{48,49} These nanoplatelets are ideal nanoscale reinforcements due

to their high aspect ratio, surface area, stiffness, thermal conductivity, and nucleation efficiency for crystallization of iPP.^{46,47,50,51} Typically, iPP-xGnP nanocomposites demonstrate improved modulus, strength, and higher crystallization temperature, along with decreased strain to failure and fracture toughness, compared to neat polyolefin resins.⁵² The apparent decrease in non-linear mechanical properties has been attributed to the presence of large xGnP agglomerates, which can facilitate crack propagation and premature failure.

The properties of iPP-nanocomposites, and polymer nanocomposites (PNCs) generally, strongly depend on the state of the dispersion of nanoparticles in the polymer matrix.⁴⁷ Empirically, it is observed that PNCs with well-dispersed nanoparticles demonstrate superior properties when compared to systems with poorer dispersion.^{47,62,63} This observed relationship between property improvements and dispersion state has been rationalized by the interphase phenomena, illustrated in Figure 1.6.^{46,64} The interphase phenomena describes three regions of an idealized particle reinforced composite material: The polymer matrix, the particle or reinforcement phase, and the interfacial region between the matrix and the particle termed the interphase. The interphase demonstrates properties distinct from the bulk polymer matrix due to nanoparticle-polymer chain interactions, and is located to within 50-100 nm of the polymer-nanoparticle interface. In traditional filled polymer composites, the volume fraction of interphase is much smaller than the volume fraction of bulk polymer matrix, due to the large size and small aspect ratio of the reinforcement phase. In PNCs, the volume fraction of interphase prevails over the bulk region due to the small size and large aspect ratio of the nanoparticles. Furthermore, the properties of PNCs are derived from the properties of this percolating interphase region. In order to form a percolating interphase region, the majority of the polymer matrix must be within 50-100 nm of a polymer-particle interface. It follows that achieving efficient

nanoparticle dispersion is critical to enhancing the properties of PNCs. In reality, the structure-property relationships of PNCs are also affected by many other factors in addition to the interphase phenomena, including crystal morphology and crosslink density. The precise physical origins of PNC property enhancements are subject to debate out of the scope of the present work.⁴⁷

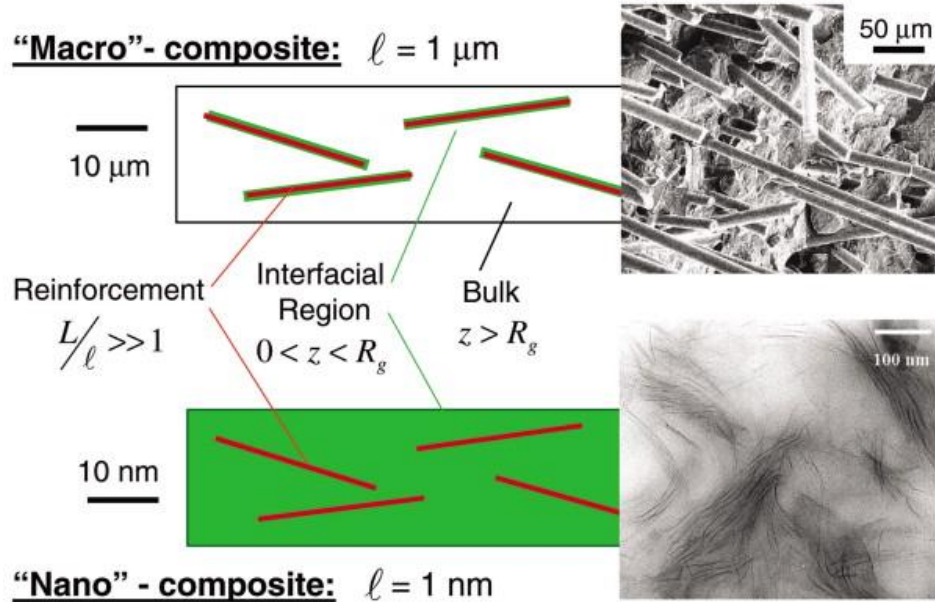


Figure 1.6: Schematic of the interphase phenomena with permission from Vaia *et al.*⁴⁶ The top “Macro” composite, or fiber reinforced composite, illustrates a filled polymer containing $1\ \mu\text{m} \times 25\ \mu\text{m}$ fibers in a polymer matrix. The bottom “Nano” composite illustrates a filled polymer containing $1\ \text{nm} \times 25\ \text{nm}$ fibers in a polymer matrix at higher magnification. The bottom composite has a percolating interphase.

In practice, it is difficult to prepare well-dispersed PNCs due to the strong tendency for nanoparticles to agglomerate, especially during conventional melt processing. Most PNC systems possess an unfavorable interaction energy between the nanoparticle and polymer matrix, which promotes the agglomeration of nanoparticles during melt processing.^{59,65,66} Accordingly several chemical modification techniques and physical processing strategies have been developed to prevent nanoparticle agglomeration, and will be discussed in sections 2.1.1 and 4.1.1, respectively.

1.4 Thesis Overview

This thesis investigates methods to influence the morphology of isotactic polypropylene (iPP) and iPP nanocomposites for the purpose of improving the mechanical properties.

In chapter 2, *in-situ* metallocene catalyzed polymerization is explored as a means to prepare iPP-nanographite nanocomposites with improved nanoparticle dispersion. The effect of nanographite on the polymerization of iPP is address, and the effectiveness of *in-situ* polymerization is compared to conventional preparation techniques.

Next, a new polymer processing method termed “Melt-Mastication” is discussed in chapter 3 as a means to prepare iPP with improved crystal morphology, and therefore thermal and mechanical properties. The fundamental aspects of iPP crystallization during polymer processing are addressed, and structure property relationships are proposed to explain the observed property improvements.

In chapter 4, Melt-Mastication is repurposed as a processing technique to prepare iPP-nanographite nanocomposites. Relationships between processing conditions and nanographite dispersion quality are identified through a quantitative stereological method, and explained through a new model describing fragmentation of nanoparticle agglomerates in shear flows.

1.5 References

1. BCC Research: 'Global Markets for Polyolefin Resins', 2013.
2. E. P. News: 'Global PP Market to Reach 62.4 Million Metric Tons', 2013.
3. L. Corporation: 'Global Polypropylene Industry 2012-2017: Trend, Profit, and Forcast Analysis', 2012.
4. C. M. A. Inc.: '2012 World Polyolefins Analysis', 2011.
5. Robert Eller: 'Current States and Future Potential for Polyolefins, TPOs, and TPES in the Global Automotive Market', 2012, Houston, TX.
6. J. C. Halpin: 'Moduli of Crystalline Polymers Employing Composite Theory', *J. Appl. Phys.*, 1972, **43**, 2235.
7. R. L. Miller and L. E. Nielsen: 'Crystallographic data for various polymers', *J. Polym. Sci.*, 1960, **44**, 391–395.
8. V. Busico, R. Cipullo and P. Corradini: 'Ziegler-Natta oligomerization of 1-alkenes: a catalyst's "fingerprint", 1. Hydrooligomerization of propene in the presence of a highly isospecific MgCl₂-supported catalyst', *Die Makromol. Chemie*, 1993, **194**, 1079–1093.
9. L. Resconi, L. Cavallo, A. Fait and F. Piemontesi: 'Selectivity in Propene Polymerization with Metallocene Catalysts', *Chem. Rev.*, 2000, **100**, 1253–1346.
10. G. Natta, P. Pino, G. Mazzanti and U. Giannini: 'A Crystallizable Organometallic Complex Containing Titanium and Aluminum', *J. Am. Chem. Soc.*, 1957, **79**, 2975–2976.
11. E. Martuscelli, M. Pracella and L. Crispino: 'Crystallization behaviour of fractions of isotactic polypropylene with different degrees of stereoregularity', *Polymer*, 1983, **24**, 693–699.
12. D. L. VanderHart, R. G. Alamo, M. R. Nyden, M.-H. Kim and L. Mandelkern: 'Observation of Resonances Associated with Stereo and Regio Defects in the Crystalline Regions of Isotactic Polypropylene: Toward a Determination of Morphological Partitioning', *Macromolecules*, 2000, **33**, 6078–6093.
13. G. Natta and P. Corradini: 'Structure and properties of isotactic polypropylene', *Nuovo Cim.*, 1960, **15**, 40–51.
14. Z. Mencik: 'Crystal structure of isotactic polypropylene', *J. Macromol. Sci. Part B*, 1972, **6**, 101–115.

15. M. I. Aroyo (ed.): 'International Tables for Crystallography', 2015, Chester, England, International Union of Crystallography.
16. B. Wunderlich: 'Macromolecular Physics', 1980, New York, NY, Academic Press.
17. J. Bandrup, E. H. Immergut and G. E.A.: 'Polymer Handbook', 2003, New York, NY, John Wiley & Sons, Inc.
18. J. Varga: 'Supermolecular structure of isotactic polypropylene', *J. Mater. Sci.*, 1992, **27**, 2557–2579.
19. D. C. Bassett and R. H. Olley: 'On the lamellar morphology of isotactic polypropylene spherulites', *Polymer*, 1984, **25**, 935–943.
20. B. Lotz, J. C. Wittmann and A. J. Lovinger: 'Structure and morphology of poly(propylenes): a molecular analysis', *Polymer*, 1996, **37**, 4979–4992.
21. J. D. Hoffman and R. L. Miller: 'Kinetic of crystallization from the melt and chain folding in polyethylene fractions revisited: theory and experiment', *Polymer*, 1997, **38**, 3151–3212.
22. R. G. Alamo, D. L. VanderHart, M. R. Nyden and L. Mandelkern: 'Morphological Partitioning of Ethylene Defects in Random Propylene–Ethylene Copolymers †', *Macromolecules*, 2000, **33**, 6094–6105.
23. R. G. Alamo, M.-H. Kim, M. J. Galante, J. R. Isasi and L. Mandelkern: 'Structural and Kinetic Factors Governing the Formation of the γ Polymorph of Isotactic Polypropylene', *Macromolecules*, 1999, **32**, 4050–4064.
24. F. Auriemma and C. De Rosa: 'Crystallization of Metallocene-Made Isotactic Polypropylene: Disordered Modifications Intermediate between the α and γ Forms', *Macromolecules*, 2002, **35**, 9057–9068.
25. R. Paukkeri and A. Lehtinen: 'Thermal behaviour of polypropylene fractions: 1. Influence of tacticity and molecular weight on crystallization and melting behaviour', *Polymer*, 1993, **34**, 4075–4082.
26. R. Paukkeri and A. Lehtinen: 'Thermal behaviour of polypropylene fractions: 2. The multiple melting peaks', *Polymer*, 1993, **34**, 4083–4088.
27. R. H. Olley and D. C. Bassett: 'An improved permanganic etchant for polyolefines', *Polymer*, 1982, **23**, 1707–1710.
28. J. J. Janimak, S. Z. D. Cheng, P. A. Giusti and E. T. Hsieh: 'Isotacticity effect on crystallization and melting in polypropylene fractions. II. Linear crystal growth rate and morphology study', *Macromolecules*, 1991, **24**, 2253–2260.

29. S. Z. D. Cheng, J. J. Janimak, A. Zhang and E. T. Hsieh: 'Isotacticity effect on crystallization and melting in polypropylene fractions: 1. Crystalline structures and thermodynamic property changes', *Polymer*, 1991, **32**, 648–655.
30. D. R. Norton and A. Keller: 'The spherulitic and lamellar morphology of melt-crystallized isotactic polypropylene', *Polymer*, 1985, **26**, 704–716.
31. K. Yamada, S. Matsumoto, K. Tagashira and M. Hikosaka: 'Isotacticity dependence of spherulitic morphology of isotactic polypropylene', *Polymer*, 1998, **39**, 5327–5333.
32. R. Phillips, G. Herbert, J. News and M. Wolkowicz: 'High modulus polypropylene: Effect of polymer and processing variables on morphology and properties', *Polym. Eng. Sci.*, 1994, **34**, 1731–1743.
33. M. Fujiyama and T. Wakino: 'Structures and properties of injection moldings of crystallization nucleator-added polypropylenes. I. Structure–property relationships', *J. Appl. Polym. Sci.*, 1991, **42**, 2739–2747.
34. M. Fujiyama, T. Wakino and Y. Kawasaki: 'Structure of skin layer in injection-molded polypropylene', *J. Appl. Polym. Sci.*, 1988, **35**, 29–49.
35. M. R. Kantz, H. D. Newman and F. H. Stigale: 'The skin-core morphology and structure–property relationships in injection-molded polypropylene', *J. Appl. Polym. Sci.*, 1972, **16**, 1249–1260.
36. G. Kumaraswamy, R. K. Verma, J. A. Kornfield, F. Yeh and B. S. Hsiao: 'Shear-Enhanced Crystallization in Isotactic Polypropylene. In-Situ Synchrotron SAXS and WAXD', *Macromolecules*, 2004, **37**, 9005–9017.
37. G. Kumaraswamy, A. M. Issaian and J. A. Kornfield: 'Shear-Enhanced Crystallization in Isotactic Polypropylene. 1. Correspondence between in Situ Rheo-Optics and ex Situ Structure Determination', *Macromolecules*, 1999, **32**, 7537–7547.
38. D. Ferrer-Balas, M. L. MasPOCH, A. B. Martinez and O. O. Santana: 'Influence of annealing on the microstructural, tensile and fracture properties of polypropylene films', *Polymer*, 2001, **42**, 1697–1705.
39. W. O'kane, R. Young and A. Ryan: 'The effect of annealing on the structure and properties of isotactic polypropylene films', *J. Macromol. Sci. Part B*, 1995, **34**, 427–458.
40. W. J. O'Kane and R. J. Young: 'The role of dislocations in the yield of polypropylene', *J. Mater. Sci. Lett.*, 1995, **14**, 433–435.

41. A. Lustiger, C. N. Marzinsky and R. R. Mueller: 'Spherulite boundary strengthening concept for toughening polypropylene', *J. Polym. Sci. Part B Polym. Phys.*, 1998, **36**, 2047–2056.
42. M. A. Kennedy, A. J. Peacock and L. Mandelkern: 'Tensile Properties of Crystalline Polymers: Linear Polyethylene', *Macromolecules*, 1994, **27**, 5297–5310.
43. H. J. Zimmermann and A. G. Hoechst: 'Structural analysis of random propylene-ethylene copolymers', *J. Macromol. Sci. Part B Phys.*, 2006,.
44. M. Fujiyama: 'Structures and Properties of Injection Moldings of Glass Fiber-filled Polypropylenes', *Int. Polym. Process.*, 1993, **8**, 245–254.
45. M. Fujiyama, Y. Kitajima and H. Inata: 'Structure and properties of injection-molded polypropylenes with different molecular weight distribution and tacticity characteristics', *J. Appl. Polym. Sci.*, 2002, **84**, 2142–2156.
46. R. A. Vaia and H. D. Wagner: 'Framework for nanocomposites', *Mater. Today*, 2004, **7**, 32–37.
47. J. Jancar, J. F. Douglas, F. W. Starr, S. K. Kumar, P. Cassagnau, A. J. Lesser, S. S. Sternstein and M. J. Buehler: 'Current issues in research on structure–property relationships in polymer nanocomposites', *Polymer*, 2010, **51**, 3321–3343.
48. P. Cassagnau: 'Melt rheology of organoclay and fumed silica nanocomposites', *Polymer*, 2008, **49**, 2183–2196.
49. V. Vladimirov, C. Betchev, A. Vassiliou, G. Papageorgiou and D. Bikiaris: 'Dynamic mechanical and morphological studies of isotactic polypropylene/fumed silica nanocomposites with enhanced gas barrier properties', *Compos. Sci. Technol.*, 2006, **66**, 2935–2944.
50. S. Chung, W. Hahm, S. Im and S. Oh: 'Poly(ethylene terephthalate)(PET) nanocomposites filled with fumed silicas by melt compounding', *Macromol. Res.*, 2002, **10**, 221–229.
51. S. Matteucci, V. A. Kusuma, S. Swinnea and B. D. Freeman: 'Gas permeability, solubility and diffusivity in 1,2-polybutadiene containing brookite nanoparticles', *Polymer*, 2008, **49**, 757–773.
52. B. Wetzel, F. Hauptert, K. Friedrich, M. Q. Zhang and M. Z. Rong: 'Impact and wear resistance of polymer nanocomposites at low filler content', *Polym. Eng. Sci.*, 2002, **42**, 1919–1927.

53. R. J. Nussbaumer, W. R. Caseri, P. Smith and T. Tervoort: 'Polymer-TiO₂ Nanocomposites: A Route Towards Visually Transparent Broadband UV Filters and High Refractive Index Materials', *Macromol. Mater. Eng.*, 2003, **288**, 44–49.
54. J. M. Pochan: 'Mechanics of Polymer–Clay Nanocomposites', *Macromolecules*, 2007, **40**, 290–296.
55. A. Vermogen, K. Masenelli-Varlot, R. Séguéla, J. Duchet-Rumeau, S. Boucard and P. Prele: 'Evaluation of the Structure and Dispersion in Polymer-Layered Silicate Nanocomposites', *Macromolecules*, 2005, **38**, 9661–9669.
56. W. Lertwimolnun and B. Vergnes: 'Effect of processing conditions on the formation of polypropylene/organoclay nanocomposites in a twin screw extruder', *Polym. Eng. Sci.*, 2006, **46**, 314–323.
57. G. Zheng, J. Wu, W. Wang and C. Pan: 'Characterizations of expanded graphite/polymer composites prepared by in situ polymerization', *Carbon*, 2004, **42**, 2839–2847.
58. H. Kim and C. W. Macosko: 'Morphology and Properties of Polyester/Exfoliated Graphite Nanocomposites', *Macromolecules*, 2008, **41**, 3317–3327.
59. P. Steurer, R. Wissert, R. Thomann and R. Mülhaupt: 'Functionalized Graphenes and Thermoplastic Nanocomposites Based upon Expanded Graphite Oxide.', *Macromol. Rapid Commun.*, 2009, **30**, 316–27.
60. H. Kim, S. Kobayashi, M. A. AbdurRahim, M. J. Zhang, A. Khusainova, M. A. Hillmyer, A. A. Abdala and C. W. Macosko: 'Graphene/polyethylene nanocomposites: Effect of polyethylene functionalization and blending methods', *Polymer*, 2011, **52**, 1837–1846.
61. D. Cho, S. Lee, G. Yang, H. Fukushima and L. T. Drzal: 'Dynamic Mechanical and Thermal Properties of Phenylethynyl-Terminated Polyimide Composites Reinforced With Expanded Graphite Nanoplatelets', *Macromol. Mater. Eng.*, 2005, **290**, 179–187.
62. Y. Kojima, A. Usuki, M. Kawasumi, A. Okada, Y. Fukushima, T. Kurauchi and O. Kamigaito: 'Mechanical properties of nylon 6-clay hybrid', *J. Mater. Res.*, 2011, **8**, 1185–1189.
63. A. Usuki, Y. Kojima, M. Kawasumi, A. Okada, Y. Fukushima, T. Kurauchi and O. Kamigaito: 'Synthesis of nylon 6-clay hybrid', *J. Mater. Res.*, 1993, **8**, 1179–1184.
64. J. Jancar: Interphase Phenomena in Polymer Micro- and Nanocomposites, in *Nano- Micromechanics Polym. Blends Compos.* 2009, Carl Hanser Verlag, pp. 241–266.

65. X. Jiang and L. T. Drzal: 'Improving electrical conductivity and mechanical properties of high density polyethylene through incorporation of paraffin wax coated exfoliated graphene nanoplatelets and multi-wall carbon nano-tubes', *Compos. Part A Appl. Sci. Manuf.*, 2011, **42**, 1840–1849.
66. W. R. Caseri: 'Nanocomposites of polymers and inorganic particles: preparation, structure and properties', *Mater. Sci. Technol.*, 2006, **22**, 807–817.

CHAPTER 2

IN-SITU POLYMERIZATION OF ISOTACTIC POLYPROPYLENE- NANOGRAPHITE NANOCOMPOSITES

Herein, *in-situ* polymerization is explored as a means for preparing Isotactic Polypropylene -Exfoliated Graphene Nanoplatelet (iPP-xGnP) nanocomposites with well dispersed xGnP nanoparticles. *In-situ* polymerization of iPP-xGnP nanocomposites was accomplished via single site metallocene catalyzed polymerization of polypropylene within a toluene dispersion of xGnP nanoparticles. Analogous iPP-xGnP composites were prepared by melt compounding of commercial Ziegler-Natta iPP with xGnP, and the morphology and properties of both iPP-xGnP nanocomposites were analyzed, and discussed with respect to the preparation condition.

It was found that the *in-situ* polymerization method did not perform as well as anticipated. The presence of xGnP decreased the reaction kinetics of iPP polymerization, presumably due to catalyst poisoning. Further, the xGnP dispersion produced by *in-situ* polymerization was poorer than the xGnP dispersion in the composites prepared by melt compounding, according to optical microscopy. Also, thermal analysis demonstrated results consistent with filled iPP, such as increases in the crystallization temperature and mechanical modulus. However, the non-linear mechanical properties were found to be superior in the *in-situ* prepared nanocomposites due to the unique chain architecture and morphology produced by this technique. Accordingly, *in-situ* prepared nanocomposites generally showed superior ductility and fracture toughness. Despite the unexpectedly poor results, the present study provided valuable information and useful insights that enabled further successes in other polyolefin-related projects.

2.1 Introduction

Polyolefin Nanocomposites (PNCs) offer opportunities to improve the properties of polyolefins with relatively small amounts of reinforcement. Compared to traditional fiber-reinforced composites, nanocomposites only require small (< 2 vol %) concentrations of reinforcement to create property enhancements.^{1,2} Accordingly, PNCs are ideally situated to penetrate new markets and add value to a variety of applications. More information about the property improvements, potential applications, and challenges of PNCs, particularly graphite nanoplatelet (GNP) reinforced PNCs, may be found in chapter 1 of this dissertation.

However, it is difficult to prepare polyolefin-GNP PNCs with enhanced properties due to challenges associated with GNP agglomeration. For example, polyolefin-GNP PNCs demonstrate significant reductions to non-linear mechanical properties, like fracture toughness and strain to failure. The apparent decrease in non-linear mechanical properties has been attributed to the presence of large GNP agglomerates, which can facilitate crack propagation and lead to premature failure. Accordingly, many researchers are investigating new PNC preparation methods to prevent agglomeration, promote efficient dispersion, and facilitate commercialization of PNCs. Currently, melt compounding through extrusion is the most studied technique to fabricate polyolefin-GNP PNCs, however this technique cannot achieve satisfactory nanoparticle dispersions under normal circumstances due to severe aggregation during melt compounding.

2.1.1 Chemical Methods for Preparation of PNCs

Recent attention has been directed toward developing new, economical techniques to prepare polyolefin-GNP nanocomposites with improved GNP dispersions. These

techniques may be classified as either chemical or physical preparation methods, the latter of which will be discussed in section 4.1.1. Chemical modification techniques include a number of methods aimed to optimize the interactions between the polymer and nanoparticles in order to promote dispersion.³

One such technique involves addition of a compatibilizing agent to a PNC system that preferentially migrates to the polymer-nanoparticle interface.^{4,5} The compatibilizing agent effectively improves the interaction between the polymer and nanoparticle interface, which removes the thermodynamic driving force for particle agglomeration and improves the spatial distribution of nanoparticles. For example, Vladimirov *et al.* improved the spatial distribution of nanosilica in iPP through addition of an isotactic polypropylene grafted with maleic anhydride (iPP-g-MA) compatibilizer. The authors rationalized that the polar functionality of the maleic anhydride comonomer enabled iPP-g-MA to interact favorably with nanosilica, while the iPP comonomer facilitated interaction with the polymer matrix. The results showed that the improved distribution resulted in increased crystallization kinetics, mechanical storage modulus, and gas barrier properties.

Another chemical modification technique involves grafting nanoparticles with polymeric structures that interact favorably with the PNC matrix, which may be accomplished via “grafting-to” or “grafting-from” techniques. The polymer structures may be compatibilizing agents, or polymers of identical composition to the matrix. In the grafting-to technique, an end functionalized polymer is attached to the nanoparticle surface. For example, Mehnert *et al.* demonstrated the grafting-to technique where functionalized polysiloxanes were reacted with hydroxyl groups on the surface of nanosilica in order to improve the spatial distribution of nanosilica in polyacrylates.^{6,7} Grafting-to techniques

are generally limited by the steric repulsions between adjacent chains, which limits the grafting density on the nanoparticle surface.⁸ In contrast, grafting-from techniques involve polymerizing chains from the nanoparticle surface. In this technique, either a nanoparticle with a reactive surface is chosen, or the surface is functionalized with an initiator, exposed to monomer, and finally the monomer is polymerized from the surface. These techniques have been demonstrated with free radical and condensation polymerization, however more controlled architectures and compositions may be achieved with controlled radical polymerization.⁹⁻¹³ Both grafting-from and grafting-to techniques have been demonstrated to improve the spatial distribution of nanoparticles, which has been attributed to improved interfacial interactions between the polymer matrix and the nanoparticle surface. However, grafting techniques often involve costly multistep chemical processes, which precludes these techniques from applications involving commodity PNCs.¹⁴

A further approach to implement nanofiller dispersion directly into a PNC is through the polymerization filling technique (PFT).¹⁵⁻¹⁷ In this technique, a polymerization catalyst is immobilized to the surface of a nanoparticle such that polymerization only occurs from the filler surface. This technique is similar to grafting-from polymerization, except that all of the matrix material is polymerized from the surface of the nanoparticle, and the polymer is not covalently bonded to the nanoparticle surface. For instance, Mülhaupt *et al.* used PFT as a means to create ultrahigh-molecular weight polyethylene nanocomposites containing uniformly dispersed nanoparticles.¹⁸ In this study, a metallocene catalyst was immobilized to the surface of several types of nanoparticles, including a type of functionalized graphite. The authors showed the PFT is an effective method to prepare PNCs with excellent nanoparticle dispersion and therefore improved

conductivity, thermooxidative stability, and barrier properties. However, PFT requires careful engineering of the nanoparticle surface chemistry, as well as optimized pretreatment methods in order to immobilize the polymerization catalyst to the nanoparticle surface.

In-situ polymerization is a PNC preparation method that demonstrates many of the benefits of other chemical modification techniques, without requiring costly processes to control the nanoparticle surface chemistry. *In-situ* polymerization involves first dispersing nanoparticles in a solvent, followed by homogeneous polymerization within the dispersion through addition of catalyst and monomer. In contrast to PFT, *in-situ* polymerization does not require a separate catalyst immobilization step prior to polymerization. This means any conventional solution polymerization chemistry may be applied to *in-situ* polymerization, provided the nanoparticle surface does not deactivate the monomer and/or catalyst. Furthermore, *in-situ* polymerization enables polymerization to occur homogeneously throughout the solution, which in many cases increases the reaction kinetics compared to PFT where polymerization is confined to the nanoparticle surface. However, in order to produce PNCs with excellent nanoparticle dispersion, this technique requires a stable dispersion of nanoparticles to be established in the polymerization medium prior to polymerization. For example, Park *et al.* prepared single wall carbon nanotube (SWCNT)-polyimide PNC through polymerization of polyimide within a solvent dispersion of SWCNTs under continuous sonication.¹⁹ The resultant PNCs exhibited a well dispersed nanoparticle phase, which the authors attribute to sonication during polymerization. It follows that *in-situ* polymerization is a promising candidate for preparation of commodity polyolefin-GNP PNCs.

2.1.2 Metallocene Catalyzed Polymerization of Polyolefins

For polypropylene, homogeneous solution polymerization is achievable with single-site group 4 metallocene catalysis.²⁰ Group 4 metallocene catalysts are pseudotetrahedral organometallic compounds in which the transition metal atom coordinates with two cyclopentadienyl ligands and two σ -ligands. One of the two σ -ligands is removed when the catalyst is activated, and becomes a vacant coordination site that will interact with the π -orbital of the monomer, propene. The cyclopentadienyl ligands include any η^5 cyclopentadienyl ligand, including cyclopentadienyl itself ($C_5H_5^-$), indenyl ($C_9H_7^-$), fluorenyl ($C_{12}H_9^-$), and any cyclopentadienyl group with attached alkyl or aryl functional groups. Investigations have shown that the structure of the polymer produced by group 4 metallocene catalysts may be controlled by the structure of the η^5 cyclopentadienyl ligand, and the ligands may be engineered to invoke elements of chirality to the polymer produced by the catalyst.^{20,21} In the case of propene polymerization, rational design of the ligand environment from the η^5 cyclopentadienyl groups can control features of the polypropylene microstructure, including the co-monomer incorporation, regio-selectivity, and stereo-selectivity and the molecular weight of the resulting polymer.²²⁻²⁴ Furthermore, the ligand environment can also sterically hinder agostic interactions between the group 4 metallocene and the growing polymer chain, effectively limiting chain termination mechanisms and increasing the molecular weight.²⁵⁻²⁷ Finally, group 4 metallocene catalysts produce polyolefins with relatively narrow molecular weight distribution ($\mathcal{D} = 2$), compared to conventional supported Ziegler-Natta catalysts ($\mathcal{D} = 5-30$).

Polypropylene polymerization also requires a co-catalyst in order to activate the metallocene catalyst. The active propylene polymerization species is a metallocene alkyl

cation, which may be produced by reacting a metallocene dichloride with a highly Lewis acidic species, known as a co-catalyst. The most pervasive co-catalyst for propylene polymerization is Methylaluminoxane (MAO), which is produced through the controlled hydrolysis of AlMe_3 . The precise structure of MAO is not well understood, but there is multinuclear NMR evidence suggesting that it is a complex mixture of several different oxidized aluminum alkyls, including residual AlMe_3 , and oligomers of MAO that are in dynamic equilibrium with AlMe_3 .²⁸ The highly Lewis acidic nature of MAO and the activated metallocene requires polymerization to occur in nonpolar, aprotic solvents such as toluene and heptane. Accordingly, it is imperative that metallocene polymerization occurs in the absence of oxygen, moisture, or any active hydrogen-bearing functional groups like alcohols and acids.

In the present study, propylene polymerization is performed with a chiral *ansa*-metallocene catalyst engineered to produce highly isotactic, high molecular weight isotactic polypropylene with excellent catalyst activity.^{29,30} The high activity catalyst, *rac*- $\text{Me}_2\text{Si}(2\text{-Me-4-Ph-1-Ind})_2\text{ZrCl}_2$, is a C_2 -symmetric zirconocene including strapped bisindenyl ligands with a methyl groups in the 2 and 2' positions and phenyl groups in the 4 and 4' positions. The phenyl groups in the 4 and 4' positions have been shown to increase the enantioselectivity of the monomer insertion process, which increases the tacticity of the polymerized polypropylene. The methyl groups in the 2 and 2' positions have been empirically shown to increase the molecular weight of the resulting polypropylene considerably. Cavallo and Guerra *et al.* proposed that substituents in the 2 and 2' positions destabilize the β -agostic interactions which eliminates chain termination mechanisms.³¹ In principle, any single site catalyst or combination of catalysts can be applied to an *in-situ*

polymerization, enabling control of the morphology and properties of the synthesized PNCs. It follows that *in-situ* polymerization is a promising method to prepare well dispersed iPP-GNP nanocomposites while also allowing control of the iPP chain microstructure through judicious selection of metallocene catalysts.

2.1.3 *In-Situ* Polymerization of iPP-Nanographite PNCs

Metallocene catalyzed *in-situ* polymerization of iPP-nanographite PNCs was previously demonstrated by other authors.^{32–36} Galland *et al.* reported that iPP-graphene nanosheet PNCs prepared through *in-situ* polymerization demonstrate improved thermooxidative stability and conductivity, as well as enhancement of the mechanical modulus with increasing nanographite loading. These studies provide a useful framework to help understand how metallocene polymerization may be used to improve the dispersion of polyolefin PNCs. However, the mechanical property analyses in these studies are not directly comparable to other iPP systems, because the iPP produced in these studies is not comparable to commercial iPP. The metallocene catalyst used, *rac*-Me₂Si(Ind)₂ZrCl₂, does not possess the correct organic ligand structure to promote adequate enantioselectivity and inhibit chain termination mechanisms. Therefore the polypropylene produced is much lower in molecular weight ($M_w > 80,000$ g/mol) and tacticity (95.4% *m*), compared to commercial iPP. These differences in chain microstructure produce suboptimal thermal and mechanical properties relative to commercial iPP, such as a low observed melting point (145 °C) compared to what is conventionally observed in iPP (165 °C). Also, the viscoelastic response of the iPP in these studies is distinct from commercial iPP, evidenced by the apparent α , β , and γ relaxations in the DMA temperature sweep experiment. Commercial iPP should only demonstrate an α transition. Another study by Muradyan *et*

al. prepared iPP-GNP PNCs through polymerization within liquid propylene. This study used a metallocene catalyst known to produce iPP of comparable M_w and tacticity to commercial iPP under normal polymerization conditions. The investigators prepared iPP-GNP PNCs with useful dielectric properties due to an excellent spatial distribution of nanoparticles, however the mechanical properties were not extensively studied. Furthermore, the study did not include investigations of the molecular weight or morphology of the polymerized iPP, so the structure-property relationships responsible for the mechanics are not clear. Finally, polymerizations in this study occurred at relatively high temperatures (>60 °C) which is known to be too high to produce polypropylene with similar M_w and tacticity to commercially useful iPP. Finally, there have been no studies to date that compare the mechanical properties of *in-situ* synthesized iPP-GNP composites with similar composites prepared by melt compounding, likely due to the differences in chain microstructure between metallocene synthesized iPP and commercial iPP.

The aim of the present study is to prepare comparable iPP-xGnP nanocomposites by two different techniques, and then investigate how the preparation method affects the properties. Isotactic Polypropylene-GNP nanocomposites were prepared by metallocene catalyzed *in-situ* polymerization within a toluene dispersion of GNPs, and compared to analogous composites prepared by melt compounding of commercial Ziegler Natta iPP with xGnP in a static mixer. Also presented is a comprehensive dispersion study at micrometer and nanometer length scales. The relationships between composite morphology and thermal/mechanical properties will be characterized and discussed. Finally, direct comparisons between of the non-linear mechanical properties of *in-situ*

prepared nanocomposites and conventionally melt compounded nanocomposites will be discussed.

2.2 Materials and Methods

2.2.1 Materials

Exfoliated Graphene Nanoplatelets (xGnP-c-750, 750 m²/g; xGnP-c-500, 500 m²/g; xGnP-c-300, 300 m²/g); were purchased from XGSciences, Inc. and used as received. The preparation method for xGnP involves microwave assisted exfoliation of intercalated graphite, detailed in chapter 1.³⁷ Polypropylene (PP9999SS) was provided by ExxonMobil. Irganox 1010 and Irgafos 168 were purchased from Ciba and used as received. Propylene gas (99.95%) was provided by Westfalen AG and purified by passage through columns of BASF R3-11G oxygen scavenger and 4 Å molecular sieves. Toluene was provided by Riedel-de-Haën and purified by passage through columns of BASF R3-11G oxygen scavenger and 4 Å molecular sieves. Methylaluminoxane (MAO) was provided by Compton GmbH and used as received. The metallocene catalyst *rac*-dimethylsilylbis(2-methyl-4-phenyl-1-indenyl)zirconium dichloride (*rac*-Me₂Si(2-Me-4-Ph-1-Ind)₂ZrCl₂) was purchased from Precious Catalyst Inc. and used as received.

2.2.2 Sedimentation Studies of xGnP-Toluene Suspensions

Sedimentation studies were performed to determine the optimal xGnP grade for *in-situ* polymerization, and also the optimal order of addition of MAO and xGnP for *in-situ* polymerization. Toluene, xGnP and MAO were added to 20 mL scintillation vials within a dry nitrogen glovebox and sealed. The vials were then subjected to bath sonication for 15 minutes, and then placed on a stationary bench. The vials were placed in front of a

fluorescent lamp, and the time to sedimentation was recorded. Sedimentation was defined as the time when all, or part, of the solution becomes optically transparent.

2.2.3 *In-Situ* Synthesis of iPP-xGnP Nanocomposites

Syntheses were performed in a 9.5 L steel reactor equipped with a mass flow controller, temperature control system, and mixing blade, shown in Figure 2.1 and described elsewhere.³⁸ The reactor is also connected to ProfiSignalGo (Delphin Technology) data acquisition software in order to record the monomer mass flow and temperature during the reaction. Prior to polymerization, xGnP was added to the reactor and heated to 90 °C for 12 hours, in order to remove any residual moisture in the xGnP or reactor. The reactor was then flushed with Argon 3 times, and then cooled to 30 °C. Toluene was introduced under constant stirring, followed by the MAO co-catalyst. The solution was allowed to equilibrate at 30 °C for 10 minutes, and then saturated with 3 bars propylene gas under constant mixing (120 RPM). To initiate the reaction, a desired volume of metallocene catalyst solution was injected into the reactor. The temperature and pressure were maintained at 30 °C and 3 bars propylene gas for the duration of the reaction.

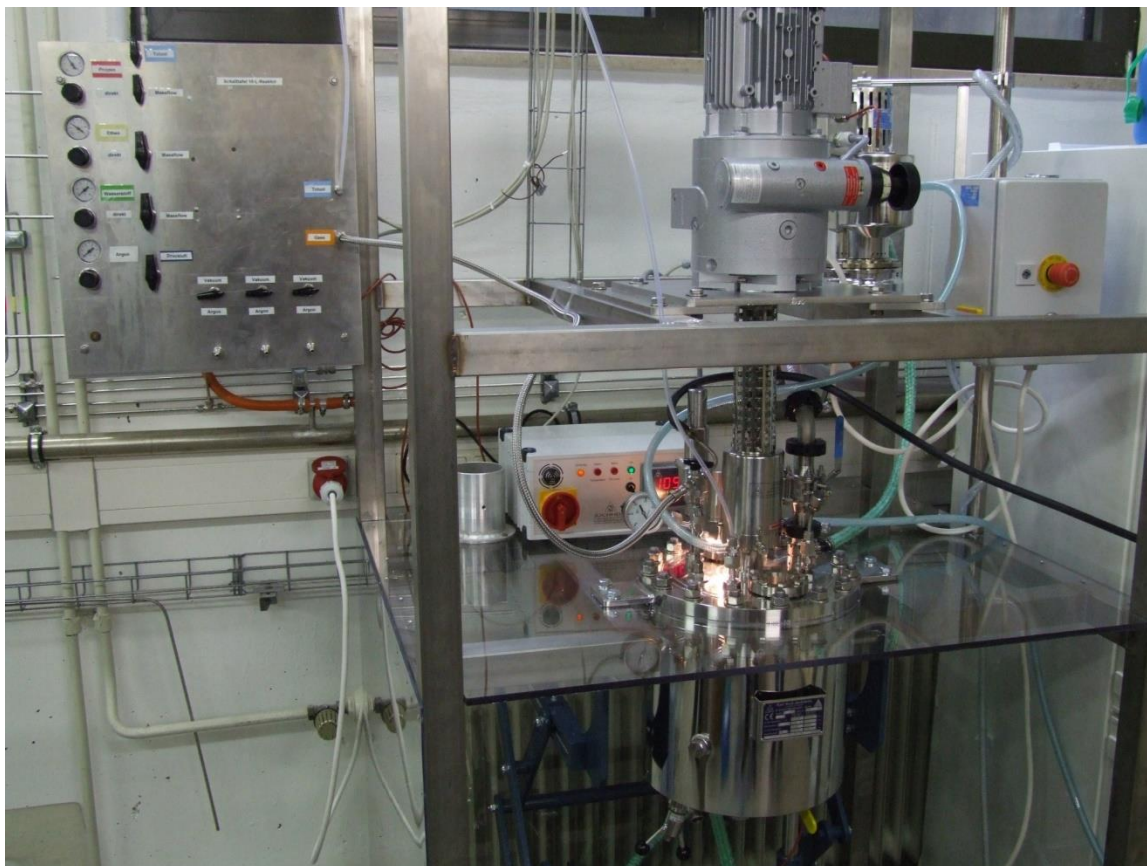


Figure 2.1: Steel reactor used for *in-situ* polymerization trials of iPP-xGnP nanocomposites. Reactor located in Professor G. Luinstra's lab at the University of Hamburg.

Small-scale synthesis trials of pure iPP were also performed in a 100 mL glass reactor with improved temperature control using a setup detailed elsewhere and shown in Figure 2.2.³⁹ Prior to polymerization, toluene, MAO, and $\text{rac-Me}_2\text{Si}(2\text{-Me-4-Ph-1-Ind})_2\text{ZrCl}_2$, were added to the glass reactor within a dry nitrogen glovebox and mixed for 10 minutes. The reactor was then sealed and connected to a gas manifold via Swagelok® QC Series quick connect lines. The solution was under constant magnetic stirring, and the glass reactor was placed in a 5 L, 30 °C water bath. The reactor was charged with propylene gas by 15 purge cycles from 0 to 3 bars, and then pressurized to 3 bars propylene gas. This reactor is assumed to have improved temperature control because it is immersed in water bath with much greater volume than the reaction volume.

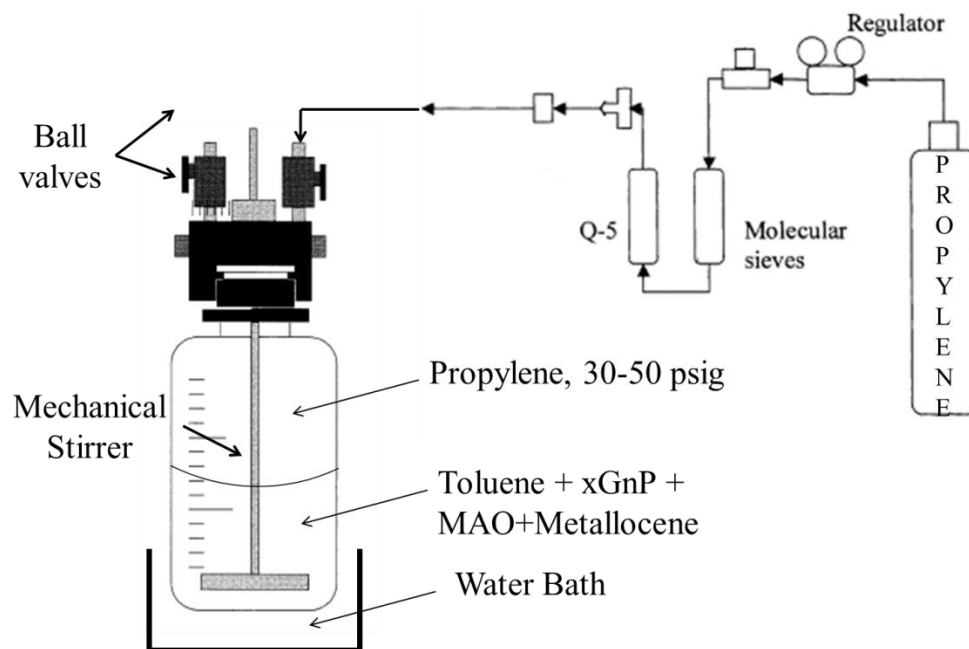


Figure 2.2: Schematic of the small scale polymerization vessel described in Coughlin *et al.*³⁹

All reactions were terminated by the addition of 10 mL of 5 wt% HCl in ethanol. The products were washed in 2 L dilute hydrochloric acid, stirred overnight, and rinsed thoroughly with ethanol. Finally, the products were dried under vacuum at 60 °C for 48 hours. The products were fine reactor powders, seen in Figure 2.3. The syntheses in the 9.5 L reactor produced enough material for mechanical testing, while the small scale syntheses in the 100 mL reactor did not. Due to the design of both reactors, it was not possible to disperse xGnP via sonication prior to or during *in-situ* polymerization.

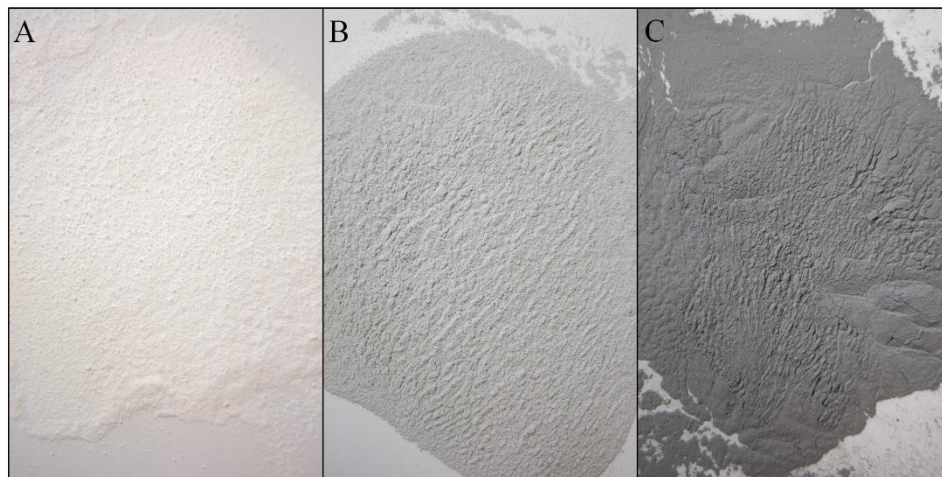


Figure 2.3: Reactor powder from *in-situ* synthesis of iPP-xGnP nanocomposites. (A) Pure iPP (IS-0) (B) 2 wt% xGnP in iPP (IS-2) (C) 4 wt% xGnP in iPP (IS-4).

2.2.4 Melt-Compounding of iPP-xGnP Composites

For comparison, iPP-xGnP PNCs were prepared by melt in a 50 mL Brabender static mixer (R. E. E. 6) operating at 200 °C for 15 minutes at 70 RPM. Commercial Ziegler-Natta isotactic polypropylene (ExxonMobil, PP9999SS), xGnP, and 0.1 wt% process stabilizers (Irganox 1010 and Irgafos 168) were dry-mixed in a plastic bag prior to addition to the mixer. Samples were quenched into a water bath and then melt pressed into mechanical testing specimens.

2.2.5 Characterization Methods

The infrared absorption profile of xGnP was characterized with a Perken Elmer Spectra 100 FTIR. A 0.04 wt% xGnP in KBr pellet was prepared and then analyzed in transmission mode.

The surface chemistry of xGnP was analyzed with XPS, using a PHI Quantum 2000 Scanning ESCA Microprobe with monochromatic Al K α radiation. A 200 μm^2 spot was selected for analysis. A low take-off angle of 10⁰ was used to avoid the mounting material.

Samples were analyzed with low resolution survey spectra of pass energy 187.9 eV as well as multiplexes at 46.95 eV for quantitative analysis. Prior to analysis, samples were dried at 100 °C in a vacuum oven for 12 hours.

Aluminum NMR (^{27}Al NMR) spectroscopy was used to probe the interaction between xGnP and the MAO co-catalyst. Spectroscopy was performed with a Bruker Avance 400 MHz NMR spectrometer operating at 104.229 MHz. The spectrometer was equipped with a temperature control unit and calibrated with an aqueous solution of AlCl_3 . Measurements were performed at 22, 60, 90, and 100 °C. Samples were prepared by vacuum transferring Toluene, MAO and xGnP into a quartz NMR tubes with 1 mm thick walls inside a dry nitrogen glovebox. The tubes were then sealed with rubber septa, removed from the glovebox, and exposed to liquid nitrogen. Next, the tubes were evacuated through the septa, and simultaneously sealed through melting the quartz glass with an oxy-hydrogen torch. Quartz tubes are necessary because conventional NMR tubes contain aluminosilicate glass, which would produce an erroneous signal in ^{27}Al NMR spectra.

Optical characterization was conducted on an Olympus optical microscope with DP71 digital camera. Film samples (50 μm thick) were prepared by compression molding at 200 °C. Samples were analyzed in transmission mode.

Transmission electron micrographs of composites were obtained with a JEOL JEM-2000FX transmission electron microscope with LaB6 electron source, at accelerating voltage 200 kV. Thin (~40 nm) sample sections were prepared using a Leica CryoUltramicrotome and Microstar diamond knife and then imaged on 400 mesh copper grids.

Isotactic Polypropylene molecular weight was characterized with high-temperature gel permeation chromatography on a Polymer Labs PL-220 GPC. Isotactic Polypropylene was removed from the PNCs via Soxhlet extraction in 1,2,4 Trichlorobenzene for 12 hours. Samples were then dissolved and analyzed in 1,2,4 Trichlorobenzene at 145 °C against polystyrene standards. Molecular weights were converted from polystyrene to polypropylene using the universal calibration method based on the Mark-Houwink constants.

Thermal properties were measured using a Thermal Gravimetric Analyzer (TA Instruments-TGA Q500), and Differential Scanning Calorimeter (TA Instruments-DSC Q200). TGA was conducted in a nitrogen atmosphere, and heated to 600 °C at 10 K/ min. DSC was performed between 20 and 200 °C at 10 °C/min. Crystallization and melting analyses were performed on the first cooling and the second heating cycle, respectively. Melting and cooling enthalpies for each sample were normalized to iPP mass.⁴⁰ To prepare samples for mechanical analysis, reactor powders were dry mixed with 0.1 wt% process stabilizers (Irganox 1010 and Irgafos 168) prior to compression molding. Square plaques were compression molded at 200 °C for 8 min and then cooled at 30 K/min. Tensile specimens were milled from 3 mm thick plaques. Tensile properties were characterized according to ASTM D 638. Testing was performed at room temperature using an Instron 4466 testing machine at a crosshead speed of 2 mm/min and a preload force of 8 N. The strain was calculated from the crosshead displacement.

Plane strain fracture toughness was characterized according to ASTM D5045 in a single-edge-notch three-point bend configuration. Samples were milled from 6 mm thick plaques and pre-notched with a diamond saw. A natural crack was made by cooling the

sample to $-20\text{ }^{\circ}\text{C}$ and displacing a fresh razor 1.5 mm into each sample with an Instron 4455 testing machine.

2.3 Results and Discussion

2.3.1 Surface Characterization of xGnP

Surface characterization of xGnP was performed to identify functional groups that could potentially inhibit *in-situ* polymerization. The polymerization catalyst and especially the MAO co-catalyst are both highly Lewis acidic compounds that are reactive with a variety of nucleophilic organic functional groups. Accordingly, FTIR and XPS were used to identify functional groups on the surface of xGnP that could potentially interact with the polymerization catalyst and co-catalyst. The surfaces of activated carbons like xGnP are known to contain nucleophilic organic functional groups.⁴¹ Additionally, Talsi *et al.* presented ^1H and ^{13}C NMR evidence suggesting trapped or immobile water molecules adsorbed to the surface of oxidized graphites.⁴² The FTIR absorptions in Figure 2.4 from $1580\text{-}1710\text{ cm}^{-1}$ and the asymmetric absorption at 3438 cm^{-1} indicate that carboxylic acids and other carbonyl-bearing functional groups are present. Also, the weak absorptions from $1100\text{-}1250\text{ cm}^{-1}$ suggest a range of tertiary and/or aromatic alcohols are present. Both classes of functional groups are well documented in active carbon literature.

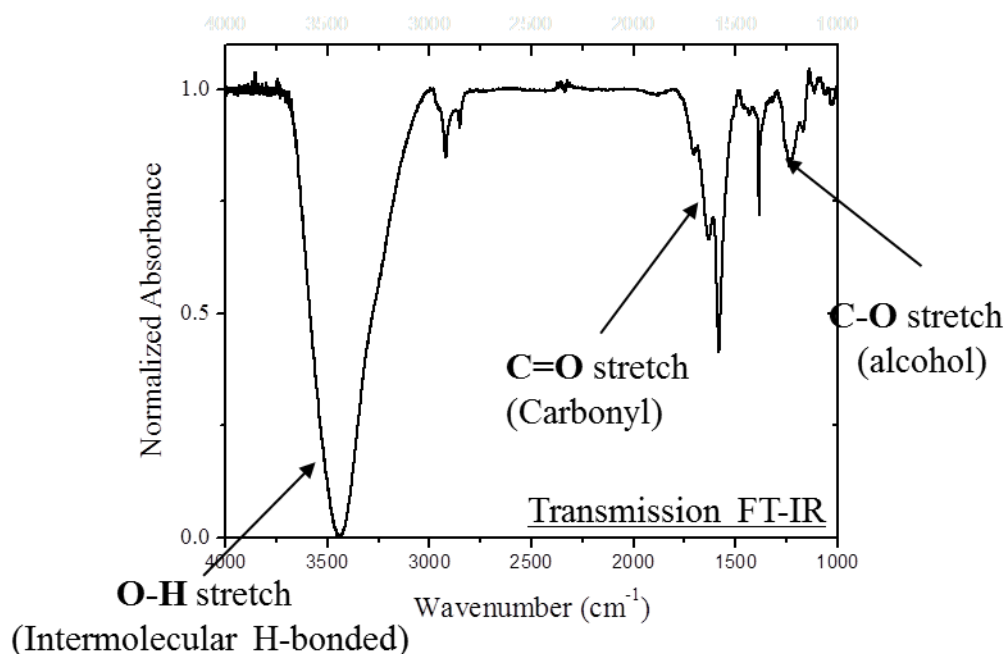


Figure 2.4: FTIR absorption spectra of xGnP-c-750 in transmission mode

XPS provides additional evidence supporting the presence of oxidized carbon functional groups (Figure 2.5). From XPS, the carbon peak demonstrates a maximum near 284 eV, corresponding to graphitic C-C bonds. Also shown is a weak feature near 288 eV, corresponding to carbonyl-bearing functional groups such as carboxylic acids, ketones, and aldehydes. Further, photoelectron emission energies consistent with oxygen were observed. The C:O ratio was determined to be 10.6:1. While the precise chemical structure of the functional groups are difficult to ascertain due to the heterogeneous nature of xGnP, it is clear that active hydrogen-bearing functional groups (-OH, C=O, and -COOH) are present. Normally, the delocalized sp^2 hybridized carbon structure of graphite is chemically stable to oxidation. However, the preparation process for xGnP exposes graphite to extreme exfoliation temperatures and strongly acidic intercalation compounds that promotes oxidation of graphite.⁴³ Once oxidation occurs, the delocalized sp^2 hybridized carbon structure is interrupted by localized sp^3 hybridized oxidation sites, which

lowers the activation energy barrier to further oxidation of adjacent carbons. Furthermore, the edges of xGnP particles are particularly susceptible to oxidation, due to the interruption of the delocalized sp^2 hybridized carbon structure.⁴⁴ Both XPS and FTIR analysis suggests oxidized carbon functional groups are present on xGnP.

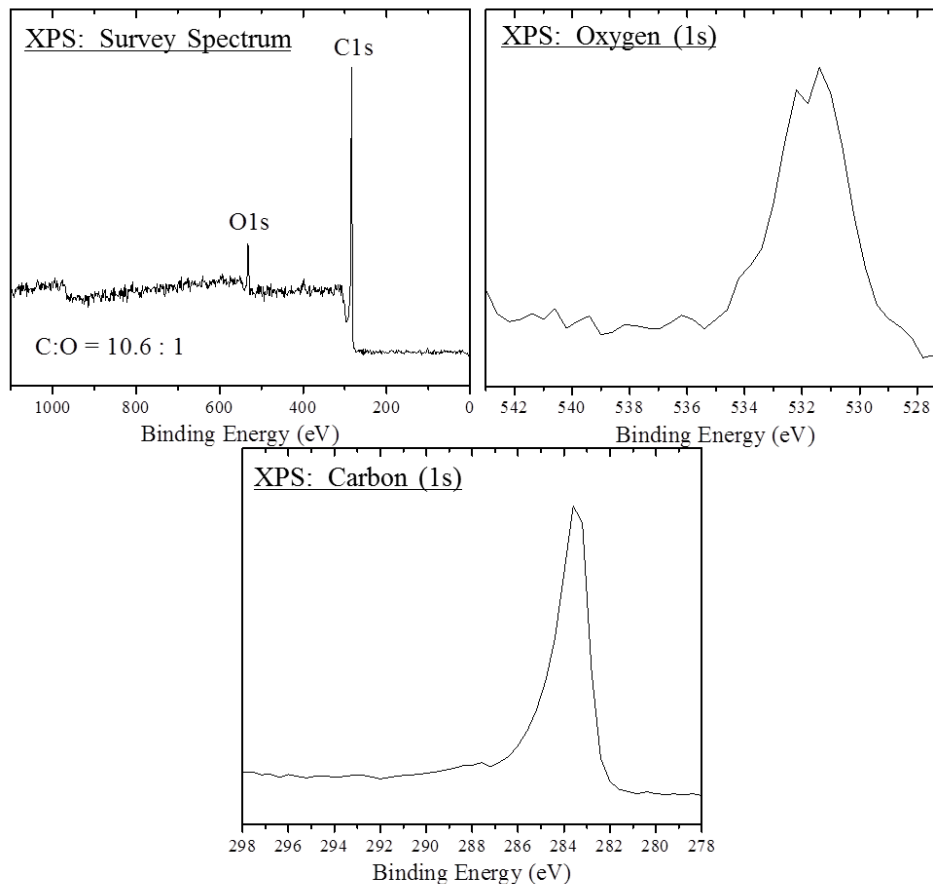


Figure 2.5: XPS spectra of xGnP-c-750. (Top Left) Survey spectrum. (Top Right) O1s spectrum. (Bottom) C1s spectrum.

2.3.2 ²⁷Al NMR Investigation of xGnP-MAO Interactions

The results from the surface characterization in section 2.3.1 show a variety of protic functional groups are present on xGnP. Alkyl aluminums like MAO are known to react vigorously with protic functional groups like alcohols, usually reducing them to

alkanes and oxidizing the alkyl aluminums to alkyl aluminum oxides. Accordingly it is reasonable to expect that xGnP will oxidize MAO and ultimately inhibit the activation of the metallocene catalyst. It is therefore prudent to investigate the behavior of the MAO co-catalyst in the presence of xGnP. However, MAO is difficult to characterize due to its air and moisture sensitivity. It is possible to perform NMR investigations of MAO within sealed NMR tubes, however conventional ^1H and ^{13}C NMR spectroscopy cannot provide adequate information to elucidate the coordination geometries of Aluminum in ^{27}Al , which is critical to observing the subtle differences between the various alkyl aluminum oxides present in MAO. Fortunately, the Aluminum-27 nucleus occurs at 100% natural abundance and is a magnetically active quadrupolar nucleus, so it is possible to perform ^{27}Al NMR spectroscopy on MAO. It follows that ^{27}Al NMR is a useful tool to understand how MAO is affected by the presence of xGnP and how to optimize the synthesis of iPP-xGnP nanocomposites.

A multinuclear NMR study by Talsi *et al.* investigated the structure of MAO through ^1H , ^{13}C , ^{17}O , and ^{27}Al NMR spectroscopy and concluded that MAO consists of oligomers with cage structure in dynamic equilibrium with AlMe_3 .²⁸ In this study, the ^{27}Al spectrum showed a narrow resonance near $\delta = 153$ ppm, corresponding to AlMe_3 , and at higher temperatures much broader signal appeared near $\delta = 110$ ppm, and is attributed to aluminoxane clusters.

In the present study, ^{27}Al NMR spectroscopy was performed on MAO/Toluene solutions (0.3 M) and MAO/Toluene-xGnP (0.5 M, 0.1% w/v and 1.5% w/v) suspensions. All spectra showed a broad parasitic resonance at $\delta = 20$ -80 ppm, which is likely due to aluminum components in the NMR probe head. This parasitic resonance has been noted

in other ^{27}Al NMR investigations. Figure 2.6-a shows a strong resonance at $\delta = 150\text{-}170$ ppm, attributed to AlMe_3 . The position of the peak increases with increasing temperature because AlMe_3 continuously equilibrates between dimeric and monomeric forms, the latter of which resonates at higher ppm and is favored at high temperatures. In contrast, the spectra of MAO/Toluene-xGnP in Figures 2.6-b and 2.6-c show much weaker AlMe_3 resonances, even with as little as 0.1% w/v xGnP in Toluene/MAO. *In-situ* polymerization of iPP-xGnP PNCs requires at least 1.5% w/v xGnP in Toluene/MAO. It appears that the behavior of the AlMe_3 is not affected by higher concentrations of xGnP. The results suggest that AlMe_3 and possibly MAO are immobilized to the xGnP surface, which would preclude them from contributing to the ^{27}Al NMR solution spectrum. The broad MAO resonance observed by Talsi *et al.* was not seen in the present study. Talsi *et al.* noted that the broad MAO resonance was only observed when MAO was treated with vacuum distillation to remove free AlMe_3 . The present study uses untreated MAO.

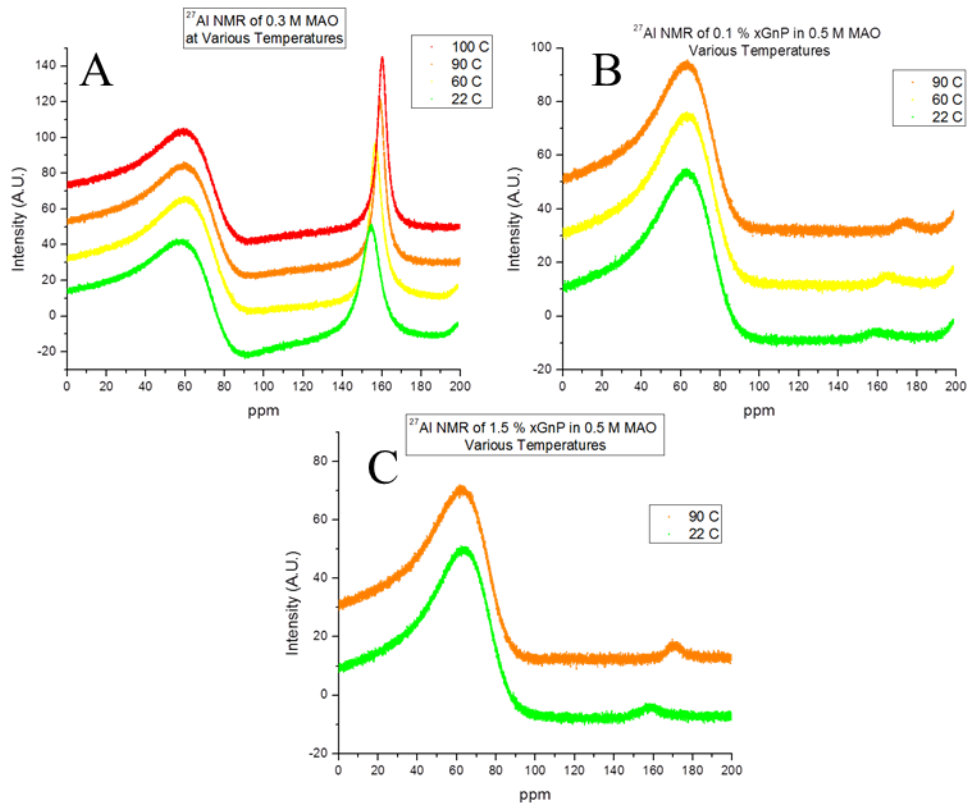


Figure 2.6: ^{27}Al NMR spectra of MAO/Toluene solutions and MAO/Toluene-xGnP suspensions. A) 0.3 M MAO/Toluene. B) 0.5 M MAO/Toluene-xGnP (0.1% w/v). C) 0.5 M MAO/Toluene-xGnP (1.5% w/v).

2.3.3 Sedimentation Studies of Toluene-xGnP Suspensions

Sedimentation studies were performed to determine the best xGnP grade for *in-situ* polymerization, and also the optimal order of addition of MAO and xGnP. *In-situ* polymerization should ideally occur in stable, homogeneous xGnP dispersions, which through polymerization will produce iPP-xGnP with excellent xGnP dispersion. However, it was empirically observed that xGnP in the Toluene polymerization solvent will sediment rapidly without mechanical agitation. The kinetics of the sedimentation process can be described as a competition between hydrodynamic drag and agglomerate density. Hydrodynamic drag depends on the size of the agglomerate and its corresponding surface area, which prevents sedimentation. However, the density of the agglomerate promotes

sedimentation, as xGnP is denser than toluene. Accordingly, xGnP agglomerates of a critical size will rapidly sediment to the bottom of the vial, whereas smaller agglomerates will slowly sediment. The existence of sedimentation suggests that xGnP is continuously agglomerating in Toluene.

The sedimentation performance of each type of xGnP is summarized in Table 2.1. The sedimentation time increased according to $xGnP-C-300 < xGnP-C-500 < xGnP-C-750$. This is expected, because xGnP-C-750 has the highest surface area, and therefore the smallest elementary size. It was also found that the presence of MAO increases the time to sedimentation. These results, combined with the results from ^{27}Al NMR, suggest there could be an interaction between MAO and xGnP that changes the surface chemistry of xGnP and impedes the kinetics of agglomeration and sedimentation. A recent study by Mülhaupt *et al.* demonstrated the preparation of ultra-high molecular weight polyethylene-graphite PNCs prepared via metallocene PFT from the surface of functionalized graphite. In this study, the graphite was functionalized with hydroxyl groups.¹⁸ The authors rationalize that the hydroxyl groups enable covalent bonding of the MAO co-catalyst to graphite, which improved the stability of graphite dispersions in nonpolar organic solvents. It is reasonable to assume that a similar mechanism may be responsible for the improved sedimentation time of xGnP with MAO.

Table 2.1: Sedimentation time in minutes of various xGnP grades in Toluene or Toluene and Methylaluminoxane (MAO)

	Toluene		0.3 M MAO	
	0.3% w/v	2% w/v	0.3% w/v	2% w/v
xGnP-C-750	13	4	22	35
xGnP-C-500	13	2	21	27
xGnP-C-300	13	2	21	18

2.3.4 *In-Situ* Synthesis of iPP-xGnP PNCs

Isotactic Polypropylene-xGnP (iPP-xGnP) nanocomposites were prepared using metallocene catalyzed polymerization of polypropylene within a toluene suspension of xGnP nanoparticles. The high activity catalyst, *rac*-Me₂Si(2-Me-4-Ph-1-Ind)₂ZrCl₂, is a C₂-symmetric zirconocene designed to polymerize high molecular weight isotactic polypropylene. Like other C₂-symmetric zirconocenes, the performance of *rac*-Me₂Si(2-Me-4-Ph-1-Ind)₂ZrCl₂ is a function of temperature. The molecular weight and tacticity of the polypropylene synthesized from this catalyst decreases with increasing reaction temperature, while the catalyst activity increases with increasing reaction temperature. For this study, the optimal reaction temperature for high molecular weight iPP with modest activity was 30 °C. Normally, iPP polymerization requires a 10,000-15,000 Al:Zr ratio, however much higher MAO concentration and Al:Zr ratios were selected in order to passivate the active hydrogens on xGnP prior to contact with the metallocene catalyst. Also, pretreatment of xGnP with MAO improves the stability of xGnP in toluene, as discussed in section 2.3.3. Accordingly, xGnP was pretreated with excess MAO for 10 minutes prior to contact with *rac*-Me₂Si(2-Me-4-Ph-1-Ind)₂ZrCl₂. When xGnP was pretreated with this method, catalyst activity was acceptable ($\geq 2 \text{ kg mmol}^{-1} \text{ bar}^{-1} \text{ hr}^{-1}$) for

all samples. Figure 2.3 shows that the color of each sample becomes progressively darker with increasing xGnP concentration. Table 2.2 summarizes the reaction parameters of the *in-situ* synthesized iPP-xGnP nanocomposites. *In-situ* synthesized samples are named “IS-*n*,” where *n* is the weight percent of xGnP determined by the char yield after TGA. Similarly, melt compounded samples are named “MC-*n*.”

Table 2.2: Reaction parameters and properties of iPP-xGnP nanocomposites prepared by *in-situ* polymerization and melt compounding. T_p = polymerization temperature set point. Propylene pressure = 3 bars. *kg iPP mmol Zr⁻¹ bar⁻¹ h⁻¹. ** M_w/M_n

Sample ID	[MAO] (mM)	T_p (°C)	Al:Zr ratio	Volume (L)	Activity*	M_w (kDa)	\bar{D} **	T_C (°C)	T_M (°C)	X_C (%)	Char Yield (%)	E (MPa)	σ_y (MPa)	ϵ_b (%)	G_{IC} (kJ/m ²)
IS-0	0.03	30	7,000:1	5	9.48	141	2.35	114.6	157.0	50.7	0.0	1620.0	38.4	12.1	14.6
IS-2	0.1	30	50,000:1	5	5.43	252	2.71	125.3	160.0	49.5	1.9	1830.0	38.5	78.0	16.2
IS-4	0.1	40	50,000:1	5	2.09	137	2.39	127.0	160.0	51.4	3.9	2000.0	43.0	5.8	6.3
IS-0_20mL	0.03	30	7,000:1	0.02	1.93	1,189	2.07	-	-	-	-	-	-	-	-
MC-0	-	-	-	-	-	135	3.55	111.7	164.0	50.7	0.0	1050.0	33.2	11.7	4.0
MC-2	-	-	-	-	-	135	3.55	130.4	165.5	58.0	2.0	1100.0	34.6	7.0	0.5
MC-4	-	-	-	-	-	135	3.55	132.8	166.0	59.6	4.0	1450.0	35.3	4.0	0.4

Table 2.2 shows an apparent decrease in the catalyst activity with increasing xGnP concentration. This trend is ascribed to both reaction temperature fluctuations and catalyst poisoning from the surface chemistry on xGnP. It could also be due to immobilized MAO on the surface of xGnP, as suggested by ^{27}Al NMR studies. Temperature fluctuations are anticipated during propylene polymerization, a highly exothermic reaction generating ~ 89 kJ/mol propylene. For this reason, the large 9.5 L reaction vessel used to polymerize samples IS-0 through IS-4 was fitted with a jacketed cooling system, and the smaller 20 mL reactor used to polymerize sample IS-0_20mL was placed in a 30 °C water bath. Nonetheless, heat transfer is a significant operational challenge in the 9.5 L reactor, so the actual polymerization temperature is likely higher than the set-point temperature (30 °C). Consequently, samples IS-0 through IS-4 demonstrated higher catalyst activity than sample IS-0_20 mL. Also, the catalyst activity decreases with increasing xGnP concentration. In fact, sample IS-4 required polymerization at 40 °C in order to achieve sufficient catalyst activity. The observed decrease in catalyst activity suggests that xGnP has a deleterious effect on the metallocene catalyst and/or MAO co-catalyst, possibly due to the active hydrogen bearing functional groups on xGnP which may deactivate the metallocene catalyst, or confine polymerization to the surface of xGnP, where the MAO is immobilized.

The trend in molecular weight and Đ is also ascribed to temperature fluctuations. Sample IS-0_20 mL showed the highest molecular weight and lowest Đ , due to efficient heat transfer during this small scale polymerization. In contrast, sample IS-0 had a much lower molecular weight and broader Đ due to heat transfer challenges inherent to larger reaction vessels. When xGnP is present, the activity is attenuated to a manageable level, thus minimizing temperature fluctuations. The result is that the molecular weight of IS-2

is higher than IS-0. Sample IS-4 had the lowest molecular weight due to the high polymerization temperature necessary to synthesize this sample.

2.3.5 Morphology of iPP-xGnP Nanocomposites

Microscopy was used to evaluate the dispersion quality of iPP-xGnP composites prepared by both melt compounding (MC-) and *in-situ* polymerization (IS-). Transmission optical microscopy was used to directly image xGnP particles in iPP, shown in Figure 2.7. Composites appear to be comprised of discrete, dark xGnP agglomerates dispersed within a continuous transparent iPP matrix. All composites possess numerous agglomerates of apparent diameter 1-10 μm ; however the IS- sample series contained several large ($>10 \mu\text{m}$) agglomerates. Surprisingly, the melt compounded sample series demonstrated superior dispersion compared to the *in-situ* synthesized sample series. The large xGnP agglomerates seen in the IS- sample series are attributed to the unfavorable nanoparticle-polymerization solvent interaction, as well as insufficient mixing conditions during polymerization. It has been shown that the poor interaction energy between graphitic nanoparticles and toluene promotes rapid nanoparticle flocculation and sedimentation.⁴⁵ Apparently, the mechanical mixing during *in-situ* polymerization does not sufficiently promote dispersive mixing of xGnP nanoparticles. The presence of large agglomerates in the IS- sample series suggests that the mixing flow field during *in-situ* polymerization cannot overcome the sedimentation kinetics, likely because it is difficult to achieve sufficient mixing shear stresses in a low viscosity polymerization solvent. In contrast, melt compounding in molten iPP promoted more fragmentation due to the comparatively higher mixing viscosity, and therefore shear stresses.

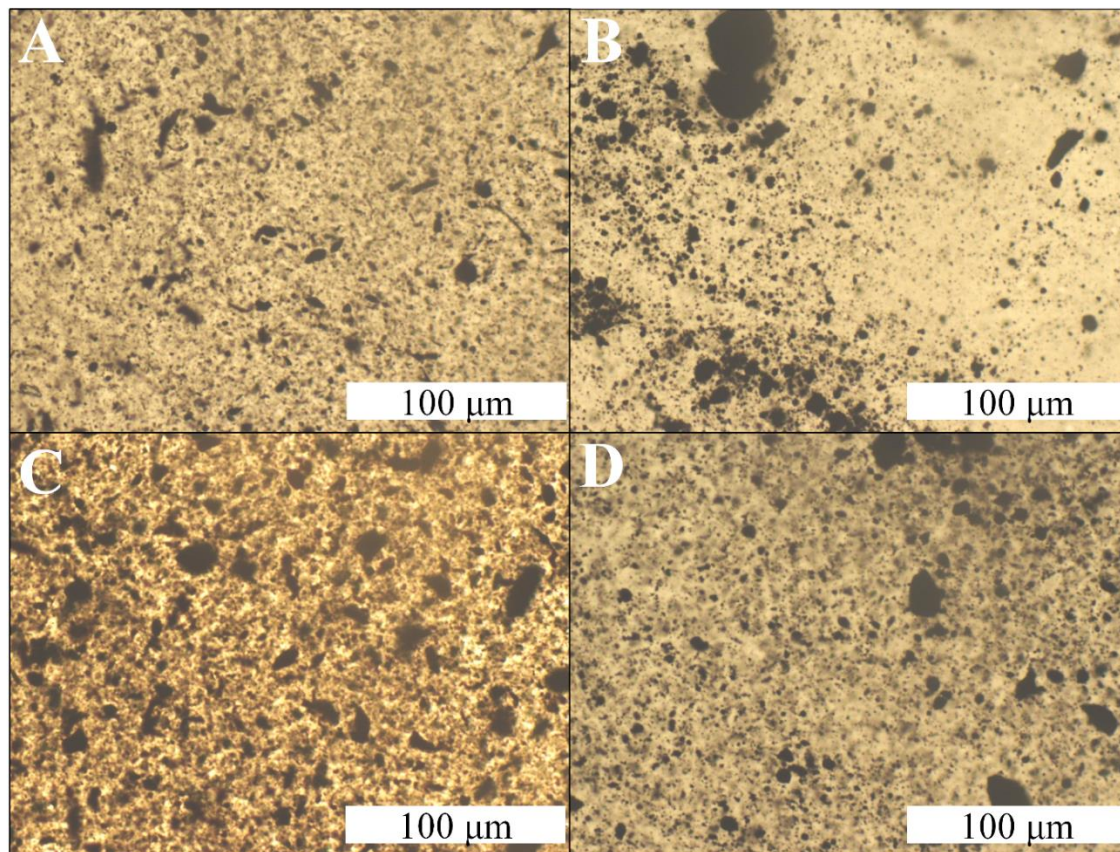


Figure 2.7: Transmission optical microscopy images of 50 μm thick iPP-xGnP films. (A) MC-2 (B) IS-2 (C) MC-4 (D) IS-4.

Transmission Electron Microscopy was used to evaluate the nano-scale dispersion of iPP-xGnP PNCs. Figure 2.8 shows several ~ 20 nm diameter spherical particles present in IS-0, which are ascribed to residual Al_2O_3 particles from the hydrolysis of MAO during workup. Samples IS-2 and IS-4 required roughly 3x the MAO concentration as IS-0, so residual Al_2O_3 particles are especially anticipated in IS-2 and IS-4. However, TEM images of IS-2 and IS-4 did not appear to contain spherical Al_2O_3 artifacts from MAO hydrolysis. One possible explanation could be that the MAO hydrolysis byproducts are confined to the xGnP surface, which would agree with the assertions from ^{27}Al NMR spectroscopy in section 2.3.2. Samples IS-2, IS-4, and MC-2 show large xGnP agglomerates of 1-5 microns in diameter, each comprised of several xGnP platelets. The results suggest that the

nanoscale dispersion of xGnP is poor for all samples. Also, there does not appear to be any exfoliated xGnP particles into graphene sheets, which is sometimes observed in other iPP-GNP PNC preparation methods.⁴⁶

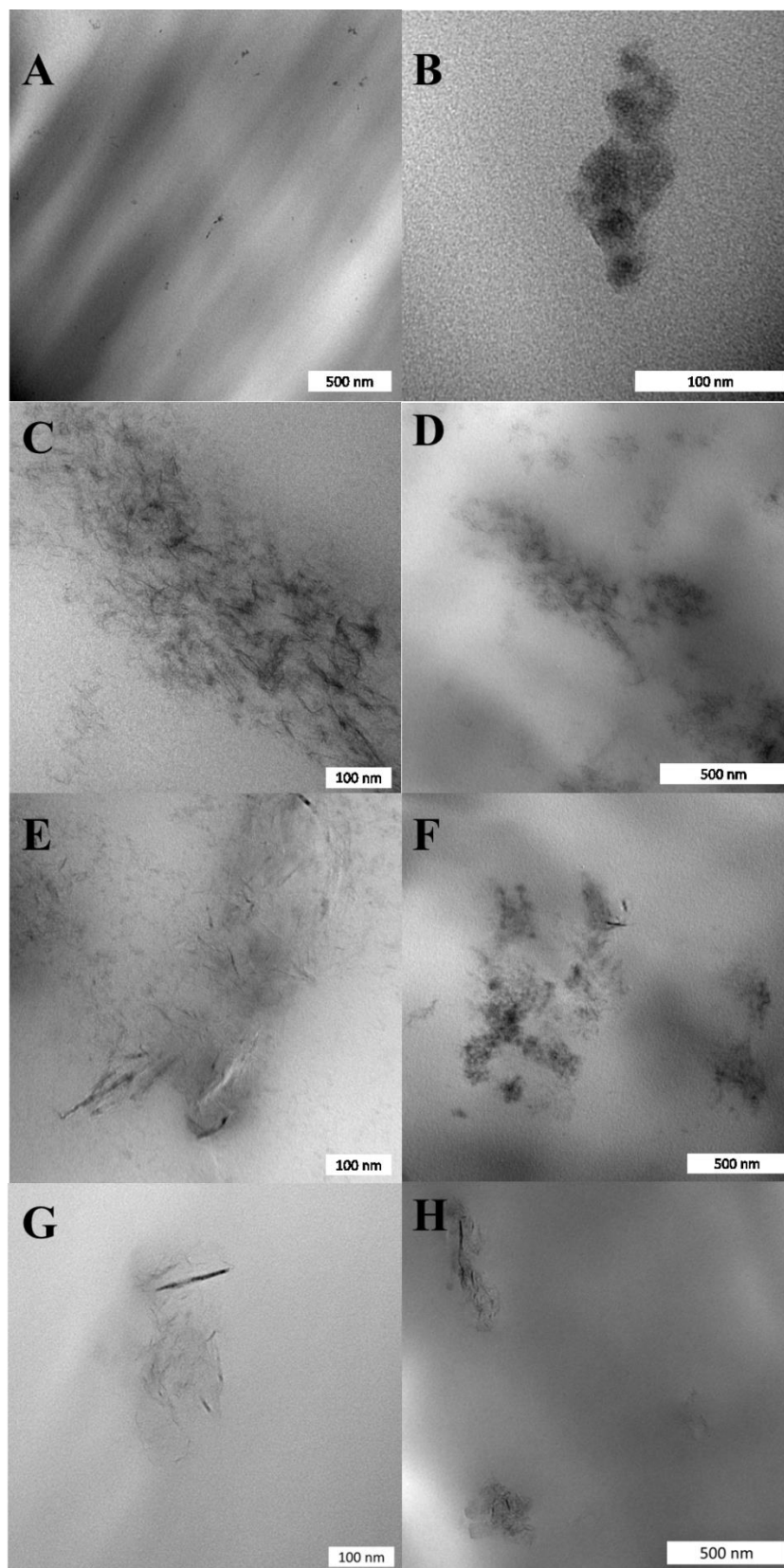


Figure 2.8: Transmission Electron Microscopy images of iPP-xGnP sections. (A,B) IS-0 (C,D) IS-2 (E,F) IS-4 (G,H) MC-2.

Thermal calorimetry was used as an indirect method to characterize the xGnP dispersion in iPP. Exfoliated graphene nanoplatelets are known nucleating agents for iPP.⁴⁷ For iPP-xGnP nanocomposites, the crystallization temperature (T_c) is expected to increase with increasing xGnP loading and/or improved dispersion. Indeed, thermal calorimetry shows increased T_c with increasing xGnP loading for all samples (Table 2.2, Figure 2.9-a). The increase relative to neat resin is greater for the MC- sample series (+21.1 K) compared to the IS- sample series (+12.4 K), suggesting melt compounding produces better xGnP dispersions than *in-situ* synthesis. However, the crystallization temperature may also be affected by the tendency of metallocene iPP to have a higher concentration of regio- and stereo-defects, as well as a higher regio- to stereo-defect ratio in the chain microstructure, compared to Ziegler-Natta iPP.^{25,48-50}

Thermal calorimetry also reveals information about other morphological features such as crystal volume fraction and lamellar thickness. Both the IS- and MC- sample series demonstrated increasing melting point (T_m) and crystal volume fraction (X_c) with increasing xGnP concentration (Table 2.2, Figure 2.9-b). However, the melting points of the IS- samples are less than those of the MC-samples, which is again attributed to the differences between metallocene iPP and Ziegler-Natta iPP chain microstructures.

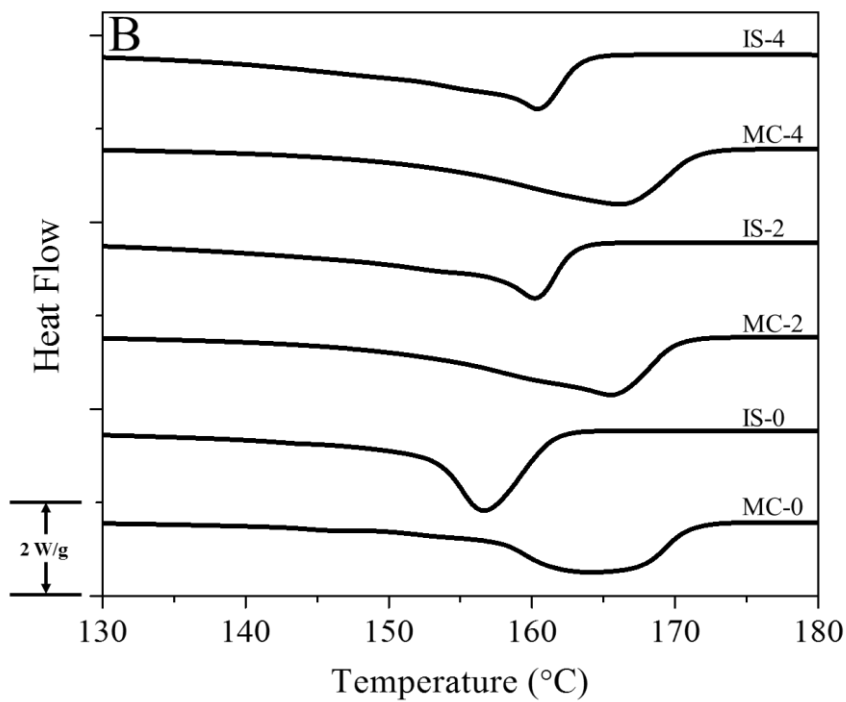
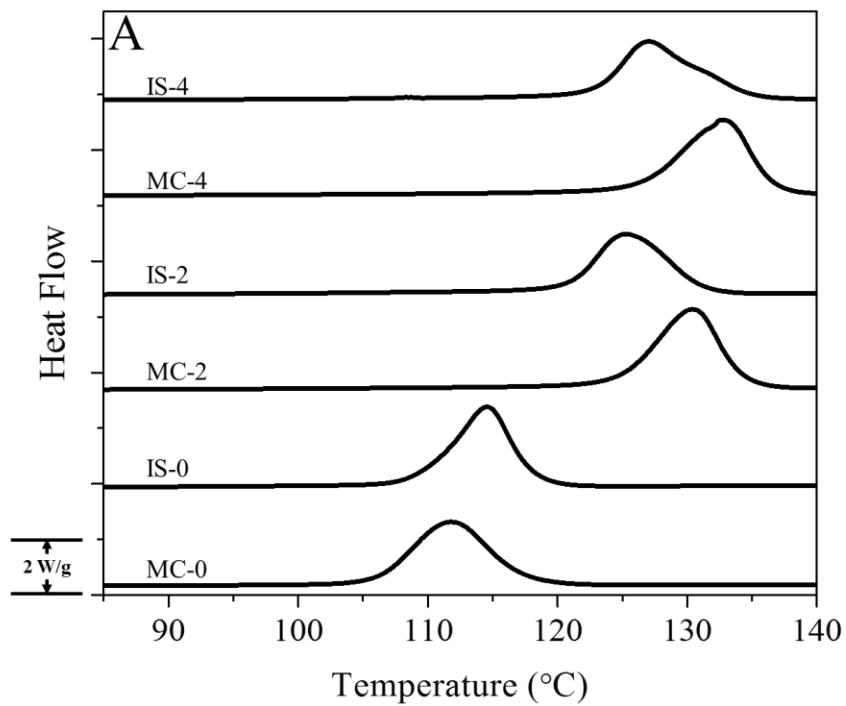


Figure 2.9: Differential Scanning Calorimetry of IS- and MC-samples. (A) cooling and (B) heating curves.

2.3.6 Mechanical Characterization

Monotonic tensile tests were performed to ascertain the effect of xGnP loading and preparation method on the linear and non-linear mechanical properties of iPP-xGnP nanocomposites. The results in Figure 2.10 show that both the IS- and MC- sample series showed modest increases in Young's modulus and yield stress with increasing xGnP loading, a common observation in nanographite reinforced PNCs.² The origin of reinforcement is difficult to precisely determine, however for PNCs it is thought to be due to a combination of factors. Nucleating agents like xGnP will impart an increase in modulus by changing the iPP crystal morphology and augmenting the crystal volume fraction. Moreover, the interfacial interaction between xGnP and the iPP matrix may affect the segmental mobility of iPP chains, contributing to reinforcement.⁵¹ Also, both the IS- and MC- sample series showed decreased ductility with increasing xGnP loading. The decrease in ductility relative to neat resin is attributed to the structural flaws created by nanoparticle agglomerates.^{52,53} Optical microscopy reveals the presence of large (~10 μm) xGnP agglomerates that could potentially serve as structural flaws and facilitate crack formation and propagation.

The IS- sample series demonstrates increased ductility compared to the MC- sample series, which is ascribed to the differences in chain microstructure of metallocene iPP and Ziegler-Natta iPP, specifically the concentration and type of regio- and stereo-defects.²⁵ Sample IS-2 demonstrated the most ductility and the largest elongation at break, likely due to its comparatively high molecular weight. The results suggest that both molecular weight and chain microstructure influence ductility, even in the presence of structural flaws. Table

2.2 and Figure 2.10 illustrate the effect of xGnP preparation method loading on the mechanical properties of iPP-xGnP PNCs.

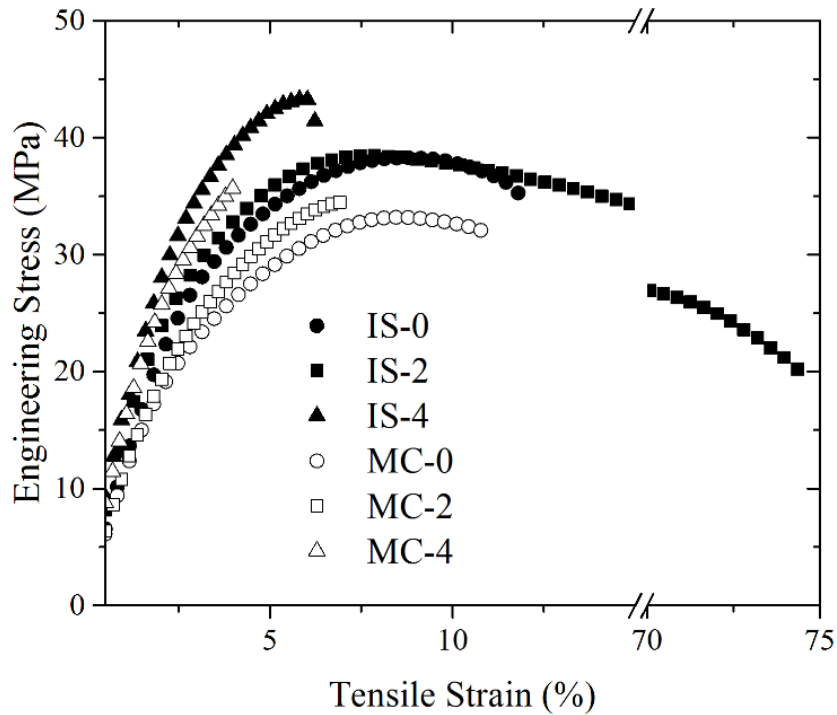


Figure 2.10: Tensile properties of iPP-xGnP nanocomposites

Another material property influenced by the non-linear mechanical properties is the fracture toughness. In the present study, the effect of xGnP nanoreinforcement on the toughness of iPP-xGnP nanocomposites was determined by plane strain fracture toughness tests in the single edge notched 3-point bend (SENB) configuration found in ASTM D5045. The results in Table 2.2 show that samples with xGnP reinforcement generally showed decreased critical strain energy release rate (G_{IC}) relative to the neat resin. The decrease in toughness is attributed to large ($>5 \mu\text{m}$) xGnP agglomerates, which are expected to decrease fracture toughness by creating flaws in the iPP matrix. However, IS-2 showed improved fracture toughness relative to the neat resin. This is likely due to the

comparatively high molecular weight of this sample. The melt compounded samples showed the largest decrease in fracture toughness (~90% decrease) relative to MC-0, while the *in-situ* synthesized composites maintained more toughness (~60% decrease) relative to IS-0. Furthermore, the IS- sample series demonstrated significantly improved fracture toughness compared to the MC- sample series, which is again attributed to the differences in chain microstructure of metallocene iPP and Ziegler-Natta iPP. Both the monotonic tensile results and fracture toughness results suggest that molecular weight, chain microstructure and xGnP loading affect the non-linear mechanical properties of iPP-xGnP nanocomposites (Table 2.2).

2.4 Conclusions

Nanocomposites of Exfoliated Graphene Nanoplatelets (xGnP-c-750) and isotactic polypropylene (iPP) are prepared via *in-situ* metallocene polymerization and compared to analogous composites of similar molecular weight prepared by melt compounding. *In-situ* polymerization of propylene was accomplished within a within a toluene solution dispersion of xGnP nanoparticles pretreated with excess Methylaluminoxane (MAO). Melt compounding was accomplished by combining commercial Ziegler-Natta iPP and xGnP and mixing in a conventional batch mixer. The *in-situ* polymerization requires excess MAO to prevent xGnP from poisoning the metallocene catalyst. Investigations by ^{27}Al NMR suggested that MAO reacts with xGnP and becomes immobilized to the xGnP surface. Dispersion analysis by optical and transmission electron microscopy shows the melt compounding technique produces nanocomposites with finer xGnP dispersions than the *in-situ* polymerization technique. All composites demonstrate improved mechanical modulus relative to neat iPP. However, the *in-situ* prepared composites demonstrate

superior non-linear mechanical properties such as ductility and toughness, likely due to the differences in chain microstructure of metallocene-iPP and commercial Ziegler-Natta-iPP.

2.5 Notes

Portions of this work were previously published by the author.⁵⁴

2.6 References

1. R. A. Vaia and H. D. Wagner: 'Framework for nanocomposites', *Mater. Today*, 2004, **7**, 32–37.
2. J. Jancar, J. F. Douglas, F. W. Starr, S. K. Kumar, P. Cassagnau, A. J. Lesser, S. S. Sternstein and M. J. Buehler: 'Current issues in research on structure–property relationships in polymer nanocomposites', *Polymer*, 2010, **51**, 3321–3343.
3. S. K. Kumar, N. Jouault, B. Benicewicz and T. Neely: 'Nanocomposites with Polymer Grafted Nanoparticles', *Macromolecules*, 2013, **46**, 3199–3214.
4. M. Modesti, A. Lorenzetti, D. Bon and S. Besco: 'Thermal behaviour of compatibilised polypropylene nanocomposite: Effect of processing conditions', *Polym. Degrad. Stab.*, 2006, **91**, 672–680.
5. V. Vladimirov, C. Betchev, A. Vassiliou, G. Papageorgiou and D. Bikiaris: 'Dynamic mechanical and morphological studies of isotactic polypropylene/fumed silica nanocomposites with enhanced gas barrier properties', *Compos. Sci. Technol.*, 2006, **66**, 2935–2944.
6. F. Bauer, H.-J. Gläsel, U. Decker, H. Ernst, A. Freyer, E. Hartmann, V. Sauerland and R. Mehnert: 'Trialkoxysilane grafting onto nanoparticles for the preparation of clear coat polyacrylate systems with excellent scratch performance', *Prog. Org. Coatings*, 2003, **47**, 147–153.
7. E. Tang, G. Cheng and X. Ma: 'Preparation of nano-ZnO/PMMA composite particles via grafting of the copolymer onto the surface of zinc oxide nanoparticles', *Powder Technol.*, 2006, **161**, 209–214.
8. C. Ligoure and L. Leibler: 'Thermodynamics and kinetics of grafting end-functionalized polymers to an interface', *J. Phys.*, 1990, **51**, 1313–1328.
9. L. S. Schadler, S. K. Kumar, B. C. Benicewicz, S. L. Lewis and S. E. Harton: 'Designed Interfaces in Polymer Nanocomposites: A Fundamental Viewpoint', *MRS Bull.*, 2011, **32**, 335–340.

10. C. Li and B. C. Benicewicz: 'Synthesis of Well-Defined Polymer Brushes Grafted onto Silica Nanoparticles via Surface Reversible Addition–Fragmentation Chain Transfer Polymerization', *Macromolecules*, 2005, **38**, 5929–5936.
11. C. Li, J. Han, C. Y. Ryu and B. C. Benicewicz: 'A Versatile Method To Prepare RAFT Agent Anchored Substrates and the Preparation of PMMA Grafted Nanoparticles', *Macromolecules*, 2006, **39**, 3175–3183.
12. X. Huang and M. J. Wirth: 'Surface-Initiated Radical Polymerization on Porous Silica', *Anal. Chem.*, 1997, **69**, 4577–4580.
13. J. Gao, J. Li, B. C. Benicewicz, S. Zhao, H. Hillborg and L. S. Schadler: 'The Mechanical Properties of Epoxy Composites Filled with Rubbery Copolymer Grafted SiO₂', *Polymers (Basel)*, 2012, **4**, 187–210.
14. P. Steurer, R. Wissert, R. Thomann and R. Mülhaupt: 'Functionalized Graphenes and Thermoplastic Nanocomposites Based upon Expanded Graphite Oxide.', *Macromol. Rapid Commun.*, 2009, **30**, 316–27.
15. W. Kaminsky, A. Funck and C. Klinke: 'In-situ Polymerization of Olefins on Nanoparticles or Fibers by Metallocene Catalysts', *Top. Catal.*, 2008, **48**, 84–90.
16. P. Dubois, M. Alexandre, F. Hindryckx and R. Jérôme: 'Polyolefin-Based Composites by Polymerization-Filling Technique', *J. Macromol. Sci. Part C Polym. Rev.*, 1998, **38**, 511–565.
17. M. Alexandre, E. Martin, P. Dubois, M. Garcia-Marti and R. Jérôme: 'Use of metallocenes in the polymerization-filling technique with production of polyolefin-based composites', *Macromol. Rapid Commun.*, 2000, **21**, 931–936.
18. M. Stürzel, F. Kempe, Y. Thomann, S. Mark, M. Enders and R. Mülhaupt: 'Novel Graphene UHMWPE Nanocomposites Prepared by Polymerization Filling Using Single-Site Catalysts Supported on Functionalized Graphene Nanosheet Dispersions', *Macromolecules*, 2012, **45**, 6878–6887.
19. C. Park, Z. Ounaies, K. A. Watson, R. E. Crooks, J. Smith, S. E. Lowther, J. W. Connell, E. J. Siochi, J. S. Harrison and T. L. S. Clair: 'Dispersion of single wall carbon nanotubes by in situ polymerization under sonication', *Chem. Phys. Lett.*, 2002, **364**, 303–308.
20. L. Resconi, L. Cavallo, A. Fait and F. Piemontesi: 'Selectivity in Propene Polymerization with Metallocene Catalysts', *Chem. Rev.*, 2000, **100**, 1253–1346.

21. J. A. Ewen: 'Mechanisms of stereochemical control in propylene polymerizations with soluble Group 4B metallocene/methylalumoxane catalysts', *J. Am. Chem. Soc.*, 1984, **106**, 6355–6364.
22. V. Busico, R. Cipullo, G. Talarico, A. L. Segre and L. Caporaso: 'High-Field ^{13}C NMR Characterization of Ethene-1- ^{13}C /Propene Copolymers Prepared with C_2 -Symmetric ansa-Metallocene Catalysts: A Deeper Insight into the Regio- and Stereoselectivity of Syndiotactic Propene Polymerization', *Macromolecules*, 1998, **31**, 8720–8724.
23. T. Tsutsui, A. Mizuno and N. Kashiwa: 'The microstructure of propylene homo- and copolymers obtained with a $\text{Cp}2\text{ZrCl}_2$ and methylaluminoxane catalyst system', *Polymer*, 1989, **30**, 428–431.
24. L. Resconi, I. Camurati and O. Sudmeijer: 'Chain transfer reactions in propylene polymerization with zirconocene catalysts', *Top. Catal.*, n.d., **7**, 145–163.
25. C. De Rosa and F. Auriemma: 'Single site metallorganic polymerization catalysis as a method to probe the properties of polyolefins', *Polym. Chem.*, 2011, **2**, 2155.
26. C. De Rosa, F. Auriemma, R. Di Girolamo and O. R. de Ballesteros: 'Crystallization of the mesomorphic form and control of the molecular structure for tailoring the mechanical properties of isotactic polypropylene', *J. Polym. Sci. Part B Polym. Phys.*, 2014, n/a–n/a.
27. J. R. Severn, J. C. Chadwick, R. Duchateau and N. Friederichs: "Bound but not gagged"--immobilizing single-site alpha-olefin polymerization catalysts.', *Chem. Rev.*, 2005, **105**, 4073–147.
28. D. E. Babushkin, N. V. Semikolenova, V. N. Panchenko, A. P. Sobolev, V. A. Zakharov and E. P. Talsi: 'Multinuclear NMR investigation of methylaluminoxane', *Macromol. Chem. Phys.*, 1997, **198**, 3845–3854.
29. W. Spaleck, F. Kueber, A. Winter, J. Rohrmann, B. Bachmann, M. Antberg, V. Dolle and E. F. Paulus: 'The Influence of Aromatic Substituents on the Polymerization Behavior of Bridged Zirconocene Catalysts', *Organometallics*, 1994, **13**, 954–963.
30. U. Stehling, J. Diebold, R. Kirsten, W. Roell, H. H. Brintzinger, S. Juengling, R. Muelhaupt and F. Langhauser: 'ansa-Zirconocene Polymerization Catalysts with Anelated Ring Ligands - Effects on Catalytic Activity and Polymer Chain Length', *Organometallics*, 1994, **13**, 964–970.
31. L. Cavallo and G. Guerra: 'A Density Functional and Molecular Mechanics Study Of β -Hydrogen Transfer in Homogeneous Ziegler–Natta Catalysis', *Macromolecules*, 1996, **29**, 2729–2737.

32. M. A. Milani, D. González, R. Quijada, N. R. S. Basso, M. L. Cerrada, D. S. Azambuja and G. B. Galland: 'Polypropylene/graphene nanosheet nanocomposites by in situ polymerization: Synthesis, characterization and fundamental properties', *Compos. Sci. Technol.*, 2013, **84**, 1–7.
33. M. A. Milani, R. Quijada, N. R. S. Basso, A. P. Graebin and G. B. Galland: 'Influence of the graphite type on the synthesis of polypropylene/graphene nanocomposites', *J. Polym. Sci. Part A Polym. Chem.*, 2012, **50**, 3598–3605.
34. F. de C. Fim, J. M. Guterres, N. R. S. Basso and G. B. Galland: 'Polyethylene/graphite nanocomposites obtained by in situ polymerization', *J. Polym. Sci. Part A Polym. Chem.*, 2010, **48**, 692–698.
35. S. V. Polschikov, P. M. Nedorezova, A. N. Klyamkina, A. A. Kovalchuk, A. M. Aladyshev, A. N. Shchegolikhin, V. G. Shevchenko and V. E. Muradyan: 'Composite materials of graphene nanoplatelets and polypropylene, prepared by in situ polymerization', *J. Appl. Polym. Sci.*, 2013, **127**, 904–911.
36. V. G. Shevchenko, S. V. Polschikov, P. M. Nedorezova, A. N. Klyamkina, A. N. Shchegolikhin, A. M. Aladyshev and V. E. Muradyan: 'In situ polymerized poly(propylene)/graphene nanoplatelets nanocomposites: Dielectric and microwave properties', *Polymer*, 2012, **53**, 5330–5335.
37. L. T. Drzal and H. Fukushima: 'Expanded graphite and products produced therefrom', US7550529, published 2013.
38. S. Scheel, A. Rosehr, A. Poepfel and G. A. Luinstra: 'Polyolefin Composite Synthesis: From Small Scale to kg Material', *Macromol. Symp.*, 2013, **333**, 227–232.
39. G. S. Constable, R. A. Gonzalez-Ruiz, R. M. Kasi and E. B. Coughlin: 'Gas Manifold for Olefin Polymerization and a Convenient Reactor Design for the Parallel Screening of Catalysts', *Macromolecules*, 2002, **35**, 9613–9616.
40. B. Wunderlich: 'Macromolecular Physics', 1980, New York, NY, Academic Press.
41. R. Bansal: 'Active carbon', 1988, New York, NY, M. Dekker.
42. H. He, T. Riedl, A. Lerf and J. Klinowski: 'Solid-State NMR Studies of the Structure of Graphite Oxide', *J. Phys. Chem.*, 1996, **100**, 19954–19958.
43. W. Zheng and S.-C. Wong: 'Electrical conductivity and dielectric properties of PMMA/expanded graphite composites', *Compos. Sci. Technol.*, 2003, **63**, 225–235.

44. H. Kim, A. A. Abdala and C. W. Macosko: 'Graphene/Polymer Nanocomposites', *Macromolecules*, 2010, **43**, 6515–6530.
45. M. Grujicic, G. Cao and W. N. Roy: 'Atomistic simulations of the solubilization of single-walled carbon nanotubes in toluene', *J. Mater. Sci.*, 2004, **39**, 2315–2325.
46. K. Wakabayashi, P. J. Brunner, J. Masuda, S. A. Hewlett and J. M. Torkelson: 'Polypropylene-graphite nanocomposites made by solid-state shear pulverization: Effects of significantly exfoliated, unmodified graphite content on physical, mechanical and electrical properties', *Polymer*, 2010, **51**, 5525–5531.
47. K. Kalaitzidou, H. Fukushima, P. Askeland and L. T. Drzal: 'The nucleating effect of exfoliated graphite nanoplatelets and their influence on the crystal structure and electrical conductivity of polypropylene nanocomposites', *J. Mater. Sci.*, 2007, **43**, 2895–2907.
48. J. J. Janimak, S. Z. D. Cheng, A. Zhang and E. T. Hsieh: 'Isotacticity effect on crystallization and melting in polypropylene fractions: 3. Overall crystallization and melting behaviour', *Polymer*, 1992, **33**, 728–735.
49. S. Z. D. Cheng, J. J. Janimak, A. Zhang and E. T. Hsieh: 'Isotacticity effect on crystallization and melting in polypropylene fractions: 1. Crystalline structures and thermodynamic property changes', *Polymer*, 1991, **32**, 648–655.
50. J. M. Gómez-Elvira, P. Tiemblo, M. Elvira, L. Matisova-Rychla and J. Rychly: 'Relaxations and thermal stability of low molecular weight predominantly isotactic metallocene and Ziegler–Natta polypropylene', *Polym. Degrad. Stab.*, 2004, **85**, 873–882.
51. H. E. Miltner, G. Van Assche, A. Pozsgay, B. Pukánszky and B. Van Mele: 'Restricted chain segment mobility in poly(amide) 6/clay nanocomposites evidenced by quasi-isothermal crystallization', *Polymer*, 2006, **47**, 826–835.
52. B. Li and W.-H. Zhong: 'Review on polymer/graphite nanoplatelet nanocomposites', *J. Mater. Sci.*, 2011, **46**, 5595–5614.
53. K. Kalaitzidou, H. Fukushima and L. T. Drzal: 'A new compounding method for exfoliated graphite–polypropylene nanocomposites with enhanced flexural properties and lower percolation threshold', *Compos. Sci. Technol.*, 2007, **67**, 2045–2051.
54. B. M. Cromer, S. Scheel, G. A. Luinstra, E. B. Coughlin and A. J. Lesser: 'In-situ polymerization of isotactic polypropylene-nanographite nanocomposites', *Polymer*, 2015, **80**, 275–281.

CHAPTER 3

MELT-MASTICATION PROCESSING OF SEMICRYSTALLINE

POLYOLEFINS

Herein, a new polymer processing method called Melt-Mastication (MM) is presented as a means to fabricate semicrystalline thermoplastic polymer articles with improved thermal and physical properties. Melt-Mastication is a low temperature mixing technique that subjects a semicrystalline polymer melt to a chaotic flow field under a three step temperature profile. The processing temperatures of MM are well below the conventional melt processing temperatures of semicrystalline polymers ($<T_m$), promoting flow induced crystallization (FIC) in the melt. Accordingly, MM produces crystal morphologies advantageous to and distinct from that of conventional polymer processing techniques.

The unique crystal morphology generated by MM is characterized through several techniques and the results are discussed with respect to the observed thermal and physical properties. In an isotactic polypropylene (iPP) system, MM increases the lamellar crystal thickness and crystal volume fraction by 51% and 37%, respectively, compared to conventionally melt-crystallized iPP prepared by compression molding. The observed increases in melting point (10.3 K) and yield strength (50%) are attributed to the increased lamellar crystal thickness. Also observed is a ~55% improvement in the elastic modulus, which is ascribed to the increased iPP crystal volume fraction. Finally, MM produces iPP with a unique hierarchical organization of lamellar crystals, distinct from the conventional spherulitic organization inherent to conventionally processed semicrystalline polymers.

The property enhancements generated through MM will potentially enable semicrystalline polymers to penetrate new markets and improve performance within existing applications.

3.1 Introduction

3.1.1 Processing of Semicrystalline Thermoplastic Polymers

Semicrystalline thermoplastic polymers are an important class of materials critical to numerous industries today, as discussed in chapter 1. One of the reasons these materials are useful is because they may be melted and formed into almost any desired shape through various polymer processing techniques. Polymer processing is any number of techniques or combination of techniques used to convert raw polymeric materials into products. Today, the prevailing semicrystalline polymer processing techniques include calendaring and coating, die forming, mold coating, molding and casting, and stretch shaping. All of these techniques possess the same elementary steps: 1) Melting, 2) flowing, 3) forming, and finally 4) cooling. Melting is the first and most critical step of polymer processing, and involves heating a solid semicrystalline polymer to a temperature above T_m . When a semicrystalline polymer reaches T_m , it undergoes a first-order phase transition where the crystalline regions of the sample become molten. Upon melting, a semicrystalline thermoplastic polymer is able to flow, and its flow behavior is well described by the basic principles of transport phenomena and polymer melt rheology. After the polymer is melted, flow may be accomplished by subjecting the molten polymer to pumping or pressurization. At the same time, the polymer is usually mixed in order to obtain uniform melt temperature and composition during processing. Finally, the flowing molten polymer is subjected to a shaping or forming process. The goal of the shaping process is to

manipulate the polymer melt into a desired size, shape and appearance. Finally, the polymer is allowed to cool well below T_m , and regain the crystal structure.¹

In addition to forming and shaping, polymer processing also influences the crystal morphology, and therefore the thermal and physical properties of semicrystalline polymer articles. As discussed in chapter 1, the properties of semicrystalline polymers such as the melting point, mechanical modulus, and gas diffusivity are directly related to the crystal morphology, including the crystal unit cell, lamellar crystal thickness, orientation, and crystal volume fraction. For example, lamellar crystal thickness (d_c) above a critical size will increase the melting point (T_m).² Also, mechanical modulus and gas diffusivity are related to crystal volume fraction (X_c).³

Accordingly, polymer processing is an opportunity to impart useful thermal and physical properties to semicrystalline thermoplastic polymers through altering the crystal morphology. Through judicious selection of polymer processing parameters, it is possible to alter the crystal morphology at several levels of organizational hierarchy and impart desired thermal or mechanical properties. For example, it is possible to change the crystal structure of isotactic polypropylene (iPP) from the standard alpha form to the less ordered mesomorphic form through significantly accelerating the rate of cooling (100-200 K/min) from the melt.⁴ Mesomorphic-iPP generally demonstrates superior ductility and poorer mechanical modulus, compared to α -iPP.^{5,6} Also, moderate rates of cooling (10-100 K/min) have been shown to produce α -iPP with reduced lamellar crystal thickness (d_c) and reduced crystal volume fraction (X_c), which generally imparts optical clarity to iPP articles.³⁷ In contrast, thermal annealing near the melting temperature of iPP has been shown to increase X_c and d_c , leading to property improvements in yield strength (σ_y), elastic

modulus (E'), and T_m .^{7,8} Alternatively, nucleating agents may be used during polymer processing to control X_c and/or the spherulite size in order to improve optical clarity or toughness. Nucleating agents are polymer additives that facilitate heterogeneous nucleation of semicrystalline polymer crystals. One example class of nucleating agents are acetals of sorbitol and xylitol, which have been successfully commercialized.^{9,10} Generally, nucleating agent are compounded with the molten semicrystalline thermoplastic polymer prior to forming and cooling. However, Torkelson *et al.* showed solid state processing techniques can enhance the effect of nucleating agents by improving their dispersion.¹¹ Furthermore, specialty nucleating agents like calcium salts of suberic acid and pimelic acid promote the β -crystal structure in iPP, which demonstrates superior toughness.¹²

3.1.2 Flow Induced Crystallization of Semicrystalline Polymer Melts

The previously discussed polymer processing strategies are useful for preparing isotropic semicrystalline polymer articles, that is, semicrystalline polymer articles that possess unoriented crystal morphologies, and therefore uniform mechanical properties in all orientations. However, specific polymer processing conditions can create structural and mechanical anisotropy through a phenomenon termed flow induced crystallization (FIC). Flow induced crystallization is accomplished by applying a sufficiently strong flow to a semicrystalline polymer melt within a specific temperature threshold, typically around or below T_m . Under these conditions, some polymer chains in the melt will assume a transient, extended conformation which will nucleate crystallization at a much faster rate compared to quiescent thermal annealing.^{8,13} The FIC process effectively decreases the degree of supercooling during crystallization, which increases X_c and d_{ac} , and therefore T_m , compared

to quiescently crystallized semicrystalline polymers. Additionally, the extended chain nucleating sites also facilitate the development of anisotropic crystal morphologies. For iPP treated with uniaxial FIC, the crystal morphology is comprised of crystal lamella that align perpendicular to the flow direction.¹⁴ Melt flows with sufficiently high deviatoric strains and strain rates, such as elongational or large shear deformations, have been shown to promote a “shish-kebab” iPP crystal morphology, where iPP crystal lamella (kebabs) are arranged around a highly oriented fibrillar bundle (shish) comprised of flow-aligned iPP chains.¹⁴⁻¹⁹ The aligned crystal morphology produced by FIC creates anisotropic mechanical properties.

Currently, FIC is commercially exploited for fabrication of anisotropic semicrystalline polymer articles with enhanced mechanical properties. For example, the mechanical modulus in the draw direction of iPP fibers can be 15-20 times greater than the modulus of isotropic iPP.⁸ Similarly, FIC processes can be used to create uniaxially or biaxially oriented iPP films with enhanced mechanical modulus in one or two directions. In a typical FIC process, the semicrystalline polymer resin is melted and extruded through a sheet die or strand die to produce films or fibers, respectively. Next, the film or fiber extrudate is subjected to FIC through simultaneous cooling and extensional flow (uniaxial or biaxial), which is usually accomplished with calendaring upon temperature controlled rollers, or film blowing.^{13,20} Film casting is an example FIC process used to create uniaxially oriented films, through extruding molten polymer through a sheet die and collecting it on revolving temperature controlled rollers. This process produces oriented crystal morphologies, and the extent of orientation may be controlled by the cooling rate

(set-point temperature of the rollers), mass flow rate (angular velocity of the rollers), and total film extension.²¹⁻²⁴

However, current FIC processes are limited to producing thin semicrystalline polymer articles, such as films and fibers. It is not possible to use FIC to fabricate bulk semicrystalline polymer articles, defined as polymer articles with substantial thicknesses in all dimensions, with currently established polymer processing techniques. For example, it is currently impractical to fabricate iPP sheets with thicknesses greater than ~2 mm with FIC techniques like film casting or blow molding. Sheet geometries greater than ~2 mm in thickness are highly difficult to produce with FIC because this process requires large elongational flow fields, which necessary requires contraction in one or two dimensions. Granted, some polymer processing techniques involving high melt flow rates, like injection molding, can induce molecular orientation in bulk polymer articles. However, this kind of orientation is unpredictable and generally undesirable because it produces problematic properties such as anisotropic mold shrinkage and non-uniform crystal morphology through the thickness of the molded article.

3.1.3 Processing Techniques for “Self-Reinforced” Semicrystalline Polymer Articles

Recently, considerable research effort and commercial interest has been invested in designing polymer processing methods to apply the benefits of FIC, specifically molecular orientation and mechanical reinforcement, to bulk polymer articles. Accordingly, new polymer processing techniques have been developed to produce so called “Self-Reinforced Polymeric Materials” (SFPM), or polymer composites where the same polymer forms both the reinforcing and matrix phases. Such materials are advantageous because they possess

the benefits of reinforced polymer composites with the recyclability of homogeneous polymers.

For example, Ward *et al.* developed a hot compaction process to produce bulk semicrystalline polymer articles with biaxial reinforcement.^{25,26} Hot compaction is a process whereby several woven fibers or tapes comprised of highly oriented semicrystalline polymers, particularly iPP, are stacked and then compressed between heated plates. Next, the stacks are subjected to narrow temperature window in order to partially melt the outer layers of the fibers or tapes. Finally, the stack is compressed such that the molten outer layers fill the volume between adjacent fibers/tapes, and the unmelted interior of the fibers/tapes maintains its orientation and provides mechanical reinforcement. The orientation of the films can be manipulated to impart uniaxial or biaxial reinforcement. Barany *et al.* expanded on hot compaction by interposing unoriented “matrix giving” films between the woven fibers in order to improve the adhesion between the matrix and reinforcement phases.^{27,28} Hot compaction was successfully demonstrated for a variety of semicrystalline thermoplastic polymers, including Polyethylene Terephthalate (PET), Polyethylene (PE), Polyamide 6,6 (PA), and iPP.^{29–33} Furthermore, thermoforming may be combined with hot compaction to produce complex parts. Hot compaction of iPP woven fabrics was successfully commercialized under trade name Curv ®. However, hot compaction is limited by a costly and cumbersome batch assembly process. It also requires a very narrow ($2 \pm ^\circ\text{C}$) temperature range, and thicker polymer articles require longer molding times to achieve uniform melting.

Another technique designed to import the benefits of FIC to bulk polymeric materials is low-temperature extrusion molding.³⁴ This process is similar to conventional

extrusion of molten semicrystalline polymers through a convergent die, except the extrusion zones near the die exit and the die itself are cooled below T_m . According, low-temperature extrusion molding generates significant increases to the melt viscosity and requires high extrusion pressures. The extensional flow near the die generates FIC, and also highly oriented molecular structures in the extrusion direction. Ehernstein *et al.* performed low-temperature extrusion molding of HDPE articles.³⁴ The resulting materials demonstrated increased mechanical strength in the extrusion direction, as well as increased T_m relative to the neat resin. Low-temperature extrusion molding was demonstrated with both HDPE and iPP systems, however this process has not been commercialized because it produces fibrillar structures with poor transverse mechanical properties, and also because the extrusion rate is relatively low in order to sufficiently cool the melt near the die exit.^{21,35,36} Closely related to low-temperature extrusion molding is solid phase extrusion. In this technique, an unoriented solid polymer preform is forced through a convergent extruder die. Examples of solid phase extrusion processes include ram extrusion, hydrostatic extrusion, and die drawing. Each technique involves mechanically deforming a solid polymer preform in a uniaxial fashion, which creates highly oriented fibrillar structures in the direction of draw. Ram extrusion and hydrostatic extrusion involve pushing the preform into the convergent die, while die-drawing involves pulling the preform through the die. Currently, die-drawing is the most advantageous form of this technique because it enables control over the draw ratio. Die drawing has been successfully applied to several semicrystalline thermoplastic polymers, including PE, iPP, PET, PTFE, and PVDF.³⁷⁻⁴⁰ However, die drawing is only useful for forming polymer articles with uniform cross section and uniaxial orientation; complex shapes and other types of

orientation are not possible. Furthermore, solid phase extrusion requires extremely high flow stresses at the exit of the die, which decreases the production rate and involves costly equipment maintenance. Finally the highly oriented fibrillar structures produce poor transverse mechanical properties.

Finally, injection molding technology has been developed to generate FIC inside a mold cavity through a process called a shear-controlled orientation in injection molding (SCORIM).^{41,42} In this technique, a molten semicrystalline polymer is injected into a mold cavity with suitably arranged pistons. Shortly after injection, the cooling melt is subjected to oscillation of the pistons in the mold cavity, which generates high shear stresses. The oscillation of the pistons creates FIC in the cooling melt, and therefore highly oriented structures and mechanical reinforcement in the final polymer article. SCORIM is advantageous because it produces bulk semicrystalline polymer articles with relatively uniform morphology through the thickness of the article.^{43,44} Also, the arrangement of pistons may be modified to produce either uniaxial or biaxial reinforcement.⁴⁵ However, SCORIM is limited to relatively small parts, as larger parts with substantial material volume will require more complex mold/piston designs. To date, this process has not been commercialized due to the prohibitively high costs associated with the required equipment. It follows that there is a need for a commercially feasible technique to produce bulk polyolefin articles with enhanced crystal morphology and improved thermal and mechanical properties through FIC.

3.2 Materials and Methods

3.2.1 Materials

Pellet form isotactic polypropylene (iPP) grade PP9999SS was kindly supplied by ExxonMobil and used as received ($T_m = 165$ °C, $T_c = 111$ °C). Grade PP9999SS is byproduct produced when an iPP polymerization reactor is transitioning between commercial iPP grades. Grade PP9999SS is not a commercial grade and cannot be found on the ExxonMobil website. It appears to be a low viscosity grade of iPP, similar to an injection molding grade. Linear low density polyethylene (LLDPE, Dowlex 2553) and high density polyethylene (HDPE-1: DMDA-8904-NT7, MFI 4.4; HDPE-2 DMDA-8007-NT7, MFI 8.3) were generously provided by Dow Plastics. Irganox 1010 and Irgafos 168 antioxidant process stabilizers were purchased from Ciba, Inc. and used as received

3.2.2 Processing with FIC via Melt-Mastication

Melt-Mastication is a low-temperature polymer processing technique that subjects a molten semicrystalline polymer to a chaotic flow field under specified cooling conditions, initiating FIC and irregular crystal morphologies. The present chapter focuses on MM of iPP. MM of other semicrystalline thermoplastic polymers will be discussed in chapter 4.2.2. The three step temperature profile is schematically represented in Figure 3.1. Each successive step is represented by a different color. In the first step, the polyolefin and oxidative stabilizers (0.05 wt% Irganox 1010 + 0.05 wt% Irgafos 168) are fully melted and compounded at 200 °C (above T_m of iPP) for 5 min at 70 revolutions per minute (RPM). The melt is then reduced at -3 K/min under continuous mixing and forced-air cooling to the mastication temperature (T_M), 153 °C, which is between T_m and T_c of iPP.

The final step includes isothermal mixing at T_M for 5 minutes. After MM, samples were immediately removed from the mixer and subjected to a forming process, which will be discussed in sections 3.2.3 and 3.2.4. For reference, control iPP samples were also prepared by conventional melt processing (CMP), or processing above the resin T_m . Here, the polyolefin and oxidative stabilizers (0.05 wt% Irganox 1010 + 0.05 wt% Irgafos 168) are melt compounded at 200 °C (above T_m of iPP) for 25 min at 70 revolutions per minute (RPM). It should be noted that samples prepared by MM and CMP have identical composition. All samples were prepared using a Brabender Intelli-Torque Plasti-Corder Torque Rheometer (C.W. Brabender, unit located at the University of Massachusetts Lowell) with 50 mL capacity. This instrument is equipped with sensors that enable continuous acquisition of the mixing torque, stock temperature, and screw speed, and representative data from these sensors is shown in Figure 3.3.

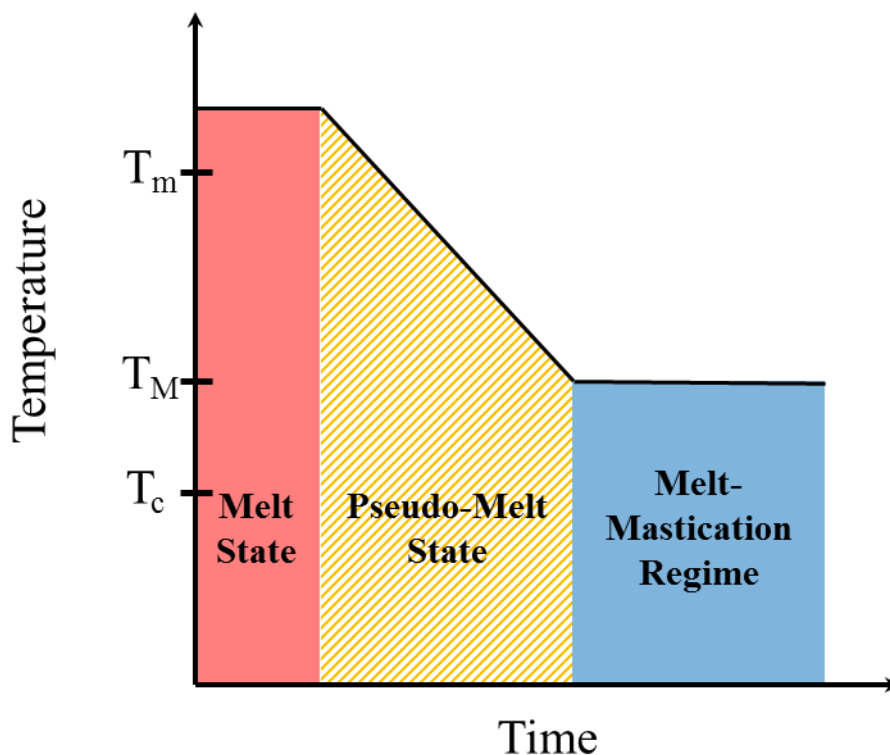


Figure 3.1: Three step temperature profile for Melt-Mastication. Step 1 (red): Melting and mixing. Step 2 (yellow): Cooling to T_M . Step 3 (blue) isothermal mixing at T_M .

3.2.3 Compression Molding of iPP

Isotactic polypropylene samples prepared by either MM or CMP were treated with compression molding in order to form the materials into mechanical testing specimens. Compression molding is accomplished by placing iPP samples between aluminum compression plates and within a mold of desired thickness. Next, the plate stack is placed into a press preheated to 200 °C, and then compressed with 5,000 lb load for 15 min. Finally, the plate stack is transferred to a 15 °C water-cooled press, which rapidly quenches iPP to room temperature within 3 minutes. It should be noted that compression molding fully melts iPP, and therefore “erases” the crystal structure produced by the preparation technique.

3.2.4 Forging of Melt-Masticated iPP

In order to prepare mechanical testing specimens and preserve the crystal structure produced by MM, a forging process was developed. Immediately after MM, iPP is a partially crystallized, highly viscous “pseudo melt” that may be formed with compressive forces at 140 °C, well below the resin T_m . Both uniaxial and biaxial forging techniques were developed for MM. Biaxial forging involves compressing the MM “pseudo melt” between preheated aluminum plates and compressing, shown in Figure 3.2A. Uniaxial forging is performed through compressing the “pseudo melt” into a channel die, shown in Figure 3.2B. In order to control sample thickness, 0.5 inch gauge blocks were placed between opposing compression plates. Forging was performed within 10 seconds after MM.

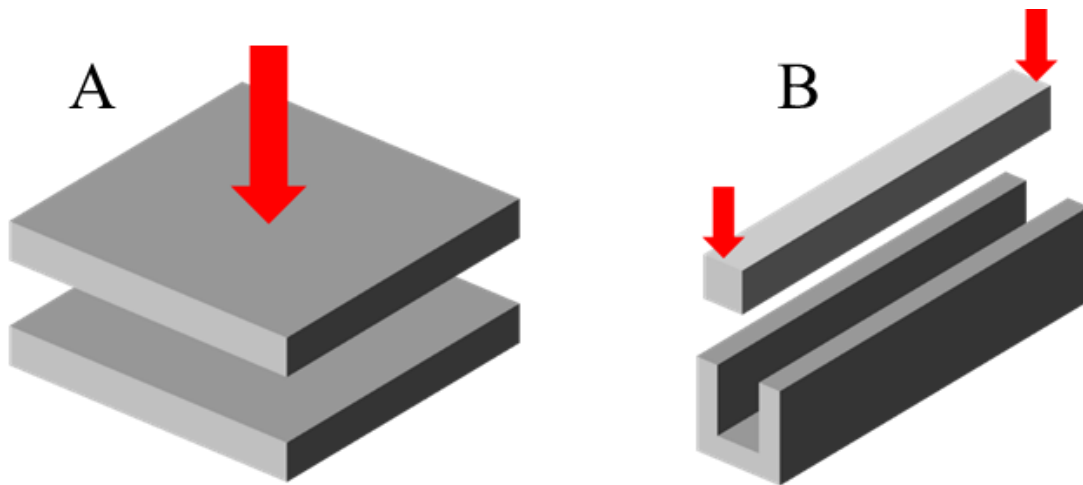


Figure 3.2: Schematic of forging tools for forming Melt-Masticated iPP “pseudo-melts” into testing specimens. A) Compression plates for forging biaxially oriented specimens. B) Channel die for forging uniaxially oriented specimens.

3.2.5 Morphological Characterization

SEM was conducted on a FEI Magellan 400 XHR-SEM. Sample surfaces were prepared by immersion in liquid nitrogen followed by fracture. Samples were then

chemically etched with established protocols (3 wt% KMnO_4 , 64.7 wt% H_2SO_4 , and 32.3 wt% H_3PO_4) in order to expose crystalline morphologies.⁴⁶⁻⁴⁸ Extreme caution was exercised when performing chemical etching, including use of PPE (lab coat, substantial goggles, gloves, butyl rubber gloves, and face shield) and other safety measures (performed within fume hood with blast shield using long tweezers). Samples were etched for 24 or 48 hours, followed by copious washing with distilled water. Before imaging, samples were treated with gold sputtering to produce a ~5 nm thick gold layer.

Transmission optical microscopy was conducted on an Olympus optical microscope with DP71 digital camera, operating in transmission mode and 500x magnification (10x eyepiece and 50x objective). Sample sections were prepared with glass knife microtomy in order to ensure consistent section thicknesses. Thin sections (10 μm x 2 mm x 2 mm) were prepared at room temperature on a Reichert-Jung FC4 Ultramicrotome.

Atomic force microscopy was achieved with a Digital Instruments Dimension 3100 AFM instrument fitted with a Silicon-Nitride tip. All images were acquired in tapping mode, and results from the tapping phase data are reported. Isotactic polypropylene sample surfaces were first cut from samples prepared by either CMP or MM. The MM samples were simply removed from the mixer without applying compression molding, nor forging. Initial cutting was performed with a diamond saw in order to produce samples suitable for microtomy. Finally, smooth samples surfaces were prepared through glass knife microtomy. In contrast to transmission optical microscopy studies, the AFM studies analyzed the sample block surface from which sections were cut.

Small-angle X-ray scattering was performed on a Ganesha 300 XL SAXS system operating in SAXS mode. The system includes a Genix Xenocs Cu K α X-ray source, producing an X-ray wavelength of 1.54 Angstroms, and the sample to detector distance was 1.041 m. Samples were mounted on a Linkam heater stage which was used to control the temperature during analysis. All samples were equilibrated at the testing temperature for 15 minutes before analysis. The lamellar long period (d_{ac}) was calculated from the scattering maximum q , with $d_{ac} = 2\pi/q$. The lamellar crystal thickness (d_c) was calculated assuming a two phase model according to: $d_c = d_{ac} * \chi_c$ where χ_c is derived from thermal calorimetry.

X-ray diffraction was achieved with a PANalytical X'PertPert Material Research Diffractometer, equipped with a $\frac{1}{2}^\circ$ divergence slit and 10 mm mask on the incident beam optics, and a 2.3° radian Soller slit on the diffracted beam optics. The scan range was $2\theta = 10 - 70^\circ$, and the scan step size was 0.016° . Isotactic Polypropylene samples were prepared by milling within a SpexCertiprep Freezer Mill. The powder samples were analyzed with a Cu K α X-ray source, producing an X-ray wavelength of 1.54 Angstroms.

High Temperature Gel Permeation Chromatography was performed to ascertain the extent of degradation incurred by iPP during processing. The molecular weight of iPP was characterized with high temperature gel permeation chromatography (HTGPC) on a Polymer Labs PL-220 GPC. Samples were dissolved and analyzed in 1,2,4-trichlorobenzene at 145°C against polystyrene standards. The absolute molecular weights were calculated via the Mark–Houwink equation using previously reported K and a values for iPP.⁴⁹

3.2.6 Thermal and Mechanical Characterization

Thermal and mechanical properties were measured using a Differential Scanning Calorimeter (TA Instruments-DSC Q200) and a Dynamic Mechanical Analyzer (TA Instruments-DMA Q800). Calorimetry was performed from 20 to 215 °C for iPP with a constant ramp rate of 10 K/min. Two heating and cooling cycles were used. Crystallization and melting analyses were performed on the first cooling and the second heating ramps, respectively. Additionally, samples were quiescently exposed to the thermal profile (section 3.2.2) of MM, but quiescently within the DSC. These samples are termed “Annealed.”

Samples for DMA (30 x 10 x 0.5 mm) were cut from 0.5 mm thick plaques and analyzed at a constant frequency of 10 Hz, oscillation amplitude 0.05% strain, and over a temperature range of 0 to 150 °C, ramp rate 3 °C/min. Unoriented Melt-Masticated samples were cut from MM-iPP pieces with a diamond saw. Biaxially oriented MM-iPP samples were prepared through biaxial forging after MM with 9 MPa forging stress. All DMA samples were performed in triplicate.

Tensile properties were characterized according to ASTM D 638. Compression molded specimens were milled from 3 mm thick plaques. Also, 3 mm thick samples prepared by MM were followed by uniaxial forging within a 0.5” wide channel die. Forging was performed with 9 MPa compressive stress, producing mildly anisotropic samples. Testing was performed at room temperature using an Instron 4466 testing machine at a crosshead speed of 2 mm/min and a preload force of 8 N. The strain was calculated from the crosshead displacement. The same setup was used to characterize the tensile stress relaxation behavior of iPP samples. Samples were strained to 1% or 3%

strain, and the resulting relaxation behavior is fitted to the Kohlrausch-Williams-Watts (KWW) or stretched exponential function.

Uniaxial compression tests were also performed on the same Instron 4466 testing machine. Cylindrical compression samples of dimensions 4.3 x 4.3 mm were milled with a guide hollow drill bit from 4.3 mm thick plaques. Samples prepared by Melt-Mastication and forging were prepared by uniaxial forging, followed by milling. Samples were lubricated on the top and bottom surfaces with soap water and PTFE tape in order to promote affine deformation during compression. Uniaxial compression tests were performed at a strain rate of 0.5 mm/mm/min.

Notched Izod impact tests were performed on an instrumented Izod impact tester, described in Appendix A.1. Rectangular samples were prepared according to ASTM D 256, and notching was performed according to ASTM D 256 Method D with a constant profile “V” notch knife. Notching was performed on an Instron CEAST manual notching machine. Notched samples were conditioned at a temperature between -30 C to 60 C for 1 hour before testing. Samples were removed from the conditioning chamber, secured into the Izod sample holder, and tested within 8 seconds. All samples were performed in triplicate.

3.3 Results and Discussion

Melt-Mastication (MM) is a new processing technique that uses flow induced crystallization (FIC) to create new morphologies and improved mechanical properties in bulk semicrystalline polymer articles. The present study focuses on MM of iPP because it was most amenable to forging after MM. Other semicrystalline polyolefins like HDPE and LLDPE could be processed with MM, however the HDPE and LLDPE pseudo melts were

intractable, and could not be forged into mechanical testing specimens. Melt-Mastication of other semicrystalline polymers like Nylon-6 polyamide solidified during MM and damaged the Brabender Plasti-corder. It is not clear why iPP performs better in MM compared to other semicrystalline thermoplastic polymers. However, there are intrinsic properties of semicrystalline polymers that are suspected to be important to MM, which are described in Table 3.1. First, the polymer must demonstrate FIC (most semicrystalline polymers do). Second, the polymer must have a large temperature separation between T_c and T_m . This is because $T_c < T_M < T_m$, therefore a larger temperature window enables more operating space for MM between solidification at T_c and complete melting at T_m . Finally the material must possess crystallinity less than ~55%. Highly crystalline materials like HDPE rapidly solidify during MM. Accordingly, the present study focused on iPP due to its large temperature separation between T_c and T_m and moderate crystallinity.

Table 3.1: Parameters of semicrystalline thermoplastic polymers relevant to MM.⁵⁰

Material	Melting Point, T_m (°C)	Non-isothermal	$T_c - T_m$	Crystal volume fraction, χ_c
		Crystallization Temperature by DSC, T_c (°C)		
iPP	165	111	54	0.45
HDPE	136	115	21	0.75
LLDPE	124	106	18	0.43
Polyamide (Nylon 6)	220	181	39	0.50

3.3.1 Optimizing Melt-Mastication Conditions for Isotactic Polypropylene

Melt-Mastication of iPP is accomplished over a three step temperature profile, illustrated in Figure 3.1. The purpose of the first step shown in Figure 3.1 is to uniformly melt iPP and compound it with antioxidant process stabilizers. During the first step, iPP appears to be a clear viscous polymer melt. In the second step, the material is cooled under

constant mixing using forced air. The fastest cooling rate obtainable with the equipment is -3 K/min. It is expected that faster cooling rates would be acceptable provided the temperature distribution remains uniform. The appearance of the melt gradually transitions from a clear polymer melt to opaque and white. In the third step, the material is no longer molten, but rather a white, highly viscous “pseudo melt” that behaves similarly to bread dough at room temperature. The pseudo-melt does not adhere to components of the mixing chamber in the same way molten iPP does. In fact, it is possible to open the mixing chamber and remove the entire iPP pseudo melt at once. The pseudo-melt may be removed from the mixer and deformed, however without mechanical perturbation it will solidify within 15 seconds. After solidification, the material must be re-melted in order to flow again.

In order to determine the optimal conditions for MM, several samples were prepared through varying the T_M and the mixing rate (RPM) and recording the mixing torque, shown in Figure 3.3. Figure 3.3A shows the temperature program of four conditions, each operating at 70 RPM. Each temperature program follows the three step profile of Figure 3.1, and includes a different T_M ranging from 153 to 200 °C. Temperatures lower than 153 °C resulted in severe degradation of iPP and/or damage to the Brabender Plasti-Corder. Figure 3.3B shows the torque generated during each temperature program in Figure 3.3A. At time $t < 500$ s, all samples are molten and in step 1 of the MM temperature protocol (Figure 3.1), therefore the torques are similar. For $t > 1000$ s, the sample temperatures reach T_M and initiate FIC. The mixing torque indicates the extent of FIC produced by each combination of conditions. The sample with $T_M = 153$ °C demonstrates the most FIC, and is therefore the optimal temperature program.

Next, the mixing rate at the optimal temperature program was varied from 70-140 RPM, and the results are shown in Figure 3.3C. Mixing rates below 70 RPM resulted in solidification of iPP and damage to the Brabender Plasti-Corder. Melt-Mastication at 100 RPM demonstrated lower mixing torque, indicating FIC was reduced. Finally, MM at 70 RPM and then increasing to 140 RPM at $t = 1500$ also reduces FIC. Accordingly the optimal conditions for MM are mixing rate are $T_M = 153$ °C and 70 RPM mixing rate. Henceforth, all samples labeled “MM-iPP” were processed at $T_M = 153$ °C and 70 RPM mixing rate.

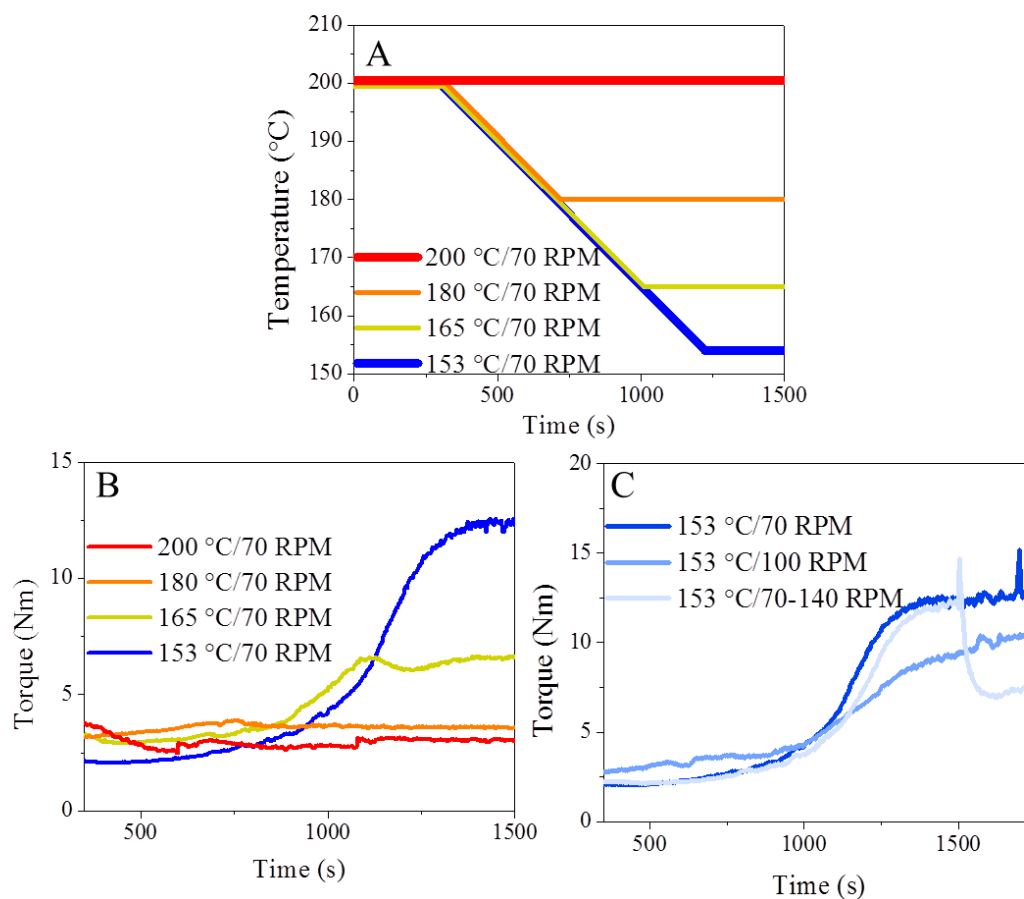


Figure 3.3: Temperature and torque vs time recorded by Brabender Plasti-Corder during optimization of Melt-Mastication processing parameters for iPP. A) Four different temperature profiles, each with different T_M . B) Torque vs. time resulting from the temperature profiles in A. C) Torque vs time from varying mixing rate.

3.3.2 Shaping of Melt-Masticated iPP

Isotactic Polypropylene prepared with MM can be formed into testing specimens by compression molding, milling techniques, or forging. Compression molding produces materials identical to those prepared by CMP. This is because compression molding fully melts iPP and “erases” the crystal morphology produced by MM. Samples may also be formed by milling pieces of iPP prepared with MM. After MM, iPP pieces are immediately removed from the Brabender Plasti-Corder and allowed to solidify. Then, samples are milled to any desired shape using a diamond saw or end mill. Milling is an ideal technique

to prepare unoriented MM samples. Finally, forging for mechanical testing specimens may be accomplished using crude molds illustrated in Figure 3.2. Two types of forging were developed to produce either uniaxial or biaxial orientation. Forging produces anisotropic materials, and the extent of anisotropy may be controlled through controlling the compressive stress imposed on the pseudo-melt. Materials forged with low compressive stresses (< 9 MPa) produce mildly anisotropic materials. Materials forged with higher compressive stress (< 90 MPa) demonstrate moderate anisotropy, demonstrated by SAXS in section 3.3.5.2. Forging with very high compressive stress (~ 900 MPa) produces highly oriented iPP, but destroys the crystal morphology, as evidenced by DSC. Forging occurs relatively rapidly, and solidified specimens are achieved with ~ 15 seconds forging. Forged samples did not change dimensions while cooling. Compared to compression molded iPP, MM-forged samples showed decreased mold shrinkage, illustrated Figure 3.4. Unlike compression molding of molten iPP, forging of the pseudo melt did not require a mold release agent, because the pseudo melt did not adhere to the forging mold. Accordingly, the flow behavior of the iPP pseudo melt during forging is quite similar to lubricated compression flow, as opposed to melt squeezing flow. Finally, a molded MM-iPP sample in Figure 3.5 shows a uniform, opaque appearance through the thickness of the material, in contrast to the sample prepared by compression molding.

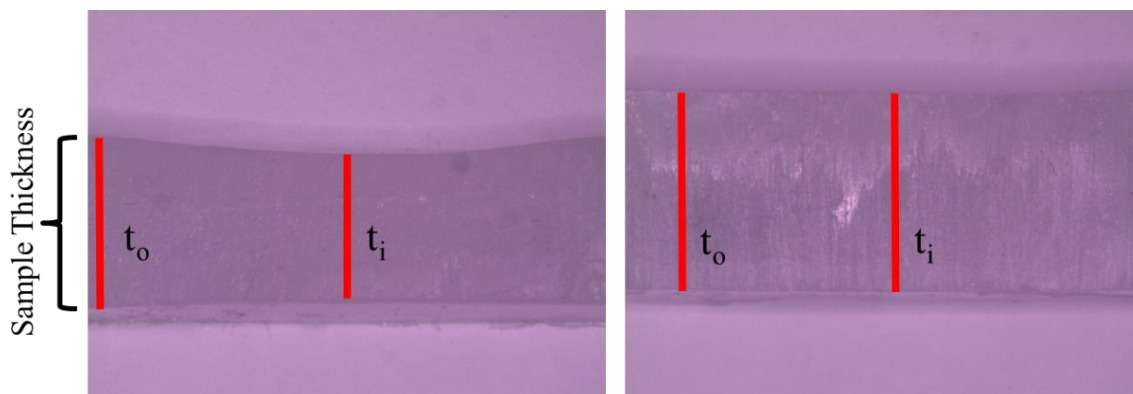


Figure 3.4: Mold shrinkage of compression molded (left) and MM (right) iPP.

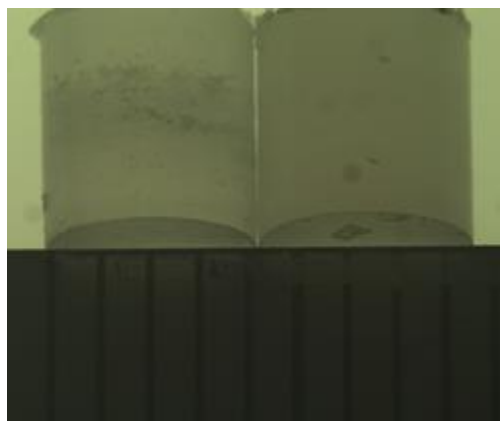


Figure 3.5: Physical appearance of iPP prepared by compression molding (left) and Melt-Mastication (right).

3.3.3 Degradation Analysis

Degradation of iPP is commonly observed during melt processing due to the high temperature conditions necessary to melt iPP, as well as the high shear stresses imposed on the flowing melt. For iPP, degradation is known to occur through a complex process, usually involving oxidation of a tertiary carbons in the iPP backbone, followed by β -scission.³ Oxygen is critical to the initiation and propagation of radicals in iPP, and the configuration of the Brabender Plasti-Corder exposes iPP to air during MM. Antioxidant process stabilizers such as hindered phenols are routinely compounded with iPP during melt processing in order to mitigate oxidative degradation pathways. The potential iPP degradation due to the high shear and compressive forces incurred by iPP during MM was

evaluated with HTGPC, and the results are summarized in Table 3.2. Without antioxidant process stabilizers (Irganox 1010 + Irgafos 168), the molecular weight of iPP treated with MM decreases relative to the virgin material, suggesting thermo-oxidative degradation occurred. However, iPP treated with process stabilizers shows the same molecular weight as the virgin material, indicating that chain scission was prevented. All samples in the present study were compounded with antioxidants.

Table 3.2: Degradation study of Melt-Masticated iPP

Sample	M_w (kg/mol)	\bar{D}
Virgin iPP	135	3.7
Melt-Masticated iPP	53	2.5
Masticated+Stabilizers	133	3.6

3.3.4 Thermal Calorimetry

Thermal Calorimetry was used to understand the impact of MM on the crystal morphology of semicrystalline polymers. High Density Polyethylene (HDPE), Linear Low Density Polyethylene (LLDPE), and iPP were analyzed with thermal calorimetry, and the results are summarized in Table 3.3. The conditions for MM of HDPE and LLDPE are listed in Table 4.1. Materials prepared by Melt-Mastication generally show an elevated crystal volume fraction χ_c and T_m compared to CMP samples. For comparison, sample “CMP_Annealing @ 154 °C” was annealed quiescently under temperature conditions identical to MM. It was found that annealing improved χ_c slightly, however MM-iPP still demonstrates the largest χ_c . The elevated T_m is ascribed to an increase in lamellar crystal thickness (d_c), which is described by the Gibbs-Thomson equation, discussed in section 1.2.2. It follows that thicker lamellar crystal require higher T_m . The elevated T_m is

commonly observed in semicrystalline polymer articles subjected to FIC, and is a result of the crystal nucleation imparted by oriented polymer structures. These oriented structures reduce the activation energy for crystal nucleation, causing crystallization to occur at a higher temperature than quiescent melt crystallization. Therefore, the results suggest that lamellar crystals formed during MM are thicker than crystals formed during quiescent melt nucleation (conventional melt processing).

Table 3.3: Summary of thermal calorimetry results of semicrystalline polymers prepared with MM. Processing parameters of each resin is discussed in section 4.2.2.

Polymer	Processing Method	T_m (°C)	X_c (%)
Isotactic Polypropylene (iPP)	Melt-Mastication	177.4	57
	Conventional Melt Processing	167.1	41.5
	CMP_Annealing @ 154 °C	167.1	48.7
Linear Low-Density Polyethylene (LLDPE)	Melt-Mastication	127.8	55.1
	Conventional Melt Processing	127.1	49.4
High Density Polyethylene #1	Melt-Mastication	138	72.3
	Conventional Melt Processing	134.8	63.9
High Density Polyethylene #2	Melt-Mastication	140.8	86.3
	Conventional Melt Processing	135.2	69.3

Interestingly, T_m of MM iPP increases by 10.3 K relative to neat iPP, which is significantly greater than the T_m of thermally annealed iPP.^{51,52} This is because FIC produces lamellar crystals that are thicker and therefore more thermally stable than can be obtained through annealing (equation 3.2). Additionally, the iPP crystal morphology produced by MM is surprisingly resilient. Figure 3.6A shows the melting behavior of iPP prepared by MM and conventional melt processing (CMP), and both curves show melting endotherms, followed by heating to 200 °C, which is 45 K above the melting temperature of iPP. It is therefore expected that the crystal morphology in both samples should be fully

molten, and the proceeding crystallization curves will be identical. However, Figure 3.6B shows that the non-isothermal crystallization temperature (T_c) of MM iPP is significantly higher (120.2 °C) than CMP iPP (111.8 °C). Apparently, a remnant of the crystal morphology in MM iPP was not fully melted and facilitated nucleation on the proceeding cooling cycle. In fact, it is necessary to heat MM iPP up to 215 °C in order to fully melt the material and recover a T_c similar to CMP iPP. The thermal resilience of MM iPP was exploited in a nucleation experiment shown in Figure 3.6B. Melt-Masticated iPP (10 wt%) was treated with cryogenic milling and compounded with iPP at 195 °C for 5 minutes. The resulting material was analyzed in thermal calorimetry and the thermal behavior showed a relatively high T_c (116.0 °C). Accordingly, MM iPP powder is a potentially useful commercial nucleating agent for iPP, not only because it is relatively inexpensive, but also because it cannot be spectroscopically identified.

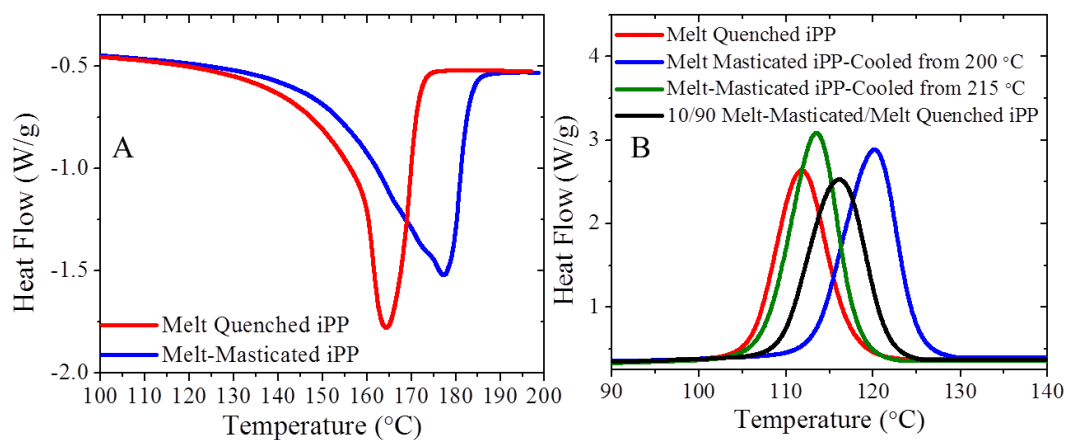


Figure 3.6: Thermal calorimetry of CMP and MM iPP, heating rate 10 K/min. A) Melting endotherms within the first heating curve, up to 200 °C. B) Non-isothermal crystallization exotherms within the first cooling curve.

High density polyethylene also demonstrates elevated T_m for similar reasons. For LLDPE, there is no discernable improvement to the melting temperature after MM, which

is attributed to chemical disorder in the chain which frustrates crystallization and prevents thick crystal lamella from forming. Further discussion of the melting behavior of iPP will occur in conjunction with discussion of SAXS results in section 3.3.5.2.

3.3.5 Morphological Structure

3.3.5.1 X-ray Diffraction

Powder diffraction studies were performed to understand aspects of the crystal structure promoted by MM. Samples were prepared by either compression molding or MM without forging, then cryogenically milled and analyzed by X-ray diffraction (XRD). The results are normalized to the peak intensity and shown in Figure 3.7.

The dominant and most stable iPP crystal type is the alpha crystal form. As discussed in section 3.1.1, most conventional processing methods produce α -iPP. The α -iPP form analyzed in XRD is characterized by peaks corresponding to crystallographic planes, specifically peaks at $2\theta = 14.0^\circ$, 16.95° , 18.5° , 21.2° and 21.85° corresponding to the (110), (040), (130), (111), and (041) crystallographic planes, respectively.⁵³ Indeed, the results confirm that the α -crystal form is the dominant form in both samples. Melt-Masticated-iPP demonstrates well defined crystal reflections, suggesting MM-iPP is highly crystalline. This result agrees well with the results from thermal calorimetry in 3.3.4. In contrast, the crystal reflections in compression molded iPP are poorly defined, and convoluted by broad intensities near $2\theta = 15.0^\circ$, and 22° .³ The broad intensities are characteristic of the mesomorphic phase, discussed in section 3.1.1. The rapid quenching step during compression molding likely promotes the formation of the mesomorphic phase.

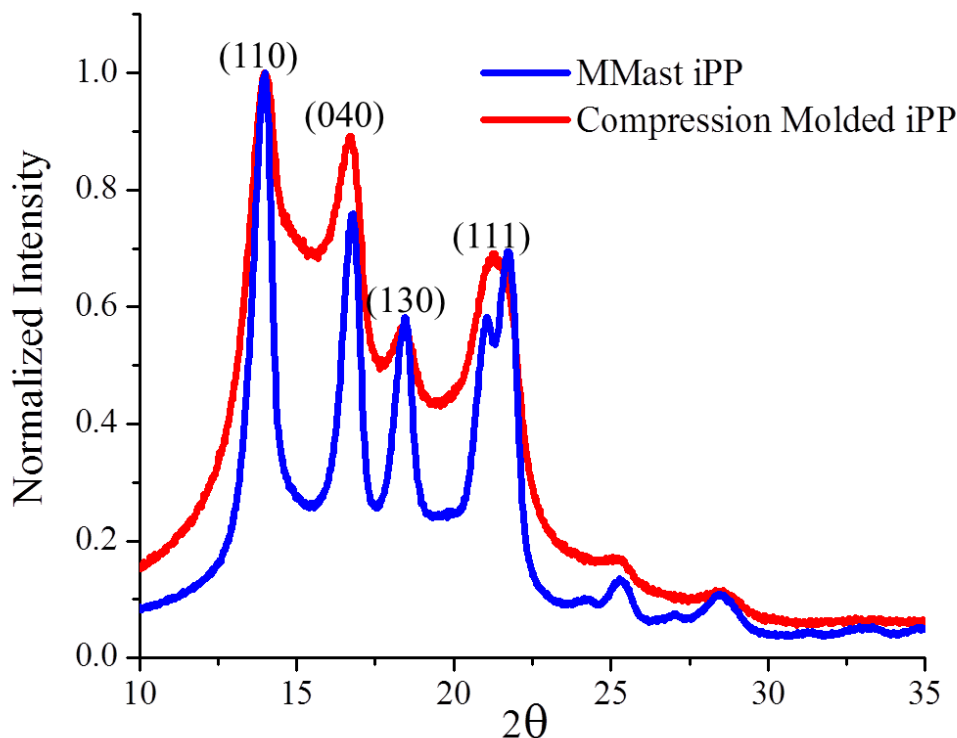


Figure 3.7: Powder diffraction profile of iPP prepared by MM or compression molding.

3.3.5.2 Small Angle X-Ray Scattering

As discussed in section 3.3.4, the high T_m of MM-iPP is ascribed to unusually thick lamellar crystals with high apparent thermal stability. However, thermal calorimetry is only an indirect measurement of d_c , and many other crystal behaviors that occur at elevated temperatures are not captured by thermal calorimetry.² Small angle X-ray scattering (SAXS) is a technique that directly evaluates electron contrast periodicities of structures with sizes commensurate with d_c . Accordingly SAXS was used in the present study to evaluate d_c of iPP prepared by MM, MM with uniaxial forging, or compression molding. Strictly speaking, SAXS of iPP determines the lamellar long period (d_{ac}), which is the electron contrast periodicity corresponding to the combined thickness of one average

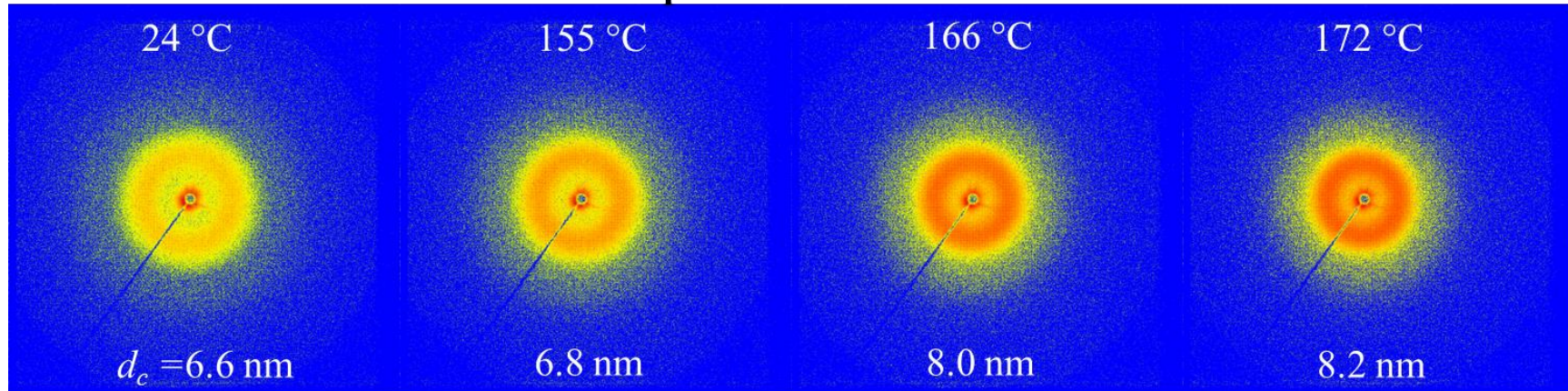
lamellar crystal and one average amorphous layer. It is possible to approximate d_c from d_{ac} by assuming iPP is comprised to a two phase structure with amorphous and crystalline regions, as discussed in 3.2.5. The two phase structure assumption is not entirely accurate, as the interfaces between amorphous and crystalline region are not sharp. The most accurate way to determine d_c is through a Fourier transform of the 1-D SAXS function to yield the electron density correlation function, however this is not possible for α -iPP because its cross-hatched morphology produces two populations of lamellar crystal thicknesses.

First, SAXS was used to evaluate d_c in both MM-iPP and compression molded iPP at temperatures near and above the iPP T_m . The 2D scattering profile and calculated d_c for each measurement are shown in Figure 3.8. The analysis yielded $d_c = 16.1$ nm for compression molded iPP and $d_c = 24.1$ nm for MM-iPP at room temperature. The scattering intensity of both samples appears to increase with increasing temperature, which is due to changes in the electron densities of the amorphous and crystalline regions during heating. Also, the d_c of compression molded iPP increases with increasing temperature, while d_c of MM-iPP remains constant with temperature.

The relationship between d_c and temperature for semicrystalline polymers is illustrated in Figure 3.9 and explained by Strobl.² The crystal structure of iPP subjected to heating is controlled by processes universal to all semicrystalline polymers, specifically melting and recrystallization. Each process may be represented as a functional relationship between temperature and d_c , illustrated in Figure 3.9. At a critical temperature T_x and critical lamellar crystal thickness $d_{c,x}$ the melting and recrystallization processes intersect. When subjected to heating, iPP with $d_c \leq d_{c,x}$ (Figure 3.9, point 1) will undergo continuous

melting/recrystallization along the recrystallization line up temperature T_x , (Figure 3.9, point 1'). Semicrystalline polymer articles prepared by processes involving quiescent melt crystallization and/or thermal annealing, such as compression molding, always produce $d_c \leq d_{c,x}$. In contrast, samples with $d_c > d_{c,x}$ will not undergo recrystallization (Figure 3.9, point 2). Instead these samples will simply melt when the temperature reaches the melting line at $T > T_x$ (Figure 3.9, point 2'). Semicrystalline polymer articles prepared by processes involving FIC, such as MM, can produce $d_c > d_{c,x}$. Accordingly, both the results from SAXS and thermal calorimetry show that MM produces unusually large d_c and high T_m , suggesting MM promotes FIC.

Compression Molded iPP



Melt-Masticated iPP

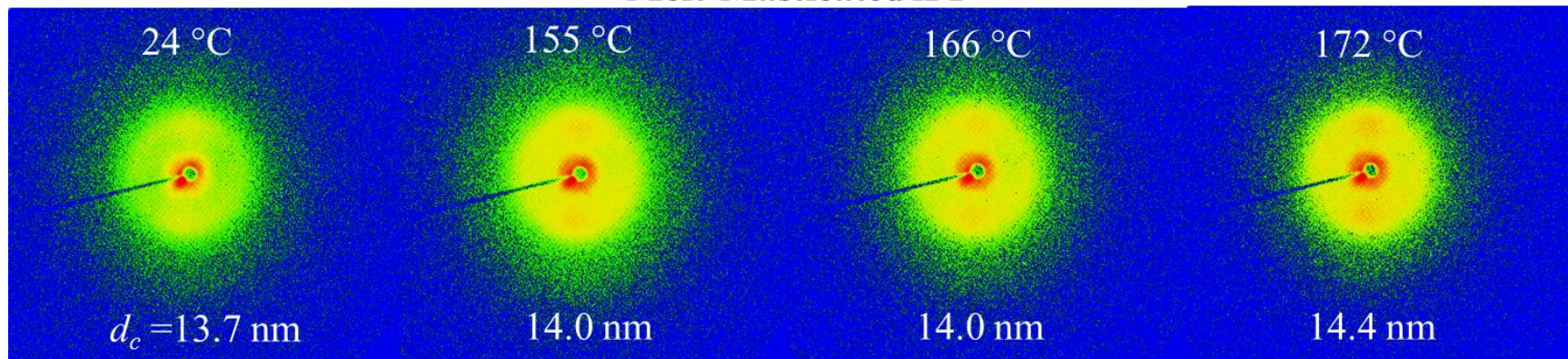


Figure 3.8: Two-dimensional SAXS scattering profile of iPP prepared by MM or compression molding, at various temperatures. The calculated lamellar crystal thickness (d_c) is listed on each image.

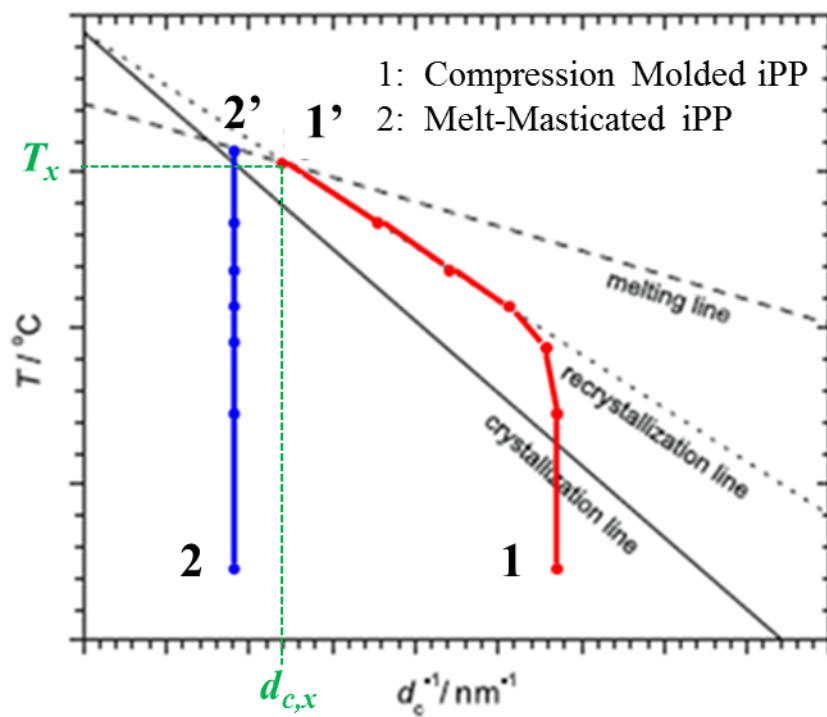
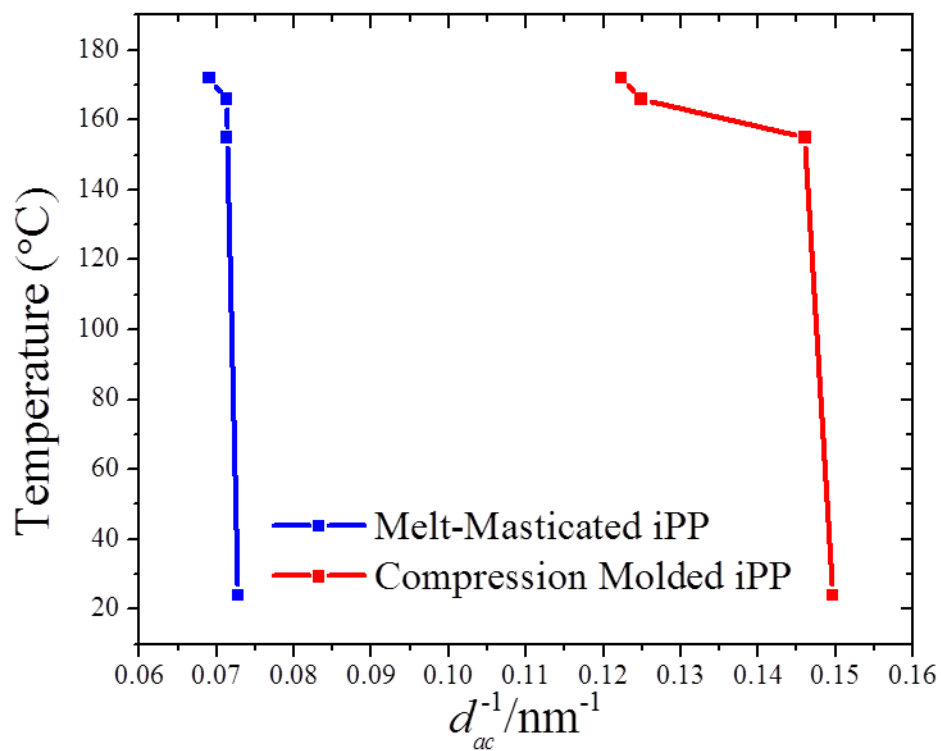
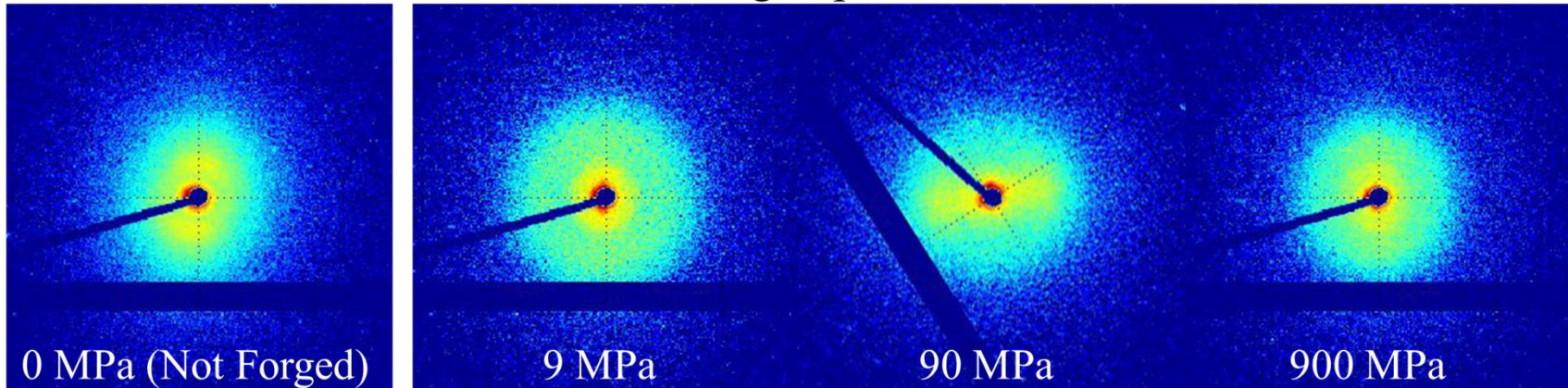


Figure 3.9: General schematic of melting, recrystallization, and crystallization processes of Polypropylene, adapted from Strobl.²

Many semicrystalline polymer processing techniques involving FIC produce oriented crystal structures, as discussed in 3.1.2. It is anticipated that the forging process proceeding MM will orient the partially crystallized structure in the pseudo-melt, ultimately producing an oriented iPP article. Accordingly, MM iPP samples were prepared with uniaxial forging with various forging stresses and the resulting orientation was evaluated with SAXS. Samples were analyzed both perpendicular and parallel to the forging flow direction, with respect to the beam direction, and the results are shown in Figure 3.10. The 2-D scattering profiles do not appear oriented when analyzed parallel to the flow direction. However the 2-D scattering profiles from perpendicular analysis show significant orientation. Furthermore, the magnitude of orientation increases with increasing forging stress. The un-forged samples did not demonstrate orientation, nor did the sample prepared by compression molding. The results show that the extent of orientation imposed by forging may be controlled by controlling the forging stress. It follows that forging may be a useful process to control the extent of mechanical anisotropy in semicrystalline polymer articles.

Imaged parallel to uniaxial flow



Imaged perpendicular to uniaxial flow

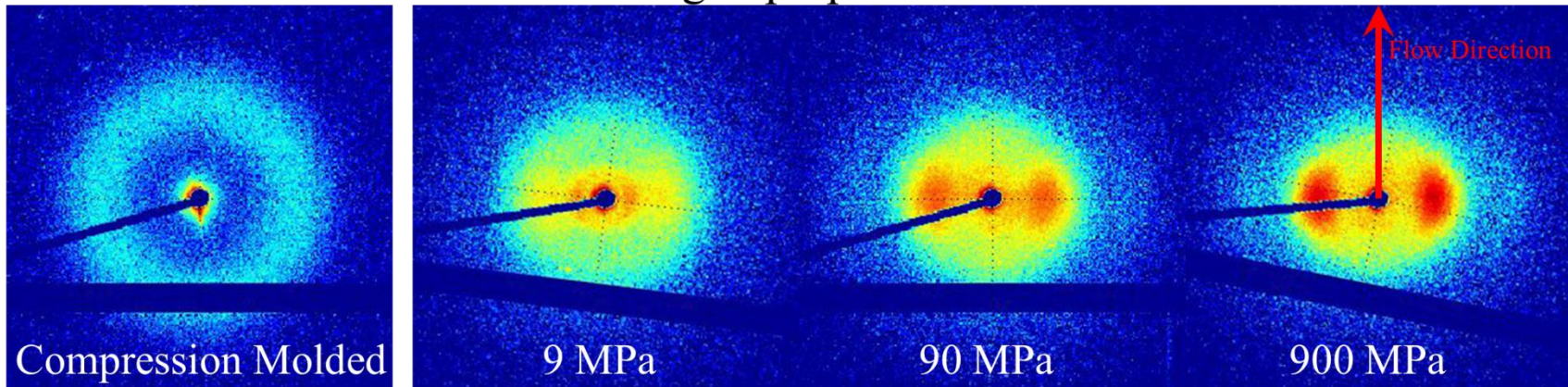


Figure 3.10: Two-dimensional SAXS scattering profile of MM-iPP uniaxially forged at several forging stresses. Top row: Imaged parallel to forging flow direction. Bottom row: Imaged perpendicular to forging flow direction. Compression molded sample was not prepared by MM. All samples at 20 °C.

3.3.5.3 Atomic Force Microscopy

The organization of lamellar crystals in iPP was investigated with atomic force microscopy (AFM). As discussed in chapter 1, the crystal morphology of α -iPP is organized into a structure hierarchy ranging from crystals, to lamella, to spherulites. Atomic force microscopy presents a useful method to directly image the dimensions of lamellar crystals, and also understand the organization of many lamellar crystals into larger structures.⁵⁴ Atomically smooth AFM samples were prepared via cryomicrotomy, and imaged in AFM tapping mode. The tapping phase data yielded images with useful contrast between crystalline (low phase, dark) and amorphous (high phase, bright) regions, shown in Figure 3.11. At high magnification, both MM-iPP and compression molded iPP show long, narrow lamellar crystals dispersed between amorphous regions. Due to the high aspect ratio of lamellar crystals, it is assumed that the thin dimension of the lamellar crystals is the c -axis, and therefore d_c may be directly measured with AFM. However, the lamellar crystals visible in the image likely intersect the test plane at random angles, so the observed lamellar thickness ($d_{c,o}$) is likely greater than the true lamellar thickness (d_c). The true average lamellar thickness may be calculated from a quantitative stereological technique developed by Ikeda *et al.*:⁵⁵

$$d_c = d_{c,o} \left(\frac{\pi}{2} \right) \quad (3.3)$$

The analysis method of Ikeda *et al.* assumes the lamellae are randomly oriented with respect to the observation plane, and that there is no inter-lamellar orientation correlation. The assumptions are valid for the present case because each 1 x 1 μm image was analyzed at 90 locations, and the results were averaged. For MM iPP, $d_c = 15.7 \pm 4.4$

nm, and for compression molded iPP $d_c = 10.4 \pm 3.2$ nm. The results agree very well with the d_c determined by SAXS.

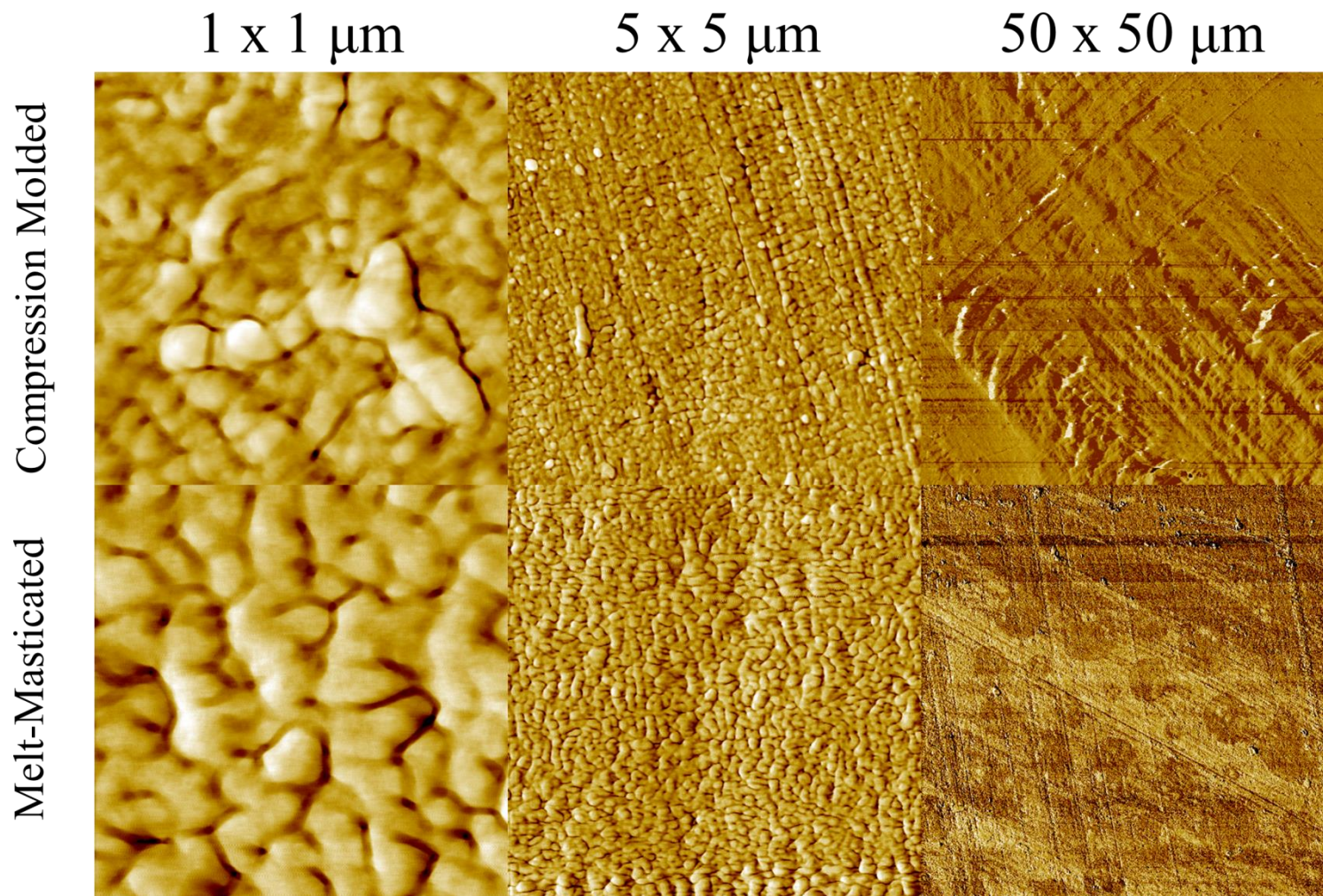


Figure 3.11: Atomic force microscopy phase mode images of iPP prepared by MM or compression molding. Dark regions = low phase angle, bright regions = high phase angle.

At lower magnification, the ordering of lamellar crystals becomes apparent in the compression molded sample. Compression molded iPP imaged at 5 x 5 μm clearly shows the typical cross-hatched morphology of α -iPP, with parent lamellae extending from the top to bottom of the image, and daughter lamella oriented orthogonal to the parent lamella. Melt-Masticated iPP at the same magnification does not show any apparent ordering of lamellae.

Finally, the lowest magnification shows the greater organization of lamella into larger structures. Compression molded iPP imaged at 50 x 50 μm shows a portion of a larger spherulite, as well as long artifacts from grooves of the microtome knife. In contrast, MM-iPP demonstrates irregular spherical domains randomly distributed throughout the material. The domain sizes range from 5 to 10 μm in diameter, and do not appear to contact neighboring domains. At this time, the structure and physical origins of these domains are not clear. However, these domains could scatter light and produce the marked opacity of MM iPP described in section 3.3.2.

3.3.5.4 Scanning Electron Microscopy

Like AFM, scanning electron microscopy (SEM) was used to understand the organizational relationship between lamellae. Compression molded and MM-iPP samples were treated with chemical etching solutions in order to remove the amorphous regions and provide contrast for the crystalline regions.^{47,56} Interestingly, MM-iPP required much longer etching times (48 hours) compared to compression molded iPP (24 hours) in order to etch enough contrast into the sample. Figure 3.12 shows the resulting images. At low magnification, the compression molded sample shows the expected organizational pattern for spherulites. Figure 3.12A shows the center of a spherulite, with the characteristic

cracking pattern that is due to preferential swelling of the etching into the amorphous iPP region, which creates surface instabilities that lead to cracking. Figure 3.12B shows another region of the same spherulite. At higher magnifications, compression molded demonstrates the characteristic cross-hatching pattern for α -iPP in Figure 3.12C, with parent lamellae propagating from the left to right side of the image, and orthogonal daughter lamellae. Melt-Masticated iPP does not show the same organizational hierarchy at low magnification (Figure 3.12D), and instead appears mostly disorganized. At high magnification, there appear to be local regions of quasi-oriented lamellae approximately 1 μm in diameter (Figure 3.F), but the larger 5-10 μm structures apparent in AFM are not visible here. Finally, MM-iPP does not show the same kind of cracking pattern seen in compression molded iPP

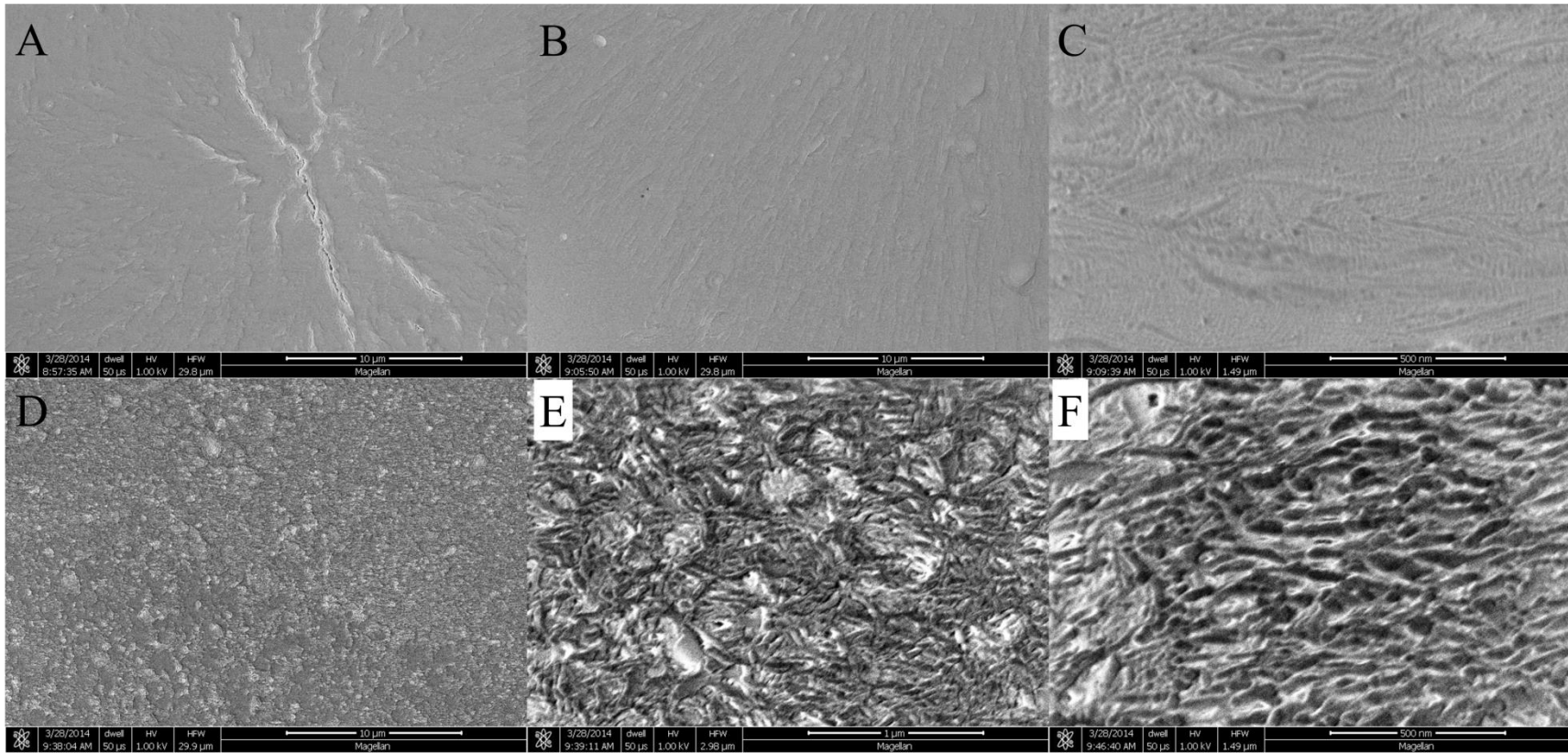


Figure 3.12: Scanning electron microscopy images of iPP surfaces treated with chemical etching. A-C: Compression Molded iPP. D-F: MM-iPP.

3.3.5.5 Polarized Optical Microscopy

Polarized optical microscopy was used to characterize the organizational structures of the iPP crystal morphology at large ($< 50 \mu\text{m}$) scales. Sample sections $\sim 10 \mu\text{m}$ thick were prepared by glass knife microtomy, which left moderate striations in the films. The results are shown in Figure 3.13. Compression molded iPP clearly shows a birefringence pattern consistent with spherulites, or structures comprised of radially organized lamellar crystals as discussed in chapter 1. However, MM-iPP analyzed under 90° crossed polarizers shows total extinction of light. The results suggest that the lamellae in MM-iPP do not organize into larger structures visible at the length scale of optical microscopy. The larger $5\text{-}10 \mu\text{m}$ structures apparent in AFM are not visible by optical microscopy.

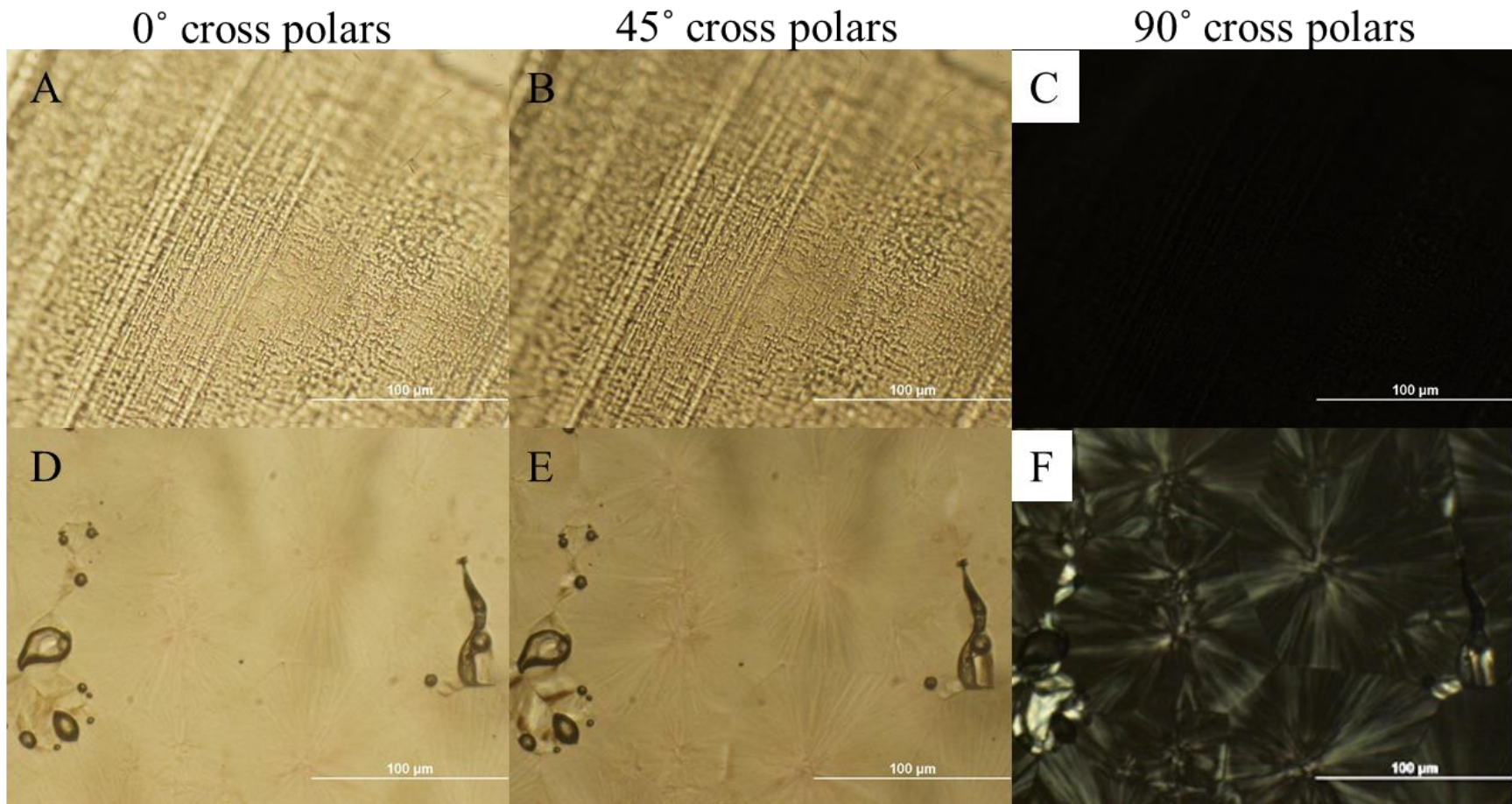


Figure 3.13: Polarized optical microscopy images of iPP prepared by glass knife microtomy. A-C: MM-iPP. D-F: Compression molded iPP. The angle between crossed polarizers is denoted at top of the image.

3.3.6 Mechanical Properties

3.3.6.1 Dynamic Mechanical Properties

Dynamic mechanical analysis was performed to elucidate the distinctions between MM and compression molded iPP, as well as biaxially oriented and unoriented MM iPP. Samples were analyzed at a constant frequency, over a temperature sweep through the glass transition temperature of iPP (~ 0 °C) up to melting. The resulting data in Figure 3.14A shows MM significantly improves the mechanical modulus of iPP. At 20 °C, the modulus of unoriented MM iPP (2366 MPa) is 29% greater than compression molded iPP (1832 MPa). The improved modulus is ascribed to the increased in crystal volume fraction produced by MM, which agrees with the thermal calorimetry results in Table 3.3. Indeed, it is well accepted that the elasticity of semicrystalline polymers is controlled by the volume fraction of crystal domains.⁵⁷ Biaxial orientation promotes further reinforcement (2794 MPa), presumably due to molecular orientation. Additionally, biaxially oriented MM iPP contracted significantly near the T_m of iPP due to latent strain energy imposed by the biaxial forging process. In fact, the heat shrinkage of MM iPP (52% ϵ) is comparable to that of a commercial biaxially pre-stressed polystyrene product, Shrinky Dinks® (60%). Both compression molded iPP and unoriented MM iPP did not contract significantly. It follows that biaxial forging is a useful method to impart mechanical reinforcement and/or orientation into MM iPP, and that the extent of reinforcement and orientation may be controlled through the forging process.

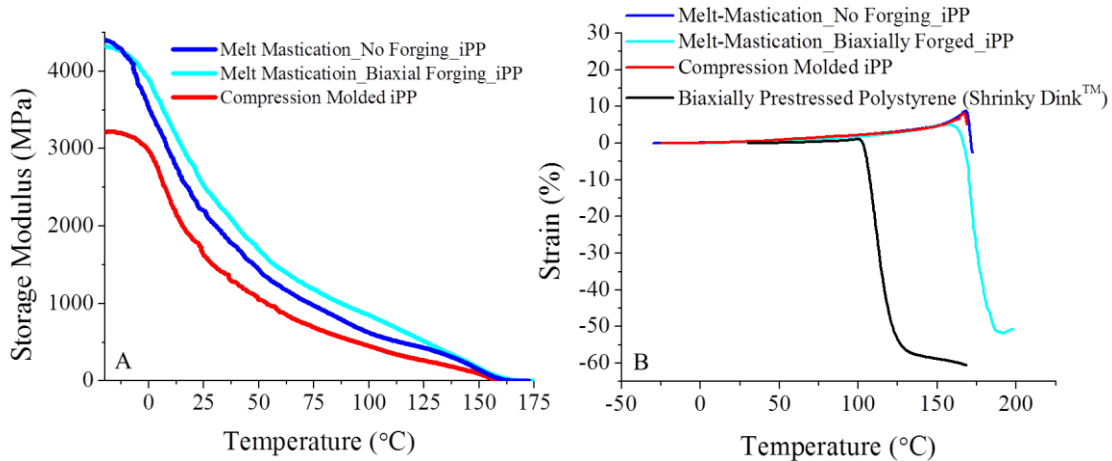


Figure 3.14: Dynamic mechanical temperature sweep of compression molded iPP, unoriented MM iPP, and biaxially oriented MM iPP. A) Storage modulus and B) Dimensional change. Modulus values recorded in Table 3.5.

3.3.6.2 Tensile Properties

Tensile tests were conducted on both compression molded iPP and MM iPP samples that were forged with mild uniaxial orientation. It was not possible to prepare unoriented MM iPP samples of sufficient size for ASTM D638 tensile tests. The resulting measurements are presented in Figure 3.15

Regardless of preparation method, all samples showed similar behaviors in tension. Below $\epsilon = 1\%$, all samples show linear elastic behavior, followed by yielding, and ultimately fracture. For all samples, yielding was preceded by fracture, while necking was not observed. Uniaxially forged iPP-MM demonstrated the highest Young's modulus, 28% larger than the compression molded iPP (Table 3.5), which agrees well with the 29% increase observed by DMA. Similar to the DMA study, the modulus increase is ascribed to the increased crystallinity observed by thermal calorimetry. For comparison, a compression molded iPP sample was annealed at 154 °C for 15 minutes after compression molding and then tested in tension. Like MM-iPP, annealed iPP demonstrates a significant increase in crystallinity and in Young's modulus. Because both MM-iPP and annealed-

iPP demonstrate increased Young's modulus, there is further credibility to the asserted relationship between crystallinity and modulus, which is also asserted elsewhere.⁷

Additionally, MM-iPP demonstrates a 30% improvement to yield strength, relative to compression molded iPP. Most models describing the deformation behavior of semicrystalline polymers assume that yield is the result of dislocations propagating through crystal lamella, and therefore d_c is the controlling parameter dictating yield activation.^{51,58} Current models are mostly based on a Young's model, which proposed a linear relationship between yield stress and d_c of ideal semicrystalline polymers.⁵¹ Since the introduction of Young's model, there is strong experimental evidence showing a linear relationship between yield stress and d_c of ideal semicrystalline polymers. Consequently, the improved yield strength of MM-iPP is attributed to the increased d_c .

The strain at break of uniaxially oriented MM-iPP and compression molded iPP are similar, while annealed iPP fails at a much lower strain. It follows that MM-iPP combines the Young's modulus of annealed iPP with the ductility of quenched, or compression molded iPP. This combination of modulus, strength and ductility not normally observed in iPP, and would be potentially advantageous in structural commercial applications, such as automotive parts. The results suggest that MM produces a unique crystal morphology that accommodates high crystallinity and d_c , while also maintaining high network connectivity in the amorphous phase to impart ductility. However, network connectivity is difficult to characterize in tension because structural flaws facilitate fracture at modest strain. Accordingly, network connectivity will be analyzed in compression in the proceeding section.

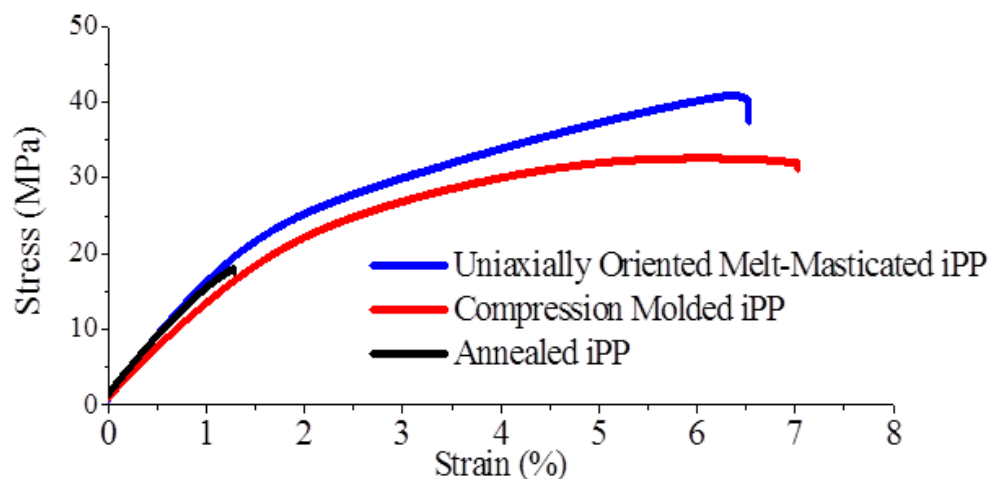


Figure 3.15: Tensile behavior of iPP prepared by compression molding, annealing, or MM with uniaxial forging. Strength and modulus recorded in Table 3.5.

Finally, the tensile response of Melt-Masticated iPP features an inflection point near 2% strain, where the slope of the stress-strain curve abruptly decreases. Such an inflection point is uncharacteristic for iPP, and does not occur in compression molded iPP. The structural origins of the inflection point are not clear from monotonic tensile tests. Accordingly, tensile stress relaxation experiments were performed to investigate the nature of the relaxation behavior at strains below (1%) and above (3%) the inflection point. The resulting relaxation spectra are presented in Figure 3.16, and fitted to the Kohlrausch-Williams-Watts (KWW) or stretched exponential equation:

$$\sigma(t) = \exp \left[-\left(t/\tau_0 \right)^\beta \right] \quad (3.4)$$

Where β represents the distribution of relaxation times and τ_0 is considered the characteristic relaxation time.⁵⁹ The results of the fitted KWW functions are presented in Table 3.4. The β does not appreciably vary for different sample preparation techniques, nor different strains, likely because the molecular structure of iPP is identical for both samples. The β parameter is through to be an indication of the intermolecular coupling strength during segmental relaxations in polymers. Intermolecular coupling is expected to

depend on the monomeric structure, as structures with bulky groups will enhance coupling between neighboring chains.⁶⁰ Therefore the β parameter is similar for both samples because both are comprised of the same iPP.

In contrast, τ_0 depends on both preparation technique and test strain. For compression molded iPP, the relaxation time decreases with increasing strain, which is expected because relaxation is thought to be an activation-energy controlled process. Imposing strain energy into the system will therefore decrease τ_0 . In contrast, MM-iPP demonstrates a significant reduction in τ_0 at 3% strain compared to 1% strain. Furthermore at 1% strain, τ_0 for MM-iPP is markedly lower than compression molded iPP. However τ_0 is comparable for both samples at 3% strain, above the inflection point of MM-iPP.

At this time, the physical origins of the MM-iPP relaxation behavior are unknown. The results could suggest that structural changes occur in MM-iPP above 1% strain. One possible explanation could be multiple deformation modes of lamellar crystals, which is commonly observed in HDPE both in tension and compression.^{61,62} However, multiple deformation modes have not been observed previously for iPP.

Table 3.4: Fitted KWW parameters from tensile stress relaxation studies of iPP at 1% and 3% strain.

Sample Name	τ_0	β
Compression Molded_1%	5,003	0.52
Compression Molded_3%	10,690	0.50
Melt-Masticated_1%	13,759	0.49
Melt-Masticated_3%	11,770	0.51

3.3.6.3 Compressive properties

Uniaxial compression tests are a useful tool to analyze the large strain behavior of semicrystalline polymers. After yield, the large strain behavior of is thought to be controlled by the connectivity of the remaining network, which consists of trapped entanglements in the amorphous phase.^{63,64} A neo-Hookean constitutive model is conventionally used to describe the large strain behavior of semicrystalline polymers after yield, and this has been experimentally verified in several systems by Haward *et al.*^{65,66} Therefore the large strain hardening response of semicrystalline polymers is expected to follow:

$$\sigma_T = Y + G_R \left(\lambda^2 - \frac{1}{\lambda} \right) \quad (3.5)$$

Where σ_T is the true stress, G_R is the strain hardening modulus, λ is the extension ratio, and the term $(\lambda^2 - \lambda^{-1})$ is the neo-Hookean strain. As discussed in chapter 1, the strain hardening behavior is an indication of the network connectivity within a deforming semicrystalline polymer. Therefore in the present study, the true stress response is plotted against neo-Hookean strain in order to determine G_R . Uniaxial compression tests were performed on compression molded iPP and unoriented MM iPP and the results are shown in Figure 3.16.

The observed compressive behavior of iPP is typical for semicrystalline polymers. There is a linear elastic response at low strain followed by yield. After yield, the material undergoes strain softening until the network dominates the mechanical response and strain hardening occurs. Melt-Masticated iPP demonstrates a 77% increase in compressive modulus and 40% increase in strength relative to compression molded iPP. These improvements to mechanical properties are ascribed to crystallinity and d_c , respectively, as discussed in the previous section.

Interestingly, the strain hardening behavior of MM-iPP is markedly greater than quenched compression molded iPP, which suggests that network connectivity is improved through MM (Table 3.5). Govaert *et al.* showed that G_R is strongly related to the thermal history of a semicrystalline polymer, specifically the rate of cooling from the melt.⁶⁴ The authors demonstrated that semicrystalline polymers rapidly quenched from the melt possess maximum G_R , and G_R decreases as the cooling rate decreases. The authors rationalize that slow crystallization from the melt allows more time for chain rearrangement, which facilitates disentanglement and therefore reduces G_R . Therefore, the highest G_R is achieved by rapidly quenching the melt, which traps entanglements in the amorphous region. In the present study, compression molding includes a melt quenching process, as discussed in section 3.2.3. It is therefore anticipated that MM-iPP should demonstrate G_R equal to or less than that of compression molded iPP. Instead, MM-iPP demonstrates a 163% increase. The strain hardening response of MM-iPP is attributed to the unique structure of the crystal morphology imparted by FIC, as well as many interlamellar tie molecules. Finally, the post-yield stress drop, or the difference between the yield stress and the local minimum in the curve after yield, is greater for MM iPP (17.43

MPa) compared to compression molded iPP (13.29 MPa). The post yield stress drop is an indication of the tendency of a material to undergo strain localization, a prerequisite to other failure mechanisms like shear banding and crazing. It follows that MM-iPP appears to favor strain localization more than compression molded iPP, likely due to a decrease in the volume fraction of the amorphous phase.

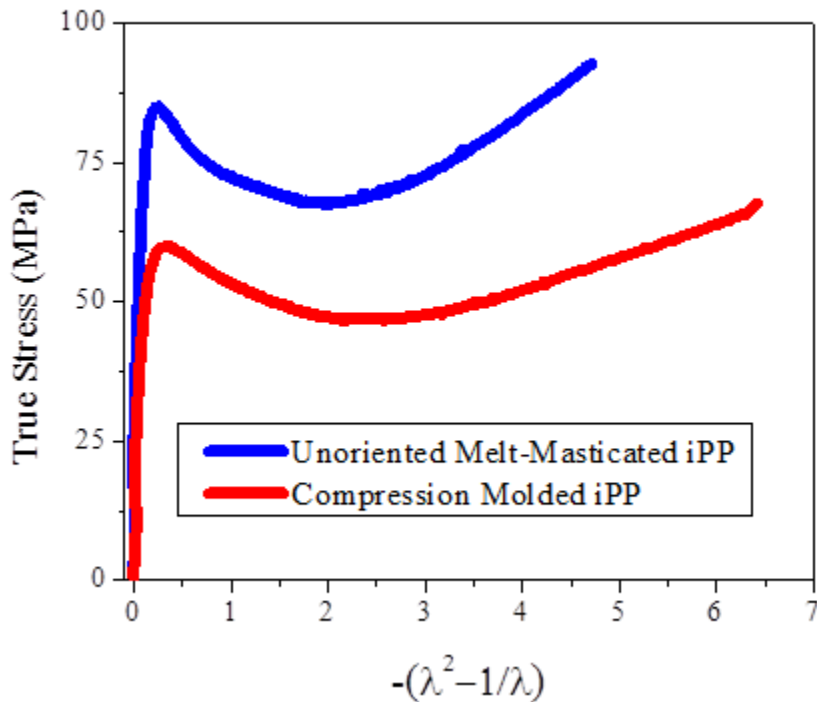


Figure 3.16: Uniaxial compressive behavior of iPP prepared by compression molding or Melt-Mastication without forging. Modulus and strength values recorded in Table 3.5.

3.3.6.4 Impact Properties

Notched Izod impact tests were performed in order to evaluate the fracture behavior of compression molded iPP and MM iPP, as well as the changes in fracture behavior through the ductile-brittle transition of iPP. Izod samples were prepared via mild uniaxial forging. The Izod values at each temperature are recorded in Figure 3.17. Testing was performed on a modified Izod impact tester (Appendix A-1), which uses force and

displacement sensors to record the impact energy as a function of displacement, presented in Figure 3.18.

The trend of iPP impact energy at regularly spaced temperature intervals is typical for semicrystalline polymers. Below the glass transition temperature of iPP (~ 0 °C), the material fractures in a brittle manner, thus the impact energy is low and relatively independent of temperature. Above the glass transition temperature, iPP fractures in a more ductile manner and demonstrates improved impact energy with increasing temperature. The results suggest that the impact properties of MM-iPP and compression molded iPP both improve above 0 °C. This critical temperature at which the impact energy improves is referred to as the “ductile brittle transition” (DBT), although the ductility of a sample is not clear from a standard notched Izod test. However, the results from the instrumented Izod test in Figure 3.18 show that the displacement at fracture increases significantly above 0 °C, which proves that the ductility of iPP also improves above the DBT. Additionally, the slopes of the impact energy vs. displacement curves, which are related to the bending modulus of the samples, do not appreciably change with temperature. Therefore, the change in ductility above the DBT is responsible for the improved impact fracture observed with increasing temperature.

The results also show that MM-iPP demonstrates superior impact resistance at nearly all temperatures. It is anticipated that the higher mechanical strength and modulus of MM-iPP results in improved impact performance. Indeed, the slopes of the curves Figure 3.18 are generally steeper for MM-iPP, indicating increased modulus. The ductility at each temperature is independent of preparation technique. Accordingly, the differences in impact performance between MM-iPP and compression molded iPP are ascribed to

changes in the modulus and strength, which corroborates conclusions about modulus and strength in sections 3.3.6.2 and 3.3.6.3.

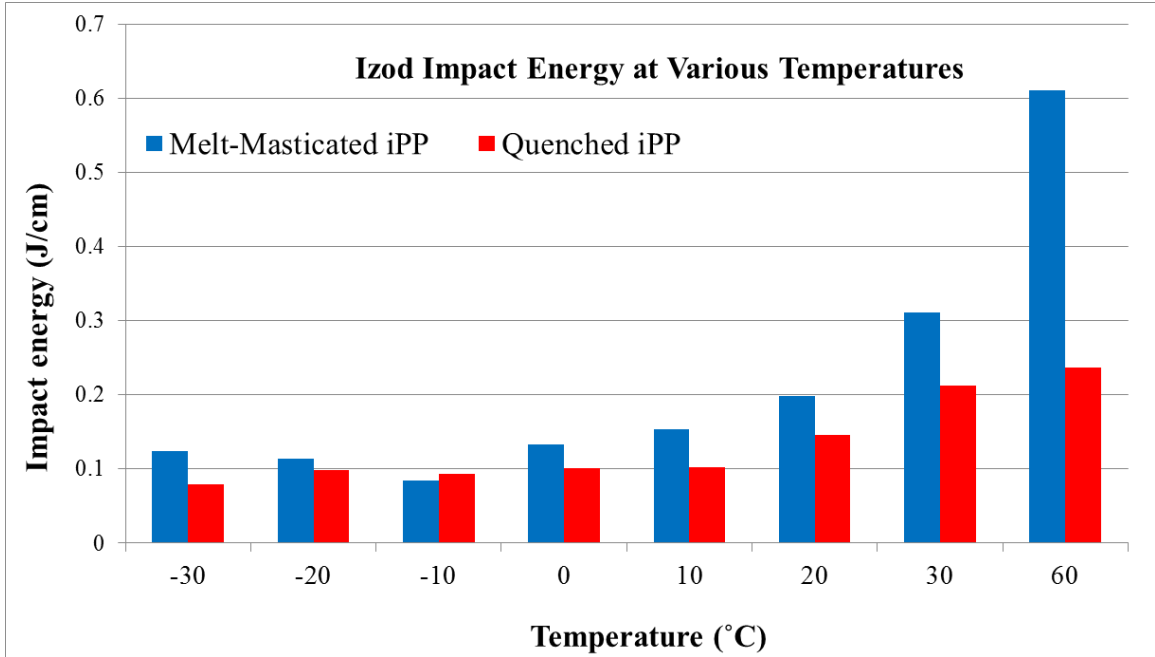


Figure 3.17: Izod Impact energy of compression molded iPP and MM-iPP conditioned at several temperatures.

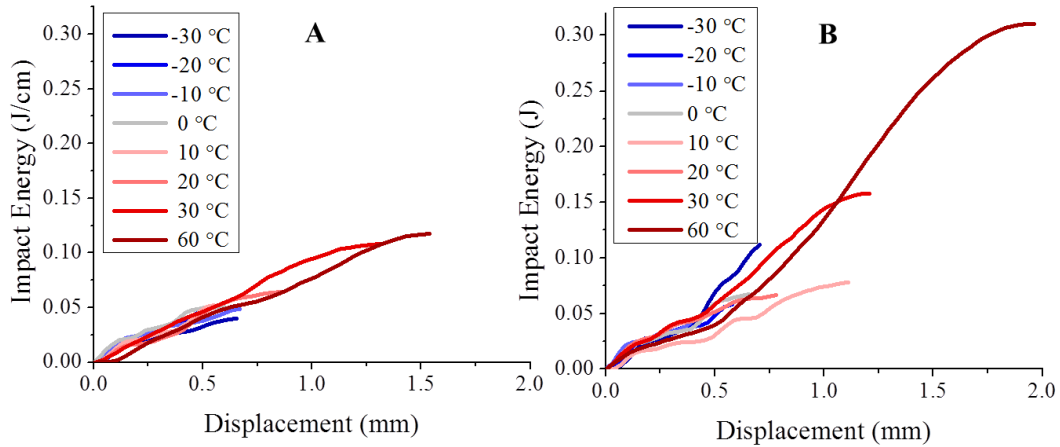


Figure 3.18: Impact energy vs displacement during Izod fracture, recorded by instrumented Izod device (Appendix A-1). A) Compression molded iPP. B) Melt-Masticated iPP.

Table 3.5: Summary of the mechanical test results of compression molded and MM iPP.

*Compression molded samples treated with annealing.

Sample	Modulus (GPa)			Strength (MPa)		Strain Hardening Modulus, Compression (G _R , MPa)	Heat Shrinkage (%)	Izod Impact Energy (J/m)
	DMA (20 °C)	Tensile	Compression	Tensile	Compression			
Compression Molded iPP	1.83	1.30 ± 0.05 (1.51 ± 0.02)*	1.36 ± 0.18	32.5 ± 1.1 (18.1 ± 0.4)*	60.6 ± 2.3	4.9 ± 1.5	-5	14 ± 3
Unoriented MM iPP	2.36	--	2.41 ± 0.16	--	85.0 ± 1.1	12.9 ± 0.7	2	--
Biaxially Forged MM iPP	2.79	--	--	--	--	--	52	--
Uniaxially Forged MM iPP	--	1.67 ± 0.12	--	42.5 ± 5.5	--	--	--	20 ± 2

3.4 Conclusions

A new semicrystalline polymer processing technique called Melt-Mastication (MM) is proposed, developed, and evaluated for an isotactic polypropylene system. Melt-Mastication is a low-temperature polymer processing technique that occurs over a three-step temperature profile. The processing conditions promote flow induced crystallization through a chaotic flow field, such that the final crystal morphology appears to be disorganized lamellar crystals. X-ray scattering at small and wide angles showed that MM produces iPP with relatively thick lamellar crystals comprised of the α -crystal type. These thick lamellar crystals produced iPP with unusually high melting point and mechanical yield stress. In addition to mechanical strength, MM-iPP also demonstrated remarkable increases to mechanical modulus and crystal volume fraction, while maintaining the ductility of standard compression molded iPP. The mechanical properties were correlated to aspects of the crystal morphology apparent from microscopy and scattering techniques.

3.5 References

1. Z. Tadmor and C. G. Gogos: 'Principles of Polymer Processing', 2nd ed. 2006, Hoboken, NJ, John Wiley & Sons, Inc.
2. G. R. Strobl: 'The Physics of Polymers: Concepts for Understanding Their Structures and Behavior', 2007, Springer Science & Business Media.
3. A. Addeo: 'Polypropylene Handbook', 2nd ed. 2005, Munich, Carl Hanser Verlag.
4. R. Androsch, M. L. Di Lorenzo, C. Schick and B. Wunderlich: 'Mesophases in polyethylene, polypropylene, and poly(1-butene)', *Polymer*, 2010, **51**, 4639–4662.
5. C. De Rosa, F. Auriemma, R. Di Girolamo, O. Ruiz de Ballesteros, M. Pepe, O. Tarallo and A. Malafrente: 'Morphology and Mechanical Properties of the Mesomorphic Form of Isotactic Polypropylene in Stereodeficient Polypropylene', *Macromolecules*, 2013, **46**, 5202–5214.

6. C. De Rosa, F. Auriemma, R. Di Girolamo and O. R. de Ballesteros: 'Crystallization of the mesomorphic form and control of the molecular structure for tailoring the mechanical properties of isotactic polypropylene', *J. Polym. Sci. Part B Polym. Phys.*, 2014, n/a–n/a.
7. D. Ferrer-Balas, M. L. MasPOCH, A. B. Martinez and O. O. Santana: 'Influence of annealing on the microstructural, tensile and fracture properties of polypropylene films', *Polymer*, 2001, **42**, 1697–1705.
8. I. M. Ward: 'Structure and Properties of Oriented Polymers', 1997, Springer.
9. M. J. Mannion: 'Polyolefin composition containing ultrafine sorbitol and xylitol cetals', US5310950, published 1994.
10. D. L. Dotson and N. A. Mehl: 'Modifying polyolefin properties, such as polypropylene clarification and nucleation', US6582503, published 2003.
11. J. M. Torkelson, C. Pierre and A. Flores: 'Enhancing the physical properties of semi-crystalline polymers via solid-state shear pulverization.', US8729223 B2, published 2013.
12. J. Varga, I. Mudra and G. W. Ehrenstein: 'Highly active thermally stable ?-nucleating agents for isotactic polypropylene', *J. Appl. Polym. Sci.*, 1999, **74**, 2357–2368.
13. G. Lamberti: 'Flow-induced crystallization during isotactic polypropylene film casting', *Polym. Eng. Sci.*, 2011, **51**, 851–861.
14. R. H. Somani, B. S. Hsiao, A. Nogales, S. Srinivas, A. H. Tsou, I. Sics, F. J. Balta-Calleja and T. A. Ezquerra: 'Structure Development during Shear Flow-Induced Crystallization of i-PP: In-Situ Small-Angle X-ray Scattering Study', *Macromolecules*, 2000, **33**, 9385–9394.
15. S. Liedauer, G. Eder, H. Janeschitz-Kriegl, P. Jerschow, W. Geymayer and E. Ingolic: 'On the Kinetics of Shear Induced Crystallization in Polypropylene', *Int. Polym. Process.*, 1993, **8**, 236–244.
16. G. Eder, H. Janeschitz-Kriegl and S. Liedauer: 'Crystallization processes in quiescent and moving polymer melts under heat transfer conditions', *Prog. Polym. Sci.*, 1990, **15**, 629–714.
17. S. Liedauer, G. Eder and H. Janeschitz-Kriegl: 'On the Limitations of Shear Induced Crystallization in Polypropylene Melts', *Int. Polym. Process.*, 1995, **10**, 243–250.

18. G. Kumaraswamy, A. M. Issaian and J. A. Kornfield: 'Shear-Enhanced Crystallization in Isotactic Polypropylene. 1. Correspondence between in Situ Rheo-Optics and ex Situ Structure Determination', *Macromolecules*, 1999, **32**, 7537–7547.
19. C. Tribout, B. Monasse and J. M. Haudin: 'Experimental study of shear-induced crystallization of an impact polypropylene copolymer', *Colloid Polym. Sci.*, 1996, **274**, 197–208.
20. F. Sadeghi, A. Ajji and P. J. Carreau: 'Study of polypropylene morphology obtained from blown and cast film processes : Initial morphology requirements for making porous membrane by stretching', *J. Plast. Film Sheeting*, n.d., **21**, 199–216.
21. H.-X. Huang: 'Self-reinforcement of polypropylene by flow-induced crystallization during continuous extrusion', *J. Appl. Polym. Sci.*, 1998, **67**, 2111–2118.
22. M. D. Shelby, M. E. Donelson, S. Weinhold and H. P. Hall: 'Process for rapid crystallization of polyesters and co-polyesters via in-line drafting and flow-induced crystallization', US6159406, published 2000.
23. P. Gilliard, C. Dehennau and P. J. A. Karsten: 'Low haze polypropylene film; free of nucleating additives', US6391432, published 2002.
24. P. Gilliard: 'Pliable crystalline polymer and process for its production', US5306796, published 1994.
25. I. M. Ward: 'Developments in oriented polymers, 1970–2004', *Plast. Rubber Compos.*, 2013,.
26. I. M. Ward and P. J. Hine: 'The science and technology of hot compaction', *Polymer*, 2004, **45**, 1413–1427.
27. T. Bárány, J. Karger-Kocsis and T. Czigány: 'Development and characterization of self-reinforced poly(propylene) composites: carded mat reinforcement', *Polym. Adv. Technol.*, 2006, **17**, 818–824.
28. A. Izer and T. Barany: 'Hot consolidated all-PP composites from textile fabrics composed of isotactic PP filaments with different degrees of orientation', *Express Polym. Lett.*, 2007, **1**, 790–796.
29. J. Rasburn, P. J. Hine, I. M. Ward, R. H. Olley, D. C. Bassett and M. A. Kabeel: 'The hot compaction of polyethylene terephthalate', *J. Mater. Sci.*, 1995, **30**, 615–622.

30. P. Rojanapitayakorn, P. T. Mather, A. J. Goldberg and R. A. Weiss: 'Optically transparent self-reinforced poly(ethylene terephthalate) composites: molecular orientation and mechanical properties', *Polymer*, 2005, **46**, 761–773.
31. P. J. Hine, I. M. Ward, M. I. A. EL Maaty, R. H. Olley and D. C. Bassett: 'The hot compaction of 2-dimensional woven melt spun high modulus polyethylene fibres', *J. Mater. Sci.*, n.d., **35**, 5091–5099.
32. P. J. Hine, I. M. Ward, N. D. Jordan, R. H. Olley and D. C. Bassett: 'A comparison of the hot-compaction behavior of oriented, high-modulus, Polyethylene fibers and tapes', *J. Macromol. Sci. Part B*, 2007,.
33. M. I. Abo El-Maaty, D. C. Bassett, R. H. Olley, P. J. Hine and I. M. Ward: 'The hot compaction of polypropylene fibres', *J. Mater. Sci.*, 1996, **31**, 1157–1163.
34. B. Pornnimit and G. W. Ehrenstein: 'Extrusion of self-reinforced polyethylene', *Adv. Polym. Technol.*, 1991, **11**, 91–98.
35. H. Huang: 'High property high density polyethylene extrudates prepared by self-reinforcement', *J. Mater. Sci. Lett.*, n.d., **17**, 591–593.
36. H.-X. Huang: 'Continuous extrusion of self-reinforced high density polyethylene', *Polym. Eng. Sci.*, 1998, **38**, 1805–1811.
37. I. M. Ward, P. D. Coates and M. M. Dumoulin: 'Solid Phase Processing of Polymers', 2000, Carl Hanser Verlag.
38. A. K. Taraiya and I. M. Ward: 'Production and properties of biaxially oriented polyethylene tubes', *J. Appl. Polym. Sci.*, 1996, **59**, 627–638.
39. J. Li and Y.-W. Lee: 'Evolution of morphology in high molecular weight polyethylene during die drawing', *J. Mater. Sci.*, 1993, **28**, 6496–6502.
40. J. Mohanraj, N. Chapleau, A. Ajji, R. A. Duckett and I. M. Ward: 'Production, properties and impact toughness of die-drawn toughened polypropylenes', *Polym. Eng. Sci.*, 2003, **43**, 1317–1336.
41. C. I. Ogbonna, G. Kalay, P. S. Allan and M. J. Bevis: 'The self-reinforcement of polyolefins produced by shear controlled orientation in injection molding', *J. Appl. Polym. Sci.*, 1995, **58**, 2131–2135.
42. Q. Guan, X. Zhu, D. Chiu, K. Shen, F. S. Lai and S. P. McCarthy: 'Self-reinforcement of polypropylene by oscillating packing injection molding under low pressure', *J. Appl. Polym. Sci.*, 1996, **62**, 755–762.

43. G. Kalay and M. J. Bevis: 'Processing and physical property relationships in injection-molded isotactic polypropylene. 1. mechanical properties', *J. Polym. Sci. Part B Polym. Phys.*, 1997, **35**, 241–263.
44. G. Kalay and M. J. Bevis: 'Processing and physical property relationships in injection-molded isotactic polypropylene. 1. mechanical properties', *J. Polym. Sci. Part B Polym. Phys.*, 1997, **35**, 265–291.
45. L.-M. Chen and K. Shen: 'Biaxial self-reinforcement of isotactic polypropylene prepared in uniaxial oscillating stress field by injection molding. II. Morphology', *J. Appl. Polym. Sci.*, 2000, **78**, 1911–1917.
46. D. C. Bassett and R. H. Olley: 'On the lamellar morphology of isotactic polypropylene spherulites', *Polymer*, 1984, **25**, 935–943.
47. A. M. Freedman, D. C. Bassett, A. S. Vaughan and R. H. Olley: 'On quantitative permanganic etching', *Polymer*, 1986, **27**, 1163–1169.
48. J. Park, K. Eom, O. Kwon and S. Woo: 'Chemical Etching Technique for the Investigation of Melt-crystallized Isotactic Polypropylene Spherulite and Lamellar Morphology by Scanning Electron Microscopy', *Microsc. Microanal.*, 2002, **7**, 276–286.
49. P. Crouzet, A. Martens and P. Mangin: 'Universal Calibration in Permeation Chromatography. Application to Polyethylenes, Polypropylene, and Ethylene-Propylene Copolymers', *J. Chromatogr. Sci.*, 1971, **9**, 525–530.
50. 'The Polymer Data Handbook', 2009, Oxford University Press, Incorporated.
51. W. O'kane, R. Young and A. Ryan: 'The effect of annealing on the structure and properties of isotactic polypropylene films', *J. Macromol. Sci. Part B*, 1995, **34**, 427–458.
52. R. Hingmann, J. Rieger and M. Kersting: 'Rheological Properties of a Partially Molten Polypropylene Random Copolymer during Annealing', *Macromolecules*, 1995, **28**, 3801–3806.
53. J.-H. Chen, F.-C. Tsai, Y.-H. Nien and P.-H. Yeh: 'Isothermal crystallization of isotactic polypropylene blended with low molecular weight atactic polypropylene. Part I. Thermal properties and morphology development', *Polymer*, 2005, **46**, 5680–5688.
54. W. Stocker, S. N. Magonov, H. J. Cantow, J. C. Wittmann and B. Lotz: 'Contact faces of epitaxially crystallized .alpha.- and .gamma.-phase isotactic polypropylene observed by atomic force microscopy', *Macromolecules*, 1993, **26**, 5915–5923.

55. T. Ikeda, V. A. Ravi and G. J. Snyder: 'Evaluation of true interlamellar spacing from microstructural observations', *J. Mater. Res.*, 2011, **23**, 2538–2544.
56. R. H. Olley and D. C. Bassett: 'An improved permanganic etchant for polyolefines', *Polymer*, 1982, **23**, 1707–1710.
57. J. C. Halpin: 'Moduli of Crystalline Polymers Employing Composite Theory', *J. Appl. Phys.*, 1972, **43**, 2235.
58. W. J. O'Kane and R. J. Young: 'The role of dislocations in the yield of polypropylene', *J. Mater. Sci. Lett.*, 1995, **14**, 433–435.
59. I. M. Hodge: 'Physical aging in polymer glasses.', *Science*, 1995, **267**, 1945–7.
60. K. L. Ngai and C. M. Roland: 'Intermolecular cooperativity and the temperature dependence of segmental relaxation in semicrystalline polymers', *Macromolecules*, 1993, **26**, 2688–2690.
61. M. F. Butler, A. M. Donald and A. J. Ryan: 'Time resolved simultaneous small- and wide-angle X-ray scattering during polyethylene deformation: 1. Cold drawing of ethylene- α -olefin copolymers', *Polymer*, 1997, **38**, 5521–5538.
62. M. F. Butler, A. M. Donald and A. J. Ryan: 'Time resolved simultaneous small- and wide-angle X-ray scattering during polyethylene deformation 3. Compression of polyethylene', *Polymer*, 1998, **39**, 781–792.
63. A. Sedighiamiri, L. E. Govaert, M. J. W. Kanters and J. A. W. van Dommelen: 'Micromechanics of semicrystalline polymers: Yield kinetics and long-term failure', *J. Polym. Sci. Part B Polym. Phys.*, 2012, **50**, 1664–1679.
64. B. A. G. Schrauwen, R. P. M. Janssen, L. E. Govaert and H. E. H. Meijer: 'Intrinsic Deformation Behavior of Semicrystalline Polymers', *Macromolecules*, 2004, **37**, 6069–6078.
65. R. N. Haward: 'Strain hardening of thermoplastics', *Macromolecules*, 1993, **26**, 5860–5869.
66. R. . Haward: 'The derivation of a strain hardening modulus from true stress-strain curves for thermoplastics', *Polymer*, 1994, **35**, 3858–3862.

CHAPTER 4

IMPROVED POLYMER NANOCOMPOSITE DISPERSIONS BY A MELT MASTICATION PROCESS

In the previous chapter, a low temperature mixing technique termed Melt-Mastication (MM) was investigated as a method to improve the thermal/mechanical properties of semicrystalline polyolefins through altering their crystal morphology. This method involved melt processing a semicrystalline polymer at a temperature between the resin melting and crystallization transitions in order to promote flow induced crystallization (FIC). Results showed that the mixing torque and resin viscosity during MM increases by a factor of 5-10 near the temperature where FIC is expected to occur. Because the mixing rate does not change, MM necessarily subjects the material to higher mixing shear stresses.

In the next part of this work, MM is repurposed as a method to prepare PNCs with enhanced nanoparticle dispersion. The approach involves melt processing a semicrystalline polymer with nanoparticles, and then subjecting the material to the MM temperature profile illustrated in Figure 3.1. Compared to conventional melt processing (CMP) methods to prepare PNCs, MM subjects the material to higher mixing torque and therefore mixing shear stresses during processing, resulting in the fragmentation of micrometer-scale agglomerates of nanoparticles. The dispersion efficiency of MM is evaluated with standard characterization techniques, as well as a quantitative stereology. Finally, a model for agglomerate fragmentation is proposed and discussed with respect to the results.

4.1 Introduction

Polymer Nanocomposites (PNCs) are a promising class of composite materials containing a nanoscale phase dispersed within a polymer matrix. These materials generated recent interest due to their apparent thermal and physical property improvements with a relatively small (< 6 vol %) concentration of well-dispersed nanoparticles. Accordingly, PNCs are potentially suitable candidates for a variety of commercial applications, including automotive materials, packaging materials, electronic applications, optical applications, and applications where accelerated polymer crystallization kinetics are desired. Further discussion on nanocomposite fundamentals, compositions and property enhancements may be found in section 1.3.

4.1.1 Physical Methods for Preparation of PNCs

In practice, it is difficult to prepare well-dispersed PNCs due to the strong tendency for nanoparticles to agglomerate, especially during conventional melt processing. Most PNC systems possess an unfavorable interaction energy between the nanoparticle and polymer matrix, which promotes the agglomeration of nanoparticles during melt processing.¹⁻³ Accordingly, several chemical modification techniques and physical processing strategies have been developed to prevent nanoparticle agglomeration.

As discussed in section 2.1.1, there are several literature examples of techniques to chemically optimize the polymer and/or nanoparticle interaction energies in order to promote dispersion. However, chemical modification techniques may not be commercially practical or economically feasible for many PNC systems due to the extra manufacturing cost and associated with industrial chemistry. Furthermore, chemical modification techniques must be optimized for each polymer-nanoparticle combination.

Physical processing strategies are an attractive alternative to overcome some of the limitations of chemical modification techniques. Physical processing strategies utilize non-conventional polymer processing conditions and equipment to promote fragmentation of nanoparticle agglomerates in PNCs, and may be classified as solid-state or melt-state strategies. Studies reporting solid-state physical processing strategies include Solid State Shear Pulverization (SSSP), Solid-State Melt Extrusion (SSME), and Solid State Ball Milling (SSBM).⁴⁻⁷ Solid State Shear Pulverization and Solid State Melt Extrusion are both techniques that subject polymeric materials to harsh pulverization conditions within a continuously cooled extruder barrel. Torkelson *et al.* showed that SSSP substantially improves the dispersion state of an Isotactic Polypropylene-Graphite nanocomposite system. Also reported were significant property improvements, including a ~100% increase in Young's modulus and reductions in the rheological and electrical percolation thresholds, apparently due to the improved dispersion state. Similarly, SSBM subjects PNCs to high shear and compressive forces through an intense ball milling process. Drzal *et al.* reported improvements to the flexural modulus and electrical conductivity for Polyetherimide-Graphene nanocomposites prepared with SSBM. Solid-state physical processing strategies are highly effective methods to improve the PNC dispersion state, but are challenged by costly manufacturing requirements associated with instrument cooling (SSSP, SSME), and inefficient batch processing (SSBM).

Melt-state physical processing strategies improve PNC dispersions by increasing the mixing shear stresses during melt compounding through non-conventional processing conditions.⁸⁻¹¹ Vermogen *et al.* demonstrated modest improvements to the dispersion of an extruded isotactic polypropylene-montmorillonite system through changing the extruder

type and screw profile. The results of this study showed a correlation between the dispersion state and the magnitude of mixing shear stress during processing. In a similar study, Vergnes *et al.* showed the dispersion of a Polypropylene/organoclay PNC may be slightly improved through increasing the extruder screw speed and decreasing the feed rate. The authors rationalized from numerical simulations that the key parameter for achieving well-dispersed PNCs is the total strain and shear rate during processing.

Generally, the effectiveness of melt-state physical processing strategies are limited by the shear thinning behavior of polymer melts.¹² Shear thinning limits the maximum mixing shear stress that may be achieved during melt processing. For example, Table 4.4 in section 4.3.4 shows that the mixing torque of an Isotactic Polypropylene melt at 200 °C increases by only 38% when the mixing rate is increased from 70 to 190 RPM. According to the model presented in section 4.3.5, a 38% increase in mixing shear stress will decrease the mean agglomerate size about 48%, which is insufficient to achieve property improvements. However from an industrial perspective, melt-state physical processing strategies are ideal for scale-up because they may be performed using commercially available polymer processing equipment. It follows that there is a need for a method to combine the economy of melt-state processing strategies with the effectiveness of solid-state physical processing strategies. The present study is an attempt to use MM to combine benefits of both strategies.

4.1.2 Methods to Evaluate PNC Dispersion State

Methods to characterize the dispersion state of PNCs are critical to understanding the structure-property relationships of these materials. Current techniques may be classified as either indirect or direct characterization methods. Indirect methods evaluate

dispersion by measuring an intrinsic material property related to dispersion, such as the non-isothermal crystallization onset temperature (T_c), thermal or electrical conductivity, melt rheology, or mechanical properties.^{2,4,5,7,13-16} For semicrystalline PNCs, T_c is affected by the presence of nanoparticles, which act as seeds for crystal nucleation.⁵ Accordingly semicrystalline PNCs with well dispersed nanoparticles will demonstrate accelerated crystallization kinetics and therefore elevated T_c . Other intrinsic material properties are strongly affected by the nanoparticle percolation threshold, which is the critical concentration of nanoparticles to form long-range connectivity. Properties sensitive to percolation threshold include conductivity (if the nanoparticles are conductive), melt rheology and mechanical properties. For example, a review by Cassagnau showed that well dispersed PNCs melts generally demonstrated a solid-like viscoelastic response at low frequencies, although there are exceptions.¹⁶ Indirect characterization methods provide useful information for comparing the relative dispersion state between similar samples, but do not directly describe details of the dispersion such as the size and spacing of nanoparticles. In contrast, direct characterization methods such as microscopy absolutely portray the dispersion state in a localized region of the PNC. These methods are useful tools to understand how aspects of the PNC dispersion change at small length scales. For example, Vermogen *et al.* used TEM to understand the exfoliation state, aspect ratio, and interparticle distance of an isotactic polypropylene-montmorillonite system. However, direct characterization methods are not useful for representing the dispersion state in the entire material, as it is difficult to capture a representative volume element with high magnification microscopy. In the following section, quantitative stereology is discussed as a method to overcome the limitations of direct and indirect characterization methods.

4.1.3 Quantitative Stereology

Quantitative Stereology (QS) is a group of statistical techniques used to infer information about three-dimensional objects from two-dimensional sections of the objects.^{17,18} Many of these techniques were originally developed for the study of metallic alloys, which often contain microscopic discrete phases distributed within a continuous phase^{19,20}. Due to the opacity of metallic alloys it is not possible to directly evaluate the three-dimensional size distribution of the discrete phases, but it is possible to evaluate the number and size of discrete phase domains from a polished two-dimensional section. Quantitative stereology provides a mathematical procedure to convert the distribution of particle sections into a spatial size distribution of particles. In the case of PNCs, QS enables quantitative evaluation of the size distribution of nanoparticle agglomerates. This technique enables data from multiple images of the same sample to be compiled into the same QS calculation. This aspect of QS is highly advantageous because it enables researchers to accumulate enough information for a representative volume element, which overcomes the limitations of direct characterization methods. It follows that QS is a useful tool to understand how PNC processing strategies affect the nanoparticle dispersion state.

The present work uses a QS method originally developed by Johnson and Saltykov to calculate the spatial size distribution of discrete spheres from their section diameters.^{20,21} This method assumes the PNC is comprised of polydisperse, spherical agglomerates randomly distributed within a continuous polymer matrix, and the two-dimensional sections randomly intersect these spherical agglomerates. The method also assumes that the largest agglomerates are always intersected at their maximum diameter, so the number of observed sections of the largest size ($i = \max$) from all spheres j [$\sum_j (N_a)_{i=\max,j}$] equals

the number of agglomerate spheres of the largest class size $[(N_v)_{j=max}]$. Any agglomerate may be sectioned either at its maximum diameter, or at a smaller diameter. It follows that the largest agglomerates may produce large or small sections, whereas the smallest agglomerates may only produce small sections, as illustrated in Figure 4.1.

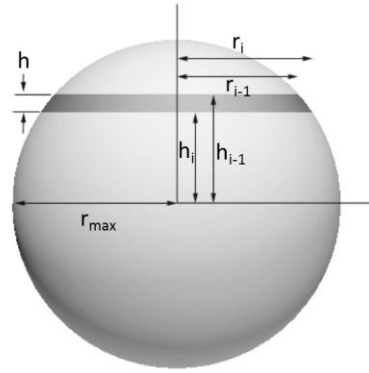


Figure 4.1 Illustration of a spherical agglomerate of maximum size intersected by random test plane h .

It is not possible to know the sphere size from which each section originates, however it is possible to calculate from geometric arguments the probability of intersecting a sphere of size j to yield sections of size i :

$$P_{i,j} = \frac{1}{r_{max}} [\sqrt{(r_{max})^2 - (r_{i-1})^2} - \sqrt{(r_{max})^2 - (r_i)^2}] \quad (4.1)$$

Where r_{max} is the maximum sphere size. Accordingly, from $(N_v)_{j=max}$ it is possible to calculate the number and sizes of sections i that will result from this largest class size $[(N_a)_{i,j=max}]$, and by simple deduction the number of spheres in the second largest class size $[(N_v)_{j=max-1}]$. A similar procedure may be applied to the next smallest class size to calculate $(N_a)_{i,j=max-1}$ and $(N_v)_{j=max-2}$. By following this iterative process

for successively smaller class sizes, it is possible to calculate the number of agglomerate spheres in all class sizes, or the size distribution of agglomerate spheres $[(N_v)_j]$.

4.2 Materials and Methods

4.2.1 Materials

Pellet form isotactic polypropylene (iPP) grade PP9999SS was kindly supplied by ExxonMobil and used as received ($T_m = 165$ °C, $T_c = 111$ °C). Grade PP9999SS is byproduct produced when an iPP polymerization reactor is transitioning between commercial iPP grades. Grade PP9999SS is not a commercial grade and cannot be found on the ExxonMobil website. Linear low density polyethylene (LLDPE, Dowlex 2553) and high density polyethylene (HDPE-1: DMDA-8904-NT7, MFI 4.4; HDPE-2 DMDA-8007-NT7, MFI 8.3) were generously provided by Dow Plastics. Irganox 1010 and Irgafos 168 antioxidant process stabilizers were purchased from Ciba, Inc. and used as received. Exfoliated Graphene Nanoplatelets (xGnP-c-750, $750 \text{ m}^2\text{g}^{-1}$) were purchased from XGSciences, Inc. and used as received. Fumed Silica (FS, $0.007 \mu\text{m}$, $395 \text{ m}^2/\text{g}$) was purchased from Sigma Aldrich and used as received. Halloysite Nanotubes (HNT) were kindly provided by Applied Minerals Inc. Carbon black (CB, Ketjenblack EC 600) was kindly provided by Akzonobel and used as received. The present study focuses primarily on iPP-xGnP nanocomposites due to the excellent contrast provided by xGnP in optical microscopy, TEM, and SEM.

4.2.2 Processing of Polyolefin Nanocomposites

Melt-Mastication (MM) is performed by compounding a semicrystalline thermoplastic polyolefin-nanocomposite melt over a three-step temperature process similar

to the process described in section 3.2.2 and illustrated in Figure 3.1. In the first step, the polyolefin, nanoparticle, and oxidative stabilizers (0.05 wt% Irganox 1010 + 0.05 wt% Irgafos 168) are melt compounded at a temperature above the melting temperature (T_m) of the polyolefin resin for time t_1 (see Table 4.1) at 70 revolutions per minute (RPM). The nanocomposite melt is then cooled at -3 K/min under continuous mixing to the mastication temperature (T_M), followed by isothermal mixing at T_M for time t_3 . As discussed in section 3.1.2, a large deviatoric strain imposed on a molten semicrystalline polymer near or below T_M promotes flow induced crystallization (FIC), which significantly increases the mixing torque. For PNCs, the higher mixing torque subjects the nanocomposite melt to intense shear and compressive forces, producing enhanced break-up of larger nanoparticle agglomerates.

In this study, MM was applied to several combinations of commodity semicrystalline thermoplastic polyolefins and commodity nanoparticles in order to show the utility of this method. Due to the differences in T_m and T_c for each resin, T_M was experimentally optimized for each resin. The optimal T_M was defined as the process temperature requiring the maximum mixing torque, without allowing the resin to solidify or undergo degradation. Generally, T_M falls within the range $T_c < T_M < T_m$, as is listed in Table 4.1. Also listed is the duration of each step during MM (t_1 , t_2 , t_3). The HDPE resins required longer times to achieve T_M , compared to the iPP resin. All samples were processed at 70 RPM.

Table 4.1: Melt-Mastication parameters for semicrystalline polyolefin resins. Values correspond to Figure 3.1. T_m and T_c were determined via differential scanning calorimetry.

	iPP	LLDPE	HDPE-1	HDPE-2
t_1 (min)	5	5	5	5
t_2 (min)	15	15	20	20
t_3 (min)	5	5	5	5
T_m (°C)	164	125	132	136
T_M (°C)	145	111	121	121
T_c (°C)	112	106	115	116

For reference, control samples were also prepared by conventional melt processing (CMP), or processing above the resin T_m . The polyolefin, nanoparticle, and oxidative stabilizers (0.05 wt% Irganox 1010 + 0.05 wt% Irgafos 168) were combined and processed above T_m at one mixing rate (70, 100, 130, 160, or 190 RPM) for 25-30 minutes. All samples from both Melt-Mastication and CMP were prepared using a Brabender Intelli-Torque Plasti-Corder® Torque Rheometer (C.W. Brabender, unit located at the University of Massachusetts Lowell) with 50 mL capacity. This instrument is equipped with sensors that enable continuous acquisition of the mixing torque, stock temperature, and screw speed. Degradation of iPP during Melt-Mastication and CMP was mitigated through the addition of antioxidant stabilizers, shown in section 3.3.3.

4.2.3 Characterization of PNC Dispersion State

The dispersion quality of iPP-xGnP nanocomposites (2 wt% xGnP) was directly characterized with microscopy techniques. Transmission optical microscopy sample sections were prepared with glass knife microtomy in order to ensure consistent section thicknesses. Thin sections (1 μm x 2 mm x 2 mm) were prepared at room temperature on a Reichert-Jung FC4 Ultramicrotome. For each sample, 5 sections were prepared. A

freshly prepared glass knife was used for each sample. Transmission optical microscopy was conducted on an Olympus optical microscope with DP71 digital camera, operating in transmission mode and 500x magnification (10x eyepiece and 50x objective).

TEM was conducted on a JEOL JEM-2000FX transmission electron microscope with LaB6 electron source, at acceleration voltage 200 kV. Very thin (40 nm) sample sections were prepared at room temperature using a Lecia CryoUltramicrotome and a Micro Star Technologies diamond knife, then imaged on 400 mesh copper grids.

SEM was conducted on a FEI Magellan 400 XHR-SEM. Samples were prepared by immersion in liquid nitrogen followed by fracture. Samples were then chemically etched with established protocols (3 wt% KMnO_4 , 64.7 wt% H_2SO_4 , and 32.3 wt% H_3PO_4) in order to expose crystalline morphologies.²²⁻²⁵ Extreme caution was exercised when performing chemical etching, including use of PPE (lab coat, substantial goggles, gloves, butyl rubber gloves, and face shield) and other safety measures (performed within fume hood with blast shield using long tweezers). Samples were etched for 24 hours, followed by copious washing with distilled water.

Quantitative stereology was performed on optical microscopy images in order to determine the three-dimensional spatial size distribution of agglomerates in 2 wt% iPP-xGnP systems prepared by either Melt-Mastication or CMP. Image analysis and processing was performed with ImageJ image processing software (National Institutes of Health, Bethesda MD, USA).²⁶ Figure 4.2 illustrates the process flow for image analysis and QS. First, the agglomerate section sizes in each image were converted to a binary image with a consistent threshold function in order to calculate $\sum_j(N_a)_{i,j}$, the total number of sections and their sizes from agglomerate spheres of all sizes (steps 1-3). Sample section

areas $< 1 \mu\text{m}^2$ were not considered because of the resolution limitations of the optical microscope. Each sample was sectioned in five different areas of the sample. One optical microscopy image was captured per section, for a total of 5 images per sample. Each image contained ~800-1200 distinguishable nanoparticle agglomerates for a total of ~4000-6000 agglomerates per sample. Next, the QS method explained in section 4.1.4 is applied to the distribution in order to calculate $(N_v)_j$ (steps 4-6). An excel spreadsheet was developed to automatically perform the iterative calculations in step 5. Finally, $(N_v)_j$ was tabulated in linear logarithmically spaced bin sizes according to the method established by Saltykov. Linear logarithmically spaced bin sizes have been found to be the most rational scale for the distribution of particles because it allows the finest subdivisions occur at small diameters, where the distribution concentrates.

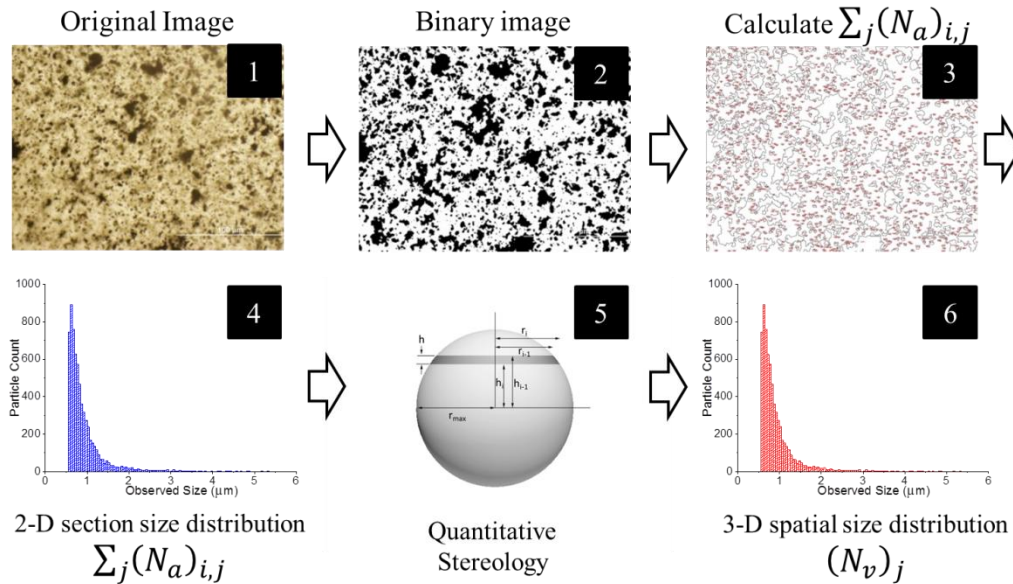


Figure 4.2: Illustration of the process flow for image analysis and Quantitative Stereology of 2 wt% iPP-xGnP nanocomposites.

Thermal and mechanical properties were measured using a Differential Scanning Calorimeter (TA Instruments-DSC Q200) a Dynamic Mechanical Analyzer (TA Instruments-DMA Q800), and a Thermal Gravimetric Analyzer (TA Instruments-TGA Q500). Calorimetry was performed from 20 to 215 °C for iPP, and 20 to 180 °C for HDPE and LLDPE, with a constant ramp rate of 10 °C/min. Two heating and cooling cycles were used. Crystallization and melting analyses were performed on the first cooling and the second heating ramps, respectively. Melting enthalpies were normalized to the mass of polyolefin in each sample. Samples for DMA (30 x 10 x 0.5 mm) were cut from 0.5 mm thick plaques and analyzed at a constant frequency of 10 Hz, oscillation amplitude 0.05% strain, and over a temperature range of 0 to 150 °C, ramp rate 3 °C/min. DMA samples were performed in triplicate. Thermal gravimetric analysis was used to verify the

nanoparticle loading in each sample, and was performed in a nitrogen atmosphere at a heating rate of 10 °C/min

Rheological properties were characterized with an AR-2000 rheometer (TA Instruments) with 25 mm parallel plate geometry. Samples were prepared by compression molding 1 mm thick plaques, followed by cutting 25 mm diameter sample disks from the plaques. Samples were analyzed under small amplitude oscillatory shear in the linear viscoelastic regime, over a frequency of 0.1-600 rad/s at 165 °C for HDPE and 1% strain. Strain sweep analysis showed that 1% strain is within the linear viscoelastic regime.

Conductivity measurements were performed via impedance spectroscopy through a custom electrode assembly and automation software reported elsewhere.²⁷ Samples of dimensions 1.6 mm x 20 mm x 20 mm were prepared by compression molding followed by diamond saw cutting. The sample surfaces were prepared by first polishing with a 9 µm polishing cloth, followed by gold sputter coating for 120 s. Care was taken to avoid gold coating the sample edges. Finally, copper conductive tape was adhered on the sample surfaces. Samples were compressed between two gold-coated stainless steel electrodes, area $A = 0.07971 \text{ cm}^2$. Through plane impedance spectroscopy was performed at room temperature using a Solartron 1260 Impedance/Gain Phase Analyzer over a range of 0.1 Hz to 10 MHz in logarithmic steps over 10 points per decade. The low-frequency portion of the impedance magnitude vs frequency spectrum forming a “plateau” was fitted to a constant magnitude function and interpreted as the bulk resistance R . The conductivity was then computed according to:

$$\sigma = \frac{t}{AR} \quad (4.2)$$

Where σ is the conductivity, A is the cross-sectional area of the electrode, and t is the sample thickness.

4.3 Results and Discussion

Herein, Melt-Mastication (MM) is evaluated as a method to achieve improved dispersions in semicrystalline polyolefin-nanocomposites compared to conventional methods. Particular focus was placed on an isotactic polypropylene-xGnP nanocomposite system due to the excellent contrast of xGnP in optical microscopy, TEM, and SEM. Several other nanocomposites were prepared with MM and analyzed to a lesser extent in order to demonstrate the utility of MM.

4.3.1 Characterization of Dispersion State via Thermal Analysis

Differential scanning calorimetry was used to indirectly characterize the nanoparticle dispersion quality in iPP, HDPE, and LLDPE nanocomposites. The nanoparticles used in this study (Fumed Silica (FS), Halloysite Nanotubes (HNT), and Exfoliated Graphite Nanoplatelets (xGnP)) are all known nucleating agents for polyolefins^{13,28,29}. The nanoparticles have dissimilar surface chemistries (xGnP = Non-polar surface chemistry; HNT, FS = Polar surface chemistry). The non-isothermal crystallization transition (T_c) of semicrystalline polymers in the presence of these nanoparticles is expected to increase with higher particle loading and/or improved dispersion.

The cooling scans of HDPE-xGnP nanocomposites prepared by Melt-Mastication (MM) and conventional melt processing (CMP) are shown in Figure 4.3 and Table 4.2 (used HDPE-2). The results indicate that the xGnP-filled samples demonstrate increased

T_c and % crystallinity (χ_c) relative to the virgin resin. Further increases in T_c are observed for nanocomposites prepared with MM (121.5 °C) compared to CMP (118.2 °C). The same is true for iPP nanocomposites with xGnP, FS, and HNT (Figure 4.4 and Table 4.3). In all cases, the polyolefin nanocomposites demonstrate increased T_c when treated with MM compared to CMP. As expected, the results show that nanoparticles serve as nucleating agents within semicrystalline polymer melts, and that MM further improves the dispersion quality. Also, MM demonstrated efficacy for several PNC compositions with varying nanoparticle surface chemistry. Considering that MM is a mechanical process that promotes dispersion through intense mixing shear, it is not surprising that its efficacy is independent of nanoparticle surface chemistry.

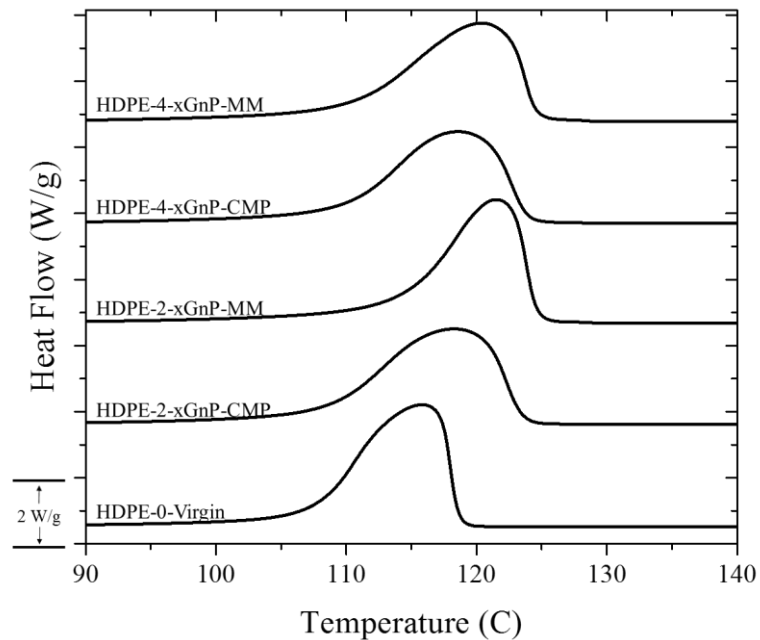


Figure 4.3: DSC cooling scans of HDPE-xGnP nanocomposites.

Table 4.2: Non-isothermal crystallization temperatures of HDPE-xGnP nanocomposites

Sample	Crystallization Temperature T_c ($^{\circ}\text{C}$)	% Crystallinity ^a
HDPE-4-xGnP-MM	120.4	86.3
HDPE-4-xGnP-CMP	118.5	84.3
HDPE-2-xGnP-MM	121.5	85.2
HDPE-2-xGnP-CMP	118.2	83.6
HDPE-0-Virgin	118.6	69.2

^a HDPE heat of fusion =295.5 J/g

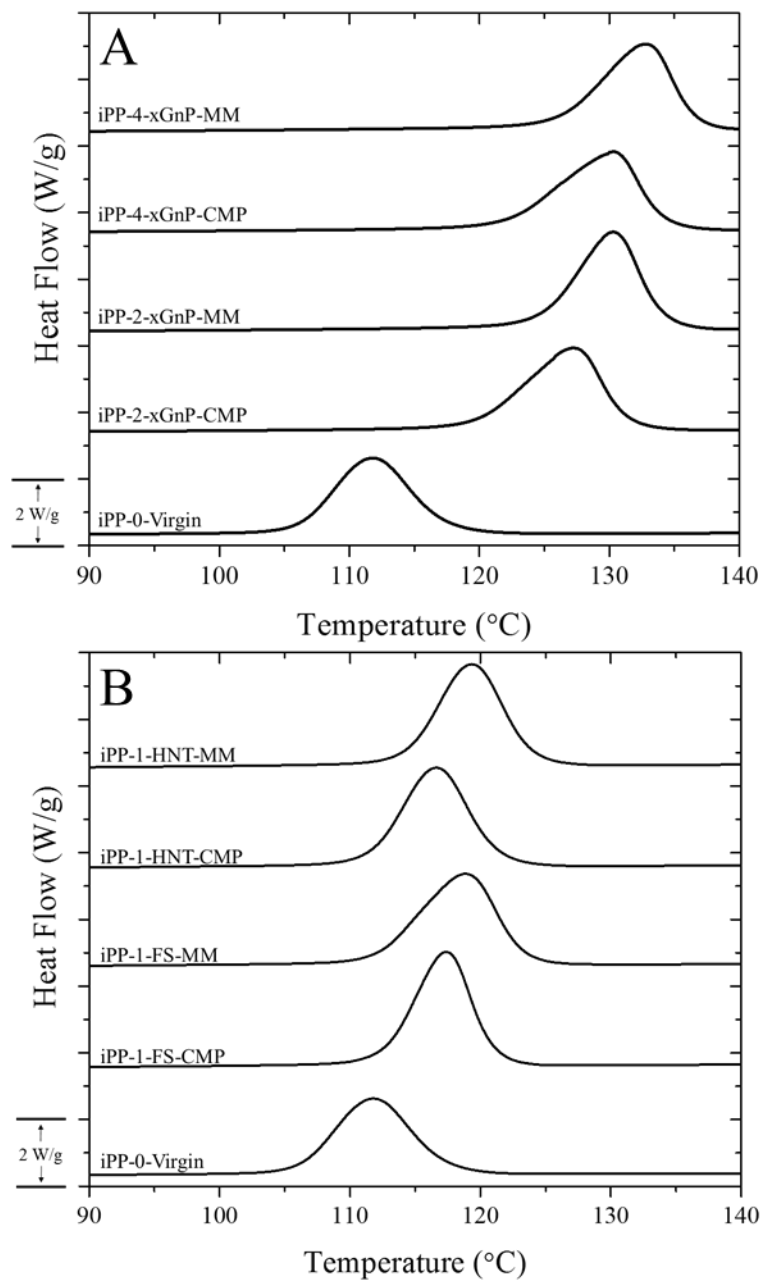


Figure 4.4: DSC cooling scans of iPP nanocomposites.

Table 4.3: Non-isothermal crystallization temperatures of iPP nanocomposites

Sample	Crystallization Temperature T_c ($^{\circ}\text{C}$)	% Crystallinity ^a
iPP-4-xGnP-MM	132.9	56.3
iPP-4-xGnP-CMP	130.4	57.0
iPP-2-xGnP-MM	130.3	55.9
iPP-2-xGnP-CMP	127.2	55.8
iPP-1-HNT-MM	119.3	55.7
iPP-1-HNT-CMP	116.6	56.6
iPP-1-FS-MM	118.9	56.6
iPP-1-FS-CMP	117.4	55.1
iPP-0-Virgin	111.7	48.7

^a iPP Heat of Fusion = 207.1 J/g

In contrast, the crystallization data of LLDPE-xGnP PNCs does not indicate the same behavior. Figure 4.5 and Table 4.4 show that LLDPE-xGnP PNCs demonstrate increased T_c relative to the virgin resin, but no dependence on the preparation method. Instead the presence of xGnP causes the crystallization peak to broaden significantly. The crystallization behavior is likely a consequence of the branched chain architecture of LLDPE, which frustrates crystallization. Furthermore, LLDPE does not undergo FIC as readily as more highly crystalline resins like HDPE and iPP, making it is more difficult to increase the mixing shear during MM of LLDPE. It follows that MM is a less efficient means to promote nanoparticle dispersion in LLDPE compared to HDPE and iPP.

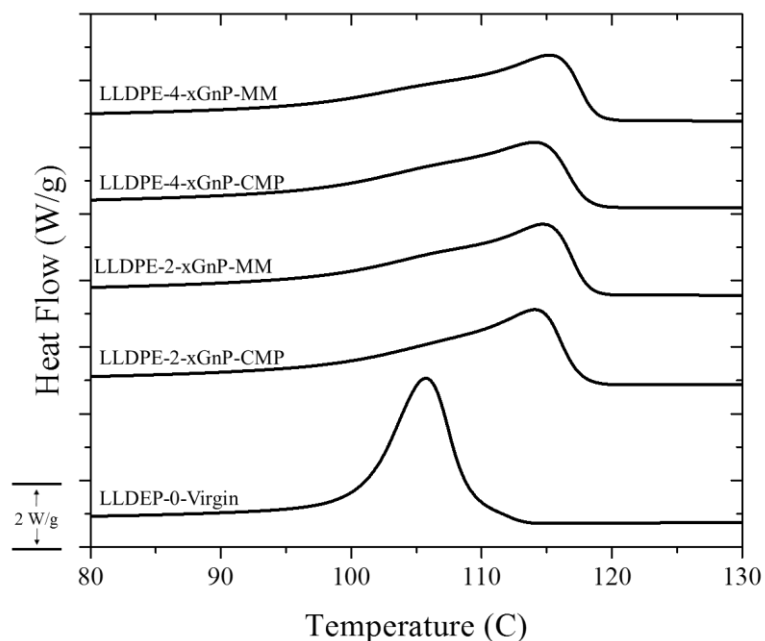


Figure 4.5: DSC cooling scans of LLDPE-xGnP nanocomposites.

Table 4.4: Non-isothermal crystallization temperatures of LLDPE-xGnP nanocomposites

Sample	Crystallization Temperature T_c ($^{\circ}\text{C}$)	% Crystallinity ^a
LLDPE-4-xGnP-MM	115.2	53.7
LLDPE-4-xGnP-CMP	114.0	55.6
LLDPE-2-xGnP-MM	115.1	52.6
LLDPE-2-xGnP-CMP	114.0	54.8
LLDPE-0-Virgin	105.7	54.4

^a HDPE heat of fusion = 295.5 J/g

Dynamic mechanical analysis was used to characterize the reinforcement efficiency of xGnP in polyolefin PNCs, which can be an indirect indication of the dispersion state. Previous work by Drzal *et al.* studying similar iPP-xGnP systems reported an 18% improvement in mechanical storage modulus with 2 wt% xGnP.³⁰⁻³³ However in the

present study, no significant change in mechanical modulus was observed for iPP- and HDPE-xGnP nanocomposites at loadings up to 4 wt%, show in Figure 4.6. The discrepancy in properties could be due to differences in sample preparation.³³ In the work reported by Drzal *et al.*, samples were prepared via injection molding with 1.1 MPa injection pressure. The authors noted that the injection molding process induced uniaxial orientation of xGnP nanoparticles, which likely contributes to reinforcement through load transfer, or altering the orientation of the crystal morphology. Samples in the present study were prepared via mild compression molding, which will produce isotropic materials, perhaps with mild biaxial orientation. Further, microscopy results in the present study did not reveal any nanoparticle orientation. Accordingly the present results suggest that DMA is not an appropriate technique for characterizing the dispersion state of polyolefin-xGnP PNCs at such low xGnP loadings.

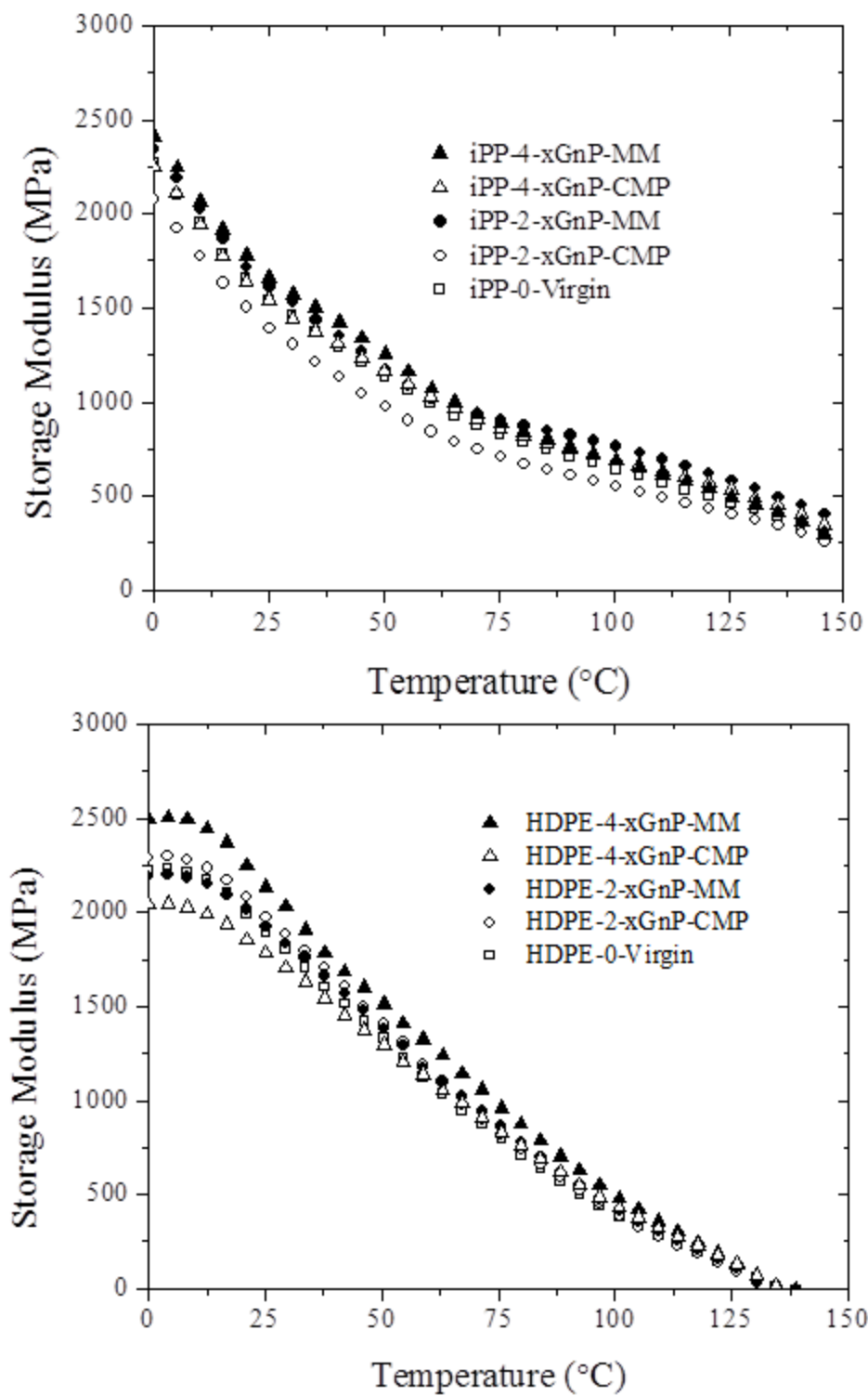


Figure 4.6: Dynamic mechanical analysis of polyolefin-xGnP nanocomposites.

4.3.2 Rheology

Rheology was used as an indirect method to evaluate nanoparticle agglomeration within xGnP-HDPE composites prepared by MM and CMP, illustrated in Figure 4.7. Rheology was used to characterize the percolation threshold, or the nanoparticle loading at which the PNC melt demonstrates a solid-like response at low frequency. For PNC melts below the percolation threshold analyzed at low frequency, the mechanical response of the melt is from the continuous polymer phase, and the storage modulus increases modestly with increasing nanoparticle volume fraction due to hydrodynamic effects.³⁴ In contrast, PNC melts above the percolation threshold demonstrate a significant increase in the low frequency storage modulus, presumably due to the formation of continuous particle networks. Drzal *et al.* showed the percolation threshold of xGnP in polyolefin melts prepared by twin screw extrusion is near 34 wt%.³⁵

Interpretation of the relationship between the dispersion state and percolation threshold of PNCs must be done with consideration of the type of nanoparticle being analyzed. The geometric and morphological characteristics of the nanoparticle can influence the manner in which the nanoparticle agglomerates, particularly with respect to the formation of percolated networks. For example, highly structured nanoparticles such as fumed silica require agglomeration to form percolated structures at relatively low loadings (~3 vol%).¹⁵ In contrast, agglomeration of platelet-shaped nanoparticles hinder the formation of percolated networks. In the latter case, a decrease in the percolation threshold indicates an improvement in dispersion quality.¹⁶

The results in Figure 4.7 indicate that MM decreases the percolation threshold of HDPE-xGnP nanocomposites, suggesting an improvement in dispersion quality. At higher

concentration (18 wt%), the composite prepared by MM demonstrates a solid-like response at low frequency, whereas the composite prepared by CMP does not. In fact, much higher loadings are required for composites prepared by CMP to demonstrate a solid-like response at low frequency. Additionally, all nanocomposites below the percolation threshold prepared by MM demonstrate higher storage modulus compared to composites prepared by CMP. These results suggest MM produces PNCs of superior dispersion quality, causing the percolation threshold to decrease.

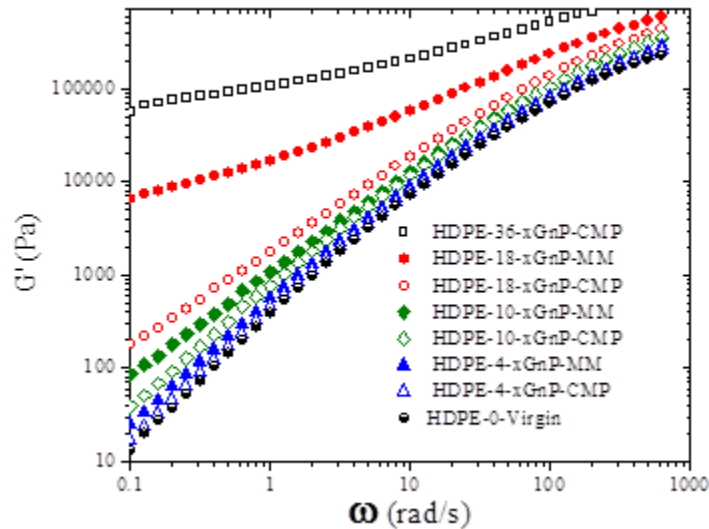


Figure 4.7: Rheological storage modulus vs angular frequency of HDPE-xGnP nanocomposites of various loadings (0 to 36 wt%).

4.3.3 Impedance Spectroscopy

Another method to characterize the percolation threshold of PNCs is through conductivity measurements. Similar to section 4.3.2, the electrical percolation threshold is the nanoparticle loading characterized by a sudden increase in conductivity. PNC melts below this threshold are poorly conductive, and the conductivity is relatively insensitive to filler concentration. Above the percolation threshold, the nanoparticles are able to form

percolating conductive pathways, resulting in a significant increase in conductivity by several orders of magnitude. In the present study, conductivity tests were performed on iPP-carbon black PNCs due to the excellent conductivity and fractal structure of carbon black.³⁶ Exfoliated Graphene Nanoplatelets (xGnP) were avoided in the present study due to the surprisingly high electrical percolation threshold of xGnP-PNCs when prepared by extrusion.³⁷ Intuitively, xGnP and CB are both high surface area, graphitic nanoparticles and should both readily facilitate conductivity, however CB is known to have a highly fractal structure, which facilitates the formation of three-dimensional conductive networks.

The conductivity results in Figure 4.8 show the conductivity of three iPP-CB (5.5 wt%) composites prepared by different techniques. The sample prepared by CMP is poorly conductive, and apparently below the percolation threshold. In contrast the samples prepared by MM are ~10,000x more conductive, suggesting they are above the percolation threshold. Because all materials have the same CB loading, the differences in conductivity must be due to changes in the dispersion state. Surprisingly, the sample prepared by MM followed by forging demonstrates a lower conductivity than the sample prepared by MM and then re-melted. This is likely due to the altered crystal structure in the former sample. The results show that MM reduces the electrical percolation threshold of iPP-CB composites, indicating an improved dispersion quality.

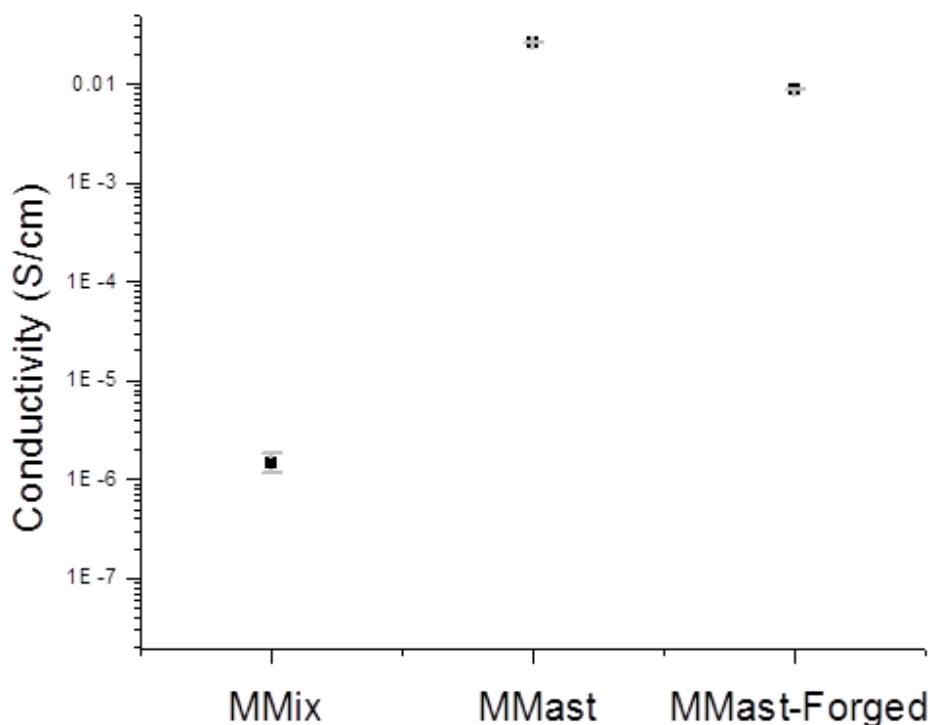


Figure 4.8: Conductivity of 5.5 wt% iPP-Carbon Black PNCs measured by impedance spectroscopy. Samples were prepared by conventional melt processing (CMP), Melt-Mastication (MM), or Melt-Mastication and forging (MM-Forged).

4.3.3 Microscopy

Optical microscopy in transmission mode was used to qualitatively compare the dispersions of a iPP-xGnP (2 wt%) sample prepared by Melt-Mastication (MM, 154°C_70 RPM), and a sample prepared by conventional melt processing (CMP, 200°C_70 RPM). Both samples were processed for the same residence time and mixing rate, hence both samples experienced the same total shear strain, or number of mixing cycles. However, sample 154°C_70 RPM required significantly higher mixing torque during the MM step, shown in Table 4.4. Optical microscopy shows that each sample comprises discrete, black

xGnP nanoparticle agglomerates within a continuous transparent iPP phase, shown in Figure 4.9. The apparent agglomerate section sizes range from ~ 0.5 to $15 \mu\text{m}$ in radius.

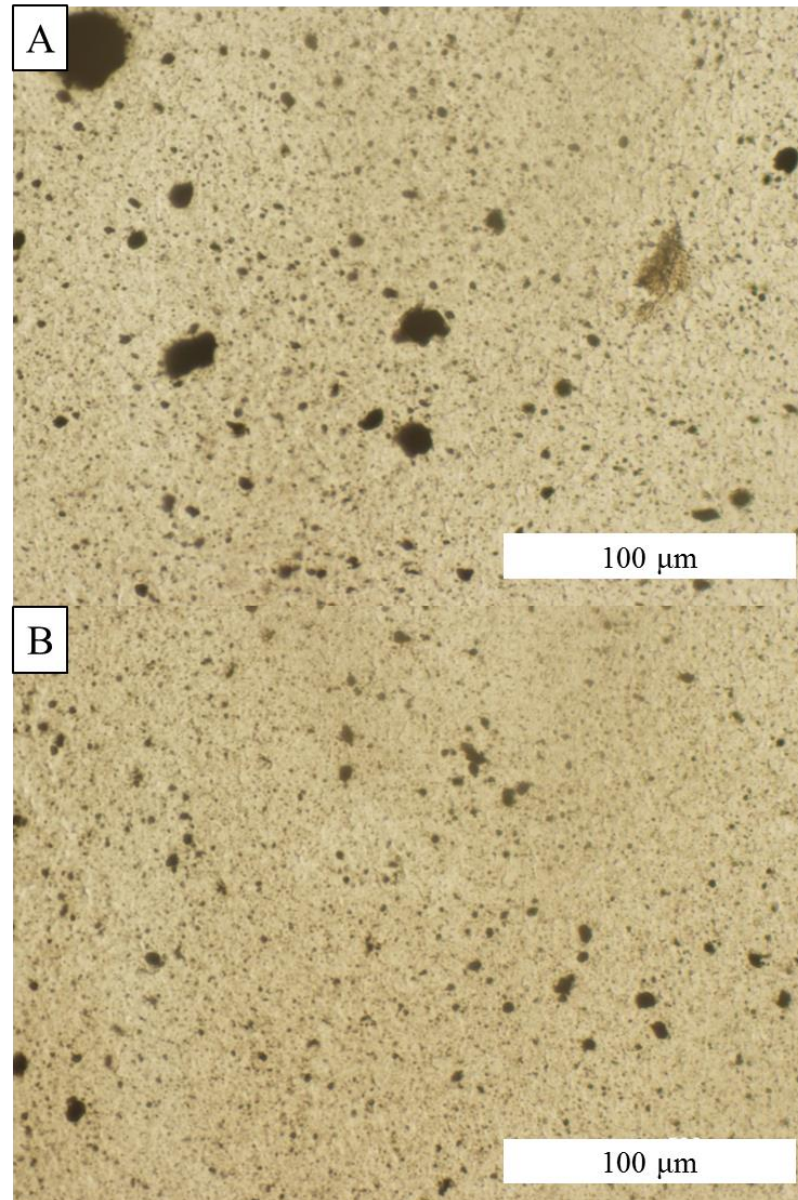


Figure 4.9: Optical microscopy of iPP-xGnP (2 wt%) PNCs. A: Sample prepared by CMP (200 °C_70 RPM). B: Sample prepared by MM (154°C_70 RPM).

Sample 154°C_70 RPM appears to have the best xGnP dispersion. The population of large agglomerate sections (radius $r > 5 \mu\text{m}$) apparent in sample 200°C_70 RPM are absent in sample 154°C_70 RPM. However the effect of MM on the smaller ($r < 0.5 \mu\text{m}$)

xGnP agglomerates is not clear from this technique due to the resolution limitations of the optical microscope. In the next section, these images will be analyzed with quantitative stereology in order to derive a statistical distinction between samples.

Transmission electron microscopy (TEM) was used to evaluate the dispersion state of the smaller ($r < 0.5 \mu\text{m}$) population fraction of nanoparticle agglomerates. TEM of samples 154 °C/70 RPM and 200 °C/70 RPM does not show an apparent distinction between the character of the nanoparticle agglomerates (Figure 4.9). Both samples have the expected platelet morphology and dimensions for xGnP, with diameter 100-500 nm, and thickness ~ 10 nm. The precise nanoparticle diameter cannot be accurately determined by this technique, as the apparent diameter is affected by the position and orientation of the nanoparticle relative to the microtome cut. Nanoparticles oriented parallel to the beam direction show the most contrast. The dark features observed in the center of the platelets at 100,000x are common features in expanded graphites and are ascribed to localized highly crystalline graphitic regions.³¹ These regions are a consequence of the xGnP fabrication procedure. Nanoparticles appear to be aggregated into 100-300 nm diameter agglomerates, and the agglomerate sizes appear independent of process conditions. Apparently, MM is not decreasing the agglomerate size at the length scale of TEM. Furthermore, MM does not appreciably exfoliate individual xGnP nanoparticles, as the nanoparticle thickness appears independent of process conditions. Other, more intense solid-state physical processing strategies like SSSP report exfoliation of graphitic nanoparticles.⁵

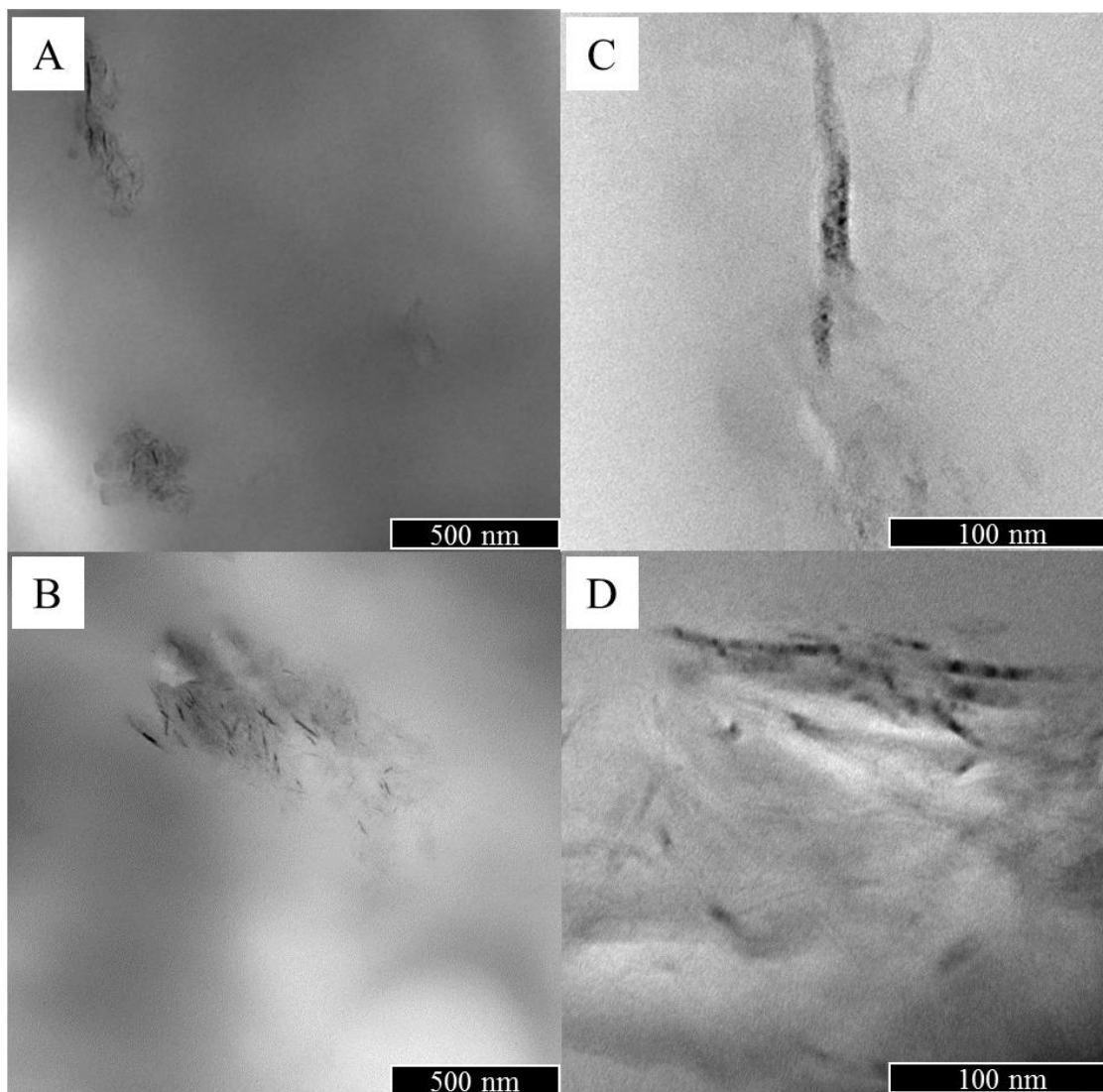


Figure 4.10: TEM images of iPP-xGnP (2 wt%) PNCs.
 A: CMP (200°C_70 RPM), 15,000x magnification, B: MM (154°C_70 RPM), 15,000x.
 C: CMP (200°C_70 RPM), 100,000x. D: MM (154°C_70 RPM), 100,000x.

Scanning electron microscopy was used to understand how xGnP influences the crystal morphology of iPP-xGnP PNCs. Thermal characterization in section 4.3.1 established that xGnP nucleates iPP crystals. A previous optical microscopy study by Drzal *et al.* showed that nucleation in iPP-xGnP systems occurs at the iPP-xGnP interface, followed by crystal growth radially outward from the interface.¹³ It follows that the iPP crystal morphology should show a radial crystal pattern, with xGnP at the center.

Isotactic Polypropylene-xGnP samples were treated with a chemical etching procedure so as to expose the crystalline regions, and the resulting images are shown in Figure 4.11. The image shows a 500nm x 100nm xGnP agglomerate, surrounded by iPP crystals. Some of the iPP crystals resemble terraced features, which is a consequence of the lamellar crystal structure inherent to iPP. There is also a radial arrangement of iPP crystals around the xGnP agglomerate, which suggests that the agglomerate in the image nucleated crystallization. Samples prepared by MM (154 °C/70 RPM) and CMP (200 °C/70 RPM) demonstrated similar crystal morphologies, provided the thermal history was erased after processing.

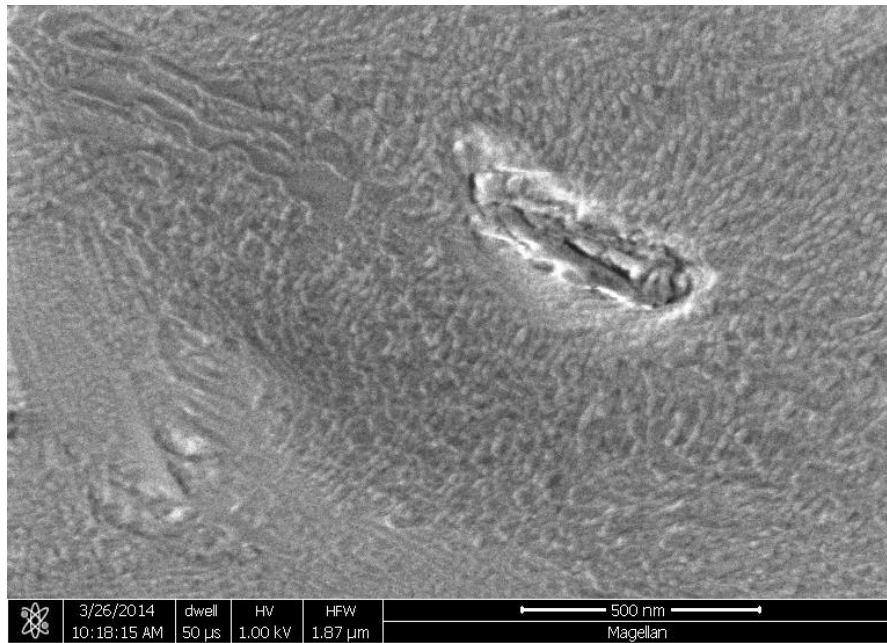


Figure 4.11: SEM image of iPP-xGnP (2 wt%) PNCs treated with chemical etching. Samples prepared by MM (154 °C/70 RPM) and CMP (200 °C/70 RPM) demonstrated similar results.

4.3.4 Quantitative Stereology

Optical microscopy images were analyzed with QS to calculate the three-dimensional spatial size distribution of agglomerates, $(N_v)_j$ in each sample. Compared to

visual analysis, QS generates a more thorough understanding of how the PNC dispersion state is affected by processing conditions. In the proceeding discussion, the QS process will first be described with samples 154 °C/70 RPM and 200 °C/70 RPM. Then, QS results from additional samples will be discussed without describing the details of the analysis process.

The two-dimensional section size distributions of samples 154 °C/70 RPM and 200 °C/70 RPM are derived from optical microscopy images similar to Figure 4.9 using image processing software, and the results are plotted in Figure 4.12. Like other small particle distributions, the distribution of agglomerate section sizes is expected to follow a lognormal distribution, with appears as a Gaussian distribution when plotted against logarithmically spaced bin sizes.^{18,38} Figure 4.12 resembles a partial Gaussian distribution truncated at $r = 0.5 \mu\text{m}$, which is a consequence of the resolution limitations of the optical microscope. Despite the resolution limitations, there are still quantitative distinctions between the distributions of samples 154 °C/70 RPM and 200 °C/70 RPM. Generally, sample 154 °C/70 RPM contains more sections of small diameter, while sample 200 °C/70 RPM contains more of the largest diameter sections. The crossover point when comparing the distributions is near $r = 1.7 \mu\text{m}$. Apparently, the processing conditions of MM which promote higher mixing shear stresses produce smaller agglomerates of nanoparticles when compared to CMP.

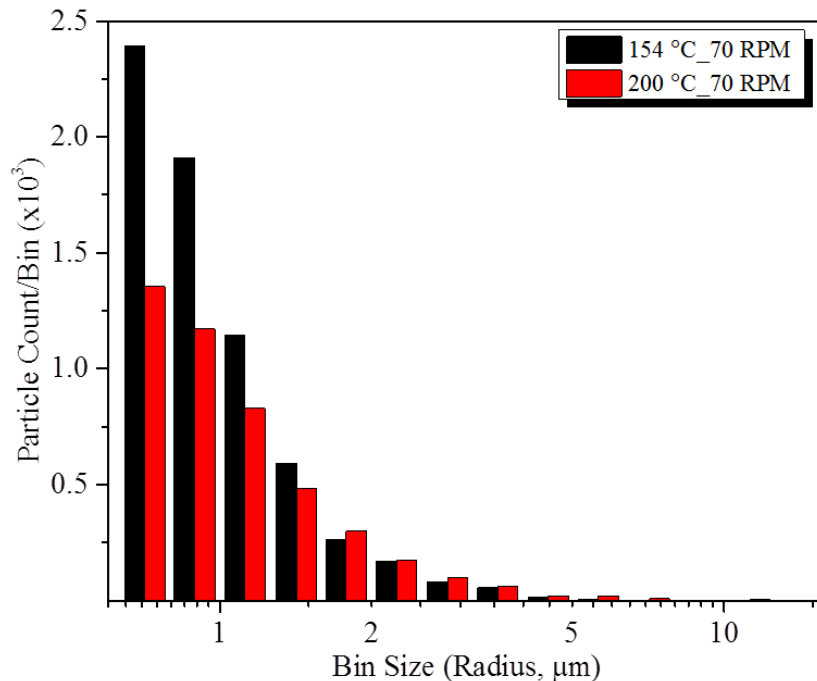


Figure 4.12: Two-dimensional section size distribution of xGnP agglomerates.

Next, the QS method described in section 4.1.4 is applied to the data in Figure 4.12 in order to calculate the three-dimensional spatial size distribution, and the results are shown in Figure 4.13. Like Figure 4.12, the resulting distributions resemble truncated Gaussian distributions. Accordingly, a Gaussian function was fitted to each distribution, assuming the smallest bin size is the maximum value, and that the truncated distribution is symmetrical to the plotted distribution. The standard deviation of the fitted distribution of sample 154 °C/70 RPM is more narrow compared to sample 200 °C/70 RPM (0.31 and 0.39 μm , respectively). The contrast between these two samples is further illustrated by the differential distribution shown in the inset of Figure 4.13. The differential histogram is sample 200 °C/70 RPM from sample 154 °C/70 RPM, so positive values indicate agglomerate populations that are greatest in sample 154 °C/70 RPM, and negative values indicate agglomerate populations greatest in sample 200 °C/70 RPM. Considering both

samples have identical volume fraction of xGnP particles, the results show that the elimination of few, large ($r > 1.7 \mu\text{m}$) agglomerates from sample 200 °C/70 RPM creates many small ($r < 1.7 \mu\text{m}$) agglomerates in sample 154 °C/70 RPM. In other words, the inset of Figure 4.14 shows which agglomerate size populations were eliminated, and which were created in sample 154 °C/70 RPM, relative to sample 200 °C/70 RPM. Another way to understand the distribution differences is through presenting the data as volume fraction of xGnP agglomerates within each bin size (Figure 4.14). For sample 200 °C/70 RPM, the agglomerate volume is heavily weighted toward a few extremely large ($r > 5 \mu\text{m}$) agglomerates.

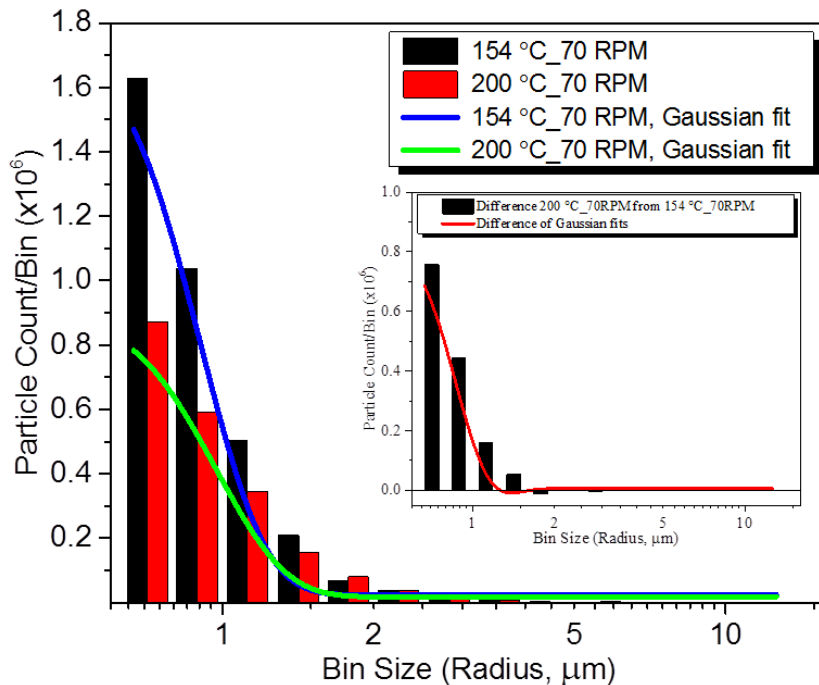


Figure 4.13: Three-dimensional spatial size distribution of xGnP agglomerates. Inset: Differential particle size distribution (200 °C/70 RPM from 154 °C/70 RPM).

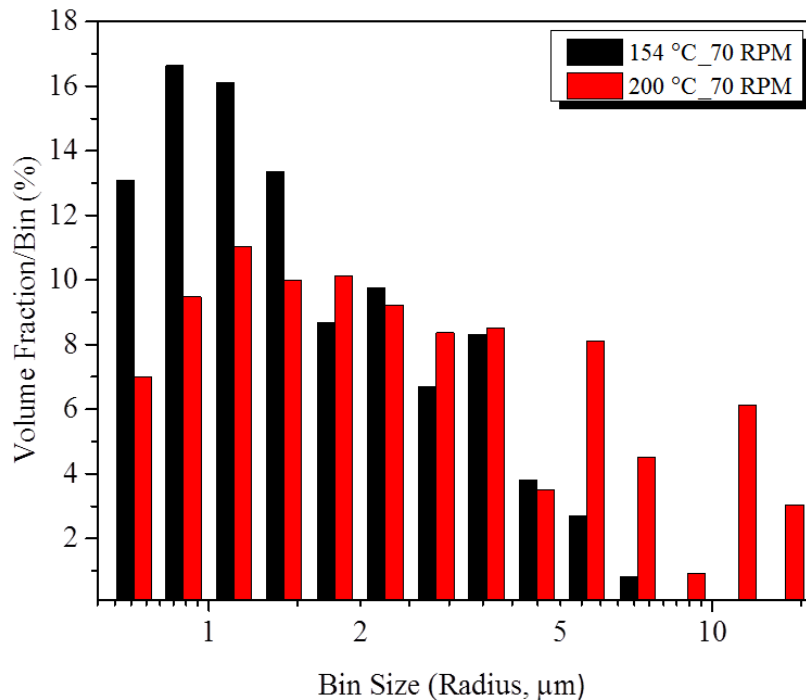


Figure 4.14: Volume fraction distribution of xGnP agglomerates.

The processing parameters were varied across additional iPP-xGnP samples in order to ascertain the effect of the processing conditions on the dispersion quality. Each sample was processed by either MM or CMP, followed by the same optical microscopy and QS analysis described previously. The processing parameters investigated were the mastication temperature (T_M), which affects the mixing shear stress, and the mixing rate (RPM) which affects the shear rate. All samples were processed for 20 minutes, therefore samples with the highest mixing rate also experienced the most mixing cycles (RPM * 20 min), which is an indication of the total strain. The process parameters of the additional samples are recorded in Table 4.5, along with the steady state mixing torques measured during processing. The steady state mixing torque is the maximum sustained mixing torque observed after the material fully melts. As discussed in the previous chapter, MM promotes FIC, which requires a substantial increase in the steady state mixing torque as the

temperature approaches T_M . The apparent range of T_M for FIC to occur is $180\text{ }^\circ\text{C} > T_M > 154\text{ }^\circ\text{C}$. Even within this range, FIC appears to be promoted most at the lowest T_M . However, processing temperatures below $154\text{ }^\circ\text{C}$ promoted excessive degradation. Also, processing times greater than 20 minutes, and shear rates above 190 RPM did not improve the dispersion quality and caused degradation.

Table 4.5: Processing parameters of iPP-xGnP PNCs.
Samples were prepared by either MM or CMP.

Sample Name	T_M ($^\circ\text{C}$)	Mixing Rate (RPM)	Steady State Mixing Torque (Nm)
<u>Melt-Mastication (MM)</u>			
154 $^\circ\text{C}$ _70 RPM	154	70	13.2
165 $^\circ\text{C}$ _70 RPM	165	70	6.5
180 $^\circ\text{C}$ _70 RPM	180	70	3.5
<u>Conventional Melt Processing (CMP)</u>			
200 $^\circ\text{C}$ _70 RPM	200	70	2.6
200 $^\circ\text{C}$ _100 RPM	200	100	2.8
200 $^\circ\text{C}$ _130 RPM	200	130	3.1
200 $^\circ\text{C}$ _160 RPM	200	160	3.5
200 $^\circ\text{C}$ _190 RPM	200	190	3.5

The agglomerate size distribution parameters of the samples in Table 4.5 are plotted in Figure 4.15. Careful inspection of the results shows that the largest agglomerates ($r > 5\text{ }\mu\text{m}$) are most affected by the steady state mixing torque. In other words, as the mixing torque increases, the largest agglomerates are most easily fragmented. This observation is referred to as a scale effect, and is commonly observed in processes involving particle size reductions, such as grinding and comminution.³⁹ As the steady state mixing torque increases, both the agglomerate dispersity and maximum size decrease with increasing mixing torque. Figure 4.15 shows the maximum observed particle size and the standard deviation of the fitted Gaussian functions for each sample distribution. There appears to

be an inverse correlation between the standard deviation and the steady state mixing torque. The standard deviation increased with increasing T_M , and decreased with increasing mixing rate. Likewise, Figure 4.15B shows an inverse correlation between the maximum observed particle size and the steady state mixing torque. Sample 154 °C/70 RPM showed the lowest standard deviation and lowest maximum observed particle size.

The changes in the agglomerate dispersion state in the present study are ascribed to differences in the magnitude of the mixing shear stresses, which are related to the mixing torque. Although shear stresses cannot be directly measured with a torque rheometer, the measured torque is an integral result of the stresses generated during mixing. It follows that because the boundary conditions of the torque rheometer are identical for all samples, the stress fields and their magnitudes are proportional to the measured torque. Thus from the steady state mixing torque data in Table 4.4, it is reasonable to assume that the mixing shear stress experienced by sample 154 °C/70 RPM is ~5 times greater than that experienced by sample 200 °C/70 RPM. In contrast, the mixing shear stress upon sample 200 °C/190 RPM is only ~1.34 times greater than sample 200 °C/70 RPM, due to the shear thinning behavior of iPP melts. Conventional methods to characterize the rheological behavior of polymer melts, such as parallel plate rheology, are not appropriate for the present study due to the transient nature of MM.

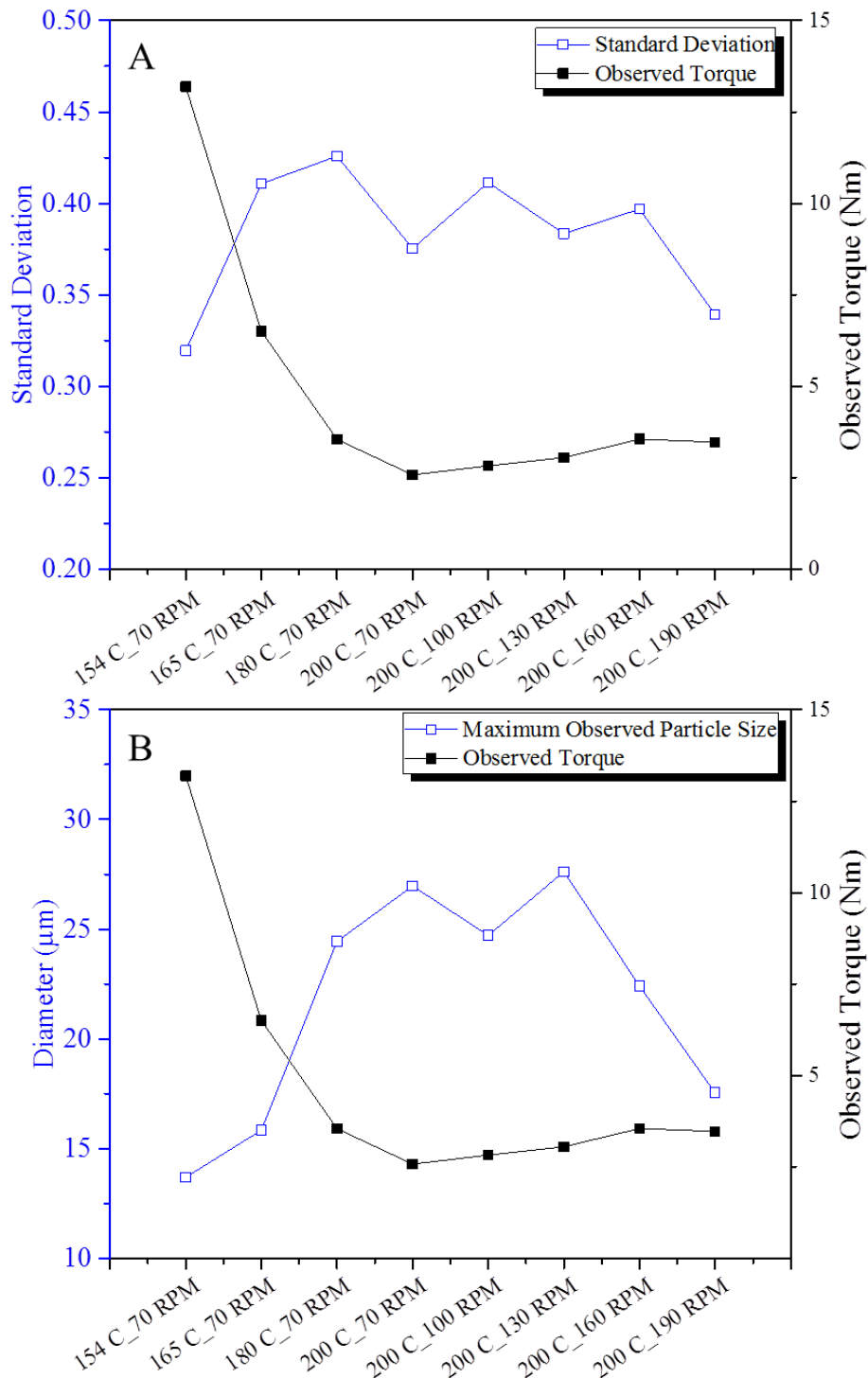


Figure 4.15: Particle size distribution characteristics and observed torque for each iPP-xGnP sample recorded in Table 4.5. A: Standard deviation of fitted Gaussian functions. B: Maximum observed particle size.

The conclusions of the present work offer interesting distinctions from other related works that investigate the effect of processing conditions on the dispersion state of PNCs. For example, studies by Vergnes *et al.* investigated the effect of changing the screw speed and feed rate of extruded PNCs, and they identified the total mixing strain (screw speed * residence time) as the critical parameter controlling the dispersion quality of iPP PNCs.^{9,40} The authors did not report the mixing torque, nor the effect of changing the processing temperature.

In fact, the present study partially supports the assertions of Vergnes *et al.*, because the CMP sample series (samples 200 °C/70 RPM through 200 °C/190 RPM) demonstrated improved dispersion quality with increasing total mixing shear (total mixing cycles = RPM * 20 minutes). Figure 4.16 presents the data in Figure 4.15, plotted against the total mixing cycles. Both the maximum observed agglomerate size and the standard deviation decrease with increasing total mixing cycles. The mixing torque also modestly increases with increasing mixing rate. It is likely that both the total number of mixing cycles and the mixing shear stress affect the dispersive mixing of nanoparticle agglomerates. However, the present study shows that increasing the mixing shear stress is the most effective method to improve the dispersion quality.

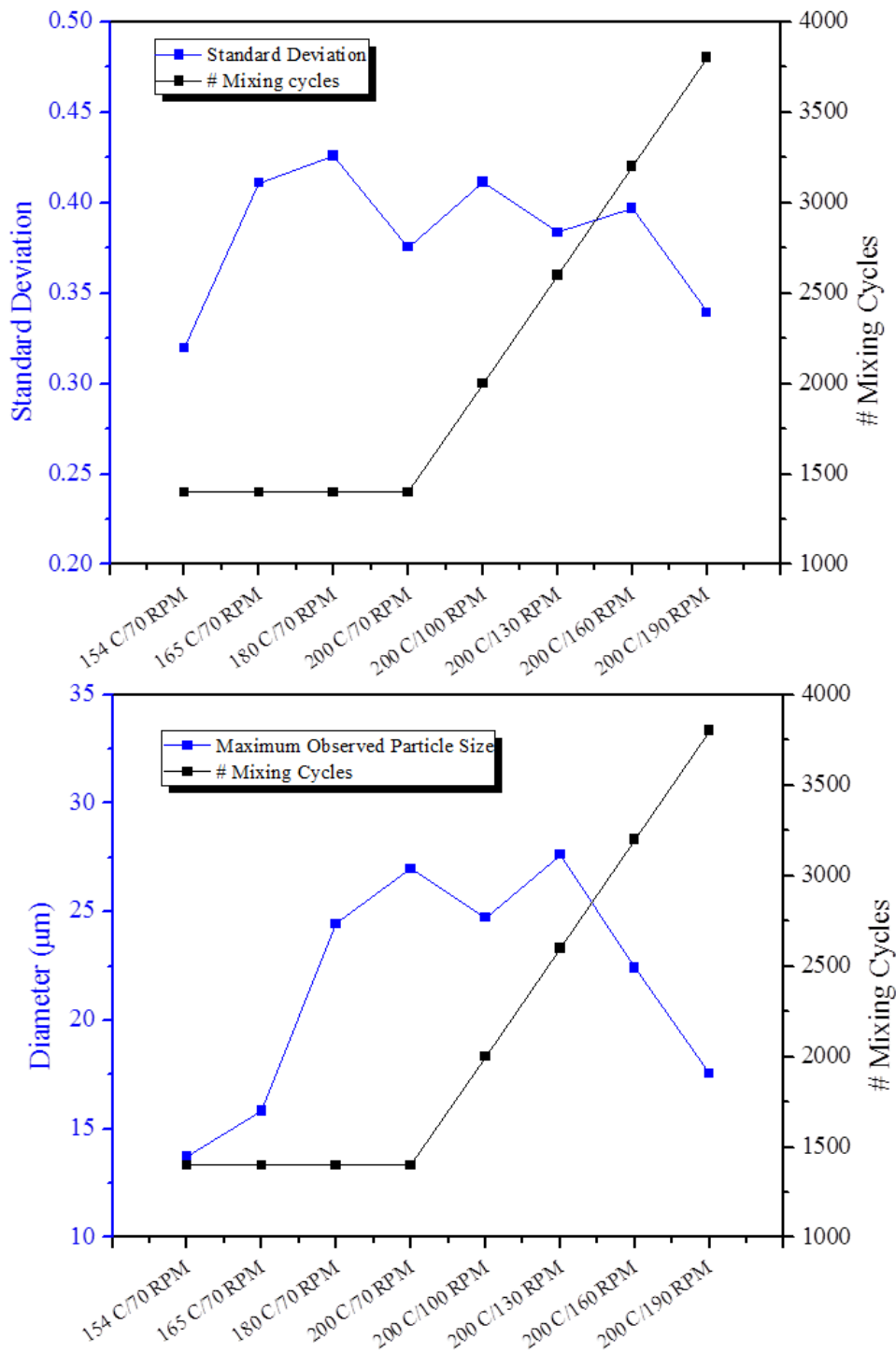


Figure 4.16: Particle size distribution characteristics and number of mixing cycles for each iPP-xGnP sample recorded in Table 4.5. A: Standard deviation of fitted Gaussian functions. B: Maximum observed particle size.

4.3.5 Model for Agglomerate Fragmentation

Presented is a model to describe the mechanism of agglomerate fragmentation during dispersive mixing processes like MM. Dispersive mixing of solid particle systems during polymer processing is an important topic both academically and industrially. For example, the dispersive mixing of carbon black into synthetic rubbers is highly relevant to the automotive tire industry. Accordingly several models describing dispersive mixing of solid agglomerates have already been proposed. However, current models of dispersive mixing do not capture the scale effect observed in the present study in Figure 4.15B, nor in other reports examining fragmentation of small particle systems.^{8,41-43} In other words, current models predict that agglomerate fragmentation is independent of agglomerate size.

Current models for agglomerate fragmentation include models based on stress analysis, fracture mechanics models, and fluid mechanics models. The stress analysis model proposed by Tadmor *et al.* assumes that fragmentation occurs when the hydrodynamic stress imparted by the flowing polymer matrix overcomes the cohesive strength of the agglomerate. In this model, the fragmentation criterion is determined by the ratio between the cohesive strength and hydrodynamic stress. However both the cohesive strength and hydrodynamic stress depend on the size of the agglomerate, so fragmentation is independent of size. Other models based on fracture mechanics and probability theory do capture the scale effect observed in the present study; however these models are not always practical. Fracture mechanics models assume that agglomerate fragmentation occurs when the agglomerates contains a critical flaw size and is exposed to hydrodynamic stresses. These models assume that larger bodies have a greater probability of containing a critical flaw size, and therefore a greater chance of undergoing

fragmentation.⁴⁴⁻⁴⁷ While these models are useful for describing fragmentation in brittle systems, they are not applicable to the present study because they require prior knowledge of the flaw distribution. Finally, models based on fluid mechanics describe the fragmentation of immiscible fluids in definable flow fields.⁴⁸⁻⁵² One model originally proposed by Taylor *et al.* and expanded by Macosko *et al.*, predicts that the fragmentation of immiscible fluids depends on the capillary number of the minority fluid (the fragmenting fluid) and the viscosity ratio between the minority and majority fluids. The model predicts that droplet size is a function of the shear rate, but only when the viscosity ratio between the minority and majority fluids is ≤ 1 .⁵³ However in the present study, the stiffness of the nanoparticle agglomerate is much greater than the viscosity of the molten polymer matrix, therefore fluid mechanics models are not appropriate.

Presented is a model for agglomerate fragmentation that captures the observed scale effect. For a PNC melt, we assume that the fragmentation of agglomerates arises only from the hydrodynamic interactions between the polymer matrix and discrete agglomerates. Fragmentation caused by agglomerate-agglomerate interactions such as collisions are not expected to be a major contributor to the present study, because PNC melts usually have very low concentration of reinforcement (<6 vol%). The proposed fragmentation criterion is the condition where the strain energy stored in a deforming agglomerate meets or exceeds the cohesive energy necessary to induce agglomerate fragmentation, shown in equation 4.3:

$$U \geq \Gamma S' \quad (4.3)$$

Where U is the strain energy, Γ is the surface energy, and S' is the surface area of the deformed agglomerate. The strain energy is an integral sum of the strain energy density

u , where u is a contraction of the stress and strain acting on the agglomerate ($u = \sigma_{ij}\epsilon_{ij}/2$) over the agglomerate volume V . Also, we consider that only distortional energy is imposed on the agglomerate and the agglomerate volume does not change. Accordingly the stress and strain tensors can be written in terms of the octahedral shear stress and strain, respectively.

$$U = \int_V u dv = \frac{1}{2} \int_V \tau_{oct} \gamma_{oct} dv = \frac{G}{2} \int_V \gamma_{oct}^2 dv \quad (4.4)$$

Here, γ_{oct} and τ_{oct} are the octahedral shear strain and stress imparted by the matrix onto the agglomerate, and G is the shear modulus of the agglomerate. The octahedral shear strain and stress are advantageous because they are derived from the second invariant of the deviatoric stress tensor, therefore they will not change as the agglomerate rotates. Finally, the mean octahedral strain is integrated over the agglomerate volume by integrating over a sphere of size R , yielding an expression for the total strain energy in the agglomerate.

$$U = \left(\frac{G}{2} \gamma_{oct}^2 \right) \left(\frac{4}{3} \pi R^3 \right) = \frac{2\pi G \gamma_{oct}^2 R^3}{3} \quad (4.5)$$

As the agglomerate undergoes deformation, its interfacial surface area increases from S to S' as shown in Figure 4.17. Once S' reaches a critical value sufficient to create two or more smaller particles, the agglomerate is considered unstable and fragmentation occurs. As stated in equation 4.3, agglomerate fragmentation is favorable when the total strain energy meets or exceeds a critical surface energy. The lowest energy condition for this to occur is the fragmentation of one agglomerate into two smaller agglomerates, shown

in Figure 4.17. Assuming the agglomerate volume is conserved, a relationship between the radii R and R' may be derived by:

$$\frac{4}{3} \pi R^3 = 2 \left(\frac{4}{3} \pi R'^3 \right) \quad (4.6)$$

$$R' = \frac{R}{2^{1/3}} \quad (4.7)$$

Similarly, the critical surface area may be described in terms of R

$$S = \frac{8\pi R^2}{2^{2/3}} = 2^{7/3} \pi R^2 \quad (4.8)$$

Rewriting equation 4.3 using equations 4.5 and 4.8

$$\frac{2\pi G \gamma_{oct}^2 R^3}{3} = \Gamma \left(\frac{8\pi R^2}{\sqrt[3]{4}} \right) \quad (4.9)$$

$$R = \frac{2^{4/3} 3\Gamma}{G \gamma_{oct}^2} \quad (4.10)$$

Finally, applying the definition of shear stress, $\tau_{oct} = G\gamma = \eta\dot{\gamma}$

$$R = \frac{2^{4/3} \Gamma G}{\left(\eta \dot{\gamma} \right)^2} \quad (4.11)$$

This model predicts that the agglomerate size R is inversely proportional to the square of mixing shear stress. Process conditions that increase the shear stress, such as MM, will generate smaller agglomerate sizes than process conditions that increase the mixing shear or total shear. Therefore, the model explains why sample 154 °C/70 RPM demonstrated a finer dispersion compared to CMP samples such as 200 °C/190 RPM, even

though the latter sample was subjected to more mixing cycles. Figure 4.17 shows that both the maximum agglomerate size and dispersity decrease with increasing mixing torque, which is proportional to shear stress. It follows that the prediction from this model agrees well with the scale effect observed in this study.

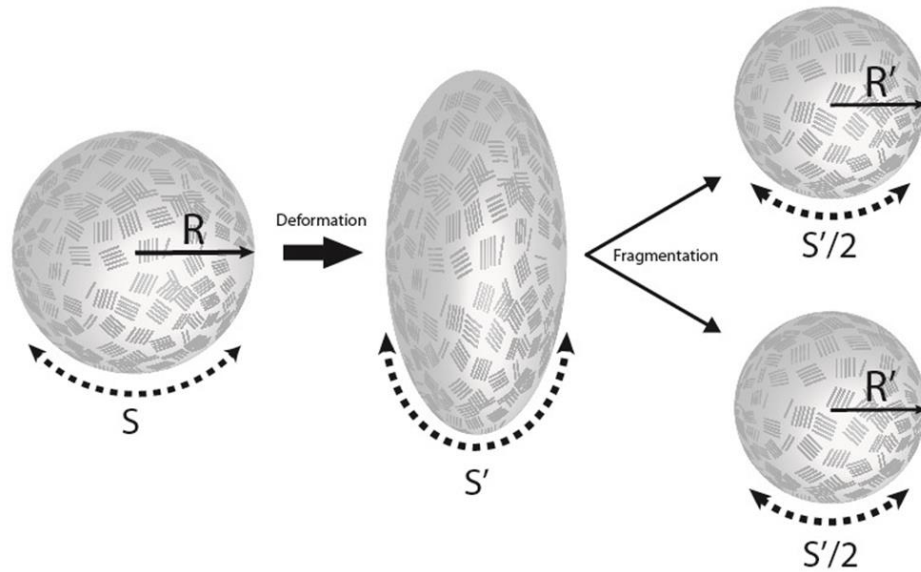


Figure 4.17: Schematic for fragmentation of exfoliated graphene nanoplatelet (xGnP) agglomerates

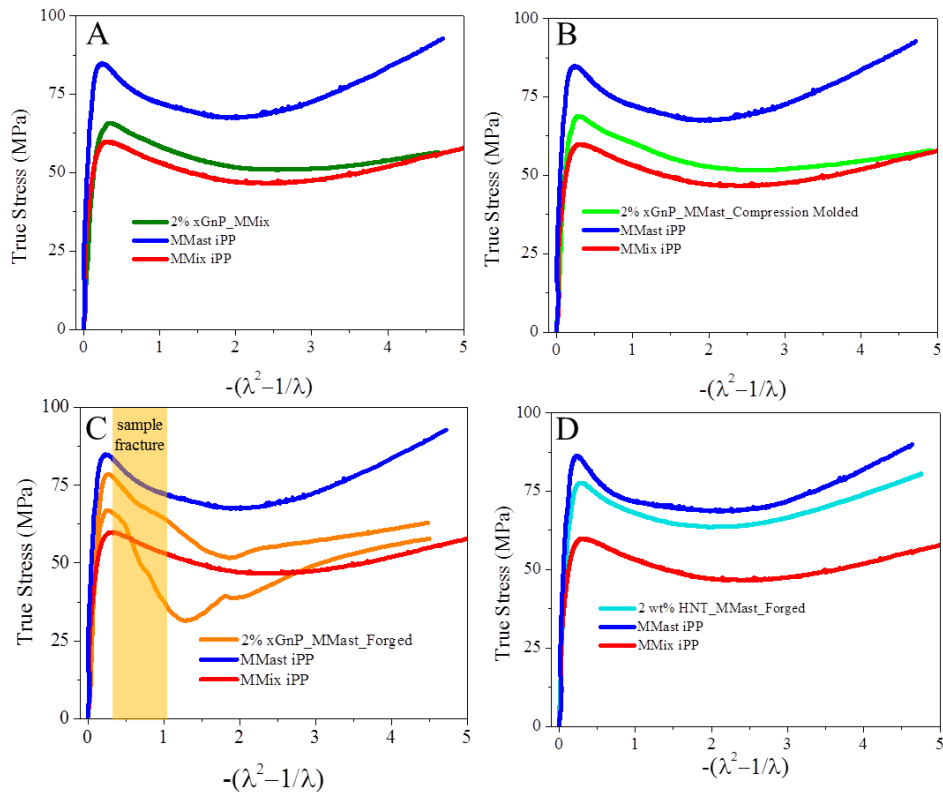
4.3.6 Mechanical properties

4.3.6.1 Uniaxial compression tests

Mechanical properties were evaluated via uniaxial compression tests in a manner similar to section 3.3.6.3. For this study, elements from the previous chapter were combined with nanoparticle reinforcement in the present chapter. Accordingly, samples were prepared either by conventional melt processing (MMix), Melt-Mastication followed by compression molding to erase the thermal history (MMast), Melt-Mastication followed by mild forging to preserve the thermal history (MMast_Forged), and each preparation technique with 2 wt% of nanoparticle loading. Uniaxial compression tests were selected

in order to suppress structural flaws (from nanoparticle agglomerates) such that post-yield behavior may be evaluated. The results are shown in Figure 4.18, and summarized in Table 4.6, where each result reflects three or more samples evaluated. All sample results are plotted alongside the results from pure iPP treated with Melt-Mastication and forging, as well as pure iPP prepared by conventional melt processing (Figure 3.16). Figure 4.18A and 4.18B compare 2 wt% iPP-xGnP nanocomposites prepared by two different techniques. The results from the previous section suggest that xGnP_MMast_Compression molded will have superior dispersion compared to xGnP_MMix. Accordingly, a slight increase in yield stress and modulus is observed, which is commonly seen in nanocomposites with improved dispersion. Figure 4.18C shows the same sample prepared with Melt-Mastication and forging, which demonstrates a significant increase in compressive modulus. The modulus (2.35 GPa) is comparable to the modulus of pure iPP prepared with Melt-Mastication and forging (2.4 GPa), which suggests the mechanical response is dominated by the crystal morphology. Interestingly, sample xGnP_MM_Forged fractured before yielding. This fracture occurred in all three xGnP_MM_Forged compression samples, and did not occur in any other samples. The fracture surface in the billet formed on a 45° angle with respect to the compression plates, which suggests the fracture was a mode II fracture. Moreover, HNT_MM_Forged, another nanocomposite prepared the same way but with a different nanoparticle also did not show fracture. The results suggest that the platelet morphology of xGnP provides weak shear planes that fracture easily along a 45° angle with respect to the compression plates, which is the direction where the sample experiences the most shear stress in uniaxial compression. These kinds of structural flaws are not suppressed in compression. However,

these kinds of failures are not observed in Figure 4.18A-B, which have the same loading and isotropic orientation of xGnP platelets. Apparently, the combination of the unique crystal morphology produced by MM and xGnP platelets leads to weakened shear planes. It is possible the xGnP platelets hinder network connectivity, as evidenced by the apparent decreased strain hardening modulus relative to pure compression molded iPP. It is not clear if this factor contributes to the susceptibility to mode II fracture. In all cases, the highest yield stress and modulus was obtained for pure iPP treated with Melt-Mastication and forging. Apparently, the crystal morphology is the dominant contributor to mechanical properties in iPP polymer nanocomposites prepared by Melt-Mastication and forging.



3

Figure 4.18: Uniaxial compression tests of iPP-nanocomposites prepared by various techniques. Data from Figure 3.16 is also plotted for comparison. A: 2 wt% xGnP in iPP, conventionally melt processed and compression molded. B: 2 wt% xGnP in iPP, Melt-Masticated and compression molded. C: 2 wt% xGnP in iPP, Melt-Masticated and forged. D: 2 wt% HNT in iPP, Melt-Masticated and forged.

Table 4.6: Tabulated results from uniaxial compression tests of Figure 4.18.

Sample	σ_y (MPa)	ϵ_y	E (GPa)	G_R (MPa)
2% xGnP_CMP	65.7	0.1	1.35	3.9
2% xGnP_MM_Compression Molded	68.9	0.09	1.6	3.6
2% xGnP_MM-Forged	N/A	N/A	2.35	N/A
2% HNT_MM_Forged	77.7	0.09	2.27	7.96
Compression Molded iPP	60.6	0.1	1.3	4.9
MM-Forged iPP	85	0.07	2.4	12.9

4.3.6.1 Izod Impact Resistance Tests

Notched Izod impact resistance tests were performed on an instrumented Izod impact tester described in Appendix 1 in order to evaluate the dependence of fracture behavior on preparation technique and presence of nanoparticles. Like the previous section, elements from the previous chapter were combined with nanoparticle reinforcement in the present chapter. Accordingly, samples were prepared either by conventional melt processing (MMix), Melt-Mastication followed by compression molding to erase the thermal history (MMast), Melt-Mastication followed by mild forging to preserve the thermal history (MMast_Forged), and each preparation technique with 0, 1, 2, or 6 wt% of xGnP loading. The results are shown in Figure 4.19, which includes both the impact energy vs displacement curves, as well as the total impact energy for each sample type averaged over 3 samples. The results show that increased nanoparticle loading generally decreases impact resistance, which is expected because nanoparticle agglomerates will provide areas for stress concentrations to occur in the nanocomposite, facilitating failure. Both the maximum impact energy and the displacement at impact are observed to decrease with increasing nanoparticle loading. The highest impact energy and displacement to impact are observed for the pure iPP, closely followed by the 1 wt% xGnP sample treated with Melt-Mastication and forging. The results again suggest the crystal morphology is the dominant contributor to mechanical properties in iPP polymer nanocomposites prepared by Melt-Mastication and forging. However, the premature fracture observed in the previous section for 2 wt% xGnP_MM_Forged is not observed in the present section, which is likely because Izod impact tests do not promote a loading condition that results in mode II failure. Instead, an Izod test promotes sample bending,

which produces nearly tensile deformation in the vicinity of the notch. Theoretically, a crack tip will demonstrate a fully triaxial loading condition; however an Izod notch is not as severe as a crack tip for promoting stress concentration. It follows that the loading condition of the notched Izod test is not conducive to mode II failure, therefore premature mode II failure is not observed in the present test.

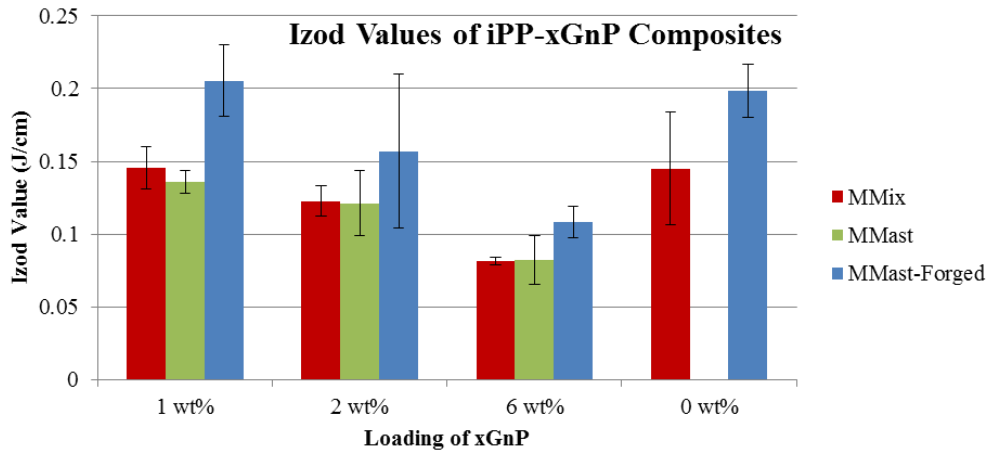
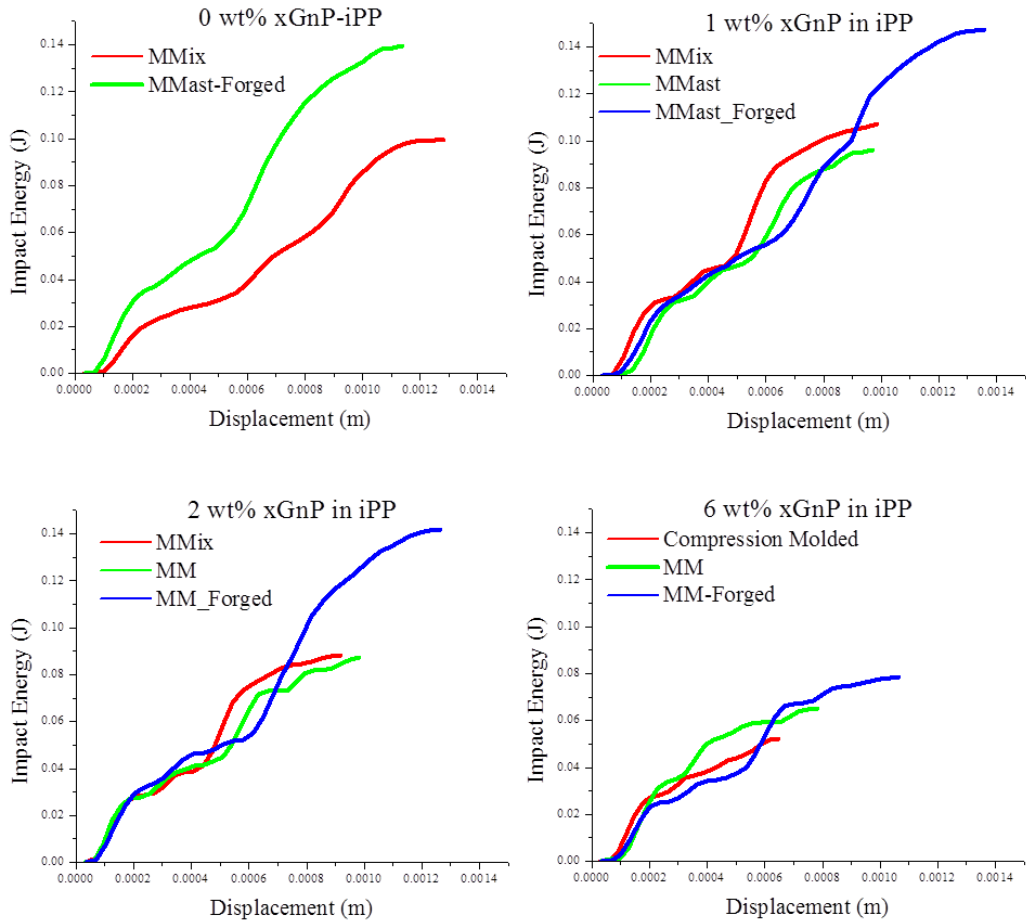


Figure 4.19: Notched Izod impact resistance tests of iPP-xGnP nanocomposites prepared by various techniques. Impact was evaluated on the instrumented Izod impact tester (Appendix 1).

4.4 Conclusions

Presented is an evaluation of a new PNC processing strategy called Melt-Mastication (MM) for PNCs with enhanced nanoparticle dispersions. Compared to a conventional melt processing method (CMP), MM improved the nanoparticle dispersion states in semicrystalline polyolefins with xGnP, FS, HNT, and CB. The parameters of MM and CMP were systematically varied in order to identify the combination of process conditions that produces the finest nanoparticle dispersion. The dispersions produced by each preparation technique were evaluated by several direct and indirect characterization methods, including a quantitative stereological treatment. The results showed that the dispersity and size of the agglomerate distributions decreased as the processing conditions were adjusted to increase the mixing torque, and therefore mixing shear stress. A mechanism for agglomerate fragmentation was proposed and discussed with respect to the results. The dispersion quality and mixing torque were most improved when samples were treated with MM.

4.5 Notes

Portions of this work were previously published by the author.⁵⁴

4.6 References

1. P. Steurer, R. Wissert, R. Thomann and R. Mülhaupt: 'Functionalized Graphenes and Thermoplastic Nanocomposites Based upon Expanded Graphite Oxide.', *Macromol. Rapid Commun.*, 2009, **30**, 316–27.

2. X. Jiang and L. T. Drzal: 'Improving electrical conductivity and mechanical properties of high density polyethylene through incorporation of paraffin wax coated exfoliated graphene nanoplatelets and multi-wall carbon nano-tubes', *Compos. Part A Appl. Sci. Manuf.*, 2011, **42**, 1840–1849.
3. W. R. Caseri: 'Nanocomposites of polymers and inorganic particles: preparation, structure and properties', *Mater. Sci. Technol.*, 2006, **22**, 807–817.
4. J. M. Torkelson and K. Wakabayashi: 'Polymer-graphite nanocomposites via solid-state shear pulverization', US7906053 B1, published 2009.
5. K. Wakabayashi, P. J. Brunner, J. Masuda, S. A. Hewlett and J. M. Torkelson: 'Polypropylene-graphite nanocomposites made by solid-state shear pulverization: Effects of significantly exfoliated, unmodified graphite content on physical, mechanical and electrical properties', *Polymer*, 2010, **51**, 5525–5531.
6. K. Wakabayashi, M. B. Stephen and M. D. Boches: 'Process for producing exfoliated and/or dispersed polymer composites and/or nanocomposites via solid-state/melt extrusion (ssme)', WO2013059321A1, published 2013.
7. X. Jiang and L. T. Drzal: 'Reduction in percolation threshold of injection molded high-density polyethylene/exfoliated graphene nanoplatelets composites by solid state ball milling and solid state shear pulverization', *J. Appl. Polym. Sci.*, 2012, **124**, 525–535.
8. A. Vermogen, K. Masenelli-Varlot, R. Séguéla, J. Duchet-Rumeau, S. Boucard and P. Prele: 'Evaluation of the Structure and Dispersion in Polymer-Layered Silicate Nanocomposites', *Macromolecules*, 2005, **38**, 9661–9669.
9. W. Lertwimolnun and B. Vergnes: 'Effect of processing conditions on the formation of polypropylene/organoclay nanocomposites in a twin screw extruder', *Polym. Eng. Sci.*, 2006, **46**, 314–323.
10. M. Modesti, A. Lorenzetti, D. Bon and S. Besco: 'Thermal behaviour of compatibilised polypropylene nanocomposite: Effect of processing conditions', *Polym. Degrad. Stab.*, 2006, **91**, 672–680.
11. K. Wang, S. Liang, R. Du, Q. Zhang and Q. Fu: 'The interplay of thermodynamics and shear on the dispersion of polymer nanocomposite', *Polymer*, 2004, **45**, 7953–7960.
12. Z. Tadmor and C. G. Gogos: 'Principles of Polymer Processing', 2nd ed. 2006, Hoboken, NJ, John Wiley & Sons, Inc.

13. K. Kalaitzidou, H. Fukushima, P. Askeland and L. T. Drzal: 'The nucleating effect of exfoliated graphite nanoplatelets and their influence on the crystal structure and electrical conductivity of polypropylene nanocomposites', *J. Mater. Sci.*, 2007, **43**, 2895–2907.
14. K. Wakabayashi, C. Pierre, D. A. Dikin, R. S. Ruoff, T. Ramanathan, L. C. Brinson and J. M. Torkelson: 'Polymer–Graphite Nanocomposites: Effective Dispersion and Major Property Enhancement via Solid-State Shear Pulverization', *Macromolecules*, 2008, **41**, 1905–1908.
15. C. Bartholome, E. Beyou, E. Bourgeat-Lami, P. Cassagnau, P. Chaumont, L. David and N. Zydowicz: 'Viscoelastic properties and morphological characterization of silica/polystyrene nanocomposites synthesized by nitroxide-mediated polymerization', *Polymer*, 2005, **46**, 9965–9973.
16. P. Cassagnau: 'Melt rheology of organoclay and fumed silica nanocomposites', *Polymer*, 2008, **49**, 2183–2196.
17. R. T. DeHoff and F. N. Rhines: 'Quantitative Microscopy', 1968, New York, NY, McGraw-Hill Book Company.
18. E. E. Underwood: 'Quantitative Stereology', 1970, Reading, Massachusetts, Addison-Wesley Publishing Company.
19. S. A. Saltykov: 'The Determination of the Size Distribution of Particles in an Opaque Material from a Measurement of the Size Distribution of Their Sections', in *Proc. Second Int. Cong. Stereol.* 1967, pp. 163–173.
20. S. A. Saltykov: 'Stereometric Metallography', 2nd ed. 1958, Moscow.
21. W. A. Johnson: 'Estimation of Spatial Grain Sizes', *Met. Prog.*, 1946, **49**, 87.
22. D. C. Bassett and R. H. Olley: 'On the lamellar morphology of isotactic polypropylene spherulites', *Polymer*, 1984, **25**, 935–943.
23. A. M. Freedman, D. C. Bassett, A. S. Vaughan and R. H. Olley: 'On quantitative permanganic etching', *Polymer*, 1986, **27**, 1163–1169.
24. R. H. Olley and D. C. Bassett: 'An improved permanganic etchant for polyolefines', *Polymer*, 1982, **23**, 1707–1710.
25. J. Park, K. Eom, O. Kwon and S. Woo: 'Chemical Etching Technique for the Investigation of Melt-crystallized Isotactic Polypropylene Spherulite and Lamellar Morphology by Scanning Electron Microscopy', *Microsc. Microanal.*, 2002, **7**, 276–286.

26. C. A. Schneider, W. S. Rasband and K. W. Eliceiri: 'NIH Image to ImageJ: 25 years of image analysis', *Nat. Methods*, 2012, **9**, 671–675.
27. T.-H. Tsai, A. M. Maes, M. A. Vandiver, C. Versek, S. Seifert, M. Tuominen, M. W. Liberatore, A. M. Herring and E. B. Coughlin: 'Synthesis and structure-conductivity relationship of polystyrene- block -poly(vinyl benzyl trimethylammonium) for alkaline anion exchange membrane fuel cells', *J. Polym. Sci. Part B Polym. Phys.*, 2013, **51**, 1751–1760.
28. V. Vladimirov, C. Betchev, A. Vassiliou, G. Papageorgiou and D. Bikiaris: 'Dynamic mechanical and morphological studies of isotactic polypropylene/fumed silica nanocomposites with enhanced gas barrier properties', *Compos. Sci. Technol.*, 2006, **66**, 2935–2944.
29. M. Liu, B. Guo, M. Du, F. Chen and D. Jia: 'Halloysite nanotubes as a novel β -nucleating agent for isotactic polypropylene', *Polymer*, 2009, **50**, 3022–3030.
30. H. Fukushima.: Graphite Nanoreinforcements in Polymer Nanocomposites (Michigan State University, 2003).
31. D. Cho, S. Lee, G. Yang, H. Fukushima and L. T. Drzal: 'Dynamic Mechanical and Thermal Properties of Phenylethynyl-Terminated Polyimide Composites Reinforced With Expanded Graphite Nanoplatelets', *Macromol. Mater. Eng.*, 2005, **290**, 179–187.
32. S. Kim, I. Do and L. T. Drzal: 'Thermal stability and dynamic mechanical behavior of exfoliated graphite nanoplatelets-LLDPE nanocomposites', *Polym. Compos.*, 2009, **31**, 755–761.
33. K. Kalaitzidou, H. Fukushima and L. T. Drzal: 'Mechanical properties and morphological characterization of exfoliated graphite–polypropylene nanocomposites', *Compos. Part A Appl. Sci. Manuf.*, 2007, **38**, 1675–1682.
34. C. W. Macosko: 'Rheology: principles, measurements, and applications', 1994, Wiley-VCH.
35. K. Kalaitzidou, H. Fukushima and L. T. Drzal: 'Multifunctional polypropylene composites produced by incorporation of exfoliated graphite nanoplatelets', *Carbon*, 2007, **45**, 1446–1452.
36. S.-P. Rwei, I. Manas-Zloczower and D. L. Feke: 'Analysis of dispersion of carbon black in polymeric melts and its effect on compound properties', *Polym. Eng. Sci.*, 1992, **32**, 130–135.

37. K. Kalaitzidou, H. Fukushima and L. T. Drzal: 'A new compounding method for exfoliated graphite–polypropylene nanocomposites with enhanced flexural properties and lower percolation threshold', *Compos. Sci. Technol.*, 2007, **67**, 2045–2051.
38. J. M. DallaValle and A. Klemin: 'Micrometitics: The Technology of Fine Particles', 1943, New York, NY, Pitman Pub. Corp.
39. J. E. Funk and D. R. Dinger: 'Predictive Process Control of Crowded Particulate Suspensions', 1994, Boston, MA, Springer US.
40. T. Lozano, P. G. Lafleur, M. Grmela and B. Vergnes: 'Modeling Filler Dispersion along a Twin-Screw Extruder', *Int. Polym. Process.*, 2013,.
41. A. Nir and A. Acrivos: 'On the creeping motion of two arbitrary-sized touching spheres in a linear shear field', *J. Fluid Mech.*, 2006, **59**, 209.
42. I. Manas-Zloczower, A. Nir and Z. Tadmor: 'Dispersive Mixing in Internal Mixers—A Theoretical Model Based on Agglomerate Rupture', *Rubber Chem. Technol.*, 1982, **55**, 1250–1285.
43. H. Rumpf: The Strength of Granules and Agglomerates, in *Agglomeration*, 1st ed., ed. W. A. Knepper 1962, New York, NY, Wiley-Interscience.
44. M. Härtelt, H. Riesch-Oppermann and O. Kraft: 'Statistical analysis and predictions of fracture and fatigue of micro-components', *Microsyst. Technol.*, 2011, **17**, 325–335.
45. G. R. McDowell and J. P. de Bono: 'On the micro mechanics of one-dimensional normal compression', *Géotechnique Lett.*, 2013, **3**, 166–172.
46. G. R. McDowell: 'On the Yielding and Plastic Compression of Sand.', *SOILS Found.*, 2002, **42**, 139–145.
47. W. L. Lim, G. R. McDowell and A. C. Collop: 'The application of Weibull statistics to the strength of railway ballast', *Granul. Matter*, 2004, **6**, 229–237.
48. G. I. Taylor: The Formation of Emulsions in Definable Fields of Flow, in *Proc. R. Soc. London*, 1934, pp. 501–523.
49. U. Sundararaj, C. W. Macosko, R. J. Rolando and H. T. Chan: 'Morphology development in polymer blends', *Polym. Eng. Sci.*, 1992, **32**, 1814–1823.
50. E. Van Hemelrijck, P. Van Puyvelde, S. Velankar, C. W. Macosko and P. Moldenaers: 'Interfacial elasticity and coalescence suppression in compatibilized polymer blends', *J. Rheol. (N. Y. N. Y.)*, 2004, **48**, 143.

51. L. Levitt and C. W. Macosko: 'Shearing of Polymer Drops with Interface Modification', *Macromolecules*, 1999, **32**, 6270–6277.
52. C. W. Macosko: 'Morphology development and control in immiscible polymer blends', *Macromol. Symp.*, 2000, **149**, 171–184.
53. F. . Rumscheidt and S. . Mason: 'Particle motions in sheared suspensions XII. Deformation and burst of fluid drops in shear and hyperbolic flow', *J. Colloid Sci.*, 1961, **16**, 238–261.
54. B. M. Cromer, E. B. Coughlin and A. J. Lesser: 'Evaluation of a new processing method for improved nanocomposite dispersions', *Nanocomposites*, 2015, **1**, 152–159.

CHAPTER 5

FUTURE WORK

5.1 Proposed Future Directions

Below are proposed extensions of the present body of work.

5.1.1 Reactor Design for *In-Situ* Polymerization of iPP-Nanocomposites

In chapter 2, the effectiveness of *in-situ* polymerization of iPP-xGnP nanocomposites was limited by the poor dispersion of xGnP in the polymerization solvent prior to the reaction. The design of the Luinstra group polymerization reactor precluded any kind of mechanical pretreatment such as pre-mixing to the xGnP-toluene suspension. The only available tool to promote mixing during polymerization was a mixing blade fitted inside the reactor, attached to a motor with low RPM limit (maximum = 120 RPM). This is because the Luinstra group polymerization reactor is not optimized for *in-situ* polymerization of nanocomposites, but rather polymerization of metallocene polyolefins. In the absence of a significant shear field, it's clear that xGnP underwent rapid sedimentation into large (1-10 μm) agglomerates.

Park *et al.* showed that *in-situ* polymerization of polyimide-carbon nanotube nanocomposites under constant bath sonication produces well dispersed nanocomposites.¹ Accordingly for the present study, it is proposed that if sonication occurs during polymerization, the dispersion quality of the final nanocomposite will improve. In fact, it was experimentally observed that sonication efficiently and rapidly disperses xGnP in toluene temporarily, however sonication during *in-situ* polymerization was not possible with the Luinstra group reactor design. Figure 5.1 shows a schematic of a modified

polyolefin polymerization vessel designed to incorporate intense sonication during *in-situ* polymerization. The vessel is similar to conventional polyolefin polymerization vessels, with the exception of multiple piezoelectric probe sonicators fitted within the reaction wall. The piezoelectric probe sonicators impose sonication to the reaction medium, of intensity greater than that of conventional bath sonication. Also, the design of the mixing blade would need to be modified to incorporate the sonication probe. Such a reactor design is advantageous because the dispersion mechanism is insensitive to nanoparticle surface chemistry and polarity.

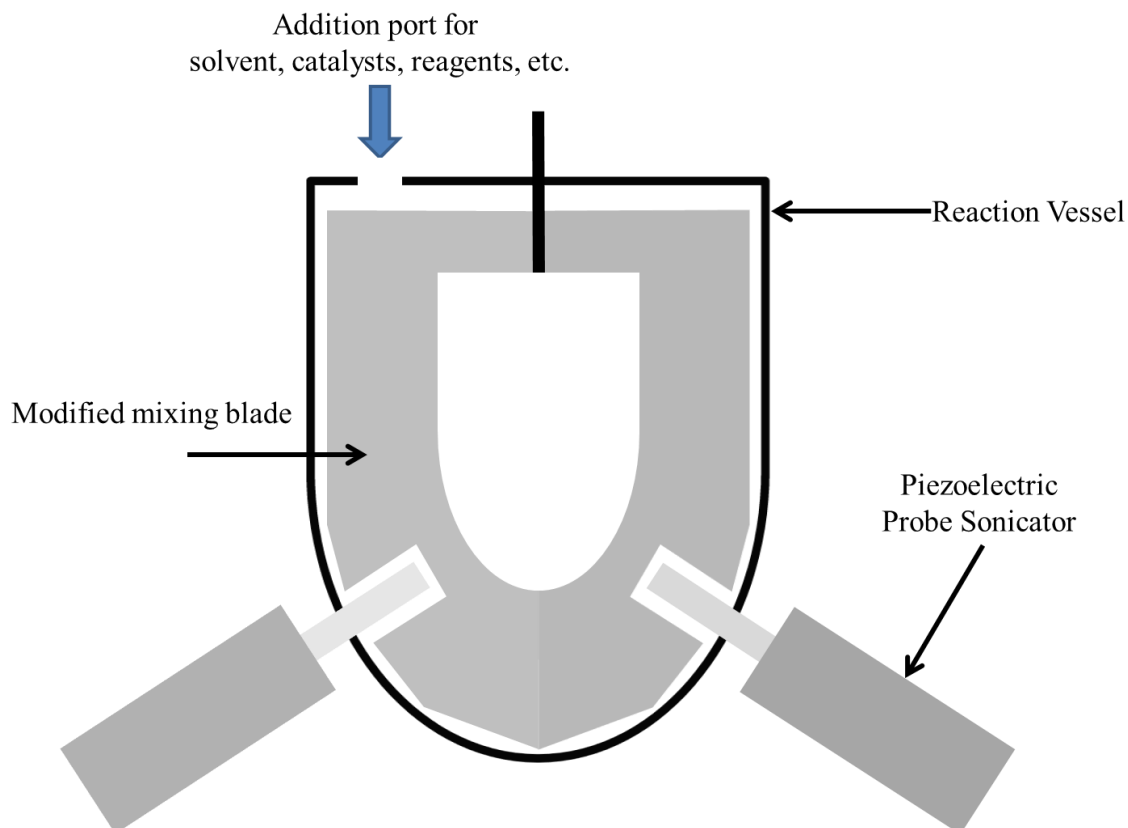


Figure 5.1: Schematic of proposed reactor design for *in-situ* polymerization of polyolefin nanocomposites

5.1.2 Alternative Nanoparticle Surface Chemistries for *In-Situ* Polymerization

Another factor limiting the effectiveness of *in-situ* polymerization of iPP-xGnP nanocomposites is the surface chemistry of xGnP. Section 2.3.1 shows xGnP nanoparticles clearly contain a variety of active hydrogen-bearing functional groups that apparently inhibit the metallocene polymerization catalyst and/or cocatalyst. It is therefore prudent to consider alternative nanoparticle surface chemistries that will not deactivate the strongly Lewis acidic metallocene catalyst complex.

One potential approach is through modifying the surface chemistry of xGnP to remove active hydrogens. For example, Macosko *et al.* reported a pyrolysis treatment technique to reduce functional groups on the surface of graphite oxide to largely non-polar,

non-protic groups.²⁻⁴ Alternatively, inorganic nanoparticles such as Aluminosilicates mineral nanoparticles or Barium Titanate may possess more suitable surface chemistries. Ideal nanoparticles should be readily dispersed in toluene and be without functional groups that deactivate metallocene catalysts.

5.1.3 Advancing Melt-Mastication Toward Commercialization

Melt-Mastication described in chapter 3 is a unique processing approach demonstrating great potential as a means to improve the mechanical strength and modulus of semicrystalline polyolefins, without reinforcing agents. However at this time, Melt-Mastication has only been demonstrated in a small scale batch reactor (50 mL capacity). In order for MM to be commercially feasible, it must be scaled-up to a continuous flow process in order to maximize production efficiency.

It is proposed that Melt-Mastication may be adopted to a continuous flow process through modification of a counter-rotating, tangential twin screw extruder design. Although popular, counter-rotating intermeshing twin screw extruder designs are likely not suitable for the present case because the intermeshing flights will divide sections of the iPP melt and transport them down the barrel via positive displacement. It was empirically observed that the MM pseudo melt does not coalesce in the same way molten as iPP. That is, once the pseudo melt is divided, it will not readily re-combine with other pseudo melt regions. The proposed design will contain two stages, where the first state is designed to melt the polymer, and the second stage facilitates MM. The proposed design should contain the following elements:

- 1: Screw design: The screw should be divided into two separate stages, the first to should contain a feeding zone with mixing elements to melt, mix, and homogenize iPP

prior to MM. The second stage will possess mixing elements to promote MM under cooling. It is proposed that the screw designs for MM should promote moderate shear and elongational flows. Accordingly, it may be necessary to adjust the distance between screws to avoid the high shear-flow regions that occur where the screw flights intersect. Also, it may be necessary to modify the screws in the MM stage with multilobal elements in order to promote moderate elongational flow fields. Elongational flow fields have been shown to promote FIC more efficiently than shear flows.

2: Temperature control. The portion of the barrel corresponding to the first mixing stage should be heated well above T_m of the mixing resin in order to facilitate melting. The remainder of the barrel should be fitted with air or water cooling mechanisms to promote cooling and Melt-Mastication.

3: Die exit. The pseudo melt should not be exposed to intense shear/elongational flow fields near the die exit. It was empirically observed that high mixing rates or intense forging flows imposed on iPP pseudo melts caused melting and loss of the beneficial crystal morphology generated by MM. Therefore the die exit should be larger than conventional die exits for conventional fiber spinning and/or film casting.

4: Continuous forging process. The forging processes discussed in section 3.2.4 are not suitable for continuous production of MM-iPP articles. It is proposed that a two-roll mill positioned near the die exit could provide a simple means to forge MM-iPP pseudo melts into plates of controlled thickness. Additionally, a two roll mill with grooves along the circumference of the rollers may be used to forge simple shapes of continuous cross section. For example, hemi-spherical grooves may be used to produce rods, and channel grooves to produce square or rectangular bars, etc.

Melt-Mastication requires processing conditions distinct from conventional polymer processing. The flow of the iPP pseudo melt resembles that of a lubricated flow of viscous liquids. It follows that many design features of standard single and twin-screw extruders are not necessary for MM. Likely, experimentation with several screw configurations will be necessary.

5.1.4 Engineering Optimized Polyolefin Resins for Melt-Mastication

In the present study, MM was performed with a conventional grade of iPP optimized for injection molding. It is not clear why this iPP grade was amenable to MM, nor what aspects of the iPP chain microstructure promote MM. Therefore, if funding permits, it may be prudent to modify the chain microstructure of iPP and/or create additives to promote flow induced crystallization (FIC) and optimized resins for MM.

There has been extensive work to understand the structural and morphological developments occurring during flow induced crystallization of iPP.^{5,6} Hsiao *et al.* proposed that the high molecular weight fraction of iPP is responsible for the formation, stability and concentration of flow-induced structures, although this assertion is still debated.⁷ It may be prudent to design iPP resins with broad or even bimodal molecular weight distribution in order to promote FIC. Another proposed approach to promote FIC is through incorporation of additives. A recent patent by the ExxonMobil corporation claims that a small weight fraction (0.2-5 wt%) of a branched hydrocarbon significantly enhances FIC.⁸ Metallocene catalysis presents an opportunity to produce polyolefins with controlled molecular weight, molecular weight distribution, branch density, and branch length that may be used to synthesize additives to enhance FIC. Finally, additives like sorbitol-based

nucleating agents or high aspect ratio nanoparticles have been shown to promote FIC, and could be beneficial for MM.^{9,10}

5.1.5 New Polyolefin “Self-Nucleation” Agents

Section 3.3.4 shows how MM may be used to create iPP lamellar crystals with high thermal stability. These thermally stable iPP crystals do not readily melt at conventional processing temperatures for iPP (200 °C), and therefore promote quiescent crystallization upon cooling. It was also shown that cryogenically ground MM-iPP promotes nucleation in conventional molten iPP. It follows that the present body of work demonstrates how iPP may be modified to “self-nucleate.” Such technology would be commercially advantageous, as nucleating agents for iPP are commonly used to promote impact properties, ductility, and optical clarity in iPP articles. Unlike conventional nucleating agents though, the composition of iPP self-nucleating agents cannot be spectroscopically identified because it is compositionally identical to the resin, which is also commercially advantageous. However, cryogenic grinding is costly and commercially impractical. Instead, it is proposed that milling solidified MM-iPP may provide sufficient means to grind MM-iPP to a fine powder appropriate for nucleation.

5.2 References

1. C. Park, Z. Ounaies, K. A. Watson, R. E. Crooks, J. Smith, S. E. Lowther, J. W. Connell, E. J. Siochi, J. S. Harrison and T. L. S. Clair: 'Dispersion of single wall carbon nanotubes by in situ polymerization under sonication', *Chem. Phys. Lett.*, 2002, **364**, 303–308.
2. H. Kim, S. Kobayashi, M. A. AbdurRahim, M. J. Zhang, A. Khusainova, M. A. Hillmyer, A. A. Abdala and C. W. Macosko: 'Graphene/polyethylene nanocomposites: Effect of polyethylene functionalization and blending methods', *Polymer*, 2011, **52**, 1837–1846.

3. P. Steurer, R. Wissert, R. Thomann and R. Mühlaupt: 'Functionalized Graphenes and Thermoplastic Nanocomposites Based upon Expanded Graphite Oxide.', *Macromol. Rapid Commun.*, 2009, **30**, 316–27.
4. H. Kim, A. A. Abdala and C. W. Macosko: 'Graphene/Polymer Nanocomposites', *Macromolecules*, 2010, **43**, 6515–6530.
5. R. H. Somani, B. S. Hsiao, A. Nogales, S. Srinivas, A. H. Tsou, I. Sics, F. J. Balta-Calleja and T. A. Ezquerra: 'Structure Development during Shear Flow-Induced Crystallization of i-PP: In-Situ Small-Angle X-ray Scattering Study', *Macromolecules*, 2000, **33**, 9385–9394.
6. A. Nogales, B. . Hsiao, R. . Somani, S. Srinivas, A. . Tsou, F. . Balta-Calleja and T. . Ezquerra: 'Shear-induced crystallization of isotactic polypropylene with different molecular weight distributions: in situ small- and wide-angle X-ray scattering studies', *Polymer*, 2001, **42**, 5247–5256.
7. R. H. Somani, L. Yang and B. S. Hsiao: 'Effects of high molecular weight species on shear-induced orientation and crystallization of isotactic polypropylene', *Polymer*, 2006, **47**, 5657–5668.
8. D. J. Lohse, C. A. Mitchell and M. Sansone: 'Polymer compositions exhibiting enhanced flow-induced crystallization', US 20090163666, published 2009.
9. L. Balzano, S. Rastogi and G. W. M. Peters: 'Flow Induced Crystallization in Isotactic Polypropylene–1,3:2,4-Bis(3,4-dimethylbenzylidene)sorbitol Blends: Implications on Morphology of Shear and Phase Separation', *Macromolecules*, 2008, **41**, 399–408.
10. A. Somwangthanaroj, E. C. Lee and M. J. Solomon: 'Early Stage Quiescent and Flow-Induced Crystallization of Intercalated Polypropylene Nanocomposites by Time-Resolved Light Scattering', *Macromolecules*, 2003, **36**, 2333–2342.

APPENDIX

DESIGN AND CONSTRUCTION OF AN INSTRUMENTED IZOD IMPACT TESTER

Herein, the design and construction of an instrumented Izod impact tester is discussed. A standard pendulum-type Izod impact tester was modified in order to derive quantitative information about the character of an impact fracture during an Izod test. Force vs. time during impact was monitored with a piezoelectric force transducer installed on the striking edge of the Izod pendulum hammer. A rotational voltage displacement transducer was installed on the axis of the swinging pendulum hammer in order to monitor displacement vs time during impact. High acquisition rate data analysis and data processing were performed through LabVIEW software. The utility of the instrumented Izod impact tester is demonstrated through contrast to the conventional Izod test. Challenges and future recommendations for the instrument are also discussed.

A.1 Introduction

The Izod pendulum impact resistance test (ASTM D256) is a testing method to evaluate the resistance of polymers to impact fracture. The essential elements of the Izod test were first proposed by Russell in 1898, and still today this test is arguably the most ubiquitous method to understand impact fracture of polymers.¹ The Izod pendulum test is comprised of a weighted pendulum hammer with striking edge that freely rotates about a pendulum axis, schematically illustrated in Figure A.1. A sample mount is positioned at the lowest point of the pendulum swing where a notched specimen is mounted in a vertical cantilever beam configuration, shown in Figure A.1. To perform the Izod test, the

pendulum hammer is first raised to an initial height, h_0 , from the lowest point of the swing and then released. The pendulum hammer swings and impacts the notched specimen a fixed distance from the notch, breaking the specimen in a single swing. Finally, the maximum height of the pendulum swing after impact relative to the lowest point of the swing, h is recorded. The energy (E) absorbed during impact is calculated by:

$$E = mg(h_0 - h) - W \quad (\text{A.1})$$

Where m is the mass of the hammer/pendulum, g is the gravitational constant (9.81 m/s²), and W is the windage and friction correction, or the energy lost to factors other than fracture of the sample. Detailed protocols to determine the windage and friction correction are provided within ASTM D256. The result of the Izod test is reported as $E/(\text{sample width})$, units J/m.

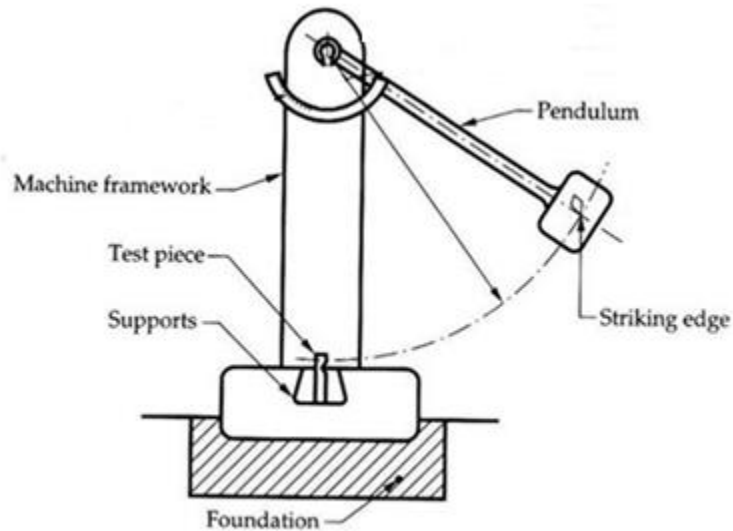


Figure A.1: Schematic representation of a conventional Izod pendulum impact resistance test machine (ASTM D256)

The Izod test is still widely accepted today due to its simplicity and efficiency. Basic commercial Izod machines cost \$15,000-20,000 and require relatively little maintenance. The test also has high sample throughput; a dedicated technician may test hundreds of samples per hour, and minimal data analysis is required. Also, the result of the Izod test is a convenient single value, which simplifies data interpretation and comparisons between similar materials. Most notably, the Izod test is widely understood and accepted in a variety of scientific disciplines and industries. It follows that the Izod test is a useful tool to derive quantitative comparisons between the impact behavior of similar materials.

However, the Izod test only provides limited information about impact failure of plastic materials. The Izod value, reported in J/m, cannot be used to derive any intrinsic material property describing fracture resistance or toughness, such as the critical strain energy release rate in mode one failure (G_{IC}). Furthermore, the Izod test does not provide information about the character of an impact failure (strain to failure, maximum strength,

yielding, etc.). Accordingly, the Izod test is not useful for comparing the fracture behavior of dissimilar materials, nor for understanding how impact failure of a particular material changes under different temperature/humidity conditions.

For example, Figure 3.17 in section 3.3.6.4 shows Izod impact energies of Isotactic Polypropylene (iPP) samples at various temperatures. Near 0°C there is an apparent increase in Izod impact energy with increasing temperature, which corresponds to the “ductile brittle transition” (DBT), the temperature above which a material is thought to demonstrate improved ductility. However, the Izod values do not provide information about how the character of the fracture changes with increasing temperature, nor why Melt-Masticated iPP outperforms Quenched iPP. In the case of Figure 3.17, the Izod impact energy results do not provide data suggesting that iPP is truly becoming more ductile above the DBT. However results from the instrumented Izod impact tester in Figure 3.18 show that iPP is indeed becoming more ductile above the DBT.

Accordingly, the present work describes how sensors may be fitted to a conventional pendulum-type Izod impact tester in order to elucidate the character of impact fracture. An Izod tester is equipped with force and displacement transducers. The resulting force and displacement data may be coordinated to force vs displacement curves, which are analyzed and discussed.

A.2 Materials and Methods

A.2.1 Materials

A rotational voltage displacement transducer (RVDT, Positek RIPS® 500) was purchased from Positek, Inc. and used as received. The piezoelectric impact cell (ICP®

quartz force sensor) with 600 lb compressive force range and 50 mV/lb sensitivity was purchased from PCB Piezotronics, Inc. and used as received. A NI 9220 I/O module (analog input, 100,000 samples/second, 16 bit digitization) and a NI cDAQ-9171 compact data acquisition chassis were purchased from National Instruments, Inc. and used as received. Testing software programs were developed through LabVIEW software (LabVIEW full development system version 2015). Stainless steel (1018 carbon steel) was purchased from McMaster Carr and used as received. Polycarbonate sheet (3/8" thick) was purchased from McMaster-Carr and used as received.

A.2.2 Construction

Both sensors were mounted to the instrument according to Figure A.2 via machined metal components. The sample clamp, including the base, floating plate, and lateral stabilization plates as well as a mounting plate for the striking hammer surface were machined from stainless steel within the University of Massachusetts Amherst Hasbrouck machine shop with the assistance of Mr. Walter Pollard. The technical drawings of each component are included in Figures A.4-A.6. Finally, the analog output from both sensors (differential, ± 10 V DC) was connected to the NI 9220 I/O module. The I/O module connected to the cDAQ-9171, which interfaced with a PC via USB.

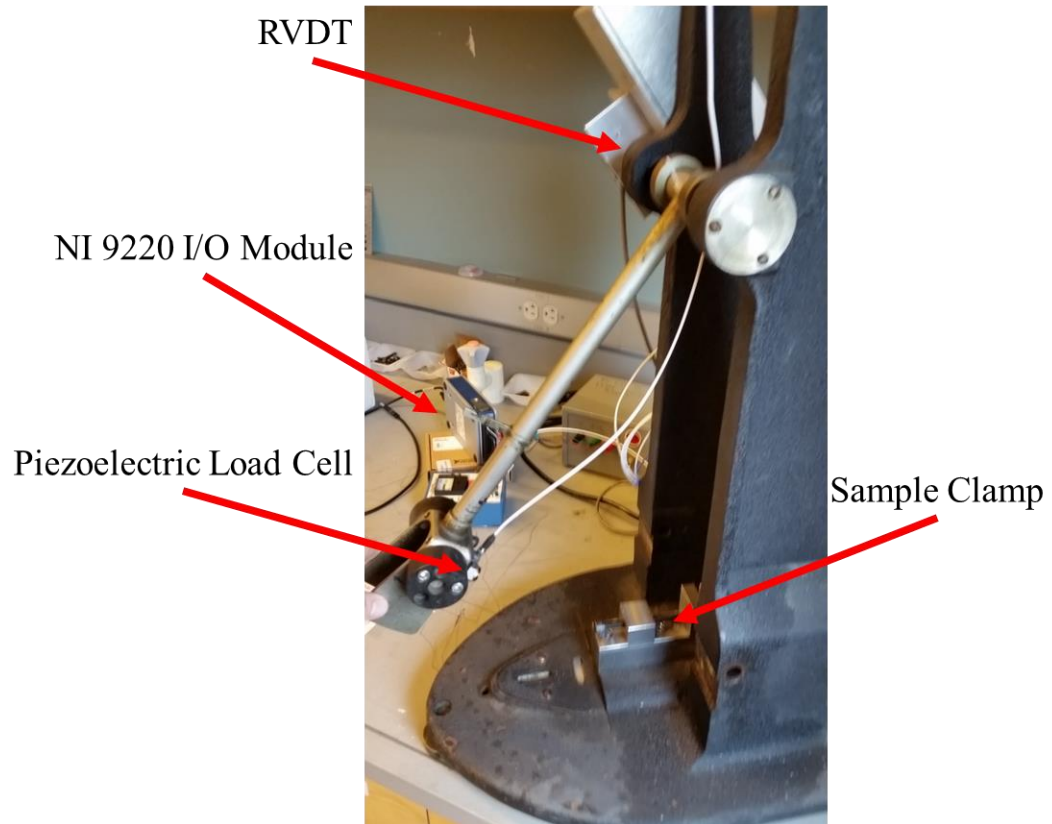


Figure A.2: Instrumented Izod impact test device.

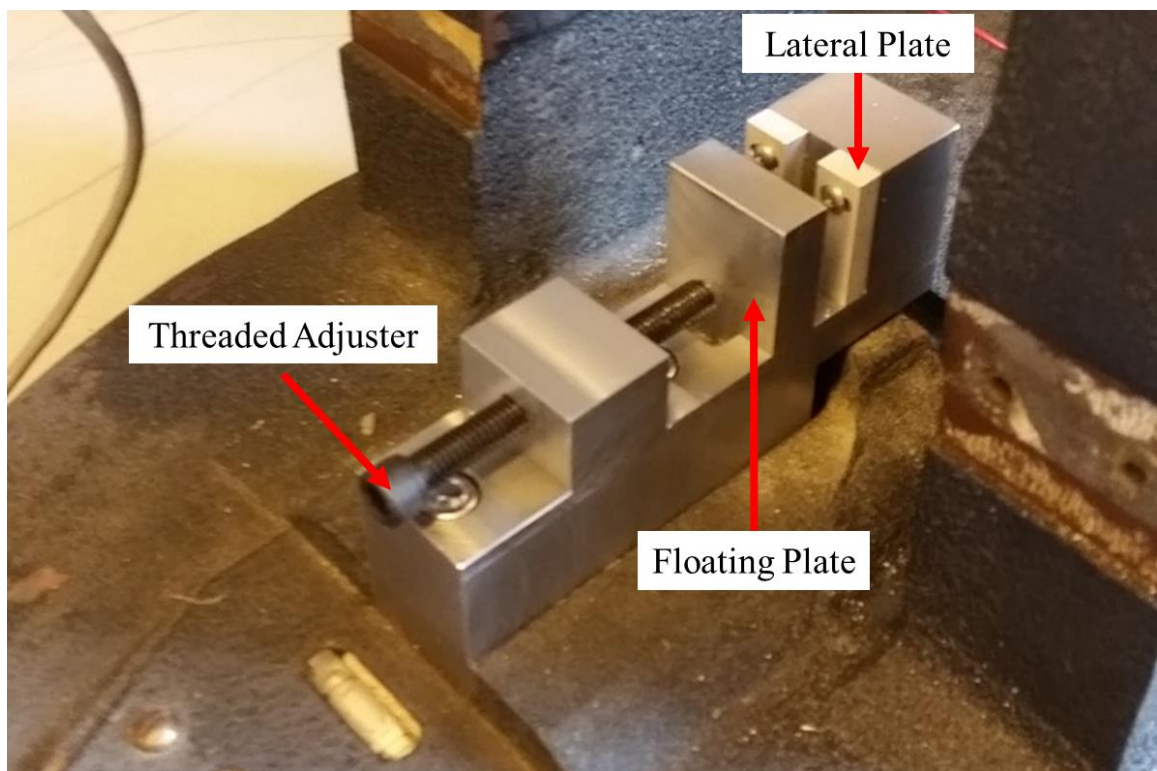


Figure A.3: Sample clamp corresponding to Figures A.4, A.5, and A.6.

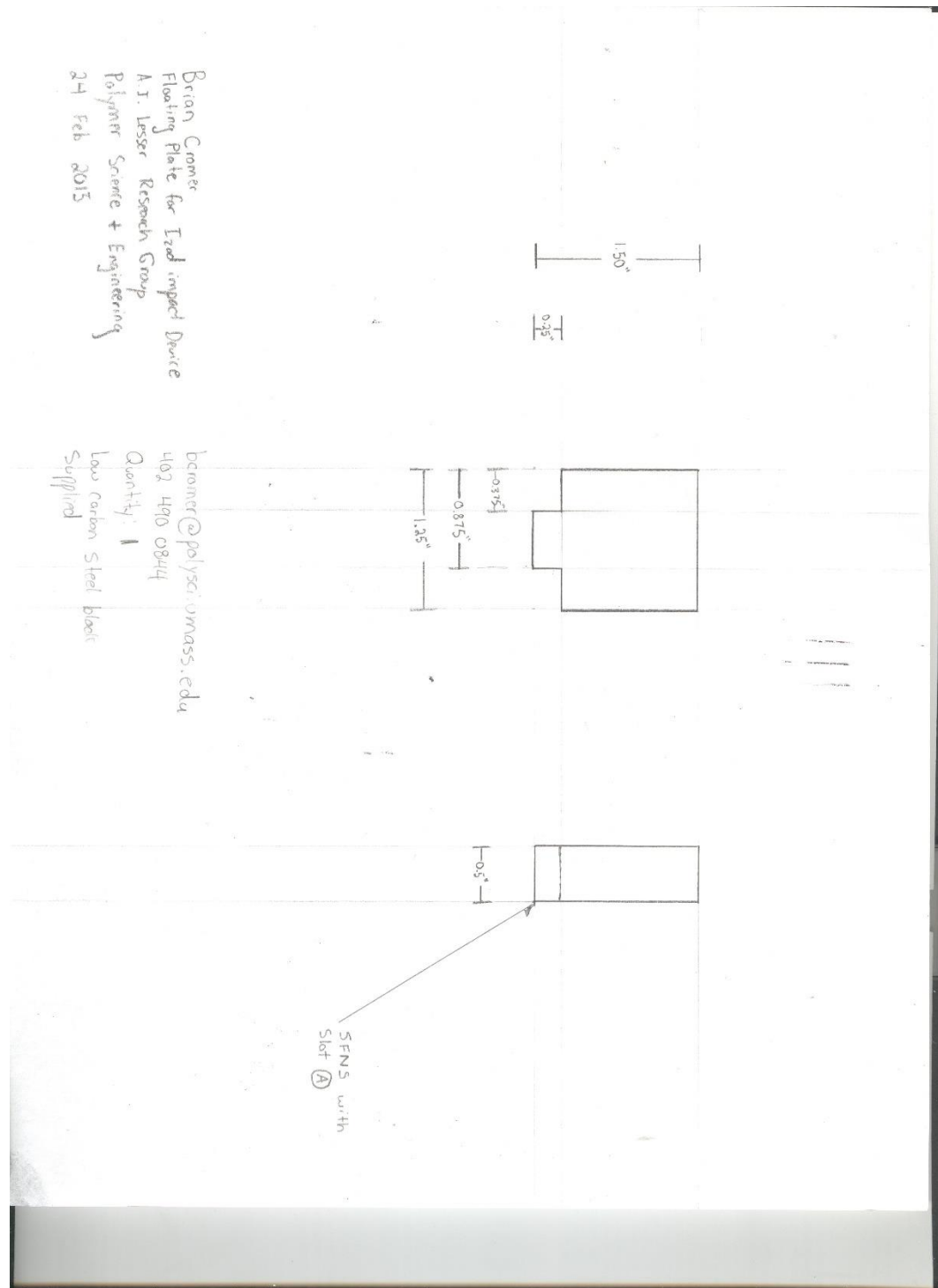


Figure A.5: Technical drawing for sample clamp floating plate of Figure A.3.

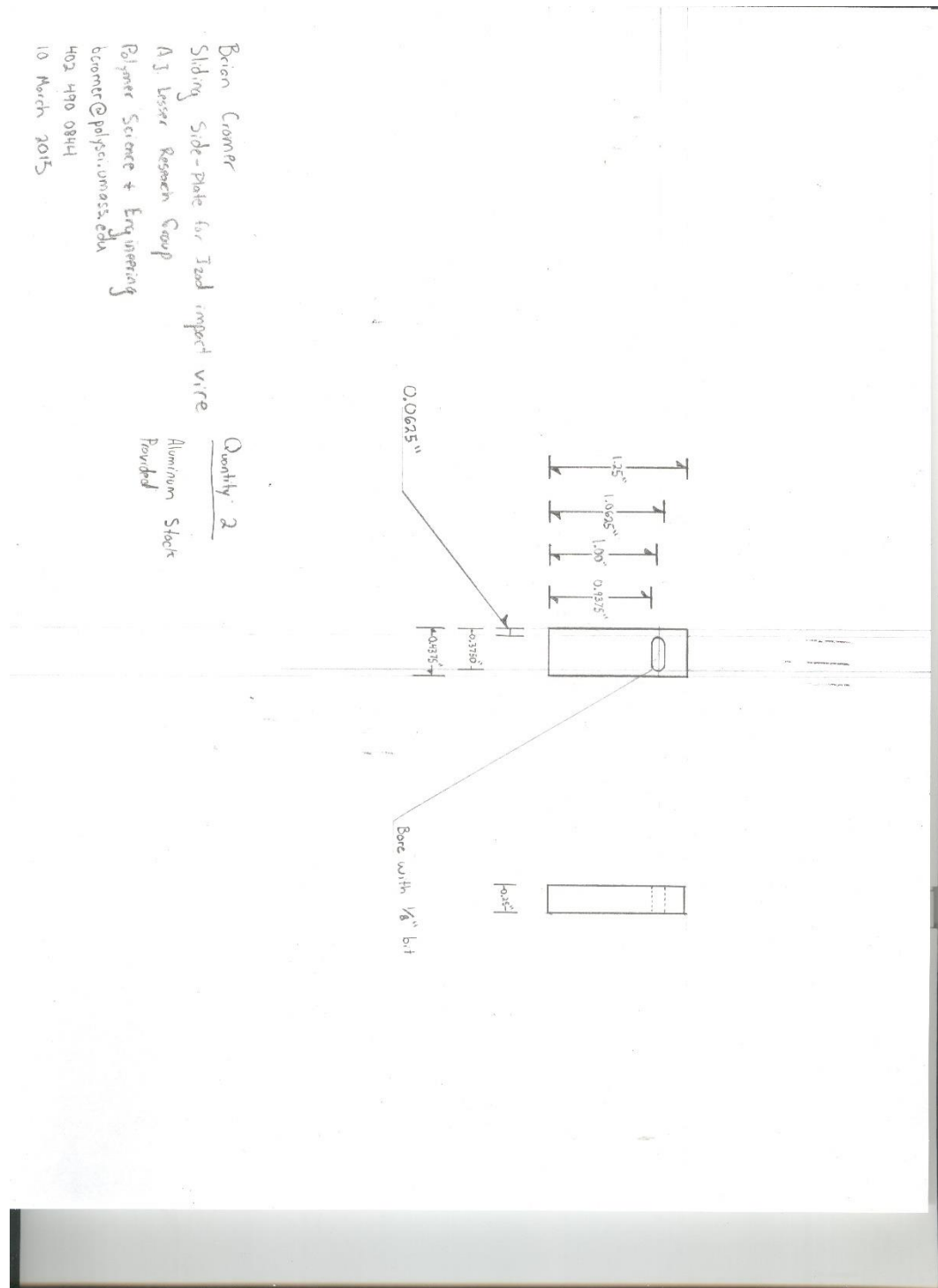


Figure A.6: Technical drawing for sample clamp lateral plates of Figure A.3.

A.3 Results and Discussion

Described are two studies demonstrating the instrumented Izod impact tester. In the first study, the pendulum is raised, released, and allowed to freely swing, and the position is recorded as a function of time. The second study includes a sub-perforating impact of un-notched polycarbonate. Additionally, Figure 3.18 and section 3.3.6.4 include a study of the impact behavior of notched iPP.

A.3.1 Free Swing Study

The free swing test was used to evaluate the performance of the RVDT. The RVDT records the angle (θ) of the Izod pendulum, relative to the neutral (vertical) position. Therefore, the horizontal displacement (d_h) of the striking hammer from the sample is calculated according to:

$$d_h = \sin(\theta) * L$$

Where L is the length of the pendulum arm. Similarly, the vertical displacement (d_v) of the striking hammer from the neutral position is calculated according to:

$$d_v = \cos(\theta) * L$$

Figure A.7 shows the horizontal position vs. time data from the free swing experiment. As expected for a swinging pendulum, the horizontal position vs. time data demonstrates sinusoidal behavior. The velocity vs. time may be calculated through simple differentiation of the horizontal position vs time, and as expected, demonstrates sinusoidal behavior with 90° phase shift relative to horizontal position vs. time.

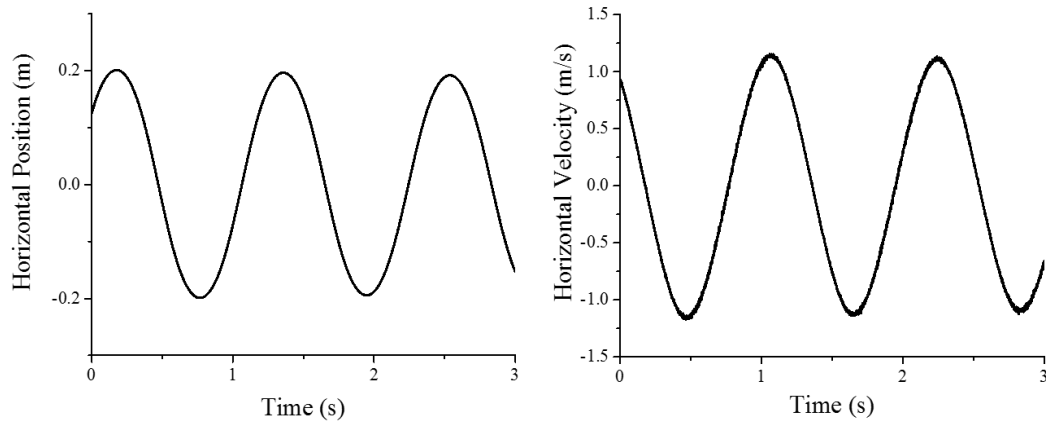


Figure A.7: Horizontal position and velocity of a freely swinging Izod pendulum.

Additionally, the total energy vs. time may be calculated according to:

$$E = mgh_y + mv^2$$

Where m is the mass of the striking hammer, g is the gravitational constant, h_y is the vertical position relative to neutral, and v is the arc velocity of the striking hammer. The total energy of an ideal swinging pendulum should be constant, however E is expected to decrease with time due to friction and windage losses. Figure A.8 shows the total energy of a swinging pendulum vs. time. There appears to be a local maximum in the total energy roughly every second, which corresponds to the bottom of the swing path when velocity is greatest. This is believed to be an artifact created by the data processing method. The data processing method to calculate kinetic energy includes differentiating the position vs time signal to determine velocity, and then squaring velocity. Accordingly, the signal error in the position vs time data is compounded by both processes, producing an artificially high value.

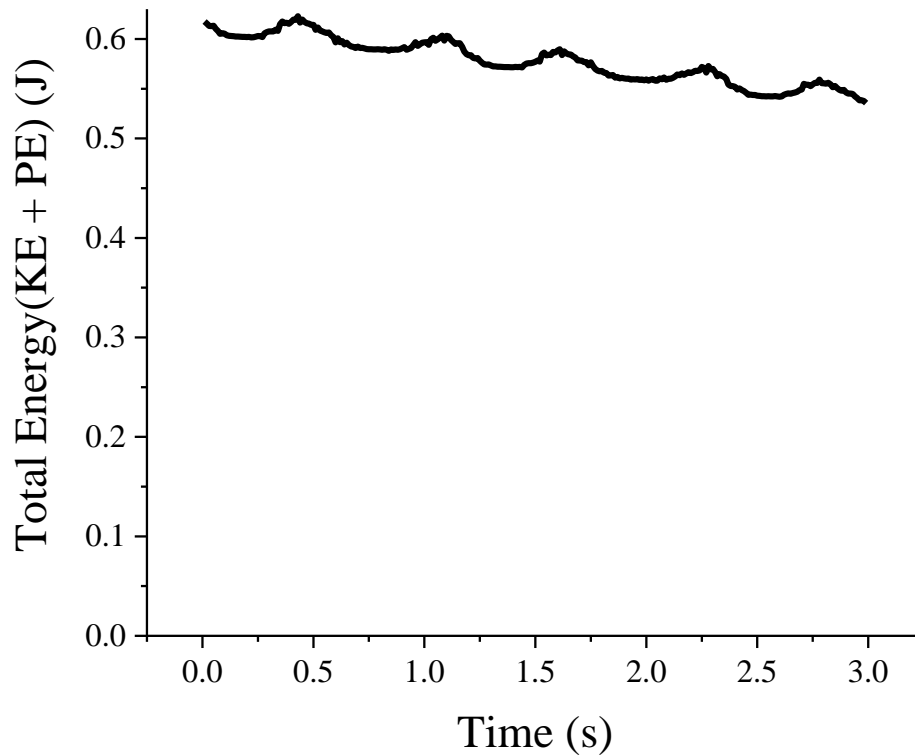


Figure A.8: Total energy of the freely swinging Izod pendulum.

A.3.2 Sub-Perforating Impact of Polycarbonate Study

Sub-perforating impact tests were performed to evaluate the performance and coordination of the force and displacement transducers. An un-notched polycarbonate sample was impacted with the striking hammer, and the hammer was allowed to rebound off the sample. The test was performed three times, each with a different hammer mass. The load vs. time and displacement vs. time results are recorded in Figure A.9. The force vs. time results show that increasing the striker mass increases both the maximum load and the time the striker is contacting the sample and decelerating. These curves also show a saw-toothed pattern, corresponding to a vibration occurring during impact. This response is attributed to the resonant frequency of the cantilever beam sample. Empirically, it was

found that the frequency of the saw-toothed pattern changed with increasing sample thickness, which suggests the vibrations are indeed a result from the sample itself. It follows that the frequency of these vibrations and the dimensions of a sample could be used as a method to determine the elastic modulus of a sample during impact. Also, the displacement vs. time data corresponds well to the force vs time data, both show the impact event occurring at the same time. Finally, a post-contact vibration is observed when the hammer is rebounding after the impact event. This is attributed to the resonant frequency of the pendulum and hammer.

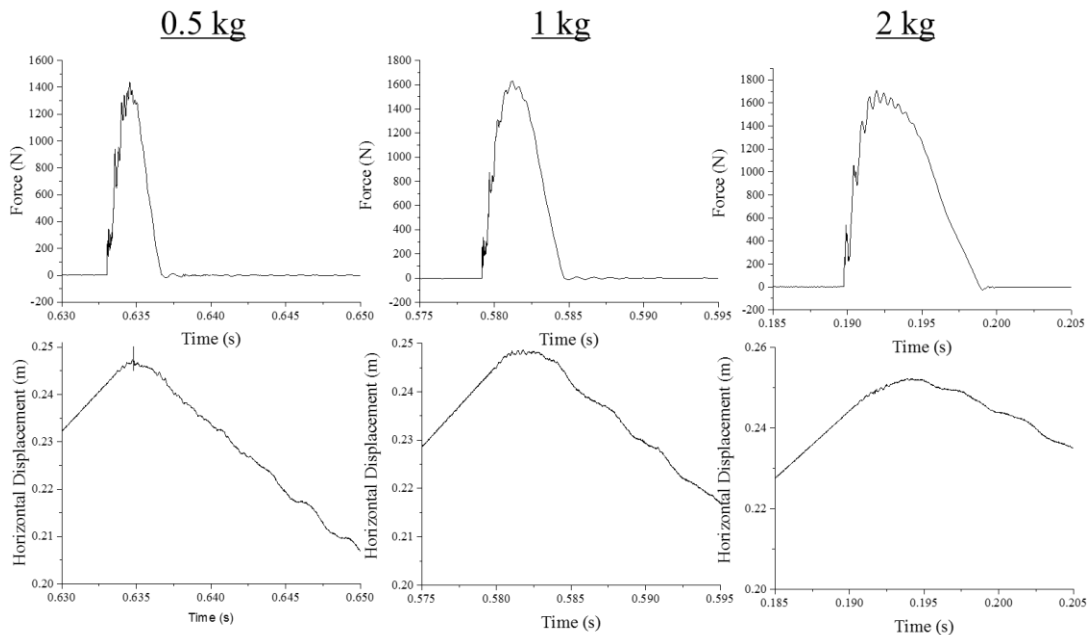


Figure A.9: Force vs. time and displacement vs. time of sub-perforating impact at various striker hammer masses.

The ensuing force vs. displacement curves of each sub-perforating impact are shown in Figure A.10. Each curve shows an apparent loading and unloading curve, which close to form a hysteresis loop. The area of this loop corresponds to the energy dissipated during impact, and likely also the strain energy imparted to the pendulum arm that results in post-contact vibration, shown in Figure A.9. As expected, the area of the hysteresis loop

increases as the hammer mass increases. Interestingly, the loading of the hammer onto the sample appears non-monotonic. The 2 kg impact event shown in Figure A.10 demonstrates that the sample loads in a saw-toothed pattern, such that there are short periods of unloading during the loading portion of the impact.

A.4 Conclusions

The design and construction of an instrumented Izod impact tester are presented and discussed. A conventional Izod pendulum testing machine was fitted with a force transducer on the striking hammer and a rotational displacement transducer in the rotational axis of the pendulum, enabling simultaneous measurement of force and displacement during impact. The device was demonstrated with two simple experiments. The device enables understanding of the force vs. displacement behavior of materials during fracture. However, the device is somewhat limited due to parasitic vibrational signals from the resonant frequencies of the cantilever sample and the pendulum arm.

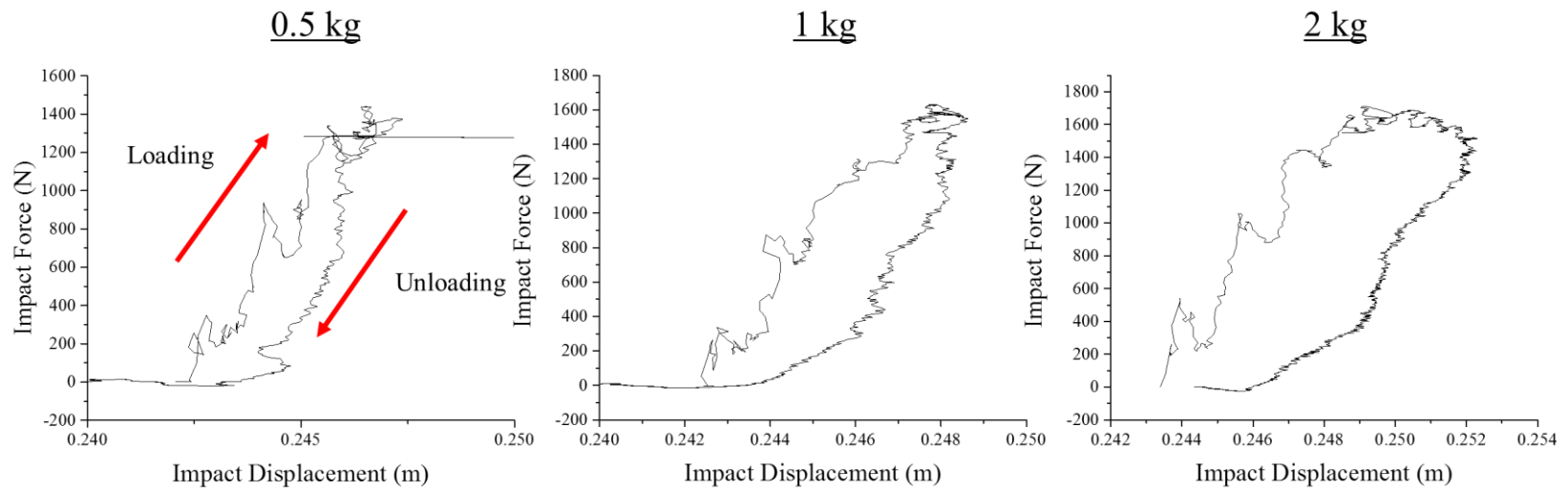


Figure A.10: Force vs. displacement curves of sub-perforating impact at various striker hammer masses.

A.5 References

1. S. B. Russell: 'Experiments with a New Machine for Testing Materials by Impact', *Trans. ASCE*, 1898, **39**, 237.

BIBLIOGRAPHY

- BCC Research: 'Global Markets for Polyolefin Resins', 2013.
- E. P. News: 'Global PP Market to Reach 62.4 Million Metric Tons', 2013.
- L. Corporation: 'Global Polypropylene Industry 2012-2017: Trend, Profit, and Forecast Analysis', 2012.
- C. M. A. Inc.: '2012 World Polyolefins Analysis', 2011.
- Robert Eller: 'Current States and Future Potential for Polyolefins, TPOs, and TPEs in the Global Automotive Market', 2012, Houston, TX.
- J. C. Halpin: 'Moduli of Crystalline Polymers Employing Composite Theory', *J. Appl. Phys.*, 1972, 43, 2235.
- R. L. Miller and L. E. Nielsen: 'Crystallographic data for various polymers', *J. Polym. Sci.*, 1960, 44, 391–395.
- V. Busico, R. Cipullo and P. Corradini: 'Ziegler-Natta oligomerization of 1-alkenes: a catalyst's "fingerprint", 1. Hydrooligomerization of propene in the presence of a highly isospecific MgCl₂-supported catalyst', *Die Makromol. Chemie*, 1993, 194, 1079–1093.
- L. Resconi, L. Cavallo, A. Fait and F. Piemontesi: 'Selectivity in Propene Polymerization with Metallocene Catalysts', *Chem. Rev.*, 2000, 100, 1253–1346.
- G. Natta, P. Pino, G. Mazzanti and U. Giannini: 'A Crystallizable Organometallic Complex Containing Titanium and Aluminum', *J. Am. Chem. Soc.*, 1957, 79, 2975–2976.
- E. Martuscelli, M. Pracella and L. Crispino: 'Crystallization behaviour of fractions of isotactic polypropylene with different degrees of stereoregularity', *Polymer*, 1983, 24, 693–699.
- D. L. VanderHart, R. G. Alamo, M. R. Nyden, M.-H. Kim and L. Mandelkern: 'Observation of Resonances Associated with Stereo and Regio Defects in the Crystalline Regions of Isotactic Polypropylene: Toward a Determination of Morphological Partitioning', *Macromolecules*, 2000, 33, 6078–6093.
- G. Natta and P. Corradini: 'Structure and properties of isotactic polypropylene', *Nuovo Cim.*, 1960, 15, 40–51.
- Z. Mencik: 'Crystal structure of isotactic polypropylene', *J. Macromol. Sci. Part B*, 1972, 6, 101–115.

- M. I. Aroyo (ed.): 'International Tables for Crystallography', 2015, Chester, England, International Union of Crystallography.
- B. Wunderlich: 'Macromolecular Physics', 1980, New York, NY, Academic Press.
- J. Bandrup, E. H. Immergut and G. E.A.: 'Polymer Handbook', 2003, New York, NY, John Wiley & Sons, Inc.
- J. Varga: 'Supermolecular structure of isotactic polypropylene', *J. Mater. Sci.*, 1992, 27, 2557–2579.
- D. C. Bassett and R. H. Olley: 'On the lamellar morphology of isotactic polypropylene spherulites', *Polymer*, 1984, 25, 935–943.
- B. Lotz, J. C. Wittmann and A. J. Lovinger: 'Structure and morphology of poly(propylenes): a molecular analysis', *Polymer*, 1996, 37, 4979–4992.
- J. D. Hoffman and R. L. Miller: 'Kinetic of crystallization from the melt and chain folding in polyethylene fractions revisited: theory and experiment', *Polymer*, 1997, 38, 3151–3212.
- R. G. Alamo, D. L. VanderHart, M. R. Nyden and L. Mandelkern: 'Morphological Partitioning of Ethylene Defects in Random Propylene–Ethylene Copolymers †', *Macromolecules*, 2000, 33, 6094–6105.
- R. G. Alamo, M.-H. Kim, M. J. Galante, J. R. Isasi and L. Mandelkern: 'Structural and Kinetic Factors Governing the Formation of the γ Polymorph of Isotactic Polypropylene', *Macromolecules*, 1999, 32, 4050–4064.
- F. Auriemma and C. De Rosa: 'Crystallization of Metallocene-Made Isotactic Polypropylene: Disordered Modifications Intermediate between the α and γ Forms', *Macromolecules*, 2002, 35, 9057–9068.
- R. Paukkeri and A. Lehtinen: 'Thermal behaviour of polypropylene fractions: 1. Influence of tacticity and molecular weight on crystallization and melting behaviour', *Polymer*, 1993, 34, 4075–4082.
- R. Paukkeri and A. Lehtinen: 'Thermal behaviour of polypropylene fractions: 2. The multiple melting peaks', *Polymer*, 1993, 34, 4083–4088.
- R. H. Olley and D. C. Bassett: 'An improved permanganic etchant for polyolefines', *Polymer*, 1982, 23, 1707–1710.
- J. J. Janimak, S. Z. D. Cheng, P. A. Giusti and E. T. Hsieh: 'Isotacticity effect on crystallization and melting in polypropylene fractions. II. Linear crystal growth rate and morphology study', *Macromolecules*, 1991, 24, 2253–2260.

- S. Z. D. Cheng, J. J. Janimak, A. Zhang and E. T. Hsieh: 'Isotacticity effect on crystallization and melting in polypropylene fractions: 1. Crystalline structures and thermodynamic property changes', *Polymer*, 1991, 32, 648–655.
- D. R. Norton and A. Keller: 'The spherulitic and lamellar morphology of melt-crystallized isotactic polypropylene', *Polymer*, 1985, 26, 704–716.
- K. Yamada, S. Matsumoto, K. Tagashira and M. Hikosaka: 'Isotacticity dependence of spherulitic morphology of isotactic polypropylene', *Polymer*, 1998, 39, 5327–5333.
- R. Phillips, G. Herbert, J. News and M. Wolkowicz: 'High modulus polypropylene: Effect of polymer and processing variables on morphology and properties', *Polym. Eng. Sci.*, 1994, 34, 1731–1743.
- M. Fujiyama and T. Wakino: 'Structures and properties of injection moldings of crystallization nucleator-added polypropylenes. I. Structure–property relationships', *J. Appl. Polym. Sci.*, 1991, 42, 2739–2747.
- M. Fujiyama, T. Wakino and Y. Kawasaki: 'Structure of skin layer in injection-molded polypropylene', *J. Appl. Polym. Sci.*, 1988, 35, 29–49.
- M. R. Kantz, H. D. Newman and F. H. Stigale: 'The skin-core morphology and structure–property relationships in injection-molded polypropylene', *J. Appl. Polym. Sci.*, 1972, 16, 1249–1260.
- G. Kumaraswamy, R. K. Verma, J. A. Kornfield, F. Yeh and B. S. Hsiao: 'Shear-Enhanced Crystallization in Isotactic Polypropylene. In-Situ Synchrotron SAXS and WAXD', *Macromolecules*, 2004, 37, 9005–9017.
- G. Kumaraswamy, A. M. Issaian and J. A. Kornfield: 'Shear-Enhanced Crystallization in Isotactic Polypropylene. 1. Correspondence between in Situ Rheo-Optics and ex Situ Structure Determination', *Macromolecules*, 1999, 32, 7537–7547.
- D. Ferrer-Balas, M. L. MasPOCH, A. B. Martinez and O. O. Santana: 'Influence of annealing on the microstructural, tensile and fracture properties of polypropylene films', *Polymer*, 2001, 42, 1697–1705.
- W. O'kane, R. Young and A. Ryan: 'The effect of annealing on the structure and properties of isotactic polypropylene films', *J. Macromol. Sci. Part B*, 1995, 34, 427–458.
- W. J. O'Kane and R. J. Young: 'The role of dislocations in the yield of polypropylene', *J. Mater. Sci. Lett.*, 1995, 14, 433–435.
- A. Lustiger, C. N. Marzinsky and R. R. Mueller: 'Spherulite boundary strengthening concept for toughening polypropylene', *J. Polym. Sci. Part B Polym. Phys.*, 1998, 36, 2047–2056.

- M. A. Kennedy, A. J. Peacock and L. Mandelkern: 'Tensile Properties of Crystalline Polymers: Linear Polyethylene', *Macromolecules*, 1994, 27, 5297–5310.
- H. J. Zimmermann and A. G. Hoechst: 'Structural analysis of random propylene-ethylene copolymers', *J. Macromol. Sci. Part B Phys.*, 2006,.
- M. Fujiyama: 'Structures and Properties of Injection Moldings of Glass Fiber-filled Polypropylenes', *Int. Polym. Process.*, 1993, 8, 245–254.
- M. Fujiyama, Y. Kitajima and H. Inata: 'Structure and properties of injection-molded polypropylenes with different molecular weight distribution and tacticity characteristics', *J. Appl. Polym. Sci.*, 2002, 84, 2142–2156.
- R. A. Vaia and H. D. Wagner: 'Framework for nanocomposites', *Mater. Today*, 2004, 7, 32–37.
- J. Jancar, J. F. Douglas, F. W. Starr, S. K. Kumar, P. Cassagnau, A. J. Lesser, S. S. Sternstein and M. J. Buehler: 'Current issues in research on structure–property relationships in polymer nanocomposites', *Polymer*, 2010, 51, 3321–3343.
- P. Cassagnau: 'Melt rheology of organoclay and fumed silica nanocomposites', *Polymer*, 2008, 49, 2183–2196.
- V. Vladimirov, C. Betchev, A. Vassiliou, G. Papageorgiou and D. Bikiaris: 'Dynamic mechanical and morphological studies of isotactic polypropylene/fumed silica nanocomposites with enhanced gas barrier properties', *Compos. Sci. Technol.*, 2006, 66, 2935–2944.
- S. Chung, W. Hahm, S. Im and S. Oh: 'Poly(ethylene terephthalate)(PET) nanocomposites filled with fumed silicas by melt compounding', *Macromol. Res.*, 2002, 10, 221–229.
- S. Matteucci, V. A. Kusuma, S. Swinnea and B. D. Freeman: 'Gas permeability, solubility and diffusivity in 1,2-polybutadiene containing brookite nanoparticles', *Polymer*, 2008, 49, 757–773.
- B. Wetzel, F. Hauptert, K. Friedrich, M. Q. Zhang and M. Z. Rong: 'Impact and wear resistance of polymer nanocomposites at low filler content', *Polym. Eng. Sci.*, 2002, 42, 1919–1927.
- R. J. Nussbaumer, W. R. Caseri, P. Smith and T. Tervoort: 'Polymer-TiO₂ Nanocomposites: A Route Towards Visually Transparent Broadband UV Filters and High Refractive Index Materials', *Macromol. Mater. Eng.*, 2003, 288, 44–49.

J. M. Pochan: 'Mechanics of Polymer–Clay Nanocomposites', *Macromolecules*, 2007, 40, 290–296.

A. Vermogen, K. Masenelli-Varlot, R. Séguéla, J. Duchet-Rumeau, S. Boucard and P. Prele: 'Evaluation of the Structure and Dispersion in Polymer-Layered Silicate Nanocomposites', *Macromolecules*, 2005, 38, 9661–9669.

W. Lertwimolnun and B. Vergnes: 'Effect of processing conditions on the formation of polypropylene/organoclay nanocomposites in a twin screw extruder', *Polym. Eng. Sci.*, 2006, 46, 314–323.

G. Zheng, J. Wu, W. Wang and C. Pan: 'Characterizations of expanded graphite/polymer composites prepared by in situ polymerization', *Carbon*, 2004, 42, 2839–2847.

H. Kim and C. W. Macosko: 'Morphology and Properties of Polyester/Exfoliated Graphite Nanocomposites', *Macromolecules*, 2008, 41, 3317–3327.

P. Steurer, R. Wissert, R. Thomann and R. Mülhaupt: 'Functionalized Graphenes and Thermoplastic Nanocomposites Based upon Expanded Graphite Oxide.', *Macromol. Rapid Commun.*, 2009, 30, 316–27.

H. Kim, S. Kobayashi, M. A. AbdurRahim, M. J. Zhang, A. Khusainova, M. A. Hillmyer, A. A. Abdala and C. W. Macosko: 'Graphene/polyethylene nanocomposites: Effect of polyethylene functionalization and blending methods', *Polymer*, 2011, 52, 1837–1846.

D. Cho, S. Lee, G. Yang, H. Fukushima and L. T. Drzal: 'Dynamic Mechanical and Thermal Properties of Phenylethynyl-Terminated Polyimide Composites Reinforced With Expanded Graphite Nanoplatelets', *Macromol. Mater. Eng.*, 2005, 290, 179–187.

Y. Kojima, A. Usuki, M. Kawasumi, A. Okada, Y. Fukushima, T. Kurauchi and O. Kamigaito: 'Mechanical properties of nylon 6-clay hybrid', *J. Mater. Res.*, 2011, 8, 1185–1189.

A. Usuki, Y. Kojima, M. Kawasumi, A. Okada, Y. Fukushima, T. Kurauchi and O. Kamigaito: 'Synthesis of nylon 6-clay hybrid', *J. Mater. Res.*, 1993, 8, 1179–1184.

J. Jancar: 'Interphase Phenomena in Polymer Micro- and Nanocomposites', in *Nano-Micromechanics Polym. Blends Compos.* 2009, Carl Hanser Verlag, pp. 241–266.

X. Jiang and L. T. Drzal: 'Improving electrical conductivity and mechanical properties of high density polyethylene through incorporation of paraffin wax coated exfoliated graphene nanoplatelets and multi-wall carbon nano-tubes', *Compos. Part A Appl. Sci. Manuf.*, 2011, 42, 1840–1849.

W. R. Caseri: 'Nanocomposites of polymers and inorganic particles: preparation, structure and properties', *Mater. Sci. Technol.*, 2006, 22, 807–817.

- S. K. Kumar, N. Jouault, B. Benicewicz and T. Neely: 'Nanocomposites with Polymer Grafted Nanoparticles', *Macromolecules*, 2013, 46, 3199–3214.
- M. Modesti, A. Lorenzetti, D. Bon and S. Besco: 'Thermal behaviour of compatibilised polypropylene nanocomposite: Effect of processing conditions', *Polym. Degrad. Stab.*, 2006, 91, 672–680.
- F. Bauer, H.-J. Gläsel, U. Decker, H. Ernst, A. Freyer, E. Hartmann, V. Sauerland and R. Mehnert: 'Trialkoxysilane grafting onto nanoparticles for the preparation of clear coat polyacrylate systems with excellent scratch performance', *Prog. Org. Coatings*, 2003, 47, 147–153.
- E. Tang, G. Cheng and X. Ma: 'Preparation of nano-ZnO/PMMA composite particles via grafting of the copolymer onto the surface of zinc oxide nanoparticles', *Powder Technol.*, 2006, 161, 209–214.
- C. Ligoure and L. Leibler: 'Thermodynamics and kinetics of grafting end-functionalized polymers to an interface', *J. Phys.*, 1990, 51, 1313–1328.
- L. S. Schadler, S. K. Kumar, B. C. Benicewicz, S. L. Lewis and S. E. Harton: 'Designed Interfaces in Polymer Nanocomposites: A Fundamental Viewpoint', *MRS Bull.*, 2011, 32, 335–340.
- C. Li and B. C. Benicewicz: 'Synthesis of Well-Defined Polymer Brushes Grafted onto Silica Nanoparticles via Surface Reversible Addition–Fragmentation Chain Transfer Polymerization', *Macromolecules*, 2005, 38, 5929–5936.
- C. Li, J. Han, C. Y. Ryu and B. C. Benicewicz: 'A Versatile Method To Prepare RAFT Agent Anchored Substrates and the Preparation of PMMA Grafted Nanoparticles', *Macromolecules*, 2006, 39, 3175–3183.
- X. Huang and M. J. Wirth: 'Surface-Initiated Radical Polymerization on Porous Silica', *Anal. Chem.*, 1997, 69, 4577–4580.
- J. Gao, J. Li, B. C. Benicewicz, S. Zhao, H. Hillborg and L. S. Schadler: 'The Mechanical Properties of Epoxy Composites Filled with Rubbery Copolymer Grafted SiO₂', *Polymers (Basel)*, 2012, 4, 187–210.
- W. Kaminsky, A. Funck and C. Klinke: 'In-situ Polymerization of Olefins on Nanoparticles or Fibers by Metallocene Catalysts', *Top. Catal.*, 2008, 48, 84–90.
- P. Dubois, M. Alexandre, F. Hindryckx and R. Jérôme: 'Polyolefin-Based Composites by Polymerization-Filling Technique', *J. Macromol. Sci. Part C Polym. Rev.*, 1998, 38, 511–565.

M. Alexandre, E. Martin, P. Dubois, M. Garcia-Marti and R. Jérôme: 'Use of metallocenes in the polymerization-filling technique with production of polyolefin-based composites', *Macromol. Rapid Commun.*, 2000, 21, 931–936.

M. Stürzel, F. Kempe, Y. Thomann, S. Mark, M. Enders and R. Mülhaupt: 'Novel Graphene UHMWPE Nanocomposites Prepared by Polymerization Filling Using Single-Site Catalysts Supported on Functionalized Graphene Nanosheet Dispersions', *Macromolecules*, 2012, 45, 6878–6887.

C. Park, Z. Ounaies, K. A. Watson, R. E. Crooks, J. Smith, S. E. Lowther, J. W. Connell, E. J. Siochi, J. S. Harrison and T. L. S. Clair: 'Dispersion of single wall carbon nanotubes by in situ polymerization under sonication', *Chem. Phys. Lett.*, 2002, 364, 303–308.

J. A. Ewen: 'Mechanisms of stereochemical control in propylene polymerizations with soluble Group 4B metallocene/methylalumoxane catalysts', *J. Am. Chem. Soc.*, 1984, 106, 6355–6364.

V. Busico, R. Cipullo, G. Talarico, A. L. Segre and L. Caporaso: 'High-Field ^{13}C NMR Characterization of Ethene-1- ^{13}C /Propene Copolymers Prepared with C_s -Symmetric ansa-Metallocene Catalysts: A Deeper Insight into the Regio- and Stereoselectivity of Syndiotactic Propene Polymerization', *Macromolecules*, 1998, 31, 8720–8724.

T. Tsutsui, A. Mizuno and N. Kashiwa: 'The microstructure of propylene homo- and copolymers obtained with a Cp_2ZrCl_2 and methylaluminoxane catalyst system', *Polymer*, 1989, 30, 428–431.

L. Resconi, I. Camurati and O. Sudmeijer: 'Chain transfer reactions in propylene polymerization with zirconocene catalysts', *Top. Catal.*, n.d., 7, 145–163.

C. De Rosa and F. Auriemma: 'Single site metallorganic polymerization catalysis as a method to probe the properties of polyolefins', *Polym. Chem.*, 2011, 2, 2155.

C. De Rosa, F. Auriemma, R. Di Girolamo and O. R. de Ballesteros: 'Crystallization of the mesomorphic form and control of the molecular structure for tailoring the mechanical properties of isotactic polypropylene', *J. Polym. Sci. Part B Polym. Phys.*, 2014, n/a–n/a.

J. R. Severn, J. C. Chadwick, R. Duchateau and N. Friederichs: "'Bound but not gagged"-immobilizing single-site alpha-olefin polymerization catalysts.', *Chem. Rev.*, 2005, 105, 4073–147.

D. E. Babushkin, N. V. Semikolenova, V. N. Panchenko, A. P. Sobolev, V. A. Zakharov and E. P. Talsi: 'Multinuclear NMR investigation of methylaluminoxane', *Macromol. Chem. Phys.*, 1997, 198, 3845–3854.

W. Spaleck, F. Kueber, A. Winter, J. Rohrmann, B. Bachmann, M. Antberg, V. Dolle and E. F. Paulus: 'The Influence of Aromatic Substituents on the Polymerization Behavior of Bridged Zirconocene Catalysts', *Organometallics*, 1994, 13, 954–963.

U. Stehling, J. Diebold, R. Kirsten, W. Roell, H. H. Brintzinger, S. Juengling, R. Muelhaupt and F. Langhauser: 'ansa-Zirconocene Polymerization Catalysts with Anelated Ring Ligands - Effects on Catalytic Activity and Polymer Chain Length', *Organometallics*, 1994, 13, 964–970.

L. Cavallo and G. Guerra: 'A Density Functional and Molecular Mechanics Study Of β -Hydrogen Transfer in Homogeneous Ziegler–Natta Catalysis', *Macromolecules*, 1996, 29, 2729–2737.

M. A. Milani, D. González, R. Quijada, N. R. S. Basso, M. L. Cerrada, D. S. Azambuja and G. B. Galland: 'Polypropylene/graphene nanosheet nanocomposites by in situ polymerization: Synthesis, characterization and fundamental properties', *Compos. Sci. Technol.*, 2013, 84, 1–7.

M. A. Milani, R. Quijada, N. R. S. Basso, A. P. Graebin and G. B. Galland: 'Influence of the graphite type on the synthesis of polypropylene/graphene nanocomposites', *J. Polym. Sci. Part A Polym. Chem.*, 2012, 50, 3598–3605.

F. de C. Fim, J. M. Guterres, N. R. S. Basso and G. B. Galland: 'Polyethylene/graphite nanocomposites obtained by in situ polymerization', *J. Polym. Sci. Part A Polym. Chem.*, 2010, 48, 692–698.

S. V. Polschikov, P. M. Nedorezova, A. N. Klyamkina, A. A. Kovalchuk, A. M. Aladyshev, A. N. Shchegolikhin, V. G. Shevchenko and V. E. Muradyan: 'Composite materials of graphene nanoplatelets and polypropylene, prepared by in situ polymerization', *J. Appl. Polym. Sci.*, 2013, 127, 904–911.

V. G. Shevchenko, S. V. Polschikov, P. M. Nedorezova, A. N. Klyamkina, A. N. Shchegolikhin, A. M. Aladyshev and V. E. Muradyan: 'In situ polymerized poly(propylene)/graphene nanoplatelets nanocomposites: Dielectric and microwave properties', *Polymer*, 2012, 53, 5330–5335.

L. T. Drzal and H. Fukushima: 'Expanded graphite and products produced therefrom', US7550529, published 2013.

S. Scheel, A. Rosehr, A. Poeppel and G. A. Luinstra: 'Polyolefin Composite Synthesis: From Small Scale to kg Material', *Macromol. Symp.*, 2013, 333, 227–232.

G. S. Constable, R. A. Gonzalez-Ruiz, R. M. Kasi and E. B. Coughlin: 'Gas Manifold for Olefin Polymerization and a Convenient Reactor Design for the Parallel Screening of Catalysts', *Macromolecules*, 2002, 35, 9613–9616.

- R. Bansal: 'Active carbon', 1988, New York, NY, M. Dekker.
- H. He, T. Riedl, A. Lurf and J. Klinowski: 'Solid-State NMR Studies of the Structure of Graphite Oxide', *J. Phys. Chem.*, 1996, 100, 19954–19958.
- W. Zheng and S.-C. Wong: 'Electrical conductivity and dielectric properties of PMMA/expanded graphite composites', *Compos. Sci. Technol.*, 2003, 63, 225–235.
- H. Kim, A. A. Abdala and C. W. Macosko: 'Graphene/Polymer Nanocomposites', *Macromolecules*, 2010, 43, 6515–6530.
- M. Grujicic, G. Cao and W. N. Roy: 'Atomistic simulations of the solubilization of single-walled carbon nanotubes in toluene', *J. Mater. Sci.*, 2004, 39, 2315–2325.
- K. Wakabayashi, P. J. Brunner, J. Masuda, S. A. Hewlett and J. M. Torkelson: 'Polypropylene-graphite nanocomposites made by solid-state shear pulverization: Effects of significantly exfoliated, unmodified graphite content on physical, mechanical and electrical properties', *Polymer*, 2010, 51, 5525–5531.
- K. Kalaitzidou, H. Fukushima, P. Askeland and L. T. Drzal: 'The nucleating effect of exfoliated graphite nanoplatelets and their influence on the crystal structure and electrical conductivity of polypropylene nanocomposites', *J. Mater. Sci.*, 2007, 43, 2895–2907.
- J. J. Janimak, S. Z. D. Cheng, A. Zhang and E. T. Hsieh: 'Isotacticity effect on crystallization and melting in polypropylene fractions: 3. Overall crystallization and melting behaviour', *Polymer*, 1992, 33, 728–735.
- J. M. Gómez-Elvira, P. Tiemblo, M. Elvira, L. Matisova-Rychla and J. Rychly: 'Relaxations and thermal stability of low molecular weight predominantly isotactic metallocene and Ziegler–Natta polypropylene', *Polym. Degrad. Stab.*, 2004, 85, 873–882.
- H. E. Miltner, G. Van Assche, A. Pozsgay, B. Pukánszky and B. Van Mele: 'Restricted chain segment mobility in poly(amide) 6/clay nanocomposites evidenced by quasi-isothermal crystallization', *Polymer*, 2006, 47, 826–835.
- B. Li and W.-H. Zhong: 'Review on polymer/graphite nanoplatelet nanocomposites', *J. Mater. Sci.*, 2011, 46, 5595–5614.
- K. Kalaitzidou, H. Fukushima and L. T. Drzal: 'A new compounding method for exfoliated graphite–polypropylene nanocomposites with enhanced flexural properties and lower percolation threshold', *Compos. Sci. Technol.*, 2007, 67, 2045–2051.
- B. M. Cromer, S. Scheel, G. A. Luinstra, E. B. Coughlin and A. J. Lesser: 'In-situ polymerization of isotactic polypropylene-nanographite nanocomposites', *Polymer*, 2015, 80, 275–281.

- Z. Tadmor and C. G. Gogos: 'Principles of Polymer Processing', 2nd ed. 2006, Hoboken, NJ, John Wiley & Sons, Inc.
- G. R. Strobl: 'The Physics of Polymers: Concepts for Understanding Their Structures and Behavior', 2007, Springer Science & Business Media.
- A. Addeo: 'Polypropylene Handbook', 2nd ed. 2005, Munich, Carl Hanser Verlag.
- R. Androsch, M. L. Di Lorenzo, C. Schick and B. Wunderlich: 'Mesophases in polyethylene, polypropylene, and poly(1-butene)', *Polymer*, 2010, 51, 4639–4662.
- C. De Rosa, F. Auriemma, R. Di Girolamo, O. Ruiz de Ballesteros, M. Pepe, O. Tarallo and A. Malafrente: 'Morphology and Mechanical Properties of the Mesomorphic Form of Isotactic Polypropylene in Stereodeficient Polypropylene', *Macromolecules*, 2013, 46, 5202–5214.
- I. M. Ward: 'Structure and Properties of Oriented Polymers', 1997, Springer.
- M. J. Mannion: 'Polyolefin composition containing ultrafine sorbitol and xylitol cetals', US5310950, published 1994.
- D. L. Dotson and N. A. Mehl: 'Modifying polyolefin properties, such as polypropylene clarification and nucleation', US6582503, published 2003.
- J. M. Torkelson, C. Pierre and A. Flores: 'Enhancing the physical properties of semi-crystalline polymers via solid-state shear pulverization.', US8729223 B2, published 2013.
- J. Varga, I. Mudra and G. W. Ehrenstein: 'Highly active thermally stable β -nucleating agents for isotactic polypropylene', *J. Appl. Polym. Sci.*, 1999, 74, 2357–2368.
- G. Lamberti: 'Flow-induced crystallization during isotactic polypropylene film casting', *Polym. Eng. Sci.*, 2011, 51, 851–861.
- R. H. Somani, B. S. Hsiao, A. Nogales, S. Srinivas, A. H. Tsou, I. Sics, F. J. Balta-Calleja and T. A. Ezquerra: 'Structure Development during Shear Flow-Induced Crystallization of i-PP: In-Situ Small-Angle X-ray Scattering Study', *Macromolecules*, 2000, 33, 9385–9394.
- S. Liedauer, G. Eder, H. Janeschitz-Kriegl, P. Jerschow, W. Geymayer and E. Ingolic: 'On the Kinetics of Shear Induced Crystallization in Polypropylene', *Int. Polym. Process.*, 1993, 8, 236–244.
- G. Eder, H. Janeschitz-Kriegl and S. Liedauer: 'Crystallization processes in quiescent and moving polymer melts under heat transfer conditions', *Prog. Polym. Sci.*, 1990, 15, 629–714.

- S. Liedauer, G. Eder and H. Janeschitz-Kriegl: 'On the Limitations of Shear Induced Crystallization in Polypropylene Melts', *Int. Polym. Process.*, 1995, 10, 243–250.
- C. Tribout, B. Monasse and J. M. Haudin: 'Experimental study of shear-induced crystallization of an impact polypropylene copolymer', *Colloid Polym. Sci.*, 1996, 274, 197–208.
- F. Sadeghi, A. Ajji and P. J. Carreau: 'Study of polypropylene morphology obtained from blown and cast film processes: Initial morphology requirements for making porous membrane by stretching', *J. Plast. Film Sheeting*, n.d., 21, 199–216.
- H.-X. Huang: 'Self-reinforcement of polypropylene by flow-induced crystallization during continuous extrusion', *J. Appl. Polym. Sci.*, 1998, 67, 2111–2118.
- M. D. Shelby, M. E. Donelson, S. Weinhold and H. P. Hall: 'Process for rapid crystallization of polyesters and co-polyesters via in-line drafting and flow-induced crystallization', US6159406, published 2000.
- P. Gilliard, C. Dehennau and P. J. A. Karsten: 'Low haze polypropylene film; free of nucleating additives', US6391432, published 2002.
- P. Gilliard: 'Pliable crystalline polymer and process for its production', US5306796, published 1994.
- I. M. Ward: 'Developments in oriented polymers, 1970–2004', *Plast. Rubber Compos.*, 2013,.
- I. M. Ward and P. J. Hine: 'The science and technology of hot compaction', *Polymer*, 2004, 45, 1413–1427.
- T. Bárány, J. Karger-Kocsis and T. Czigány: 'Development and characterization of self-reinforced poly(propylene) composites: carded mat reinforcement', *Polym. Adv. Technol.*, 2006, 17, 818–824.
- A. Izer and T. Barany: 'Hot consolidated all-PP composites from textile fabrics composed of isotactic PP filaments with different degrees of orientation', *Express Polym. Lett.*, 2007, 1, 790–796.
- J. Rasburn, P. J. Hine, I. M. Ward, R. H. Olley, D. C. Bassett and M. A. Kabeel: 'The hot compaction of polyethylene terephthalate', *J. Mater. Sci.*, 1995, 30, 615–622.
- P. Rojanapitayakorn, P. T. Mather, A. J. Goldberg and R. A. Weiss: 'Optically transparent self-reinforced poly(ethylene terephthalate) composites: molecular orientation and mechanical properties', *Polymer*, 2005, 46, 761–773.

- P. J. Hine, I. M. Ward, M. I. A. EL Maaty, R. H. Olley and D. C. Bassett: 'The hot compaction of 2-dimensional woven melt spun high modulus polyethylene fibres', *J. Mater. Sci.*, n.d., 35, 5091–5099.
- P. J. Hine, I. M. Ward, N. D. Jordan, R. H. Olley and D. C. Bassett: 'A Comparison of the Hot-Compaction Behavior of Oriented, High-Modulus, Polyethylene Fibers and Tapes', *J. Macromol. Sci. Part B*, 2007,.
- M. I. Abo El-Maaty, D. C. Bassett, R. H. Olley, P. J. Hine and I. M. Ward: 'The hot compaction of polypropylene fibres', *J. Mater. Sci.*, 1996, 31, 1157–1163.
- B. Pornnimit and G. W. Ehrenstein: 'Extrusion of self-reinforced polyethylene', *Adv. Polym. Technol.*, 1991, 11, 91–98.
- H. Huang: 'High property high density polyethylene extrudates prepared by self-reinforcement', *J. Mater. Sci. Lett.*, n.d., 17, 591–593.
- H.-X. Huang: 'Continuous extrusion of self-reinforced high density polyethylene', *Polym. Eng. Sci.*, 1998, 38, 1805–1811.
- I. M. Ward, P. D. Coates and M. M. Dumoulin: 'Solid Phase Processing of Polymers', 2000, Carl Hanser Verlag.
- A. K. Taraiya and I. M. Ward: 'Production and properties of biaxially oriented polyethylene tubes', *J. Appl. Polym. Sci.*, 1996, 59, 627–638.
- J. Li and Y.-W. Lee: 'Evolution of morphology in high molecular weight polyethylene during die drawing', *J. Mater. Sci.*, 1993, 28, 6496–6502.
- J. Mohanraj, N. Chapleau, A. Ajji, R. A. Duckett and I. M. Ward: 'Production, properties and impact toughness of die-drawn toughened polypropylenes', *Polym. Eng. Sci.*, 2003, 43, 1317–1336.
- C. I. Ogbonna, G. Kalay, P. S. Allan and M. J. Bevis: 'The self-reinforcement of polyolefins produced by shear controlled orientation in injection molding', *J. Appl. Polym. Sci.*, 1995, 58, 2131–2135.
- Q. Guan, X. Zhu, D. Chiu, K. Shen, F. S. Lai and S. P. McCarthy: 'Self-reinforcement of polypropylene by oscillating packing injection molding under low pressure', *J. Appl. Polym. Sci.*, 1996, 62, 755–762.
- G. Kalay and M. J. Bevis: 'Processing and physical property relationships in injection-molded isotactic polypropylene. 1. mechanical properties', *J. Polym. Sci. Part B Polym. Phys.*, 1997, 35, 241–263.

- G. Kalay and M. J. Bevis: 'Processing and physical property relationships in injection-molded isotactic polypropylene. 1. mechanical properties', *J. Polym. Sci. Part B Polym. Phys.*, 1997, 35, 265–291.
- L.-M. Chen and K. Shen: 'Biaxial self-reinforcement of isotactic polypropylene prepared in uniaxial oscillating stress field by injection molding. II. Morphology', *J. Appl. Polym. Sci.*, 2000, 78, 1911–1917.
- A. M. Freedman, D. C. Bassett, A. S. Vaughan and R. H. Olley: 'On quantitative permanganic etching', *Polymer*, 1986, 27, 1163–1169.
- J. Park, K. Eom, O. Kwon and S. Woo: 'Chemical Etching Technique for the Investigation of Melt-crystallized Isotactic Polypropylene Spherulite and Lamellar Morphology by Scanning Electron Microscopy', *Microsc. Microanal.*, 2002, 7, 276–286.
- P. Crouzet, A. Martens and P. Mangin: 'Universal Calibration in Permeation Chromatography. Application to Polyethylenes, Polypropylene, and Ethylene-Propylene Copolymers', *J. Chromatogr. Sci.*, 1971, 9, 525–530.
- 'The Polymer Data Handbook', 2009, Oxford University Press, Incorporated.
- R. Hingmann, J. Rieger and M. Kersting: 'Rheological Properties of a Partially Molten Polypropylene Random Copolymer during Annealing', *Macromolecules*, 1995, 28, 3801–3806.
- J.-H. Chen, F.-C. Tsai, Y.-H. Nien and P.-H. Yeh: 'Isothermal crystallization of isotactic polypropylene blended with low molecular weight atactic polypropylene. Part I. Thermal properties and morphology development', *Polymer*, 2005, 46, 5680–5688.
- W. Stocker, S. N. Magonov, H. J. Cantow, J. C. Wittmann and B. Lotz: 'Contact faces of epitaxially crystallized alpha- and gamma-phase isotactic polypropylene observed by atomic force microscopy', *Macromolecules*, 1993, 26, 5915–5923.
- T. Ikeda, V. A. Ravi and G. J. Snyder: 'Evaluation of true interlamellar spacing from microstructural observations', *J. Mater. Res.*, 2011, 23, 2538–2544.
- I. M. Hodge: 'Physical aging in polymer glasses.', *Science*, 1995, 267, 1945–7.
- K. L. Ngai and C. M. Roland: 'Intermolecular cooperativity and the temperature dependence of segmental relaxation in semicrystalline polymers', *Macromolecules*, 1993, 26, 2688–2690.
- M. F. Butler, A. M. Donald and A. J. Ryan: 'Time resolved simultaneous small- and wide-angle X-ray scattering during polyethylene deformation: 1. Cold drawing of ethylene- α -olefin copolymers', *Polymer*, 1997, 38, 5521–5538.

- M. F. Butler, A. M. Donald and A. J. Ryan: 'Time resolved simultaneous small- and wide-angle X-ray scattering during polyethylene deformation 3. Compression of polyethylene', *Polymer*, 1998, 39, 781–792.
- A. Sedighiamiri, L. E. Govaert, M. J. W. Kanters and J. A. W. van Dommelen: 'Micromechanics of semicrystalline polymers: Yield kinetics and long-term failure', *J. Polym. Sci. Part B Polym. Phys.*, 2012, 50, 1664–1679.
- B. A. G. Schrauwen, R. P. M. Janssen, L. E. Govaert and H. E. H. Meijer: 'Intrinsic Deformation Behavior of Semicrystalline Polymers', *Macromolecules*, 2004, 37, 6069–6078.
- R. N. Haward: 'Strain hardening of thermoplastics', *Macromolecules*, 1993, 26, 5860–5869.
- R. Haward: 'The derivation of a strain hardening modulus from true stress-strain curves for thermoplastics', *Polymer*, 1994, 35, 3858–3862.
- J. M. Torkelson and K. Wakabayashi: 'Polymer-graphite nanocomposites via solid-state shear pulverization', US7906053 B1, published 2009.
- K. Wakabayashi, M. B. Stephen and M. D. Boches: 'Process for producing exfoliated and/or dispersed polymer composites and/or nanocomposites via solid-state/melt extrusion (ssme)', WO2013059321A1, published 2013.
- X. Jiang and L. T. Drzal: 'Reduction in percolation threshold of injection molded high-density polyethylene/exfoliated graphene nanoplatelets composites by solid state ball milling and solid state shear pulverization', *J. Appl. Polym. Sci.*, 2012, 124, 525–535.
- K. Wang, S. Liang, R. Du, Q. Zhang and Q. Fu: 'The interplay of thermodynamics and shear on the dispersion of polymer nanocomposite', *Polymer*, 2004, 45, 7953–7960.
- K. Wakabayashi, C. Pierre, D. A. Dikin, R. S. Ruoff, T. Ramanathan, L. C. Brinson and J. M. Torkelson: 'Polymer–Graphite Nanocomposites: Effective Dispersion and Major Property Enhancement via Solid-State Shear Pulverization', *Macromolecules*, 2008, 41, 1905–1908.
- C. Bartholome, E. Beyou, E. Bourgeat-Lami, P. Cassagnau, P. Chaumont, L. David and N. Zydowicz: 'Viscoelastic properties and morphological characterization of silica/polystyrene nanocomposites synthesized by nitroxide-mediated polymerization', *Polymer*, 2005, 46, 9965–9973.
- R. T. DeHoff and F. N. Rhines: 'Quantitative Microscopy', 1968, New York, NY, McGraw-Hill Book Company.

- E. E. Underwood: 'Quantitative Stereology', 1970, Reading, Massachusetts, Addison-Wesley Publishing Company.
- S. A. Saltykov: The Determination of the Size Distribution of Particles in an Opaque Material from a Measurement of the Size Distribution of Their Sections, in Proc. Second Int. Cong. Stereol. 1967, pp. 163–173.
- S. A. Saltykov: 'Stereometric Metallography', 2nd ed. 1958, Moscow.
- W. A. Johnson: 'Estimation of Spatial Grain Sizes', Met. Prog., 1946, 49, 87.
- C. A. Schneider, W. S. Rasband and K. W. Eliceiri: 'NIH Image to ImageJ: 25 years of image analysis', Nat. Methods, 2012, 9, 671–675.
- T.-H. Tsai, A. M. Maes, M. A. Vandiver, C. Versek, S. Seifert, M. Tuominen, M. W. Liberatore, A. M. Herring and E. B. Coughlin: 'Synthesis and structure-conductivity relationship of polystyrene- block -poly(vinyl benzyl trimethylammonium) for alkaline anion exchange membrane fuel cells', J. Polym. Sci. Part B Polym. Phys., 2013, 51, 1751–1760.
- M. Liu, B. Guo, M. Du, F. Chen and D. Jia: 'Halloysite nanotubes as a novel β -nucleating agent for isotactic polypropylene', Polymer, 2009, 50, 3022–3030.
- H. Fukushima.: Graphite Nanoreinforcements in Polymer Nanocomposites (Michigan State University, 2003).
- S. Kim, I. Do and L. T. Drzal: 'Thermal stability and dynamic mechanical behavior of exfoliated graphite nanoplatelets-LLDPE nanocomposites', Polym. Compos., 2009, 31, 755–761.
- K. Kalaitzidou, H. Fukushima and L. T. Drzal: 'Mechanical properties and morphological characterization of exfoliated graphite–polypropylene nanocomposites', Compos. Part A Appl. Sci. Manuf., 2007, 38, 1675–1682.
- C. W. Macosko: 'Rheology: principles, measurements, and applications', 1994, Wiley-VCH.
- K. Kalaitzidou, H. Fukushima and L. T. Drzal: 'Multifunctional polypropylene composites produced by incorporation of exfoliated graphite nanoplatelets', Carbon, 2007, 45, 1446–1452.
- S.-P. Rwei, I. Manas-Zloczower and D. L. Feke: 'Analysis of dispersion of carbon black in polymeric melts and its effect on compound properties', Polym. Eng. Sci., 1992, 32, 130–135.

J. M. DallaValle and A. Klemin: 'Micrometitics: The Technology of Fine Particles', 1943, New York, NY, Pitman Pub. Corp.

J. E. Funk and D. R. Dinger: 'Predictive Process Control of Crowded Particulate Suspensions', 1994, Boston, MA, Springer US.

T. Lozano, P. G. Lafleur, M. Grmela and B. Vergnes: 'Modeling Filler Dispersion along a Twin-Screw Extruder', *Int. Polym. Process.*, 2013,.

A. Nir and A. Acrivos: 'On the creeping motion of two arbitrary-sized touching spheres in a linear shear field', *J. Fluid Mech.*, 2006, 59, 209.

I. Manas-Zloczower, A. Nir and Z. Tadmor: 'Dispersive Mixing in Internal Mixers—A Theoretical Model Based on Agglomerate Rupture', *Rubber Chem. Technol.*, 1982, 55, 1250–1285.

H. Rumpf: *The Strength of Granules and Agglomerates*, in *Agglomeration*, 1st ed., ed. W. A. Knepper 1962, New York, NY, Wiley-Interscience.

M. Härtelt, H. Riesch-Oppermann and O. Kraft: 'Statistical analysis and predictions of fracture and fatigue of micro-components', *Microsyst. Technol.*, 2011, 17, 325–335.

G. R. McDowell and J. P. de Bono: 'On the micro mechanics of one-dimensional normal compression', *Géotechnique Lett.*, 2013, 3, 166–172.

G. R. McDowell: 'On the Yielding and Plastic Compression of Sand.', *SOILS Found.*, 2002, 42, 139–145.

W. L. Lim, G. R. McDowell and A. C. Collop: 'The application of Weibull statistics to the strength of railway ballast', *Granul. Matter*, 2004, 6, 229–237.

G. I. Taylor: *The Formation of Emulsions in Definable Fields of Flow*, in *Proc. R. Soc. London*, 1934, pp. 501–523.

U. Sundararaj, C. W. Macosko, R. J. Rolando and H. T. Chan: 'Morphology development in polymer blends', *Polym. Eng. Sci.*, 1992, 32, 1814–1823.

E. Van Hemelrijck, P. Van Puyvelde, S. Velankar, C. W. Macosko and P. Moldenaers: 'Interfacial elasticity and coalescence suppression in compatibilized polymer blends', *J. Rheol. (N. Y. N. Y.)*, 2004, 48, 143.

L. Levitt and C. W. Macosko: 'Shearing of Polymer Drops with Interface Modification', *Macromolecules*, 1999, 32, 6270–6277.

C. W. Macosko: 'Morphology development and control in immiscible polymer blends', *Macromol. Symp.*, 2000, 149, 171–184.

F. Rumscheidt and S. . Mason: 'Particle motions in sheared suspensions XII. Deformation and burst of fluid drops in shear and hyperbolic flow', *J. Colloid Sci.*, 1961, 16, 238–261.

B. M. Cromer, E. B. Coughlin and A. J. Lesser: 'Evaluation of a new processing method for improved nanocomposite dispersions', *Nanocomposites*, 2015, 1, 152–159.

A. Nogales, B. . Hsiao, R. . Somani, S. Srinivas, A. . Tsou, F. . Balta-Calleja and T. . Ezquerra: 'Shear-induced crystallization of isotactic polypropylene with different molecular weight distributions: in situ small- and wide-angle X-ray scattering studies', *Polymer*, 2001, 42, 5247–5256.

R. H. Somani, L. Yang and B. S. Hsiao: 'Effects of high molecular weight species on shear-induced orientation and crystallization of isotactic polypropylene', *Polymer*, 2006, 47, 5657–5668.

D. J. Lohse, C. A. Mitchell and M. Sansone: 'Polymer compositions exhibiting enhanced flow-induced crystallization', US 20090163666, published 2009.

L. Balzano, S. Rastogi and G. W. M. Peters: 'Flow Induced Crystallization in Isotactic Polypropylene–1,3:2,4-Bis(3,4-dimethylbenzylidene)sorbitol Blends: Implications on Morphology of Shear and Phase Separation', *Macromolecules*, 2008, 41, 399–408.

A. Somwangthanaroj, E. C. Lee and M. J. Solomon: 'Early Stage Quiescent and Flow-Induced Crystallization of Intercalated Polypropylene Nanocomposites by Time-Resolved Light Scattering', *Macromolecules*, 2003, 36, 2333–2342.